RUPERTO-CAROLA UNIVERSITY OF HEIDELBERG

Measurement of neutral mesons and direct photons in Pb–Pb collisions at $\sqrt{s_{\mathrm{NN}}} = 2.76$ TeV with the ALICE experiment at the LHC

by

Lucia Leardini

Physikalisches Institut
Ruperto-Carola University of Heidelberg

A thesis submitted in partial fulfillment for the
degree of Doctor of Natural Science

Heidelberg 2017

Dissertation
submitted to the
Combined Faculties of the Natural Sciences and Mathematics
of the Ruperto-Carola University of Heidelberg, Germany
for the degree of
Doctor of Natural Sciences

put forward by
Lucia Leardini
born in Cattolica, Italy

Oral examination: 20 November 2017

Measurement of neutral mesons and direct photons
in Pb–Pb collisions at $\sqrt{s_{\rm NN}} = 2.76$ TeV
with the ALICE experiment at the LHC

Referees: Prof. Dr. Johanna Stachel

Prof. Dr. Hans-Christian Schultz-Coulon

Abstract

The Quark-Gluon Plasma (QGP) is a strongly interacting matter with high temperature and energy density, where partons are deconfined. It is hypothesised being the same state the universe was in just a few microseconds after the Big Bang. Experimentally, the QGP is studied at accelerator experiments using heavy-ions. The presence of a deconfined phase after the ultra-relativistic collisions is expected to influence the system evolution. The search for modifications induced on the particle production is carried out taking elementary particle collisions as reference measurement.
The research presented in this thesis focuses on the study of neutral meson and direct photon production in lead ion collisions at $\sqrt{s_{\mathrm{NN}}} = 2.76$ TeV with the ALICE detector at the Large Hadron Collider. The neutral pion and η mesons are reconstructed via their photon decay channel, exploiting the photon conversions in the detector material. A modification of the meson spectra is observed and investigated further with the comparison to similar experimental results as well as theoretical models.
The measurement of neutral mesons is essential for the study of direct photon production, since decay photons are the largest background for this signal. The photon excess signal on top of the decay photon background in the transverse momentum interval $1 < p_{\mathrm{T}} < 1.6$ GeV/c is measured with a significance of 1.5 σ. In this region, direct photons are expected to originate from a phase of the QGP where the system is thermalised. In an attempt to describe the phenomenon behind the observed signal, comparisons to several theoretical predictions have been performed.

Das Quark Gluon Plasma (QGP) ist ein Phasenzustand stark wechselwirkender Materie bei hoher Temperatur und Energiedichte, in dem Partonen nicht mehr in Hadronen eingeschlossen sind und von dem angenommen wird, dass es der Zustand zu Beginn des Universums kurz nach dem Urknall war. Das QGP wird experimentell in Beschleunigerexperimenten mit Schwerionen untersucht. Insbesondere werden Abweichungen der Teilchenproduktion im Vergleich zu Referenzmessungen in elementaren Teilchenkollisionen betrachtet.
Diese Dissertation befasst sich mit der Untersuchung der Produktion neutraler Mesonen und direkter Photonen in Pb–Pb Kollisionen bei einer Schwerpunktenergie von $\sqrt{s_{\mathrm{NN}}} = 2.76$ TeV mit dem ALICE Detektor am Large Hadron Collider. Neutrale Pionen und η Mesonen werden durch ihren Photonenzerfallskanal via Photonenkonversion im Detektormaterial rekonstruiert. Die beobachtete Modifikation der Mesonenspektren wird dann mit anderen experimentellen Ergebnissen und theoretischen Modellen verglichen. Die Messung neutraler Mesonen ist wesentlich für die Untersuchung der Produktion direkter Photonen, da Zerfallsphotonen den größten Untergrund für dieses Signal darstellen. Im Transversalimpulsintervall $1 < p_{\mathrm{T}} < 1.6$ GeV/c wird mit einer Signifikanz von 1.5 σ ein Überschuss direkter Photonen gemessen. In diesem Transversalimpulsbereich wird erwartet, dass die aus der thermalisierten QGP-Phase stammenden Photonen zur Produktion beitragen. Um das dem beobachteten Signal zu Grunde liegende Phänomen genauer einzuordnen, wurden Vergleiche mit mehreren Theorievorhersagen durchgeführt.

Contents

Introduction

Scientific research is a travel in uncharted territory. We leave behind the solid ground of fundamental knowledge and walk on the path built by our predecessors. We improve it, solidifying the foundations on which we will step next and increasing the details of the map that will lead us to a better understanding of our world. The farther away we go, the more uncertain the path becomes, it splits and loses the well defined edges. Even though we may encounter dead ends, given by wrong assumptions, they are not failures. They instruct us to search somewhere else, or to look at things in a different way. And experiments, like torches in the night, shed light on our steps and help us along the way.
Physics has come from assuming solid objects as basic structure of matter to theorise and prove that the inner workings of matter are all but trivial shapes, they are a multitude of elements interacting with each other and whose complexity increases the closer we look.
On the opposite end of the horizon is the origin of the universe. How it came to be what we see today is still explained only with a collection of theories edging towards the most probable scenario.
The Quark-Gluon Plasma is the linking point between these two extremes: a deconfined medium which is expected after a heavy-ion collision, and that is theorised to have formed after the Big Bang. Ultra-relativistic heavy-ion collisions are the perfect tool to study this phenomenon. They not only allow for the study of fundamental interactions and their influence on matter but, at the same time, recreate in the laboratory the same conditions that about billion of years ago followed the Big Bang, before the fundamental forces coagulated particles into objects such as stars and planets that compose the universe we know today.
The aftermath of the heavy-ion collisions is investigated with the most sophisticated machines and technologies. The results delivered by the experimental apparatuses are compared to state-of-the-art theoretical models to deepen and improve our knowledge of the underlying phenomena.

The focus of the doctoral research presented in this thesis is the study of the neutral pion and η meson production and the direct photon measurement in Pb–Pb collisions at a centre-of-mass energy of $\sqrt{s_{\mathrm{NN}}} = 2.76$ TeV. The two-photon decay channel is used to reconstruct the neutral mesons. The photons are measured exploiting their conversion in electron-positron pairs, mediated by the detector material.
Neutral meson production is interesting in its own right, especially for the η meson, which was never measured at this energy before. Furthermore, its dependence on the particle multiplicity and momentum can shed light on which production mechanisms are involved. The presence (or absence) of deviations from the expected behaviour is investigated with the comparison of the neutral pion and η meson to the charged pion and kaon measurements,

a comparison motivated by the similarities between these particles, such as quark content and mass. Last, the neutral mesons, whose most probable decay channel is a photonic one, are needed to quantify the background of the direct photon measurement. A rather good knowledge of the decay photon background is an essential baseline for a good direct photon measurement.
Photons are electromagnetic probes of the Quark-Gluon Plasma and, as such, they do not interact with the QCD matter. While in general particle production is bound to the study of the later stages of the heavy-ion collisions, direct photons, *i.e.* photons not coming from particle decays, can access information on the early phases instead such as, for example, the temperature of the initial QGP medium.

The thesis is structured as follows. The first chapter is dedicated to the theoretical background of the measurements presented here. A brief and generic description of the behaviour of matter and of the strong interaction under extreme conditions is given, followed by how this can be studied in heavy-ion collisions. The most important observables are listed, together with the motivations for the measurements that are object of this thesis and how these fit in the overall picture.
The second chapter introduces the ALICE detector at the Large Hadron Collider.
The subsequent three chapters are of a more technical nature and illustrate the steps taken from obtaining the best possible data sample, extracting the signal and applying the efficiency corrections to the final results.
Chapter six gathers the most significant results for the neutral meson measurement achieved in the course of this doctoral research. These are compared to other ALICE measurements, similar results from other experiments and theoretical predictions.
Chapter seven and eight introduce, respectively, the electromagnetic cocktail simulation for the estimation of the decay photon contribution and the analysis details to obtain the photon sample to be used in the direct photon measurement.
Chapter nine presents the final direct photon results and compares them to theory models.
The conclusions reached are summarised in the last chapter.

Chapter 1

From basic Quantum Chromodynamics to the Quark-Gluon Plasma

In this chapter, a general introduction to the theory describing the strong interaction is presented. The steps that brought us from a simple picture to the collection of theoretical models and experimental evidences that compose our knowledge of the state of the matter known as Quark-Gluon Plasma will be given.

1.1 Quantum Chromodynamics

Quantum Chromodynamics (QCD) is a non-abelian gauge field theory describing the strong interaction. Its history started in the early 1960s, when Gell-Mann [1] and Ne'eman [2] independently introduced the flavour SU(3) group representation to explain the observation of the kaons, hyperons and Δ resonances. Later on, Gell-Mann [3] and Zweig [4] hypothesised that baryons and mesons are made up of quarks, elementary particles with fractional electromagnetic charge. However, the existence of the Δ^{++} and Ω^{-} baryons was yet unexplained: composed of three up quarks and three strange quarks, respectively, they appeared to violate Pauli exclusion principle. The pieces fell into place in 1971, when Fritzsch and Gell-Mann introduced for the first time three additional charges, the colour charges, and the SU(3) colour symmetry [5, 6]. This theory agrees with the results obtained by Feynman for the parton model [7], in which partons are identified with quarks. Experimental confirmation came from the results of inelastic electron-proton collisions obtained at the Stanford Linear Accelerator Centre (SLAC) [8] and from the ratio of the hadronic to the muon cross-section for electron-positron annihilation [9, 10]. The ratio is expected to be dependent on the square of the quark electric charge and on the number of colours. Experimentally, this dependence has been found to be $R = 3\sum_{flavour} q_f^2$, with q_f electric charge of the quark of flavour f, over a wide range of centre-of-mass energies. In the SLAC experiment, the scaling behaviour of the measured inelastic cross sections of electron-proton scattering, introduced by Bjorken [11], can be explained assuming the proton constituents to be point-like objects, as in the parton model.

QCD shares common features with its sister theory describing the electromagnetic interaction, Quantum Electrodynamics (QED), such as having particle charges (electric charge and colour charge) and being mediated by the exchange of a massless boson (photons and gluons) [12]. Yet, the differences that characterise QCD make it a more elaborate theory. The most striking fact is that not only quarks, but also gluons carry colour. This means that they can self-interact, adding gluon-only interaction vertexes and bound states of interacting gluons, called *glueballs*, and thus bringing a new level of complexity to the calculations.
Another significant difference between QED and QCD is the running coupling constant, where "running" indicates that it is not actually a constant but it depends on the interaction energy. In QED, the coupling constant is small at low energies, $\alpha \approx 1/137$, and increases with larger transferred momentum Q. The behaviour is rather the opposite in QCD. For quarks and gluons, the strong coupling constant α_s is described at leading order (LO) by

$$\alpha_s(Q^2) = \frac{\alpha_s(\mu^2)}{1 + (\alpha_s(\mu^2)/12\pi)(11n_c - 2n_f)\ln(Q^2/\mu^2)} \tag{1.1}$$

where n_c is the number of colours, n_f the number of quark flavours and μ the energy scale [12].

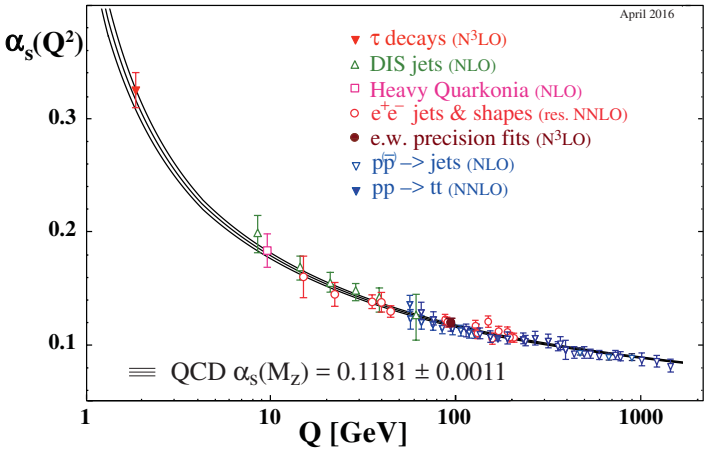

FIGURE 1.1: Running coupling constant of the strong interaction as a function of the energy scale, the transferred momentum Q. The value of α_s at the Z boson mass is reported. The points indicate the measurements of α_s at discrete energy scales Q, with the level of approximation used for extracting the value given in parentheses in the legend [9].

The strong coupling constant cannot be estimated at low energies, for $Q^2 = 0$, because its value is too large to allow for perturbative calculations (pQCD), as it can also be seen in Figure 1.1. At low energies, the potential between quarks is parametrised as $V_{q\bar{q}}(r) = -4\alpha_s/3r + Kr$, where the first term is the Coulomb term and the second term is the "elastic" force characteristic of the strong interaction. For increasing radius, the potential that keeps two quarks together also increases, as if it was an elastic string connecting the quarks. At some point, the potential necessary to pull the two quarks apart is large enough to create another quark pair, hence the elastic string snaps and a new quark-antiquark pair is formed. This phenomenon is referred to as *infrared slavery*: at low energy, quarks are confined into hadrons and no unbound state is observed. At high energies, basically the opposite behaviour is observed and is called *asymptotic freedom*[1]. For $11n_c > 2n_f$, which is the case with the

[1]This discovery was of such importance that Gross, Wilczek and Politzer were awarded the Nobel Prize for it in 2004.

3 colours and 6 flavours of the Standard Model, the anti-screening effect of the gluons is stronger than the screening given by the quarks: the strong coupling constant is small and the coupling is weak. This is one of the most significant results in QCD, as it allows for the use of Feynman diagrams and perturbative calculations to describe the strong interaction. Therefore, the coupling constant can be rewritten as a function of the energy scale at which α_s is small. Given $\Lambda_{QCD} = \ln \mu^2 - 12\pi/[(11n_c - 2n_f)\alpha_s(\mu^2)]$ and the explicit colour number,

$$\alpha_s(Q^2) = \frac{12\pi}{(33 - 2n_f)\ln(Q^2/\Lambda^2_{QCD})}. \tag{1.2}$$

It needs to be noted that n_f also depends on Q^2, since the number of flavours accessible depends on the energy available. Likewise Λ_{QCD}, which can be understood as the energy scale at which pQCD diverges, depends on the number of flavours. It is then more convenient to quote the value for α_s calculated at the Z boson mass, $M_Z = 91.18$ GeV, which gives $\alpha_s(M_Z) = 0.1181 \pm 0.0011$. The results for $\alpha_s(Q^2)$ at discrete energy scales Q are also shown in Figure 1.1 for different level of approximation.

As mentioned above, Λ_{QCD} is giving the limits of validity of pQCD. The standard treatment of QCD in the low-energy regime is Lattice QCD (LQCD), introduced by Wilson [13]. The starting point of LQCD is moving from a Minkowski to an Euclidean space-time, achieved with a Wick rotation, for which $t \to -i\tau$. Space-time is then discretised and interpreted as a lattice where the spacing a provides the ultraviolet cut-off, *i.e.* the finite size limit. The physical quantities of interest are still well defined for $a \to 0$, where the QCD environment in a continuous space is recovered. The non-perturbative treatment consists in the numerical evaluation of the path integrals defining QCD on the lattice. The discretisation also allows for computer simulation, using the Monte Carlo method, where the size of the lattice is only limited by the computing resources. The statistical uncertainties of the lattice calculations are due to the Monte Carlo simulation statistics, while the systematic uncertainties are mainly originating from working with a finite volume.

The existence of *asymptotic freedom* hints that there is a transition point between the phase where quarks and gluons are bound and hadronic matter dominates, and the phase where hadrons become unbound and partons are free [14–16]. A phase transition could take place if certain critical conditions of high temperature and/or high net baryon densities are reached. Such a scenario is expected when colliding heavy nuclei at relativistic energies: the high energy density permits quarks and gluons to roam freely in a Quark-Gluon Plasma state.

In the following chapters, more details will be given on the QCD phase transition, on the stages and evolution of the system in a heavy-ion collision.

1.1.1 QCD phase transition

A transition between hadronic matter and a deconfined state of quarks and gluons is expected to occur when sufficiently high temperature and density are reached [17]. The concept of a maximum temperature for the hadronic matter was first introduced by R. Hagedorn [18] in 1965: he concluded that the exponentially increasing number of hadronic states imply a limiting temperature above which matter cannot exist. With the advent of the QCD, this idea was interpreted differently. The limiting temperature is seen as delineating a transition from the commonly know hadronic matter to a new state where quarks and gluons are the

degrees of freedom.

QCD provides, in the form of chiral symmetry restoration, a way to pin down at which conditions of temperature, pressure and energy density the phase transition takes place. The finite up and down quark masses lead to the explicit breaking of chiral symmetry, with the pions as Goldstone bosons [19]. Furthermore, chiral symmetry is also spontaneously broken, giving rise to a non-vanishing chiral condensate $\langle\bar{\psi}\psi\rangle$ [19]. It is hypothesised that chiral symmetry restoration and a vanishing chiral condensate reflect a phase transition, associated with a drastic change in the thermodynamic observables. While the chiral condensate is the order parameter in the chiral limit of vanishing quark masses, the expectation value of the renormalised Polyakov loop [20] can be taken as an indication of deconfinement, in a pure gauge theory and in the limit of infinitely heavy quark masses. The Polyakov loop is related to the free energy of a static quark anti-quark pair. These two quantities, the chiral condensate and the Polyakov loop, are used to study the chiral and deconfinement transitions, respectively, using lattice QCD calculations, which assume two light quarks and a heavier one, referred to as (2 + 1), in order to extract the relevant thermodynamic observables. Chiral symmetry restoration and deconfinement are not identical observables, but are thought to be closely correlated. The result of the LQCD calculations assuming physical values for the quark masses, such as $m_{u,d}/m_s = 1/27$, gives, in the continuum limit, a value of $T_c = (154 \pm 9)$ MeV for the chiral transition temperature [21]. This result, obtained by the HotQCD Collaboration [21], is in agreement with the values obtained by the Budapest-Wuppertal Collaboration [22, 23].

From LQCD studies it is also evident that the nature of the transition (whether first or second order or a cross-over) to deconfined matter depends on the mass and flavours of the quarks considered in the lattice calculations [20, 24, 25]. In Figure 1.2, left, the conclusions about the nature of the phase transition from the most recent lattice calculations are summarised. In this representation, the light (up and down) quarks have degenerate mass, $m_u = m_d = m_l$, and the heavier strange quark has mass m_s. Furthermore, a zero

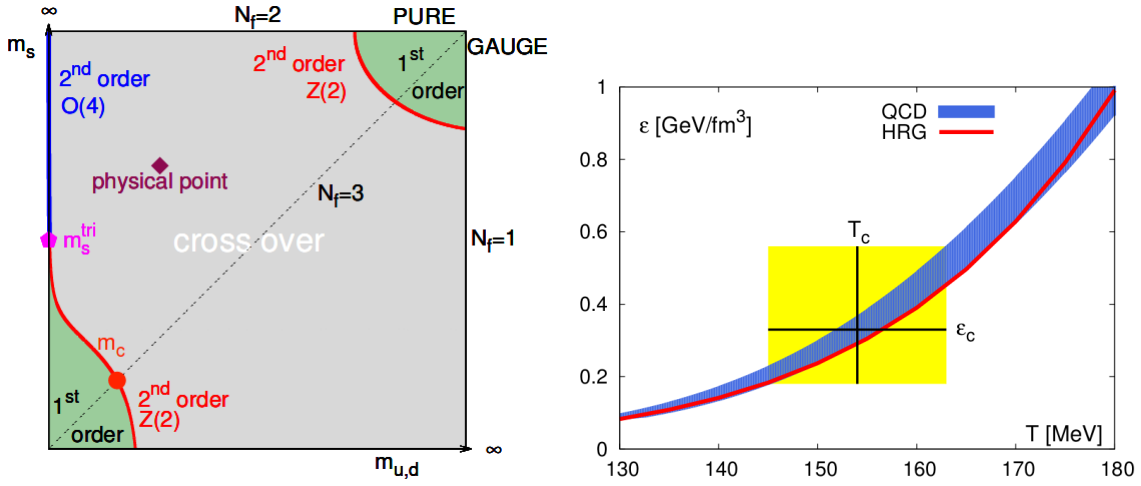

FIGURE 1.2: Left: Columbia plot. Schematic representation of the QCD phase transition as a function of the light quarks (up and down) and of the strange quark, assuming zero baryon chemical potential [20]. N_f indicates the number of flavours. Right: Energy density versus temperature in the (2+1) LQCD calculation with physical quark masses. The blue band represent the continuum limit extrapolated from [21] while the red line is the Hadron Resonance Gas (HRG) result [18, 26–28].

baryon chemical potential, which quantifies the net baryon density, *i.e.* the difference between baryon and anti-baryon densities, is assumed. For $m_l, m_s \to 0$ and number of flavours $N_f = 3$ (2+1) and for $m_l, m_s \to \infty$ and $N_f = 0$, the chiral phase transition is of first order and, for the second case, a pure gauge theory is recovered. The first order regions are delimited by lines representing second order transitions. For intermediate values of the quark masses, a cross-over between confined and deconfined phase is expected. There is consensus nowadays that the latter is the most realistic scenario, as also shown by the "physical point" indicating the LQCD results using physical quark masses. A more extensive description of the plot can be found in [20] and in the references therein.
In a procedure similar to the one used to extract T_c, the critical energy density ϵ_c for (2+1) LQCD calculations with physical quark masses can be obtained too. In Figure 1.2, right, the energy density is plotted against the temperature. The blue and red bands represent, respectively, the continuum limit, as estimated from [21], and the Hadron Resonance Gas (HRG) result [18, 26–28], based on the resonances listed in [9]. The hadron resonance gas is used to describe the hadronic matter that exists before the transition to deconfined phase, where the equation of state used to describe the QCD matter is that of a free gas of hadrons. For the critical temperature $T_c = (154 \pm 9)$ MeV, the corresponding critical energy density is $\epsilon_c = (0.34 \pm 0.16)$ GeV/fm^3 [20]. Both T_c and ϵ_c are indicated with black lines in Figure 1.2, right, with the yellow shaded area representing their uncertainties.
The most common way to visualise the QCD phase diagram is as a function of the temperature and net baryon density, as shown in Figure 1.3. In this sketch, the main focal points of both lattice calculations and heavy-ion physics are summarised: the study of the phase transition, of the hadronic interaction at high temperature and/or high baryonic density and the search for the critical point. The study of ultra-relativistic heavy-ion collisions at different centre-of-mass energies is used to map the boundary between the confined and deconfined phase and to experimentally search for the critical point of the QCD phase diagram. An example of the former is given in Figure 1.4, left. The points shown here are obtained from fits to the hadronic yields in head-on heavy-ion collisions at varying centre-of-mass energy [29]. The critical point is hypothesised as a second order transition point separating the cross-over region from a first order transition one. The latter, whose existence has not yet been confirmed, is indicated in Figure 1.3 with the yellow band at larger values of

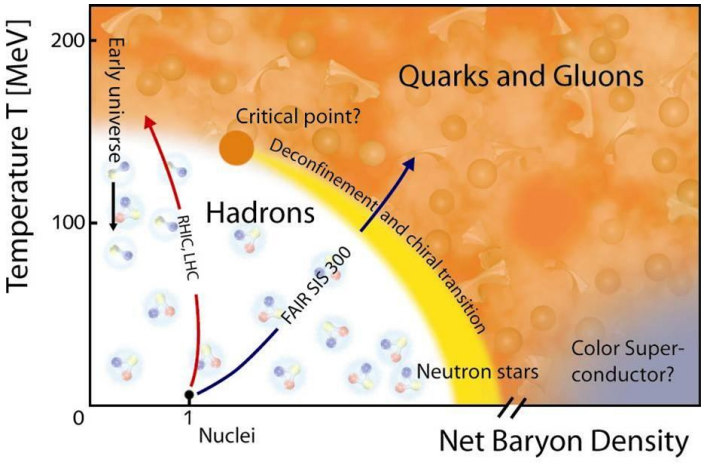

FIGURE 1.3: Sketch of the QCD phase diagram as a function of the net baryon density and temperature [30].

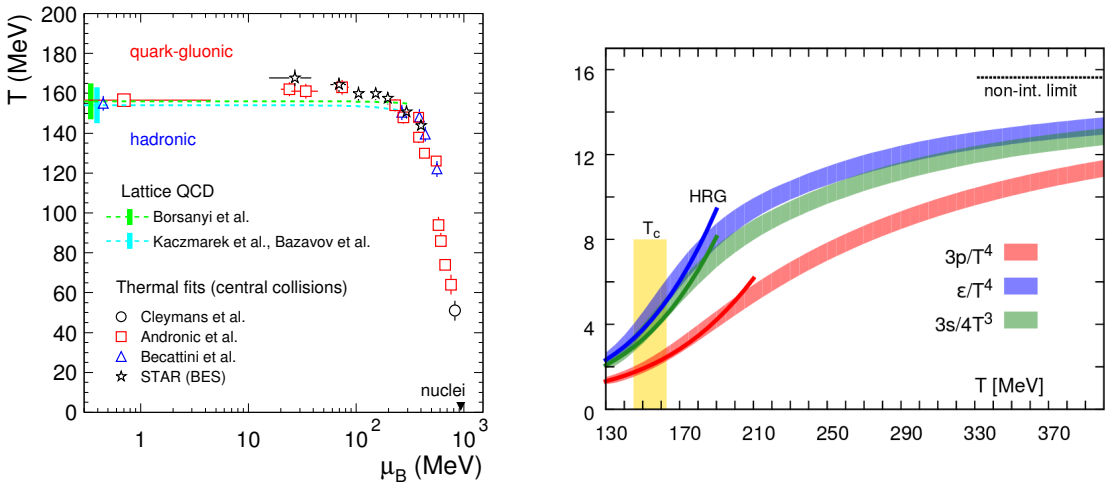

FIGURE 1.4: Left: QCD phase diagram showing the results of thermal fits to hadron yields for several centre-of-mass energies. The dashed lines indicate the temperature at the cross-over, calculated with LQCD [29]. Compared to the given reference, the points from the STAR experiment and from Beccattini *et al.* have been updated here with recent results, as in [31] and [32], respectively. Right: Pressure, energy density and entropy as a function of the temperature T for the highly improved staggered quark (HISQ) action [33]. The critical temperature T_c is indicated with the shaded area. The solid lines indicate the results obtained with the HRG calculations, while the dashed line in the top right corner represents the results for an ideal non-interacting gas of quarks and gluons. For more details see text and reference [20].

μ_B. On the theory side, LQCD shows increasing accuracy for calculations at non-vanishing baryon chemical potential, though they are obtained using coarse lattices and are not yet precise enough to give unambiguous results. Recent calculations put the critical point above $\mu_B/T > 2$ and $T/T_c(\mu_B = 0) > 0.9$ [20, 34]. Rather good results are instead obtained with lattice calculations using physical quark masses to determine the bulk thermodynamic observables such as pressure (P), energy density (ϵ) and entropy (s). The starting point of these calculations is the trace of the energy-momentum tensor, or trace anomaly, defined as $\Delta = (\epsilon - 3p)/T^4$ [33]. The results are shown in Figure 1.4, right, together with the results from the HRG model. It can be observed that the HRG is in good agreement with the lattice calculated thermodynamic observables, an agreement that still holds in the cross-over region. The Stephan-Boltzmann limit, dashed line in the top right corner, is used as reference for a non-interacting gas of massless quark and gluons. In the Stephan-Boltzmann limit, the relation between the energy density and the pressure is $\epsilon = 3p$; thus the trace anomaly, also called interaction measure, can be used to judge the strength of the interaction. The large difference between the non-interacting limit and the calculated thermodynamic observables that can be seen in Figure 1.4 indicates that the plasma of quark and gluons is still subject to (strongly coupled) interactions.

1.2 Evolution of a heavy-ion collision

To investigate the transition region of the QCD phase diagram between hadronic and deconfined matter, a high temperature and energy density environment has to be provided. Heavy-ion collisions are the only available tool to produce and study the Quark-Gluon Plasma in the laboratory.
The first experimental programs dedicated to the study of relativistic heavy-ion collisions were at the Lawrence Berkeley National Laboratory (LBNL) during the early 1970s, where the Bevalac accelerated heavy ions for fixed target experiments. The study of heavy-ion collisions continued at the Brookhaven Alternating Gradient Synchrotron (AGS), at the CERN Super Proton Synchrotron (SPS) and at the GSI heavy-ion synchrotron (SIS-18) with scientific programs including light ion beams and heavy-ion targets and then heavy-ion beams. Nowadays, the Relativistic Heavy Ion Collider (RHIC) at Brookhaven and the Large Hadron Collider (LHC) at CERN are carrying on the Quark-Gluon Plasma research.
The space-time evolution of the system after a heavy-ion collision is schematically sketched in Figure 1.5.

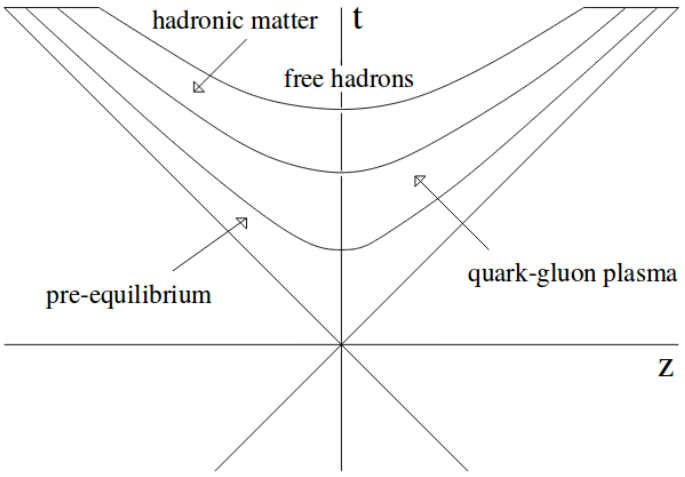

FIGURE 1.5: Schematic representation of the space-time evolution of a heavy-ion collision [35].

The incoming ions follow the light-cone lines on the negative side of the time axis until the origin, at which the collisions takes place. The geometry of the colliding nuclei and their collision itself can be described by the Glauber model [36], introduced in more detail in Section 3.1.1. Its assumption of independent binary collisions between nucleons belonging to two different nuclei shows to be a satisfactory approximation. Once the quarks and gluons degrees of freedom are liberated, the system goes through a pre-equilibrium phase. The partons interact with soft and hard scattering until they thermalise at a time $\tau_0 \sim 1$ fm/c. At this point, the Quark-Gluon Plasma is assumed to have formed. The first attempts to model this phase of the system evolution using ideal hydrodynamics immediately showed remarkable agreement with the experimental results [37–39]. The basic requirements for hydrodynamics to give a good description are that the system has to be in local thermal equilibrium, so that its thermodynamic properties are defined, and that the mean free paths (local relaxation times) have to be small compared to the liquid cell size (macroscopic time scale) [40]. These requirements and the good agreement shown with the experimental results

point to a strongly interacting system that behaves like a fluid. The agreement to the data is further improved with the inclusion of viscosity. Shear and bulk viscosity are two basic quantities for the study of the thermalised system, usually expressed in relation to the entropy density s of the system. The shear viscosity η opposes the pressure gradient that pushes the system outwards, dampening expansion anisotropies. Similarly, the bulk viscosity ζ is the dissipative factor acting on the system volume expansion, and may also influence the shear viscosity [41].
As the system expands, its temperature and energy density decrease. The matter passes from the QGP phase to a hadron gas phase. At this stage, as the particles move farther apart from each other, the inelastic collisions stop first, given their smaller mean free path length, then followed by the elastic collisions. These two steps are often referred to as chemical (the particle species are fixed) and kinetic (the particle momentum distributions are fixed) freeze-out, respectively. In particular, the relative particle abundances at the chemical freeze-out as they are investigated by the hadronic thermal model predictions [42, 43] are important to study the phase transition boundary and its temperature. After the kinetic freeze-out, the free hadrons do not interact anymore and the final stage of the collision evolution is reached.

Centrality of a heavy-ion collision: brief introduction
Several heavy-ion measurements will be described in the following sections, thus it is helpful to introduce now the concept of centrality of an nucleus-nucleus (A–A) collision, *i.e.* the interpretation of the particle multiplicity when the colliding elements are not single protons but nuclei with an extended transverse area. The detailed description is given in Section 3.1.1.
Colliding nuclei can be simplified as disks (not spheres, as they are Lorentz contracted) and the distance between their centres is called impact parameter. In Figure 1.6 a simplified sketch is shown. When two nuclei collide with zero or small impact parameter, in what is called a head-on collision, the interaction area is large and the number of nucleons participating is high. The larger the impact parameter, the smaller the overlapping area between nuclei, thus the number of participant nucleons is also lower. The former type of collision is called central collision, the latter semi-central or peripheral, if the nuclei are just grazing each other. Centrality is expressed in percentiles, where low values indicate more central collisions.

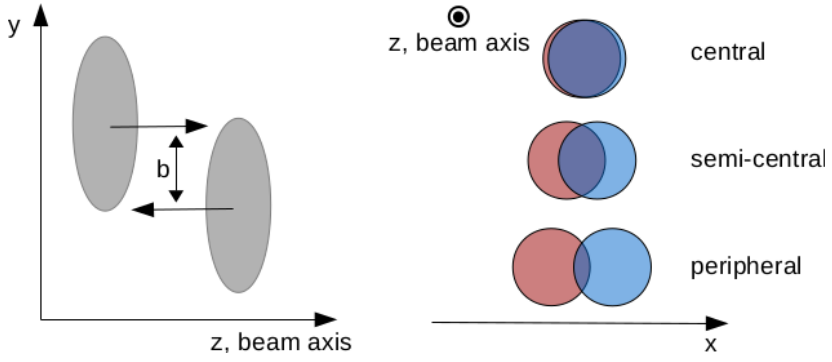

FIGURE 1.6: Sketch illustrating the centrality of a nucleus-nucleus collision.

Other recurrent quantities are the mean number of nucleons participating in the collision, $\langle N_{\text{part}} \rangle$, and the centre-of-mass energy per nucleon, $\sqrt{s_{\text{NN}}}$.

1.3 Quark-Gluon Plasma signatures

There is not a unique signature that allows one to understand the Quark-Gluon Plasma formation and evolution in its entirety. While some signatures deliver a stronger message than others on the existence and characteristics of the phenomenon, it is the collection of them all that helps in forming a complete picture. Depending on the particle or the quantity analysed, different stages of the collisions can be accessed. In the following sections, some of the most relevant observables for the Quark-Gluon Plasma studies and for this work are introduced.

1.3.1 Charged particle and energy density dependence on $\sqrt{s_{\mathrm{NN}}}$

One of the first measured and most basic observables in both pp and A–A collisions is the charged particle pseudorapidity[2] density, $\mathrm{d}N_{\mathrm{ch}}/\mathrm{d}\eta$. The multiplicity of particles produced in a collision can be related to the collision geometry, given the strong dependence on the impact parameter, to the initial energy density and can be used to distinguish which processes, between hard and soft scatterings, drive the particle production.
In Figure 1.7, left, the mean charged particle pseudorapidity density, $\langle \mathrm{d}N_{\mathrm{ch}}/\mathrm{d}\eta \rangle$, is plotted as a function of $\sqrt{s_{\mathrm{NN}}}$ for several results from central A–A, p–A(d–A) and pp (p$\bar{\mathrm{p}}$) collisions. The results are fitted with a power-law function that describes very well the data and highlights the much stronger dependence on collision energy of the heavy-ion results, giving an exponent value of 0.155 for the heavy-ion data points and of 0.103 for pp (p$\bar{\mathrm{p}}$). It is also

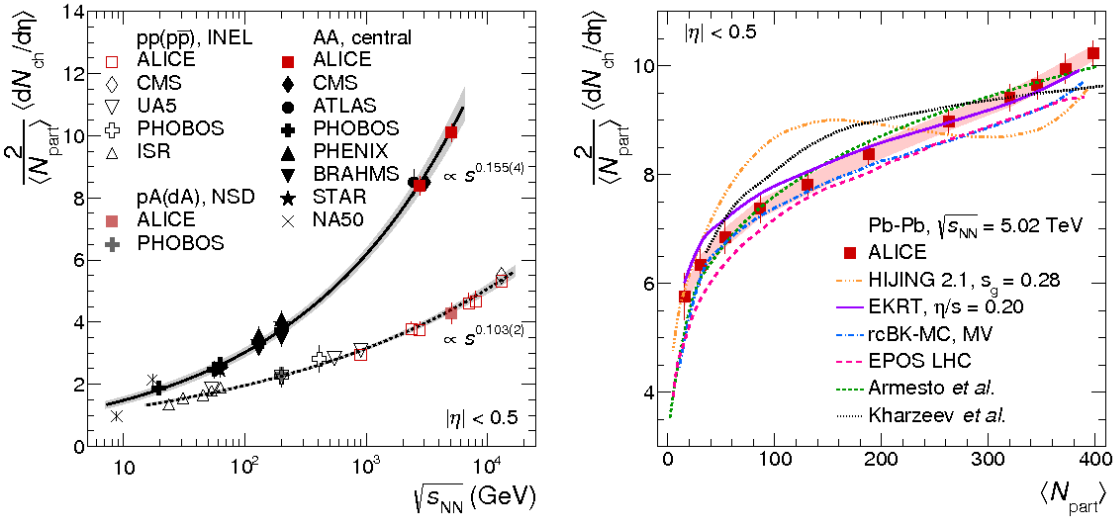

FIGURE 1.7: Left: Dependence of $\langle \mathrm{d}N_{\mathrm{ch}}/\mathrm{d}\eta \rangle$ on the centre-of-mass energy per nucleon [44]. The particle density, normalised per participant pair, is shown for central Pb–Pb [45–48] and Au–Au [49–53] collisions at the LHC and RHIC, respectively, for inelastic pp and p$\bar{\mathrm{p}}$ collisions [54–56] and for non-single diffractive (NSD) p–A and d–A collisions [57, 58]. The solid and dashed lines are the power-law fit to the A–A and pp (p$\bar{\mathrm{p}}$) results, respectively. The shaded grey bands represent the uncertainties on the extracted power-law dependencies. Right: Comparison of $\langle \mathrm{d}N_{\mathrm{ch}}/\mathrm{d}\eta \rangle$, measured for the centrality range 0–80% in Pb–Pb collisions at $\sqrt{s_{\mathrm{NN}}} = 5.02$ TeV, to theoretical predictions [59–67], as a function of N_{part}.

[2] Rapidity and pseudorapidity are defined in Section 2.2

interesting to observe that the p–A and d–A results fall on the same line as the pp ones. It is a hint that multiple nucleon collisions are not the only responsible for the strong energy dependence in A–A collisions, as they also take place with the p–A and d–A systems.
With increasing collision energy, it is expected that hard processes, involving a larger momentum transfer, become dominant over the soft ones. A better understanding of the particle production mechanisms can be reached comparing $\langle \mathrm{d}N_{\mathrm{ch}}/\mathrm{d}\eta \rangle$ to theory predictions, as shown in Figure 1.7, right. The charged particle density is shown here as a function of N_{part}, in order to exploit its sensitivity to the impact parameter. The models used for the comparison are described with more detail in [44]. With exception of HIJING, which uses pQCD together with soft interactions, the other models combine together elements from pQCD, gluon saturation and hydrodynamics, with a resulting good description of the data.
Another global observable that gives insight into the initial characteristics of the system and, more precisely, into the initial energy density, is the transverse energy pseudorapidity density, $\langle \mathrm{d}E_{\mathrm{T}}/\mathrm{d}\eta \rangle$. The transverse energy density is related to the charged particle density by $\mathrm{d}E_{\mathrm{T}}/\mathrm{d}\eta \sim \langle p_{\mathrm{T}} \rangle \mathrm{d}N_{\mathrm{ch}}/\mathrm{d}\eta$ and, within the Bjorken model [68], can be used to calculate the initial energy density ϵ with

$$\epsilon = \frac{1}{A \cdot \tau_0} \frac{\mathrm{d}E_{\mathrm{T}}}{\mathrm{d}y} = \frac{1}{A \cdot \tau_0} J(y, \eta) \frac{\mathrm{d}E_{\mathrm{T}}}{\mathrm{d}\eta} \tag{1.3}$$

where $A = \pi R_{\mathrm{Pb}}^2$ is the transverse area considering a Pb–Pb collision, $\tau_0 = 1$ fm/c is the QGP formation time and $J(y, \eta) \approx 1$ is the Jacobian of the transformation from pseudorapidity to rapidity.
The ratio $\langle \mathrm{d}E_{\mathrm{T}}/\mathrm{d}\eta \rangle / \langle \mathrm{d}N_{\mathrm{ch}}/\mathrm{d}\eta \rangle$ is shown in the left side of Figure 1.8 for a compilation of Pb–Pb collision measurements, as a function of $\sqrt{s_{\mathrm{NN}}}$. The ratio seems to saturate or have a weaker energy dependence at and above RHIC energies. Comparing with the extrapolation from lower energies (grey band), it can be seen that the LHC data deviate from

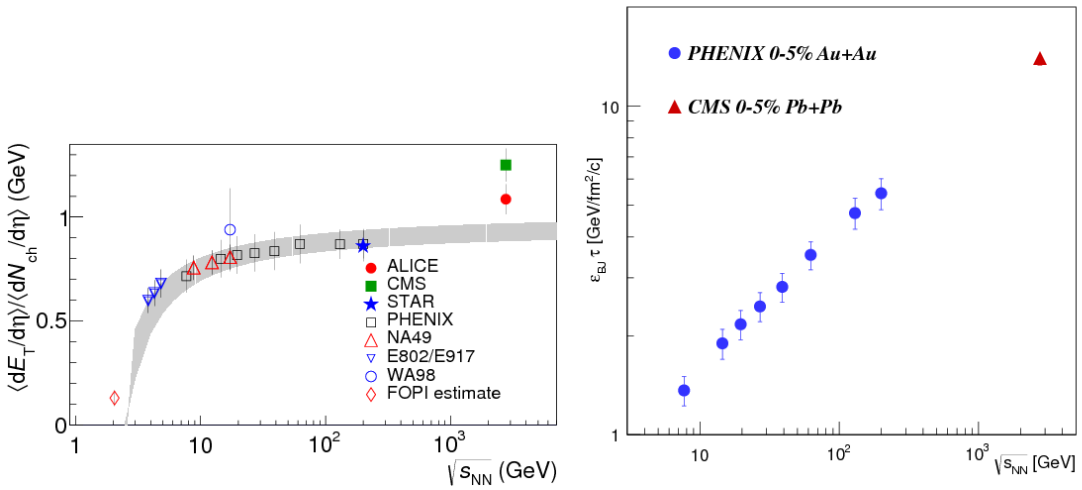

FIGURE 1.8: Left: Energy dependence of the ratio of the mean transverse energy density over the mean charged particle density in Pb–Pb collisions at $\sqrt{s_{\mathrm{NN}}} = 2.76$ TeV measured with ALICE [69] and at other energies [70–75]. The shaded band represents the extrapolation from lower energies, where the uncertainty of the fit is given by the width of the band [73]. Right: Bjorken energy density multiplied by the formation time τ as a function of $\sqrt{s_{\mathrm{NN}}}$ for central Pb–Pb and Au–Au collisions, measured with CMS [76] and PHENIX [75], respectively. Error bars represent the total statistical and systematic uncertainty.

this trend. This suggests that an increase in the collision energy not only increases the particle production, but also the mean energy per particle. Figure 1.8, right, shows the Bjorken energy density, multiplied with the formation time τ. Considering the value of $\epsilon_c = (0.34 \pm 0.16)$ GeV/fm^3 obtained from LQCD, mentioned in Section 1.1.1, it can be observed that the estimation of the initial energy density from the lowest collision energy at PHENIX, $\sqrt{s_{\mathrm{NN}}} = 7.7$ TeV, is already well above this value.

1.3.2 Hadron spectra and in-medium modification

The distribution of particles created in heavy-ion collisions suffers modifications due to the presence of a QGP medium. These alterations trace back to the characteristics of the medium itself. In particular, observables such as the temperature and density of the system, interaction and hadronisation mechanisms and modifications induced by the presence of QCD matter are all information contained in the particle spectra.

Chemical and kinetic freeze-out temperatures. In the previous sections, it was mentioned how Hagedorn deduced a maximum temperature for hadronic matter by studying the hadron yields and how they can be used, similarly, to determine the temperature of the chemical, T_{ch}, and kinetic, T_{kin}, freeze-out. The system after hadronisation expands and cools down until the mean free path is such that inelastic collisions stop: chemical freeze-out, the particle abundances are set. Afterwards, elastic collisions continue until the kinetic freeze-out is reached: hadrons have fixed momentum distributions. Fits to the hadronic yields using the statistical models [29, 77, 78] are employed to extract the temperature T_{ch}, as it was shown in Figure 1.3. T_{kin} is also extracted from fitting charged pion, kaon and proton spectra, but the underlying model in this case is one which includes effects due to a transverse expansion, the Blast-Wave Model [79]. More details on this model will be given in the next section, where the collective expansion of the medium will be addressed.
The extracted T_{ch} and T_{kin} are shown in Figure 1.9 as a function of the centre-of-mass energy.

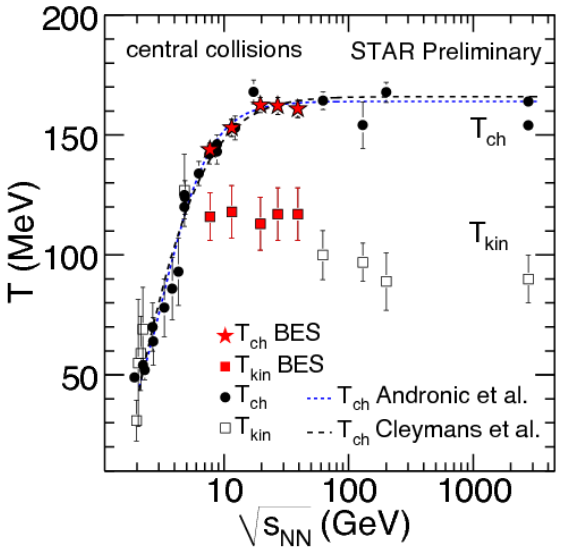

FIGURE 1.9: Energy dependence of the chemical and kinetic freeze-out temperatures for central nucleus-nucleus collisions measured at STAR and BES [80]. The dashed lines represent the thermal model predictions [29, 77].

All the results are obtained from fits based on central nucleus-nucleus collision measurements. The behaviour of the two temperatures can be explained by theories that have opposing assumptions, thus it is still under investigation [81]. On one hand, the existence of a prolonged hadronic phase whose lifetime is proportional to the centre-of-mass energy could explain the behaviour of T_{ch}, which increases sharply with $\sqrt{s_{\mathrm{NN}}}$ until it plateaus around 10 GeV, and of T_{kin}, which decreases with $\sqrt{s_{\mathrm{NN}}}$. This would also explain the difference observed between the freeze-out of light and heavy hadrons. On the other hand, this same difference is explained as being due to strong resonance decays in models where chemical and kinetic freeze-out coincide (single freeze-out picture).

In-medium modifications of the hadronic spectra. The most apparent evidence that the particles undergo some sort of modification due to the presence of the Quark-Gluon Plasma is given by the nuclear modification factor:

$$R_{\mathrm{AA}} = \frac{\mathrm{d}^2 N_{\mathrm{AA}}/\mathrm{d}p_{\mathrm{T}}\mathrm{d}y}{\langle T_{\mathrm{AA}}\rangle \mathrm{d}^2\sigma_{\mathrm{pp}}/\mathrm{d}p_{\mathrm{T}}\mathrm{d}y}. \tag{1.4}$$

The numerator of this ratio is the particle spectrum measured in Pb–Pb collisions. In the denominator, the particle spectrum measured in pp collisions is scaled with the nuclear overlap function, $\langle T_{\mathrm{AA}}\rangle = \langle N_{\mathrm{coll}}\rangle/\sigma_{\mathrm{NN}}^{\mathrm{inel}}$, calculable with the Glauber Model, introduced in Section 3.1.1, and which relates the mean number of binary collisions with the inelastic nucleon-nucleon cross section. The pp measurement is taken as the reference vacuum measurement, thus a nuclear modification factor smaller than one indicates a modification (suppression) of the particle spectra, that are otherwise expected to scale with N_{coll} from pp to Pb–Pb collisions. This quantity is mainly studied as a function of the transverse momentum and for different centrality intervals.
Shown in Figure 1.10, left, is the transverse momentum dependence of the charged hadron nuclear modification factor in central Pb–Pb collisions at $\sqrt{s_{\mathrm{NN}}} = 2.76$ TeV measured by ALICE [82] and CMS [83]. Also reported here are the photon [84], Z^0 [85] and $\mathrm{W}^{\pm}$ [86] production measured in central Pb–Pb collisions by CMS. The Pb–Pb data is compared with the charged hadron nuclear modification factor measured in minimum bias (non-single diffractive, NSD) p–Pb collisions at $\sqrt{s_{\mathrm{NN}}} = 5.02$ TeV centre-of-mass energy with ALICE [87]. The Pb–Pb results can be explained using the sketch in Figure 1.10, right. The interaction of two partons can generate back-to-back jets, *i.e.* collimated emission of particles in opposite directions. In the presence of QCD matter, as it happens in A–A collisions, the partons interact with the surrounding medium and lose energy [89]. The energy loss is larger in the case of the jet taking the longer path to the surface of the system. Consequently, the yields of the particles originating from the fragmentation of these partons will result reduced. This phenomenon, referred to as jet quenching, does not take place in a pp collision. Therefore, when comparing the spectra in the two systems, the suppression due to the parton energy loss is evident and reflects the density of the strongly interacting matter created in the collision. The nuclear modification factor reaches its minimum around 6 GeV/c and then increases again towards higher p_{T}. This is attributed to a smaller relative energy loss for high-p_{T} particles, a behaviour in agreement with several theoretical models, whose direct comparison can be found in [82]. An increase is also observed at low-p_{T}, where the particle collective motion is responsible for the characteristic shape of the R_{AA}, that will be explained in more

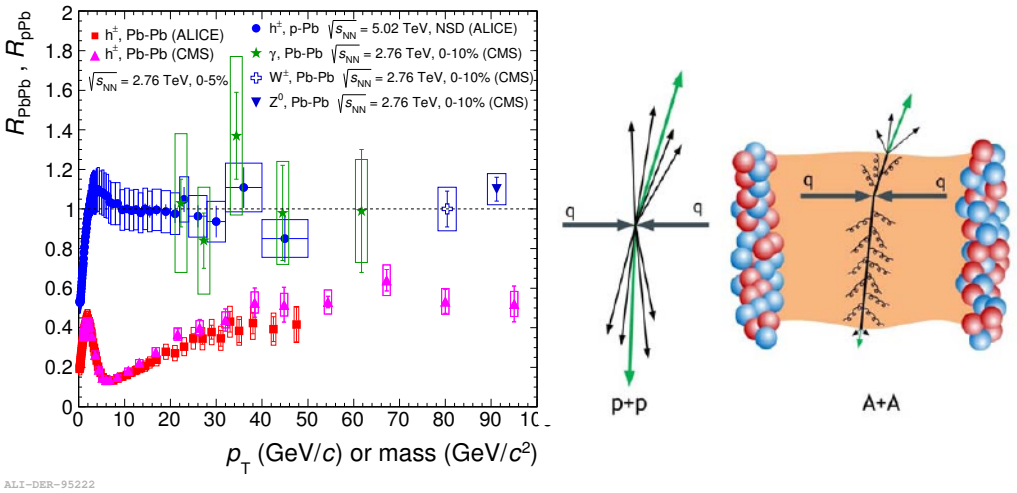

FIGURE 1.10: Left: ALICE charged hadron nuclear modification factor R_{AA} measurements in Pb–Pb [82] and p–Pb [87] collisions at centre-of-mass energy $\sqrt{s_{NN}} = 2.76$ TeV and 5.02 TeV, respectively, are compared with the same measurement from the CMS experiment [83]. Also shown, the measurements for γ, $W^{\pm}$ and Z^0 bosons production at $\sqrt{s_{NN}} = 2.76$ TeV from the CMS experiment [84–86]. Right: Jet quenching. Contrary to what happens in pp collisions, the particle jet that has to traverse a strongly interacting medium in the aftermath of a nucleus-nucleus collision suffers significant energy loss [88].

detail in Section 1.3.3. In the p–Pb case, no QGP is expected to form and the nuclear modification factor for this system stays at unity, also indicating that the R_{AA} suppression is a final state effect and not due to the initial interaction between nuclei (cold nuclear matter effect). Similarly, particles that are not affected by strong interactions, like γ, Z^0 and $W^{\pm}$, also have R_{AA} equal to one, confirming the scaling with the number of collisions mentioned above.

The centrality dependence of the charged particle R_{AA} is shown in Figure 1.11. Here, the ALICE measurement is shown for nine centrality intervals, from peripheral collisions (top leftmost panel) to most central collisions (bottom rightmost panel). It is interesting to observe the suppression changing from small and p_T-independent to an increasingly pronounced effect and a clear transverse momentum dependence towards higher collision centrality. This is understandable considering the higher multiplicities reached in central nucleus-nucleus collisions, with the subsequent formation of a much denser medium. On the other hand, in a peripheral collision, where the nuclei only graze each other, the environment is closer to what can be found in a pp collision.

Neutral mesons. The neutral pion and η meson, which will be the first measurement object of this research work, and the other neutral mesons, such as ω, η', ϕ, etc., are expected to lose energy just like the charged hadrons. While some of the heavier neutral mesons (ω and ϕ) have been measured in pp collisions, this is very difficult in A–A collisions due to the high statistics required for such measurements. So far, ALICE has only measured neutral pions in Pb–Pb collisions at $\sqrt{s_{NN}} = 2.76$ TeV. The π^0 nuclear modification factor as a function of the transverse momentum is shown in Figure 1.12, left, for different centrality intervals. Similarly as for the charged hadrons, the highest suppression is observed in the most central collisions, while it decreases towards the peripheral ones. In Figure 1.12, right, the ALICE result for 0–10% Pb–Pb collisions is compared with lower energy results from RHIC and

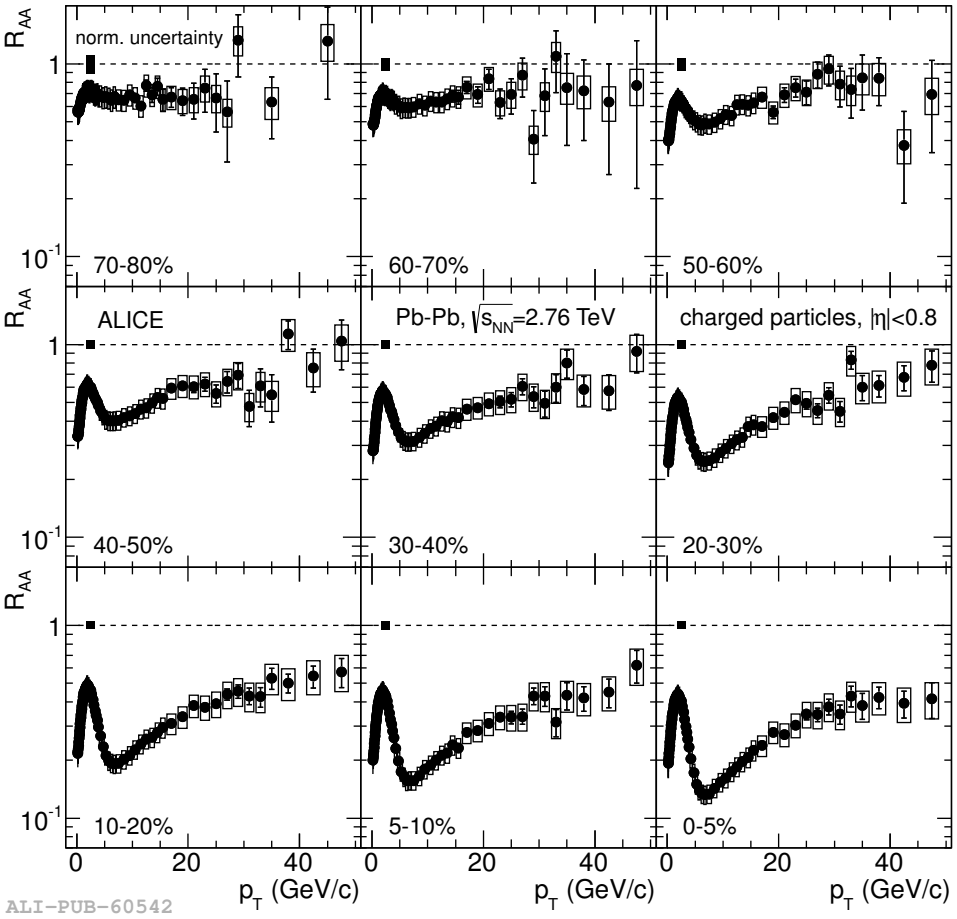

FIGURE 1.11: Centrality dependence of the charged particle nuclear modification factor as a function of transverse momentum for Pb–Pb collisions at $\sqrt{s_{\mathrm{NN}}} = 2.76$ TeV [82]. The measurements are shown for nine centrality intervals, from peripheral collisions, 70–80% centrality (top leftmost panel) to the most central collisions, 0–5% centrality (bottom rightmost panel). The boxes at unity represent the normalisation uncertainty.

SPS. It is interesting to observe here the "turn on" of the jet quenching, starting with the RHIC results and showing an increasing suppression with increasing centre-of-mass energy. This thesis work will contribute to the ALICE results with an updated neutral pion measurement and with the first η meson measurement in Pb–Pb collisions at the LHC.

1.3.3 Collective flow

Using hydrodynamics, the QGP can be described as a fluid with small but significant viscosity. This plasma of strongly interacting quark and gluons, which is referred to as a fireball, expands outwards due to its energy density, which creates a pressure gradient with the outside vacuum. The partons are correlated with each other and their collective motion, or flow, continues until hadronisation. The study of the collective flow, given its origin in the early stages after the collision, can add details to what is already known of the QGP properties and improve the knowledge of the equation of state. The addition of shear and bulk viscosity to the hydrodynamical description of the system, mentioned in Section 1.2 and described in [41], is one of such improvements.

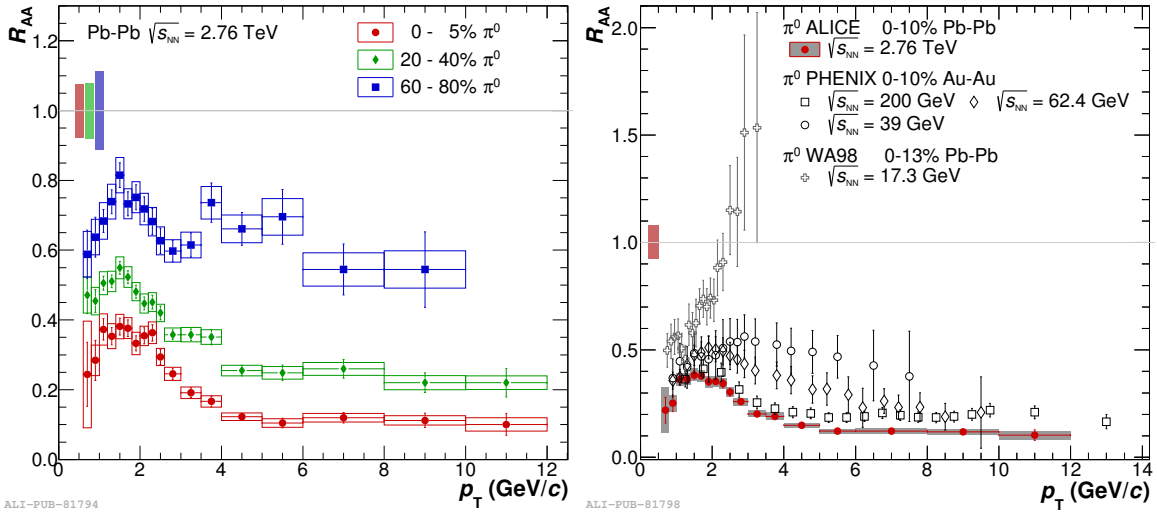

FIGURE 1.12: Neutral pion nuclear modification factor as a function of transverse momentum. Left: ALICE π^0 R_{AA} for the centralities intervals 0–5%, 20–40% and 60–80% in Pb–Pb collisions at $\sqrt{s_{\mathrm{NN}}} = 2.76$ TeV [90]. The statistical uncertainties are represented by the vertical bars, the systematic uncertainties by the boxes. The boxes at unity represent the pp normalisation uncertainty and the nuclear overlap function uncertainty, added in quadrature. Right: Results for the π^0 R_{AA} measured in the 0–10% centrality class in Pb–Pb collisions at $\sqrt{s_{\mathrm{NN}}} = 2.76$ TeV with ALICE, in Au–Au collisions at $\sqrt{s_{\mathrm{NN}}} = 39$, 62.4 [91], and 200 GeV [92] with PHENIX and in 0–13% Pb–Pb collisions at WA98 [93].

Different types of collective flow have been identified and will be described in the following paragraphs.

Radial flow

As mentioned before, at the kinetic freeze-out elastic interactions stop and the hadron momentum distributions are fixed. It is assumed that the free hadron momentum distributions are the same as the momentum distributions of the particles within the fireball (Cooper-Frey freeze-out [94]). Since hydrodynamics is no longer valid at this point, a static thermal source emitting particles at a certain temperature T was initially adopted for the description of the invariant momentum spectrum. The discrepancy emerging from the model comparison to the π^- transverse mass (m_{T}) spectrum measured by NA35 in S–S collisions at 200A GeV [95] showed that this picture is too simplistic. The missing ingredients were the feed-down from resonance decays and the longitudinal flow, already postulated by Bjorken [11] in his 1D-hydrodynamical model. Though after this inclusion the spectral shape seemed to be understood, theory and other experimental results suggested the need to introduce a transverse flow. One of the theoretical reasons is, for example, that a purely longitudinal expansion is inconsistent with the pressure gradients that are expected to develop within the fireball. Similarly, results from AGS [96] show a flattening of the transverse mass spectra for $p_{\perp} \lesssim m$ consistent with the presence of a transverse flow. Therefore, the model was changed to a particle spectrum described by the superposition of radially boosted thermal sources [79]. It can be written as a function of the transverse mass m_{T} as:

$$\frac{\mathrm{d}n}{m_{\mathrm{T}}\mathrm{d}m_{\mathrm{T}}} \propto \int_0^R r\mathrm{d}r m_{\mathrm{T}} I_0\left(\frac{p_{\mathrm{T}}\sinh(\rho)}{T}\right) K_1\left(\frac{m_{\mathrm{T}}\cosh(\rho)}{T}\right), \tag{1.5}$$

where I_0 and K_1 are modified Bessel functions, $\rho = \tanh^{-1}\beta_r(r)$ is the boost angle and $\beta_r(r) = \beta_s(r/R)^n$ is the transverse velocity profile from the centre of the source to the surface of the fireball R, dependent on the surface velocity β_s. The shape of the profile is given by n. This is referred to as Blast-Wave Model [79]. The spectral shape follows an exponential with slope parameter $1/T_{\rm eff}$. For sufficiently large $p_{\rm T}$, the effective temperature $T_{\rm eff}$ is connected to the production temperature T as

$$T_{\rm eff} = T\sqrt{\frac{1+\beta_r}{1-\beta_r}}. \tag{1.6}$$

Pion, kaon and proton transverse momentum spectra are fitted with the Blast-Wave function in order to extract the kinetic freeze-out temperature $T_{\rm kin}$. The parameter T, the mean transverse velocity $\langle\beta_r\rangle$ and the flow profile parameter n are left free to vary.
Figure 1.13, left, shows the comparison of the particle spectra measured at ALICE, STAR and PHENIX for central collision. The expected flattening of the spectra at $p_\perp \lesssim m$ is visible here, especially for the proton yields. Figure 1.13, right, shows the results of Blast-Wave fits to the ALICE [97] and STAR [98] pion, kaon and proton measurements from peripheral (left side) to central (right side) collisions. It can be observed that the mean transverse velocity increases for more central collisions, while $T_{\rm kin}$ decreases, both for ALICE and STAR results. This dependence is interpreted as a faster expanding system in central collisions, with a radial flow almost 10% larger at LHC than at RHIC energies. On the other hand, in peripheral collisions the particles do not have time to build up flow before the freeze-out is reached, at temperature higher than in central collisions, thus leading to a fireball with shorter lifetime [99].

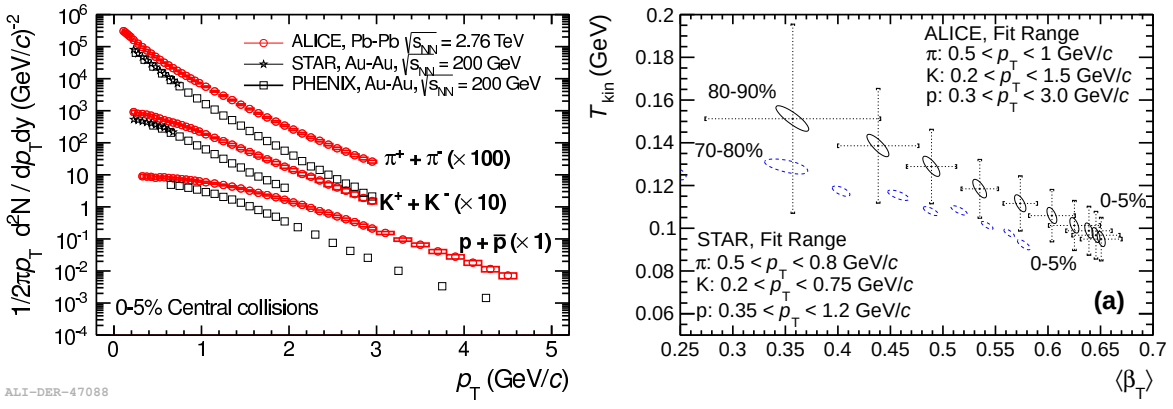

FIGURE 1.13: Left: ALICE particle spectra measured in 0–5% Pb–Pb collisions at $\sqrt{s_{\rm NN}}$ = 2.76 TeV, compared to RHIC results from Au–Au collisions at 200 GeV in the same centrality class [53, 100]. The boxes represent the systematic uncertainties while the statistical uncertainties are smaller than the symbol size. Right: Kinetic freeze-out temperature $T_{\rm kin}$ as a function of the mean transverse velocity ($\langle\beta_T\rangle = \langle\beta_r\rangle$), for different centrality intervals, obtained from Blast-Wave fits to ALICE measurements of pion, kaon and proton transverse momentum spectra [97], compared to results from STAR [98]. The ALICE uncertainties (solid contours) include bin-by-bin systematic uncertainties, while the dashed error bars represents the full systematic uncertainty. For STAR, only statistical uncertainties are shown (dashed contours).

Anisotropic flow

In non-central heavy-ion collisions, the interaction region has an almond shape (see Figure 1.6) that will be more or less elliptic depending on the impact parameter. The particles will collectively move with a certain angular distribution: the initial spacial anisotropy causes larger pressure gradients on the short axis of the ellipse and smaller on the longer axis. With the subsequent particle interactions, the spacial anisotropies will translate into momentum anisotropies, as illustrated in Figure 1.14.

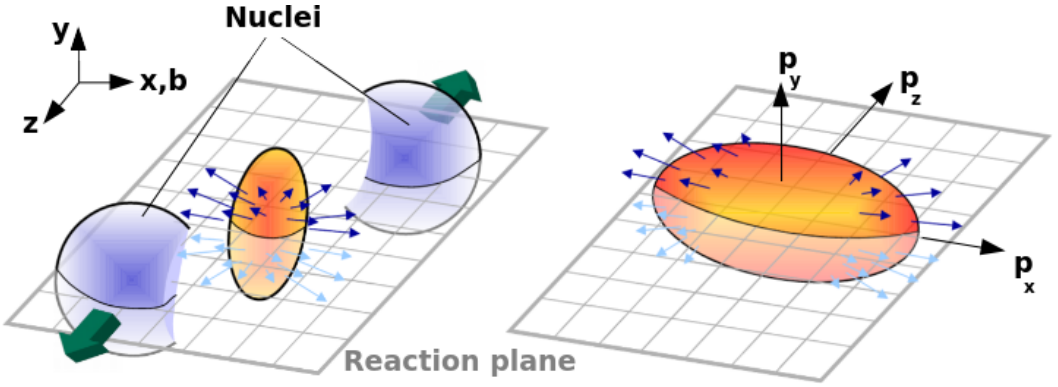

FIGURE 1.14: Three-dimensional representation of a non-central nucleus-nucleus collision. The coordinate system is indicated and the grey grid shows the reaction plane. The initial spacial anisotropy, left picture, becomes momentum anisotropy, right picture, due to larger pressure gradients acting on the transverse direction and to the subsequent particle scattering. Picture modified from [101].

An effective characterisation of the collective flow and its anisotropic components is performed using a Fourier expansion [102] for the azimuthal distribution of the final state particles:

$$E\frac{\mathrm{d}^3N}{\mathrm{d}^3p} = \frac{\mathrm{d}^2N}{2\pi p_{\mathrm{T}}\mathrm{d}p_{\mathrm{T}}\mathrm{d}y}\left(1 + 2\sum_{n=1}^{\infty} v_n \cos\left[n(\varphi - \psi_n)\right]\right), \tag{1.7}$$

where φ is the azimuthal angle and ψ_n is the angle of the n-th order symmetry plane of the initial state, which must be estimated event-by-event. The Fourier coefficient v_n represents the magnitude of the n-th order contribution to the collective flow. This coefficient is also studied event-by-event and is calculated averaging over all the particles. With $\phi = \varphi - \psi_n$, it is defined by

$$v_n(p_{\mathrm{T}}) = \frac{\int \mathrm{d}\phi \mathrm{d}N/\mathrm{d}\phi \cos(n\phi)}{\int \mathrm{d}\phi \mathrm{d}N/\mathrm{d}\phi} = \langle\cos(n\phi)\rangle. \tag{1.8}$$

The event plane method, one of the methods used to extract the flow components, assumes a perfect knowledge of the reaction plane. Experimentally, this is not possible since the detectors used to estimate the reaction plane angle have a finite resolution, depending on the number of particles measured. The reconstructed reaction plane angle is given by

$$\psi_{n,rec} = \frac{1}{n}\arctan 2(Q_{n,y}, Q_{n,x}) \tag{1.9}$$

where the arguments of the arc-tangent are the two components of the event flow vector, representing the distribution of the detected particles in the forward (and backward) direction. Hence, the reconstructed flow components have to be corrected for the resolution of the reconstructed reaction plane. Other methods that do not depend so heavily on the number of

measured particles to achieve a good resolution, the scalar products or the cumulant method, are now preferred.
The scalar product (SP) method calculates the particle correlations using the flow vector scalar product with the unit vector of the analysed particles, $u(\eta, p_{\mathrm{T}}) = e^{in\phi}$, averaged over the events. The flow coefficients will be then given by:

$$v_n\{\mathrm{SP}\} = \frac{\langle u_n^A(\eta, p_{\mathrm{T}}) \cdot \frac{Q^*_{n,B}}{M_B} \rangle}{\sqrt{\langle \frac{Q_{n,A}}{M_A} \cdot \frac{Q_{n,B}}{M_B} \rangle}} \tag{1.10}$$

with A and B indicating two subevents, M_A and M_B their respective multiplicities and Q^* the complex conjugate of the flow vector.
The cumulants method is a two step procedure in which two- or four-particle correlations are obtained. The first step consist in estimating a reference flow. Subsequently, the correlations between the particles analysed and this reference flow are established, averaged over all the particles in an event and then over all the events. The cumulants for two and four particles are defined as

$$c_n\{2\} = \langle\langle e^{in(\phi_1-\phi_2)} \rangle\rangle, \qquad c_n\{4\} = \langle\langle e^{in(\phi_1+\phi_2-\phi_3-\phi_a)} \rangle\rangle - 2\langle\langle e^{in(\phi_1-\phi_2)} \rangle\rangle^2. \tag{1.11}$$

The relation between the cumulants and the flow coefficients is

$$v_n\{2\}^2 = c_n\{2\}, \qquad v_n\{4\}^4 = -c_n\{4\} \tag{1.12}$$

In all of these methods, non-flow effects, uncorrelated to the initial geometry, can bias the particle correlations. Non-flow contributions coming, for example, from resonance decays and jets, need to be accounted for and minimised.
Radial flow can be considered the flow coefficient of order zero, corresponding to an isotropic flow. It is significant for central nucleus-nucleus collisions, while it becomes less so with increasing impact parameter, for which the anisotropic flow components become relevant.
The directed flow, or v_1, is caused by the repulsive action of the early interacting matter of the nuclei on the rest of the incoming nucleons. The deflection pushes the nuclear remnants in opposite directions depending on rapidity. The v_1 will be larger for non-central collisions and significant for large rapidities. Given that it is negligible at midrapidity ($y \approx 0$), it will not be discussed further here, but details can be found in [103].
The origin of the second order flow coefficient, v_2, is the elliptic shape of the overlap region between the two colliding nuclei, from which it takes the name of elliptic flow. The v_2 depends on centrality: it is small for central collisions and then grows for more peripheral ones, where the asymmetry of the interaction area becomes more and more pronounced. An example of this can be seen in Figure 1.15. Here the p_{T}-dependence of the elliptic flow for identified hadrons from Pb–Pb collisions at $\sqrt{s_{\mathrm{NN}}} = 2.76$ TeV measured with ALICE is shown. From the top left to the bottom right panels, it can be observed that the flow increases the more peripheral the collisions are, *i.e.* the more asymmetric the interaction area is. Furthermore, the elliptic flow has different p_{T}-dependence for different particle species, as observed also for the radial flow. At low-p_{T}, the mass ordering of the v_2 is explained considering the influence of the radial flow on the particle during the hadronic phase. In Section 1.3.3, it was explained how the radial flow causes a depletion of the low-p_{T} region of the hadron spectra, proportional to the hadron mass. The heavier particles are pushed towards higher transverse momentum

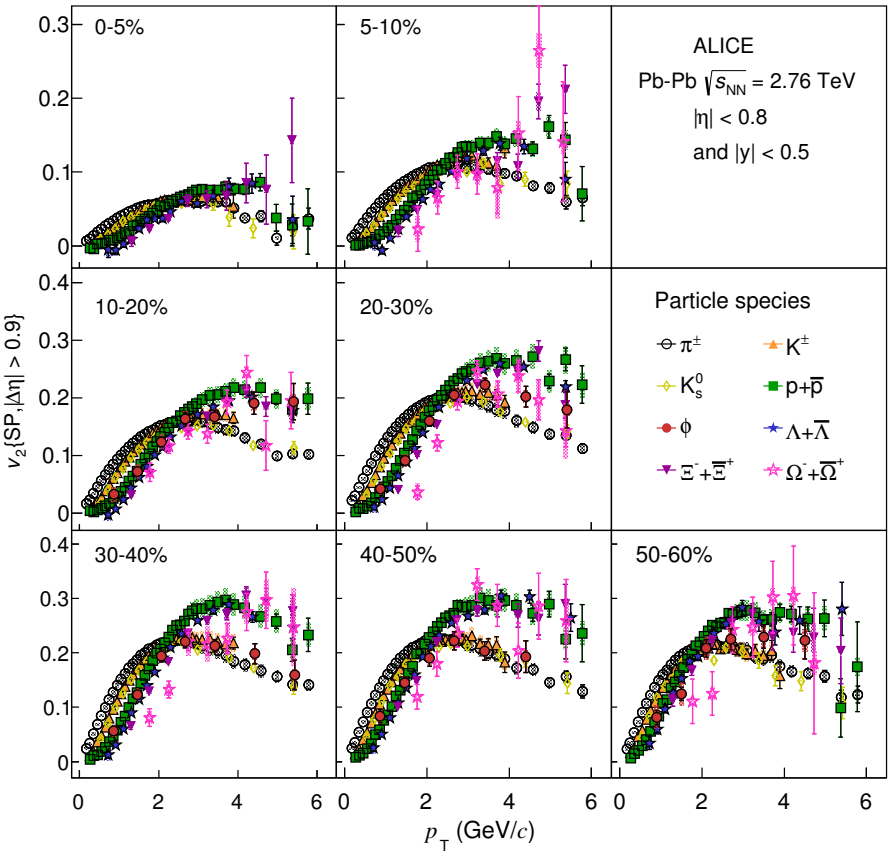

FIGURE 1.15: Transverse momentum dependence of the elliptic flow v_2 for identified particles in centrality intervals measured in Pb–Pb collisions at $\sqrt{s_{NN}} = 2.76$ TeV with ALICE [104].

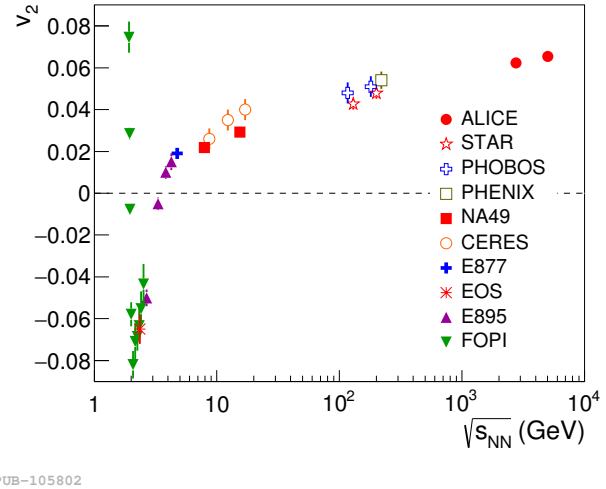

FIGURE 1.16: Energy dependence of the integrated elliptic flow v_2 for the 20–30% most central Pb–Pb collisions measured at $\sqrt{s_{NN}} = 5.02$ TeV [105] and $\sqrt{s_{NN}} = 2.76$ TeV [106] with ALICE, compared with results from lower energy experiments (references can be found in [106]).

and their differential v_2 is reduced at low-p_{T}. This blue-shifting effect can also be seen above 2 GeV/c, where the mass ordering reverses. The v_2 of lighter particles reaches a maximum and then decreases while the heavier particle maximum is pushed towards higher p_{T}.
The energy dependence of the elliptic flow is shown in Figure 1.16. The p_{T}-integrated results from ALICE are compared to results from lower energy experiments and clearly highlight the growth in magnitude of the elliptic flow with increasing collision energy.
Triangular flow, v_3, and higher order harmonics depend weakly on the collision centrality and on the reaction plane. These flow coefficients originate from fluctuations in the initial collision geometry and from local maxima in the energy density of the fireball. Details can be found in [107, 108].

1.3.4 Charmonia

Bound states of charm and anticharm quarks are called charmonia. Their large mass, much larger than the QCD energy scale, $\Lambda_{QCD} \sim 200$ MeV, or alternatively, of any temperature that can be reached in a heavy-ion collision, allows for a non-relativistic, pQCD treatment of heavy quark mesons. Moreover, and for the same reason, the charmonia formation time, $t = 1/m_Q$, is small and so hadrons with heavy quarks will be produced at early times and probe the early stages of the collisions.
The yields of hadron from lighter quarks undergo modifications due to the Quark-Gluon Plasma formation, as described in Section 1.3.2. Likewise, medium-induced modifications are expected also for the heavier kind of hadrons. An important difference here is that, while the lighter hadron radius is about 1 fm, the charmonia radii range from 0.2 to 0.5 fm. Matsui and Satz predicted a suppression of the J/ψ production due to colour screening and identified this as a signature for the QGP formation [109]. The colour screening [110], which is analogous to its QED counterpart, has a characteristic radius dependent on temperature. The deconfinement happens when the screening radius becomes smaller than the hadron radius, at which point the bound state is no longer possible. Thus, the J/ψ suppression is motivated by the fact that $c - \bar{c}$ pairs, which find themselves immersed in a quark-gluon plasma with a screening radius smaller than the J/ψ binding radius, cannot form the bound state. Instead, open charm states will form later during hadronisation. In [109], the comparison of the J/ψ to the dilepton spectrum from the Drell-Yan mechanism in pp is indicated as the observable that should show clearly the J/ψ suppression, if measured in the kinematic range in which Drell-Yan dominates over thermal dilepton emission. Given the small radii of the charmonium states, one also expects that they can survive longer than lighter mesons within the QGP and experience the deconfined stage before melting. One very peculiar feature of this theory is that a sequential melting of the charmonium states should be observed: first ψ', then χ_c and last prompt (directly produced) J/ψ.
Models competing with the colour screening picture are the suppression due to comover collisions [111, 112], which could occur in deconfined and confined medium alike, but deemed negligible [113], and enhancement through regeneration [114, 115]. The latter introduces the concept of 'exogamous' charmonium formation: charm and anticharm quarks from different 'parent' collisions could create together a charmonium state. If the number of charm quarks at hadronisation is high enough and the binding force between the pairs strong enough, this leads to an enhancement of the final charmonia production.

The J/ψ production was studied at the CERN SPS in pp, fixed target and A–A collisions [116–119]. The J/ψ suppression became evident only with the results from Pb–Pb collisions. In Figure 1.17, the J/ψ and ψ' to Drell-Yan cross section ratio is shown for several collision systems. The black line at unity indicates the expected nuclear absorption pattern. It is easy to observe that for Pb–Pb collisions both mesons show a distinct deviation from this line, in agreement with the color screening theory, as indicated in [110].

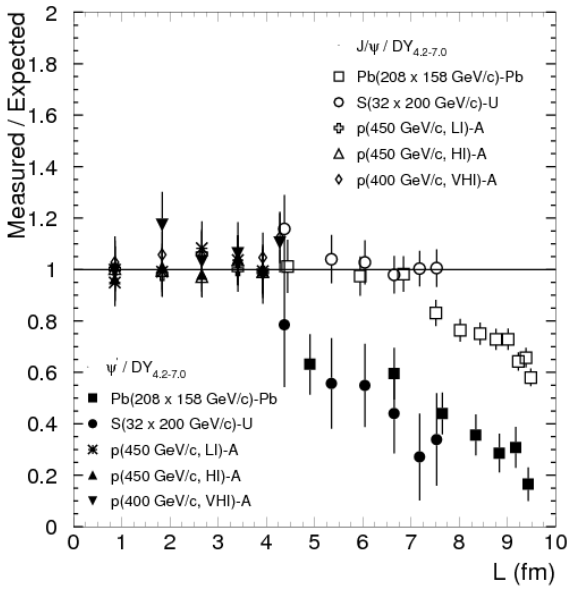

FIGURE 1.17: Ratio of the J/ψ and ψ' cross section to the Drell-Yan cross section as a function of the nuclear matter length L, for several collision systems. The data ratios are compared to the expected nuclear absorption pattern (black line at unity) [120].

The $c\bar{c}$ cross section grows with the centre-of-mass energy of the collision, thus it could be possible to observe the onset of the regeneration at higher collision energy with RHIC and the LHC. These results are shown in Figure 1.18, where the R_{AA} of the inclusive (prompt and from decays) J/ψ as a function of N_{part} measured with ALICE in Pb–Pb collisions at $\sqrt{s_{\mathrm{NN}}} = 2.76$ TeV is compared to the PHENIX measurement in Au–Au collisions at 200 GeV. For both measurements, at midrapidity in the $J/\psi \to e^+e^-$ channel and at forward rapidity in the $J/\psi \to \mu^+\mu^-$ channel, a similar behaviour can be observed, even though the suppression is larger in the forward than in the central rapidity region. The PHENIX measurement shows an increasing suppression towards more central collisions (larger $\langle N_{\mathrm{part}} \rangle$). On the other hand, the ALICE results, while consistent with PHENIX in peripheral collisions, are definitely higher in central collisions, confirming that at high collision energy and for a large number of nucleon-nucleon collisions a charm quark regeneration process is taking place, leading to an enhancement of the J/ψ production. The results are also compared with the respective statistical hadronisation model predictions [114]. The predictions, which pre-date the experimental results by several years and where the largest uncertainty is given by the $c\bar{c}$ production cross section, show a good agreement with the data for both RHIC and LHC measurements.

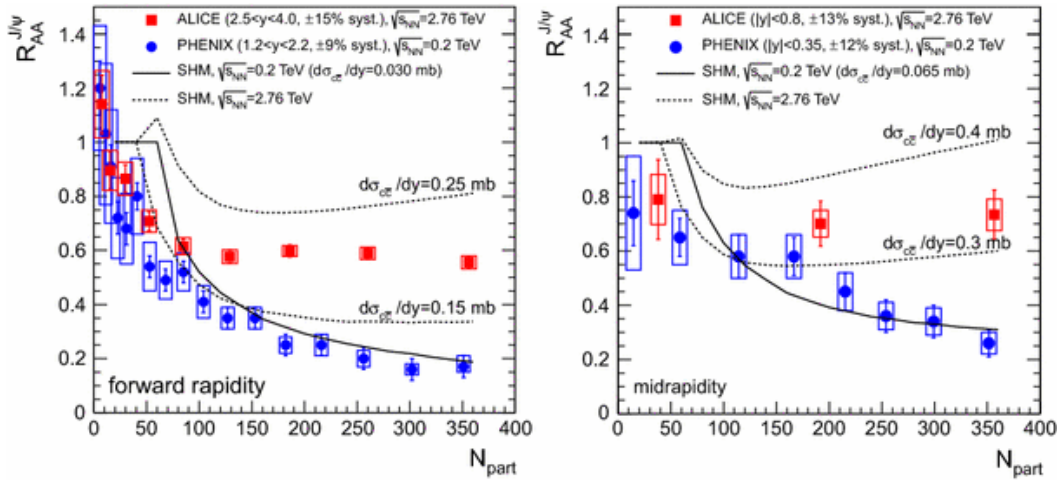

FIGURE 1.18: Inclusive J/ψ nuclear modification factor as a function of $\langle N_{\rm part} \rangle$ measured with ALICE in Pb–Pb collisions at $\sqrt{s_{\rm NN}} = 2.76$ TeV and with PHENIX in Au–Au collisions at 200 GeV [121]. Left: Measurements at forward rapidity in the $J/\psi \to \mu^+\mu^-$ decay channel. Right: Measurements at midrapidity in the $J/\psi \to e^+e^-$ channel. The results are compared with predictions from the statistical hadronisation model (SHM) [115].

1.3.5 Strangeness

Strangeness enhancement is considered as a potential signature of the QGP formation [122, 123]. Two aspects of this observable are studied. The first is the enhancement with respect to the light quarks, which increases in magnitude from pp to A–A collisions, since it is expected to scale with the number of participant nucleons. Strangeness is in fact absent in the initial colliding objects, so any strangeness in the final state must be produced after the collision and the more nucleons are present, the more collisions can take place. The second aspect of strangeness enhancement is the one involving multi-strange baryons in heavy-ion compared to pp collisions.

Strangeness is a conserved quantity under the strong interaction: for every strange particle produced, a sister antiparticle must also be created to have zero net strangeness in the system. For this reason, the two typical production scenarios, hadron gas from pp collisions on one hand and QGP from A–A collisions on the other, are quite different.

In a hadron gas, strangeness is produced via hadron re-scattering. The threshold for direct strange hadron production is very high: a pair of strange hadrons need to be created, in order to conserve strangeness, and the production threshold will be given by twice the particle rest mass. Instead, the indirect production in incremental steps has a much lower threshold. It starts with a pion-nucleon interaction producing the lighter strange hadrons, followed by further interactions of these particles, which give the heavier hadrons (*e.g.* $\pi + N \to K + \Lambda$, then $\pi + \Lambda \to K + \Xi$ and $\pi + \Xi \to K + \Omega$).

With the formation of a Quark-Gluon Plasma, strange production is much simpler. One of the crucial points for taking strangeness enhancement as a deconfinement signature is that in the presence of a Quark-Gluon Plasma, gluon fusion ($gg \to s\bar{s}$) becomes the dominant production channel of strangeness, in addition to quark-antiquark annihilation ($q\bar{q} \to s\bar{s}$). Helping the case is the fact that in a deconfined medium quarks are stripped down to the bare masses, and therefore the production threshold is just given by twice the strange quark mass.

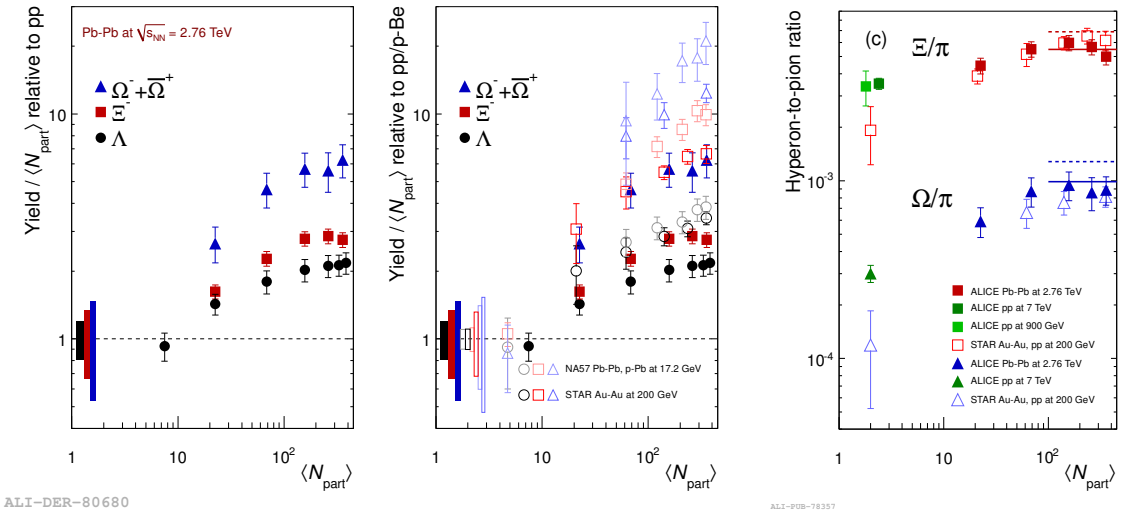

FIGURE 1.19: Enhancement the Λ, Ξ and Ω baryons as a function of the mean number of participant nucleons, $\langle N_{\rm part}\rangle$, measured in Pb–Pb collisions at $\sqrt{s_{\rm NN}}$ = 2.76 TeV with ALICE, full symbols, left panel. These results are compared with what has been measured in Au–Au collisions at 200 GeV with STAR and in Pb–Pb and p–Pb collisions at 17.2 GeV with NA37, both with open symbols, middle panel. The boxes at unity represent the statistical and systematic uncertainty in the pp baseline. Right panel: Hyperon to pion ratios as a function of $\langle N_{\rm part}\rangle$, measured in pp and A–A collisions with ALICE and STAR [124]. The solid and dashed lines indicate the thermal model calculations by Andronic *et al.* [29] and THERMUS [78] with T = 164 MeV and T = 170 MeV chemical freeze-out temperature.

The enhancement of multi-strange hadrons goes also in support of considering strangeness a QGP signature. The reason lies in the difference between the partonic and hadronic equilibration times. In the partonic case, the equilibration time is about 10 fm/c, which is roughly the time-span of a heavy-ion collision, ending with the hadronisation phase. The equilibration time in a hadron gas is about 30 fm/c for hadrons with strangeness equal to one. This value is an order of magnitude larger for multi-strange hadrons, thus making their production very difficult [131].

The enhancement is quantified as the ratio of the yields measured in Pb–Pb collisions over the yields measured in pp collisions, normalised to the mean number of participant nucleons. The results from SPS [132, 133], RHIC [134] and LHC [124] are summarised in Figure 1.19. The ratios are all larger than one and increase as a function of $\langle N_{\rm part}\rangle$. The increase in the ratio is also observed as a function of the strangeness content, while it seems to decrease with increasing collision energy. This dependence on the energy can be understood studying the hyperon to pion ratios in the different collision systems, in particular Ξ/π, Figure 1.19, right: while different centre-of-mass energies show similar enhancement in A–A collisions, in agreement with the thermal models calculations (solid and dashed lines), the increase of the ratio with energy is larger in pp collisions. The reason is that with more energy available, the production of multi-strange hadrons is less suppressed. This increasing trend is confirmed by enhanced production in high-multiplicity pp collisions [135].

In Figure 1.20, the ratios of the $p_{\rm T}$-integrated yields of strange and multi-strange hadrons over $\pi^+ + \pi^-$ are shown as a function of the average charged particle density, $\langle {\rm d}N_{\rm ch}/{\rm d}\eta\rangle$. The high-multiplicity pp results are compared to the same measurement in p–Pb [129, 130] and Pb–Pb [124] from ALICE. The trend of the ratios in pp is similar to that observed in p–Pb collisions, for increasing multiplicities, until it bridges to the Pb–Pb results. No significant

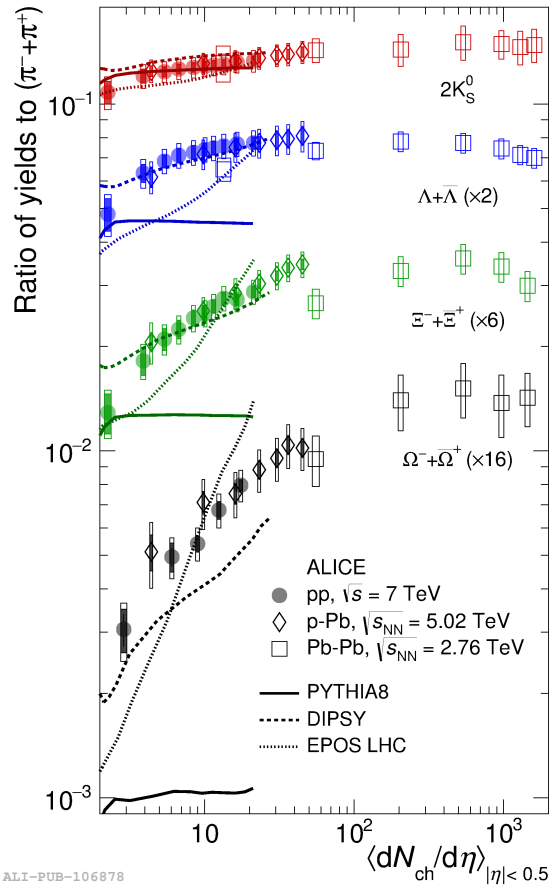

FIGURE 1.20: Ratios of the p_{T}-integrated yields of strange and multi-strange hadrons over $\pi^+ + \pi^-$ as a function of $\langle \mathrm{d}N_{\mathrm{ch}}/\mathrm{d}\eta \rangle$, measured in high-multiplcity pp collisions at 7 TeV. The boxes represent the total systematic uncertainty (empty) and uncorrelated contributions across multiplicity bins (dark shaded). The data are compared to Monte Carlo calculations [67, 125–128] and to results obtained in Pb–Pb and p–Pb collisions with ALICE [124, 129, 130].

energy dependence is observed for strange and multi-strange hadrons at the LHC. What seems to emerge is, instead, that the enhanced strangeness production depends on the final state environment.

1.3.6 Photons

Photons are electromagnetic probes for the QGP studies. Being colour-neutral, they do not interact with the medium, which is dominated by strong interactions. Furthermore, they are produced during all of the stages the system undergoes after the collision, so they directly probe the entire evolution of the fireball.

Photons can be categorised according to their origin, in order to distinguish the information they carry and their characteristics. The first classification splits them in direct and decay photons. Direct photons are all photons not produced by hadronic decays, as opposed to the decay photons. The latter are emitted only once the system hadronises and constitute the largest contribution to the total photon yield. As such, they are the main background for the direct photon measurement.

1.3.6.1 Direct photons

Direct photons can be further catalogued in prompt, pre-equilibrium and thermal photons.

Prompt photons

Prompt photons originate from initial hard parton scatterings. The main production mechanisms are quark-gluon Compton scattering (a), quark-antiquark annihilation (b) and bremsstrahlung radiation (c) from parton fragmentation. The Feynman diagrams for these processes are shown in Figure 1.21. In the presence of a medium, parton-medium interactions can also take place and give photon emission.

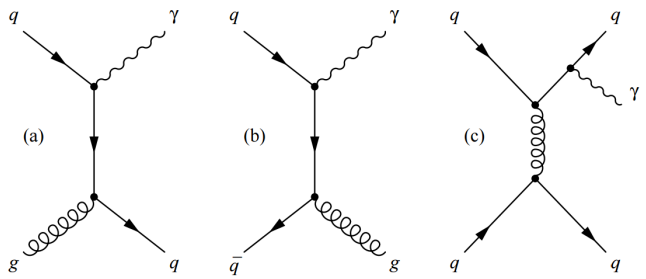

FIGURE 1.21: Feynman diagrams of prompt photon production via Compton scattering (a), quark-antiquark annihilation (b) and bremsstrahlung radiation (c) from quark fragmentation [136].

The prompt photon emission rates can be calculated with pQCD and dominate the high-p_{T} part of the direct photon spectrum. The rates are obtained folding the amplitudes of the processes shown in Figure 1.21 with the parton distribution functions inside the nucleus. The total prompt photon production cross section is given by [137]:

$$\sigma^{\gamma} = \sigma^{(D)} + \sigma^{(F)} = \sigma^{(D)}(\mu_R, M, M_F) + \sum_{k=q,\bar{q},g} \sigma_k^{(F)}(\mu_R, M, M_F) \otimes D_{\gamma/k}(M_F) \qquad (1.13)$$

where the term indicated with (D) refers to the first two Feynman diagrams and has cross section $\sigma^{(D)}$. The photon from the direct production takes part in the hard scatterings as a colourless parton. The fragmentation production, indicated with (F) and with cross section $\sigma_k^{(F)}$, can be thought as the NLO correction to the LO processes of the isolated production. The fragmentation of a high-p_{T} parton k into a photon, represented by the third diagram, is described by the fragmentation functions $D_{\gamma/k}(M_F)$. While the fragmentation photons are affected by the parton energy loss, this is not the case for the isolated photons. The parameters μ_R, M and M_F are the renormalisation, initial-state factorisation and fragmentation scales.

The expected behaviour in heavy-ion collision is a scaling from the pp cross section proportional to the number of nucleon-nucleon collisions. This behaviour can be observed in Figure 1.22, left, where the direct photon yields for pp and Au–Au collisions at 200 GeV measured at PHENIX are shown, compared to NLO pQCD calculations. Data and calculation, the latter properly scaled to the corresponding centrality with the nuclear overlap function T_{AA}, are in agreement for $p_{\mathrm{T}} > 3$ GeV/c, showing that the same hard scattering processes

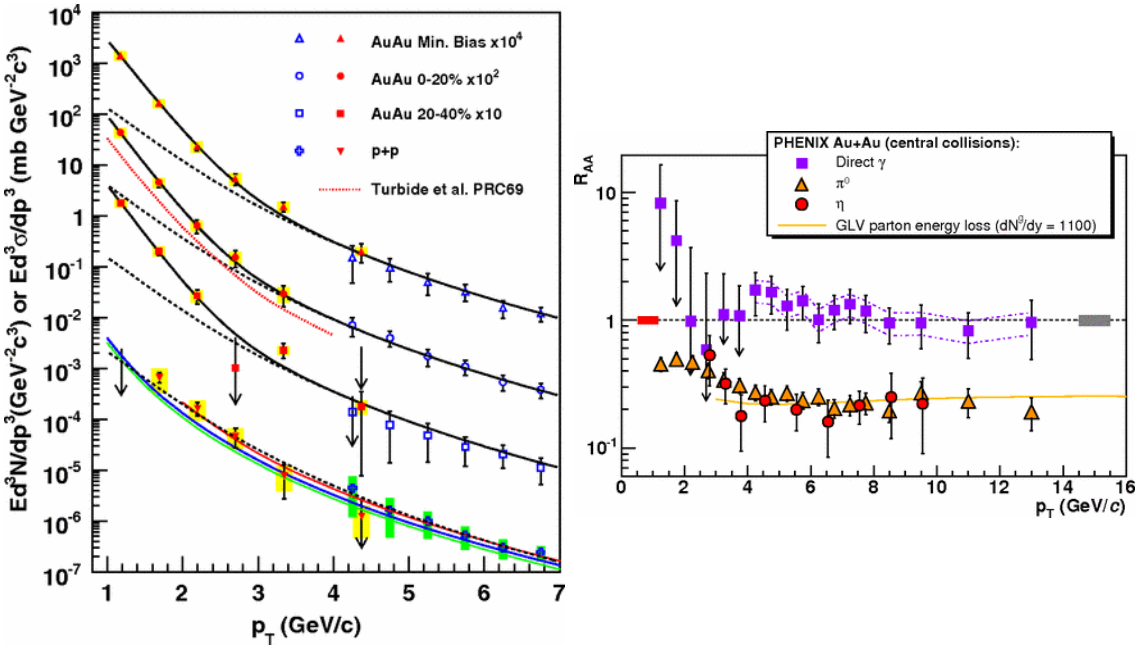

FIGURE 1.22: Left: Direct photon invariant cross section (pp) and yield (Au–Au) as a function of transverse momentum. The filled and empty points indicate two different analyses, [138] and [139, 140] respectively. The arrows indicate upper limits. The curves plotted with the pp data are NLO pQCD calculations [139]. The black curves are a modified power-law fit (dashed lines) and an exponential plus power-law fit (solid lines) to the pp data, scaled by T_{AA} to match the Au–Au data. The dotted red curve plotted together with the 0–20% centrality data is the theory calculation mentioned in the legend [141]. Right: Nuclear modification factor of direct photons [140], π^0 [142] and η [143] mesons measured in central Au–Au collisions at 200 GeV. The error bars include all uncertainties and the bands at unity represent the normalisation uncertainty. The pp reference for the γ R_{AA} is a NLO pQCD calculation [140, 144–147] where the theoretical scale uncertainties are indicated by the dash-dotted lines around the points. The yellow curve is a parton energy loss prediction for the pion suppression factor in a medium with initial gluon density $\mathrm{d}N^g/\mathrm{d}y = 1100$ [148, 149].

drive the prompt photon production in pp and nucleus-nucleus collisions. A similar conclusion can be drawn from Figure 1.22, right, where the direct photon nuclear modification factor is plotted together with the π^0 and η meson ones. The prompt photon measurement is also meant to highlight in-medium modifications, if they exist. It is clear that this is not the case, as expected for an electromagnetic probe: while the mesons show the suppression due to the parton energy loss, the direct photon measurement sits at unity for $p_{\mathrm{T}} > 3$ GeV/c. At low-p_{T}, in both plots form Figure 1.22, an excess with respect to the pp baseline and the pQCD calculation can be observed. In this transverse momentum region, the prompt photon is no longer the dominant contribution and the direct photon yield is given mainly by thermal photons, as it will be discussed in one of the next paragraphs.

Pre-equilibrium photons

The study of pre-equilibrium photons, defined as photons emitted during the early, non-equilibrium phase of the system evolution, is a relatively unexplored field that has been attracting more attention in recent times. In particular, the pre-equilibrium photon contribution, in relation with the thermal one, can help in constraining the onset of thermalisation in semi-peripheral and proton-nucleus collisions.

After the collision, the system can be described as a Glasma [150], an over-occupied strongly interacting and longitudinally expanding plasma dominated by gluons (hence the name). The strong interaction, even in the high-energy QCD environment where the coupling is weak, is caused by the over-occupation.
The pre-equilibrium photon production will be computed using lattice classical statistical methods within the bottom-up thermalisation scenario [151]. This model postulates a fast thermalisation of the system, which is first reached by the soft part of the gluons liberated during the heavy-ion collision. The thermalised soft gluons, which are much higher in number than the primary hard gluons, form a thermal bath. The hard gluons, and the system, thermalise when all their energy is lost to the thermal bath.
The pre-equilibrium temporal evolution is split into three phases, depending on the gluon saturation scale Q^2, defined by the typical gluon transverse momentum, and α_s. The processes considered in calculating the photon yields are Compton scattering and annihilation, but the different phases are characterised by the occupation number of the hard gluons. The first stage is the over-occupied one, with the hard gluon occupation number larger than one. In stage two, the soft gluon component becomes dominant and leads to the formation of the thermal bath in stage three. At the end of this stage, the system has reached the thermal equilibrium.
The description of the Glasma within the bottom-up thermalisation is considered the right approach, as opposed to the somewhat rough assumptions currently used in the hydrodynamical models [152]. Nevertheless, the photon thermal rates calculated with both methods point to a contribution from pre-equilibrium photons relevant for the explanation of some of the discrepancies seen in the comparison of data and theory.

Thermal photons

Thermal photons are emitted during the Quark-Gluon Plasma phase, which acts as a thermal source, as a result of parton scattering (diagrams *a* and *b* from Figure 1.21) or produced during the hadronic (hadron gas) phase, from meson-meson or meson-baryon interactions, *e.g.* $\pi + \pi \rightarrow \rho + \gamma$, $\rho + \pi \rightarrow \pi + \gamma$. Certain models also include the contribution from meson-meson and meson-baryon bremsstrahlung [153]. The thermal photon emission rate can be calculated as for the prompt photon case, exchanging the parton distributions in the nucleus for the thermal distribution functions.
An estimation of the temperature of the thermalised system can be extracted from the thermal photon yields, similarly to what is done for the hadrons and the freeze-out temperatures. Figure 1.23, left, shows the direct photon invariant yields measured with ALICE in Pb–Pb collisions at $\sqrt{s_{\rm NN}} = 2.76$ TeV [154] and with PHENIX in Au–Au collisions at 200 GeV [155]. Both the ALICE and PHENIX direct photon spectra have been fitted with an exponential function at low-$p_{\rm T}$. For the PHENIX data, the contribution from prompt photons, estimated from a parametrisation of the direct photon measurement in pp collisions, has been subtracted before the fit. The inverse of the slope parameter gives an effective temperature $T_{\rm eff}^{\rm ALICE} = 304 \pm 11^{\rm stat} \pm 45^{\rm sys}$ MeV and $T_{\rm eff}^{\rm PHENIX} = 239 \pm 25^{\rm stat} \pm 7^{\rm sys}$ MeV, and therefore a slightly hotter medium produced at LHC than at RHIC. Unfortunately, the relation of the effective temperature to the actual initial temperature of the medium is not straightforward. It was illustrated in Section 1.3.3 that the effective temperature is related to the true initial temperature through the radial flow velocity, meaning that what we extract from the fit is the blue-shifted value. A good knowledge of the emission rates is needed to extract the initial

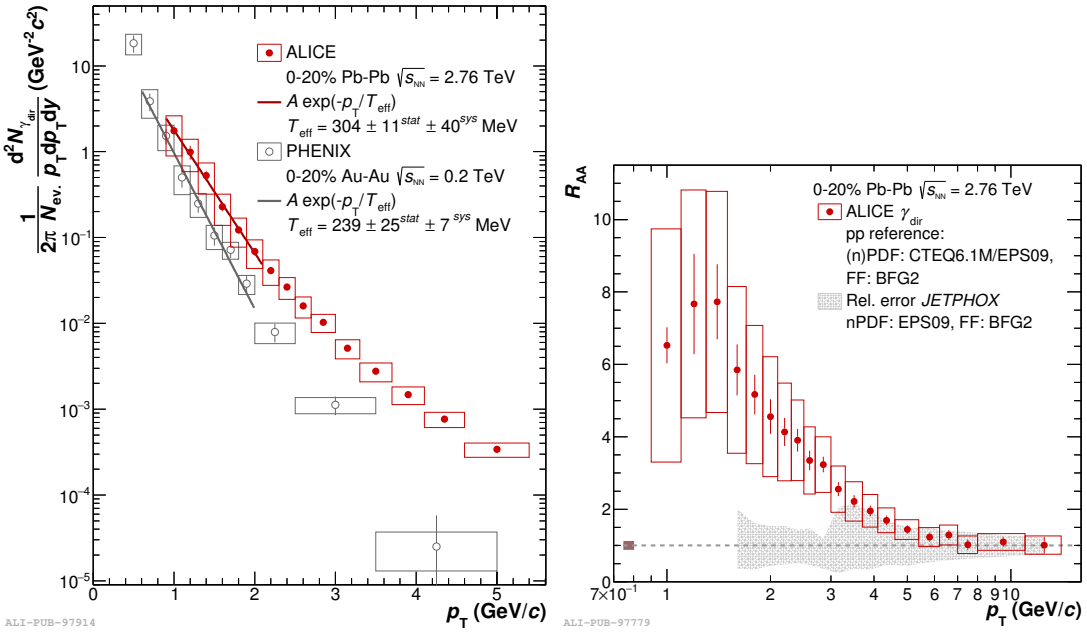

FIGURE 1.23: Left: Direct photon spectra measured in 0–20% Pb–Pb collisions at $\sqrt{s_{\rm NN}} = 2.76$ TeV with ALICE [154] and in Au–Au collisions at 200 GeV with PHENIX [155]. The solid lines represent the fit to the data. Right: Direct photon $R_{\rm AA}$ in 0–20% Pb–Pb collisions at $\sqrt{s_{\rm NN}} = 2.76$ TeV with ALICE. An NLO pQCD calculation for the direct photons in pp at the same centre-of mass energy [156] has been taken as baseline. The coloured band at unity represents the normalisation uncertainty while the grey band indicates the uncertainty from the JETPHOX calculation with similar PDF and FF as for the NLO calculation.

temperature since also later stage photon emission needs to be taken into account.
Figure 1.23, right, is shown as a continuation on Figure 1.22, right. The direct photon $R_{\rm AA}$ in ALICE is also calculated taking a NLO pQCD calculation as pp baseline [156] and also here the excess above unity is clear, showing an $R_{\rm AA} > 6$. Several theory groups are working on estimating the direct photon production in heavy-ion collisions [153, 156–158] and while the starting point is common in the assumption of the QGP formation and of the dominance of photons from hard scattering at high-$p_{\rm T}$, the system evolution is treated differently, thus delivering predictions with various level of agreement with the data, as it can be seen in Figure 1.24.

1.3.6.2 Decay photons

Photons from hadron decays are the largest contribution to the total photon yield, constituting also the largest background for the direct photon measurement. The highest yield of photons from hadron decays is due to the neutral pion and η meson. They both decay into two photons with a branching ratio of 98.8% and 39.4%, respectively, and give almost the totality of the photon decay yield. Contributions from η' and ω follow with a much smaller fraction, while photons from ϕ and ρ^0 mesons are negligible [9]. In addition to these direct contributions, the feed-down from heavier particles decaying into hadrons with photon decays need also to be accounted for, *e.g.* $K^0_s \to \pi^0 + \pi^0$.
Table 1.1 summarises the decay photon sources, their decays and branching ratio, while Figure 1.25 shows the fraction of the single photon source over the total photon yield from

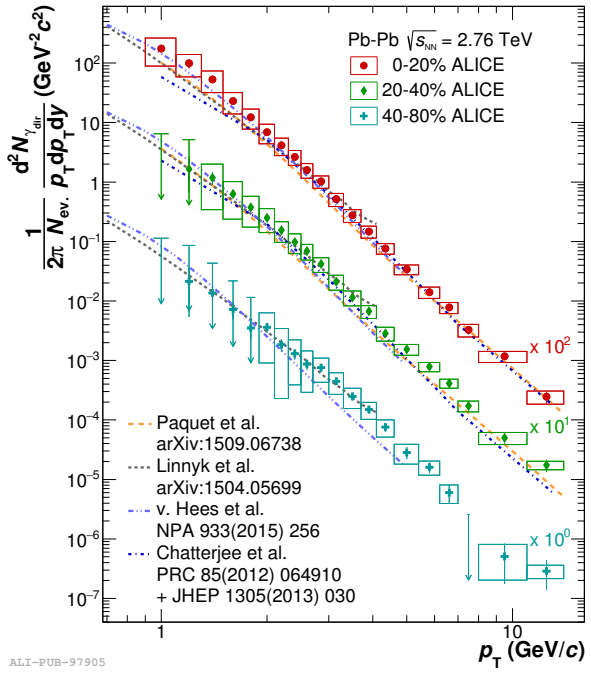

FIGURE 1.24: Comparison of the direct photon spectra measured in the 0–20%, 20–40% and 40–80% central Pb–Pb collisions at $\sqrt{s_{\rm NN}} = 2.76$ TeV with ALICE [154] to the most recent theoretical calculations [153, 156–158]. The bars on the data indicate statistical uncertainties, boxes the systematic uncertainties. The arrows represent upper limits.

decays. The single sources are obtained from a data driven simulation, called cocktail simulation, which is used to estimate the decay photon background. The cocktail simulation production will be described in Chapter 7.

Source	Decay	B.R.(%)
π^0	$\gamma\gamma$	98.8
	$e^+e^-\gamma$	1.17
η	$\gamma\gamma$	39.4
	$\pi^+\pi^-\gamma$	4.22
	$e^+e^-\gamma$	6.9×10^{-3}
η'	$\pi^0\gamma$	29.1
	$\omega\gamma$	2.62
	$\gamma\gamma$	2.21
ω	$\pi^0\gamma$	8.28
	$\eta\gamma$	4.6×10^{-4}
ρ^0	$\pi^+\pi^-\gamma$	9.9×10^{-3}
	$\pi^0\gamma$	6.0×10^{-4}
ϕ	$\eta\gamma$	1.3
	$\pi^0\gamma$	1.27×10^{-3}
	$\omega\gamma$	<5 (CL=84%)

TABLE 1.1: List of the most relevant decay photon sources with the relevant photon decays and branching ratios [9].

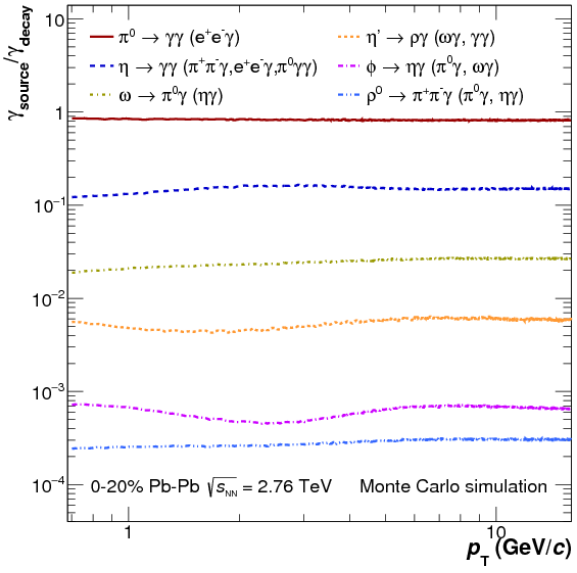

FIGURE 1.25: Relative contributions to the total decay photon yields as a function of the decay photon transverse momentum [154].

Chapter 2

A Large Ion Collider Experiment at the Large Hadron Collider

The Large Hadron Collider (LHC) [159] is the largest and most powerful existing particle accelerator. It is located at CERN, the European Organisation for Nuclear Research near the city of Geneva, astride the border between Switzerland and France. CERN was founded in 1954 and since then it has been exploring the most fundamental aspects of physics. The research is conducted using the most advanced and sophisticated instrumentation and has lead to break-through discoveries in particle physics.
In this chapter, a general description of the LHC and its experiments will be given. More details will be provided on the ALICE detector and sub-detectors that are relevant for this thesis, as well as a brief description of the software used for the processing of the reconstructed data.

2.1 The LHC – The Large Hadron Collider

The LHC is the largest collider in the world. It is the last step of the accelerator complex at CERN and uses the already existing 27 km tunnel that hosted the previous accelerator, the Large Electron Positron (LEP) collider. The LHC can collide hadrons (protons) and heavy-ions. Differently from the LEP machine, which was colliding particle and anti-particle and thus needing only one ring for the two beams, the LHC has two rings with counter-rotating beams. The double ring of the hadron accelerator is equipped with superconducting magnets and is segmented into eight units, or sectors, eight arcs and eight insertions. A total of 1232 dipole bending magnets are contained in the arcs and keep the beams on the circular orbit, providing a nominal dipole magnetic field of 8.33 tesla. The insertions consist of straight sections with a transition region at each end, whose structure changes depending on whether they are used for injection, to collide beams within an experiment, for beam cleaning or dumping. To focus the beam in these transition regions, 392 quadrupole magnets are used.

Before being ready to collide, protons need to be accelerated to the desired energy. This is done in steps, using the CERN accelerating chain, shown in Figure 2.1. Hydrogen atoms are stripped of their orbiting electrons to obtain protons, that are injected from a linear

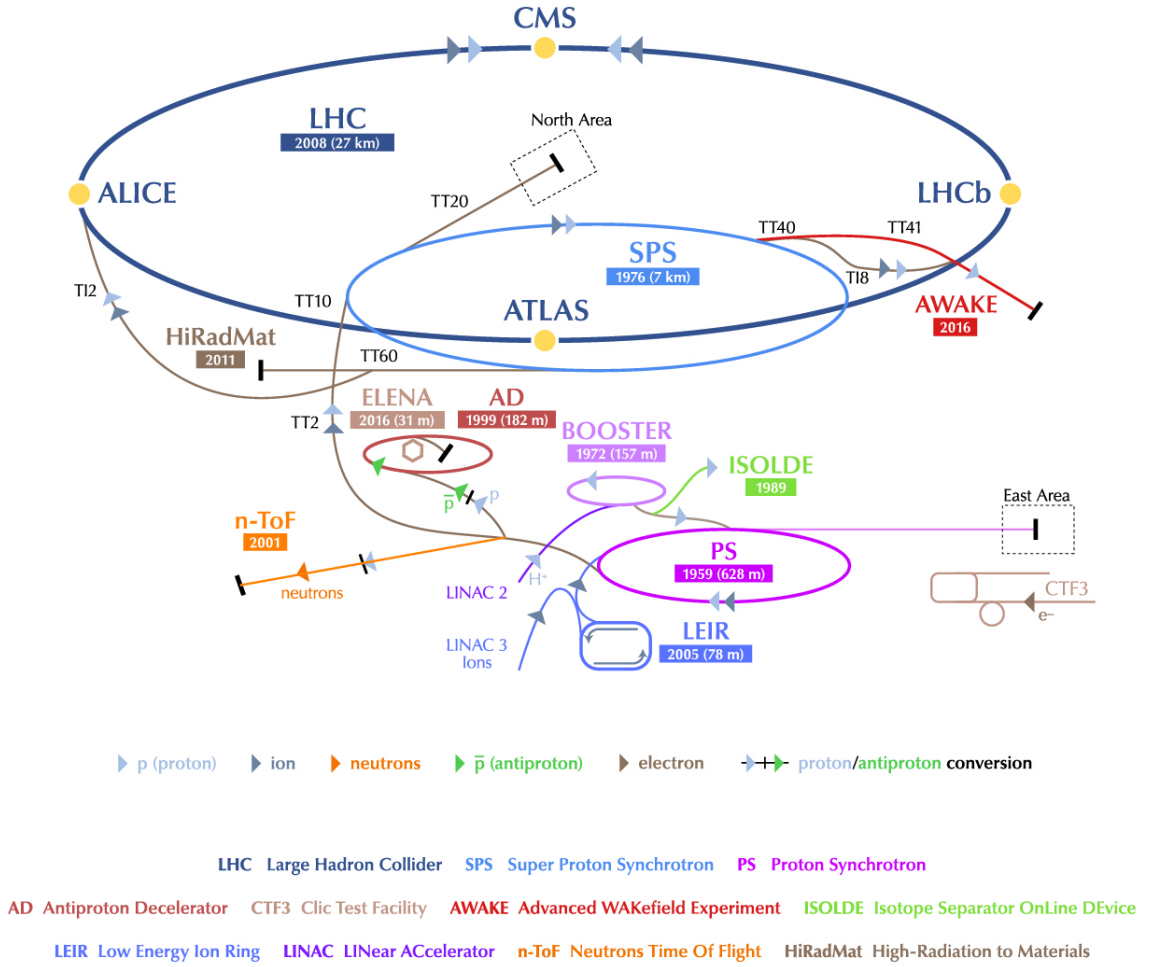

FIGURE 2.1: The CERN accelerator complex [160]. A LINAC is the first step in the acceleration chain for both protons and ions. Protons continue onward in the Booster, while ions go to the LEIR. The chain coincides for the two starting from the PS, then on to the SPS and to the LHC. The energy values reached in each step are given in the text.

accelerator (LINAC 2) into the Proton Synchrotron Booster (PSB) with an initial energy of 50 MeV. Here, they are accelerated to an energy of 1.4 GeV before passing to the Proton Synchrotron (PS) to be further accelerated up to 25 GeV. The beam is then sent to the Super Proton Synchrotron (SPS) before being injected into the LHC with an energy of 450 GeV. The machine can also accelerate heavy-ions. Lead ions are obtained heating a high purity solid lead sample to a temperature of about 800°C. The lead vapour, similarly to the hydrogen case, is ionised by an electron current. The ions are accelerated and stripped of electrons in successive steps, going through a linear accelerator (LINAC 3), a Low Energy Ion Ring (LEIR) and the PS and passing through carbons foils until $^{208}Pb^{82+}$ reaches the SPS where the energy is brought to $450 \cdot Z/A = 177$ GeV/u (energy per nucleon) before being injected into the LHC. Both protons and heavy-ion beams, consisting of finite bunches of particles, are injected into the LHC in both clockwise and anticlockwise direction. The bunches are brought to the desired energy before the collisions start, and they keep circulating in the ring for several hours before it is necessary to dump the beam. A beam dump occurs either when the beam is not collimated, meaning the transverse size is not optimal for collisions anymore, or when the desired luminosity is lost, due to the gradual loss of particles.

The collisions take place within the experiments sitting in caverns and centred around the interaction points.
There are seven experiments connected to the LHC. The main large experiments are ALICE (A Large Ion Collider Experiment) [161], ATLAS (A Toroidal LHC ApparatuS) [162], CMS (Compact Muon Solenoid) [163] and LHCb (the LHC beauty experiment) [164]. On a smaller scale are TOTEM (Total, elastic and diffractive cross-section measurement) [165], LHCf (LHC forward) [166] and MoEDAL (Monopole and Exotics Detector at the LHC) [167, 168].

2.2 ALICE – A Large Ion Collider Experiment

ALICE is a general-purpose, heavy-ion detector. Its physics program investigates the QCD phase transition and the characteristics of the Quark-Gluon Plasma, a strongly interacting state of the matter with high energy density and temperature (refer to Chapter 1 for more details).
Since heavy-ion collisions are the experiment main focus, ALICE is designed to withstand their high particle density environment and process and record the large amount of data generated. The detector is 26 m long and 16 m high and wide, with a total weight around 10000 t. It has high granularity and it is designed to measure charged particle multiplicity up to $\mathrm{d}N_{ch}/\mathrm{d}y \approx 8000$ from a minimum transverse momentum of $p_{\mathrm{T}} \approx 0.15$ GeV/c [169]. The variety of sub-detectors allows particle identification up to 20 GeV/c.
The layout of the ALICE detector is shown in Figure 2.2. The experiment is divided in a central barrel, fully contained in the solenoid magnet of the L3 experiment at LEP, and a muon arm. The muon spectrometer is partially inside the central barrel, where the hadron absorber is situated, followed by two muon tracking chambers at the edge of the solenoid and by a third chamber, enclosed in a dipole magnet. The spectrometer is completed by two more tracking chambers and, behind an iron wall, two trigger chambers. The beam pipe passing through the chambers is surrounded by a low angle absorber. The central barrel detectors are dedicated to particle tracking and identification. From the inside-out, there are the Inner Tracking System (ITS), the Time Projection Chamber (TPC), the Transition Radiation Detector (TRD) and the Time-of-Flight (TOF) detector, all of which have full azimuthal coverage. On the outer layers and with reduced azimuthal acceptance are the ring imaging Cerenkov (HMPID, High Momentum Particle IDentification) detector and two electromagnetic calorimeters, the photon spectrometer (PHOS) and the EMCal. During the first LHC long shut down (years 2013-2015), a dijet calorimeter, the DCal, has been installed opposite from the EMCal and has been active in the second LHC data taking run (from 2015 to nowadays). Near the interaction point (IP) and some distance away along the beam pipe are located several small detectors: V0, T0, PMD, FMD and ZDC. The PMD (Photon Multiplicity Detector) and the FMD (Forward Multiplicity Detector) are used to measure particle multiplicity while the other detector are used for event characterisation.
In the following sections, only the detectors relevant to the measurements in this thesis will be described.

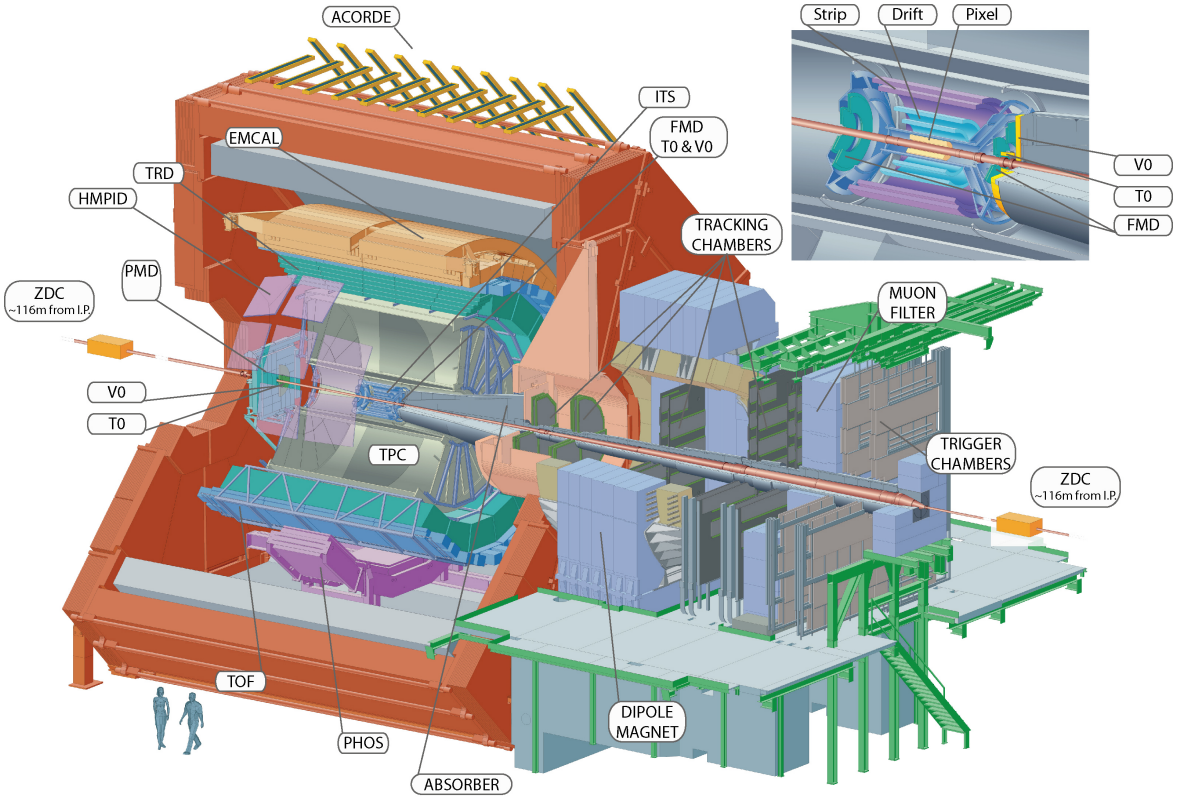

FIGURE 2.2: The ALICE detector schematics [161].

ALICE coordinate system

ALICE has a right-handed Cartesian coordinate system, with the origin in the IP. The z-axis is aligned with the beam pipe, pointing away form the muon arm. The half of the detector on the positive part of the z-axis is called A side, while the one on the negative part is the C side. The x-axis is pointing left, facing the A side. The y-axis points upwards, towards the surface. The azimuthal angle φ, between the x and y-axis, counts clockwise with the observer facing the A side. The polar angle θ increases from the positive part of the z-axis towards the y-axis.
Other relevant quantities are the rapidity in the laboratory system, defined as

$$y = \frac{1}{2}\ln\left(\frac{E + p_z}{E - p_z}\right) \tag{2.1}$$

where E is the energy of the particle considered and p_z is the particle longitudinal momentum component, along the z-axis. Derived form the rapidity is the pseudorapidity, $\eta = -\ln[\tan(\theta/2)]$, with θ polar angle, calculable without the knowledge of the particle mass and that is almost equivalent to y for highly relativistic particles. The ALICE central barrel pseudorapidity range is $|\eta| < 0.9$, while the range is $-4.0 < \eta < -2.5$ for the muon spectrometer.

ITS – Inner Tracking System

The ITS [161, 170] is the innermost of the ALICE barrel detectors. It is composed of 6 cylindrical silicon detectors, covering the radius from 4 to 44 cm. From the inside-out, the layers are two Silicon Pixel Detectors (SPDs), two Silicon Drift Detectors (SDDs) and two Silicon Strip Detectors (SSDs). The ITS provides primary vertex reconstruction with resolution better than 100 μm in the z-direction and is the first step of the tracking and particle identification (PID) systems. In particular, the SDD and SSD provide particle identification via $\mathrm{d}E/\mathrm{d}x$ in the non-relativistic region. The ITS works in tandem with the TPC, as it provides particle tracking and identification at low momentum (below 200 MeV/c), helps improving the angle and momentum resolution and rejects the out-of-bunch pile-up.

TPC – Time Projection Chamber

The TPC [171] design was inspired by the need for full azimuthal coverage in a mid-rapidity detector, with high momentum resolution and a good energy loss measurement for PID. The TPC is a cylindrical barrel centred around the IP and filled (at the time relevant for this thesis) with a mixture of Ne-CO_2 (90%-10%). The gas active volume extends radially from 85 to 250 cm. The axis of the barrel is aligned with the magnetic field and the field cage ensures a uniform axial electric field with the central electrode at 100 kV. The drift field is 400 V/cm and the drift time $\sim$ 94 μs. The read-out chambers are Multi-Wire Proportional Chambers (MWPC) with cathode pad read-out. They are installed in 18 trapezoidal sectors on each of the two end-plates and have different size depending on whether they are part of the inner or outer read-out, to accommodate the large radius coverage and the varying track multiplicity density. The Inner Read-Out Chambers (IROCs) extend from 84.8 to 132 cm while the Outer Read-Out Chambers (OROCs) from 134.6 to 246.6 cm. The IROCs have a total of 5504 pads, divided in 63 pad rows with pad size 4×7.5 mm^2 ($r\phi \times r$). The OROCs have small and large pads, of size 6×10 and 6×15 mm^2, in 64 and 32 rows for a total of 5952 and 4032 pads, respectively. The total number of read-out channels is 557568.
The charged particles passing through the detector ionise the gas. The electrons produced in the ionisation drift in the electric field towards the MWPCs on the end plates, where the signal clusters give a precise measurement of the x and y coordinate. The z coordinate is retrieved from the drift time in the gas together with the beam collision time reference provided by the T0 detector. These measurements together, with their high precision, allow for a three-dimensional reconstruction of the initial charged particle track and make the TPC the main charged particle tracking system. The TPC is also the main PID system: the particles are identified via their specific energy loss ($\mathrm{d}E/\mathrm{d}x$), described by the Bethe-Bloch function. The particle momentum is measured from the track curvature in the magnetic field, from a minimum of 100 MeV/c to beyond 100 GeV/c. The momentum resolution is better than 2.5% for electrons of 4 GeV/c and the $\mathrm{d}E/\mathrm{d}x$ resolution is about 5%(6%) for pp (central Pb–Pb) collisions.

TRD – Transition Radiation detector

The TRD [172] has tracking, identification and triggering capabilities, contributing to the overall experiment performance. In particular, it is meant to improve the electron identification above 1 GeV/c, via the characteristic properties of the transition radiation and with a better pion rejection. The detector working principle is based on the radiation produced by relativistic electron crossing material of different dielectric constants. The radiation, which are photons in the X-ray range, deposits energy in a ionisation gas and is detected with a method similar to the one used for the TPC. The discrimination of electrons from pions is possible though the characteristic transition radiation signal distribution, which is absent in the pion case.
The TRD sits at 2.9 m from the IP, has full azimuthal coverage and pseudorapidity coverage of $|\eta| < 0.84$. It is composed of 18 supermodules, each module is segmented in five stacks in the longitudinal direction and in six layers in the radial direction for a total of 552 read-out chambers. The chambers consist of a fibre/foam (laminated Rohacell/polypropylene) sandwich radiator, a drift region with a mixture of Xe-CO_2 (85%-15%) as counting gas and a MWPC with pad read-out.
The TRD was not fully installed at the time relevant for this thesis and it is not used for this work. Even if not completed, it was still used for triggering in pp and p–Pb collisions. Since 2015 the detector is complete and participating in the data taking.

TOF – Time-of-Flight detector

TOF is a cylindrical Multi-gap Resistive Plate Chamber (MRPC) detector, segmented into 18 azimuthal sectors and 5 sectors along the z-axis, at 370 cm from the IP [161]. The chambers consist of resistive glass plates, on which a high and uniform electric field is applied that immediately amplifies the ionisation produced by a charged particle in an electron avalanche. The PID is achieved with a time-of-flight measurement, which is characteristic for each particle. The time-of-flight is calculated as the difference between the time of the hit measured by the TOF and the time of the interaction, that can be measured by the T0 detector, by the LHC central timing or by the TOF itself, if enough tracks are present for global timing. The time resolution is about 80 ps. The detector position and full azimuthal coverage are optimal for a good measurement at intermediate momentum, extending the K/π separation to 2.5–3 GeV/c and the p/K separation to 3.5–4 GeV/c. Moreover, TOF is used to resolve the TPC dE/dx crossings.

PHOS – Photon Spectrometer

The PHOS spectrometer consists of a highly segmented electromagnetic calorimeter (PHOS) and a multi-wire proportional chamber as Charged Particle Veto (CPV) detector [161]. At the time of the data taking of interest for the results in this thesis, three PHOS modules were installed at a radius of 460 cm from the IP and covering the pseudorapidity range $-0.12 \leq \eta \leq 0.12$ and from 260 to 320° of the azimuthal angle. The detector is made of a dense lead-tungsten scintillator ($PbWO_4$) with a 2 cm Molière radius ($20X_0$). The crystals

are kept at a temperature of $-25°$ C to increase the light yield, *i.e.* improve the energy resolution.

EMCal – Electromagnetic Calorimeter

The EMCal [173] is a lead-scintillator sampling calorimeter (77 layers of 1.4 mm Pb and 1.7 mm polystyrene scintillators) located at about 4.5 m from the beam pipe. It has cylindrical geometry and covers pseudorapidity $|\eta| < 0.7$ and $\Delta\phi = 107°$, almost azimuthally opposite to PHOS. The size of the detector has been constrained by the space available in the barrel. The EMCal has high granularity (6×6 cm^2 cells) and moderate energy resolution ($\sigma_{E(\mathrm{GeV})}/E = 5.1\%/E \oplus 11.1\%/\sqrt{E} \oplus 1.7\%$ [174]).

V0 detector

The V0 detector [175] consists of two scintillator counters, V0A and V0C, located at either side of the IP, respectively at 340 cm and pseudorapidity $2.8 < \eta < 5.1$ (on the A side) and at 90 cm and pseudorapidity $-3.7 < \eta < -1.7$ (in front of the hadronic absorber, on the C side). The V0 detectors are used for event triggering and characterisation, since the multiplicity recorded during an event relates to the centrality in nucleus-nucleus collisions. Moreover, these detectors are used to reject pile-up and beam-gas interactions [169].

T0 detector

The T0 detector [176] is also composed of two separate detector, T0A and T0C, located at about 370 cm and 70 cm from IP, respectively and with pseudorapidity coverage of $5 < \eta < 4.6$ and $-2.9 < \eta < -3.2$. The T0 are arrays of 12 Cherenkov counters each, with a quartz radiator and a photomultiplier tube.
It has an overlapping capabilities with the V0, but it is foremost used for triggering and as timing reference for detectors such as the TPC and TOF. It is also important for the synchronisation with the central LHC machine clock (for beam tuning and monitoring).

ZDCs – Zero Degree Calorimeters

Together with the V0 detectors, the ZDCs are used to calculate the number of non-interacting nucleons, thus, indirectly, the centrality of an A–A collision. The number of nuclei participating in a collisions is given by $N_{participants} = A - N_{spectator}$, where the number of non-interacting (spectators) nuclei can be estimated by the energy deposit on the ZDCs. Installed at 116 m from the IP, these sampling calorimeters have a dense absorber and quartz fibers that detect the Cerenkov radiation produced by the hadronic shower. In order to detect both neutrons and protons, the ZDC is composed of two separate detectors: the ZN for neutrons is placed at zero degrees between the beam pipes, while the ZP for the protons is external to the outgoing beam pipe, in the direction of magnetic deflection of the positive particles. In addition, two electromagnetic calorimeters (ZEM), also of alternated lead plates and quartz fibers and located at 7 m from the IP, are used to distinguish between central and (very)

peripheral A–A collisions. Since the energy deposit in the hadronic calorimeters is small in both cases, they measure the energy of the particles emitted at forward rapidity, which increases monotonically with the collision centrality.

2.3 The ALICE software framework

The reconstruction of the data recorded by the experiment is done using a software framework specific for ALICE. The base on which this is built is Root [177, 178], written in the object-oriented language C++. Root contains many of the functions and tools necessary to a physics data analysis, such as fitting and unfolding routines and analytic functions. This is a common software in physics, used by several fields. Since Root is not enough to cover the many functionalities required by the ALICE data processing and analysis, the AliRoot and AliPhysics software frameworks [179] have been developed.
Aliroot contains the core classes. Here are defined the data types, the classes describing the experiment geometry or used for the detector calibration and alignment. The data reconstruction code is also here, for particle tracking and identification.
AliPhysics contains the day-to-day classes that every user employs in analysing the data. It is a frequently changed set of classes, to keep up with analyses adjustments. It also contains the code to access the Grid and use the shared computing resources.
In the ALICE software framework there are several other branches dedicated, for example, to Monte Carlo simulations with the possibility of using several different kind of event generators, or to access the stored data. This latter is called Alienv (ALICE environment), and allows the user to directly access the processed and reconstructed data and Monte Carlo simulation productions.

2.4 The other LHC experiments

ATLAS

ATLAS [162] is a general-purpose high-energy physics detector that focuses on high-precision studies of the Standard Model and contributes to the study of the Higgs boson, and searches for physics beyond the Standard Model. The detector has symmetric geometry, with large pseudorapidity acceptance and almost full azimuthal coverage. In order to cope with the high interaction rate delivered by the LHC, high granularity detectors, fast electronics and a highly efficient triggering system have been adopted. ATLAS magnet is a thin superconducting solenoid with three large superconducting toroids (one barrel and two end caps) that surround the inner detectors, delivering a magnetic field of 2 tesla. The inner detectors consist of semiconductor pixel and strip detectors and straw-tube tracking detectors. Part of the inner barrel detectors are also the electromagnetic and hadronic calorimeters, while the muon chambers are the outermost detectors and also sit at the end caps.

CMS

CMS is a multi-purpose detector with symmetric geometry [163], at whose centre sit a silicon pixel and strip tracker, a lead-tungsten scintillating crystal electromagnetic calorimeter and a brass-scintillator sampling hadron calorimeter, surrounded by a high magnetic field (4 T) and large-bore superconducting solenoid. The detector is also equipped with four muon detector stations. The large bending power is essential to measure the high energy particle momenta with high precision. The physics program covers the study of the Standard Model that lead to the discovery, together with ATLAS, of the Higgs boson, the search for exotic physics and dark matter candidates. CMS, sharing the same physics goals as ATLAS but equipped with an alternative design ensures the experimental confirmation of discoveries made by either of the two detectors.

LHCb

LHCb [164] is the experiment dedicated to beauty (heavy flavour) physics and to the characterisation of charge-parity (CP) symmetry violation in the charm and beauty sectors. The possibility of tuning the luminosity at the experiment interaction point independently allows LHCb to have optimal conditions. The detector has a flexible trigger and good vertex and momentum resolution, essential to study B-mesons. LHCb is a single-arm spectrometer with forward angular coverage.
LHCb has also recently enlarged its physics program, studying not only pp collisions but also proton-lead and lead-lead collisions [180, 181].

LHCf

Two detectors, sitting at 140 m at either side of the ATLAS collision point, make up the LHCf experiment [166]. They study particles produced in the forward direction, at nearly zero degrees with respect to the proton beam direction. This setup is adopted in order to simulate cosmic radiation in the more controllable environment of the laboratory.

TOTEM

TOTEM [165] is designed to measure protons coming from a collision at small angle with high precision. The experiment surrounds CMS for almost half a kilometre. The combination of its capabilities with those of CMS could deliver results with much higher precision.

MoEDAL

MoEDAL [167, 168] is primarily dedicated to the search of magnetically charged particles (magnetic monopoles). The experiment sits at the interaction point of LHCb and consists of stacks of plastic nuclear-track detectors, working as a camera passively looking for particle predicted by theories beyond the Standard Model.

Chapter 3

Data sample and Monte Carlo simulations

In this chapter, the data sample and the Monte Carlo simulations used in the measurements presented in this thesis will be introduced. Moreover, the event selection criteria and centrality estimation will be described. The detector condition during data taking will also be reported, since it is relevant to the analysis.

3.1 Data sample and event selection

The lead-lead collision data used in this work have been recorded during the data taking period that took place at the end of 2011. It is the second heavy-ion run (the first was in 2010) of what is referred to as LHC Run1, the machine active period that extends from 2008 till 2013. For the 2011 lead run, a total of 358 bunches per beam were injected in the machine, with 200 ns spacing from one bunch to the other. The LHC provided ALICE with an interaction rate of ≈ 4 kHz. The instantaneous luminosity at which ALICE took data was of the order of 10^{26} s^{-1} cm^{-2}, one order of magnitude higher than in 2010, leading to a total integrated delivered luminosity of 146 μb^{-1} [169]. During data taking, a minimum bias trigger and two centrality triggers were active at the same time. The minimum bias trigger used is called MB$_{\rm OR}$: hits are required in the SPD and in one of the V0 detectors. In addition, signals are also required in both ZDCs to suppress the electromagnetic interactions between nuclei. Both the minimum bias and the centrality trigger for semi-central (not head-on) collisions were downscaled. The online trigger selection ensures that the events recorded are high purity beam-beam hadronic interactions. The background is estimated using control triggers that tag events where one of the two bunches has no collision partner or the beam is passing the luminous region. Rare triggers were also active, but are not interesting for this work.

As mentioned above, the luminosity in the second lead run is much higher than before and it was estimated that the data produced would exceed the capabilities of transfer to the storage system. To cope with the increased event rate, a data reduction had to be applied already online, within the event, to reduce the data size. This is achieved using the High Level Trigger (HLT) and the Huffman encoding to store only TPC clusters instead of raw

signals and compress the data [182–184].
An offline event selection is generally applied to all types of data samples collected (pp, p–Pb, Pb–Pb). It cross checks that the type of event is correct according to the online trigger and repeats the selection using offline the stored information. Lastly, it is required that the z-coordinate of the primary vertex of the collisions lies within 10 cm of the ALICE geometrical centre (origin of the coordinate system). This requirement is specific for the neutral meson and direct photon measurements and ensures the good quality of the reconstructed events selected.

3.1.1 Centrality definition in ALICE

Events in nucleus-nucleus collisions can be classified according to the geometrical overlap of the colliding nuclei, simplifying, the centrality, and on the subsequent particle multiplicity produced [185].
At the time of the collision, the spacial position of the two nuclei is characterised by the impact parameter, b, the distance between their respective centres, as it was shown in the left sketch of Figure 1.6. For $b = 0$, the collision is said to be head-on. For larger values, that can range up to the sum of the radii, the collisions are more and more peripheral.
A direct measurement of b, of the geometry of the collision and of the number of nucleons effectively participating is not possible. Instead, the average charged particle multiplicity and the energy deposited in the ZDCs are used to relate the geometry of the collision to its multiplicity. This connection is possible because, on one hand, the average charged-particle multiplicity is expected to monotonically decrease for increasing values of the impact parameter. On the other hand, the energy on the ZDCs is directly proportional to the number of spectators, the nucleons that do not participate in the collision. An example can be seen in Figure 3.1.

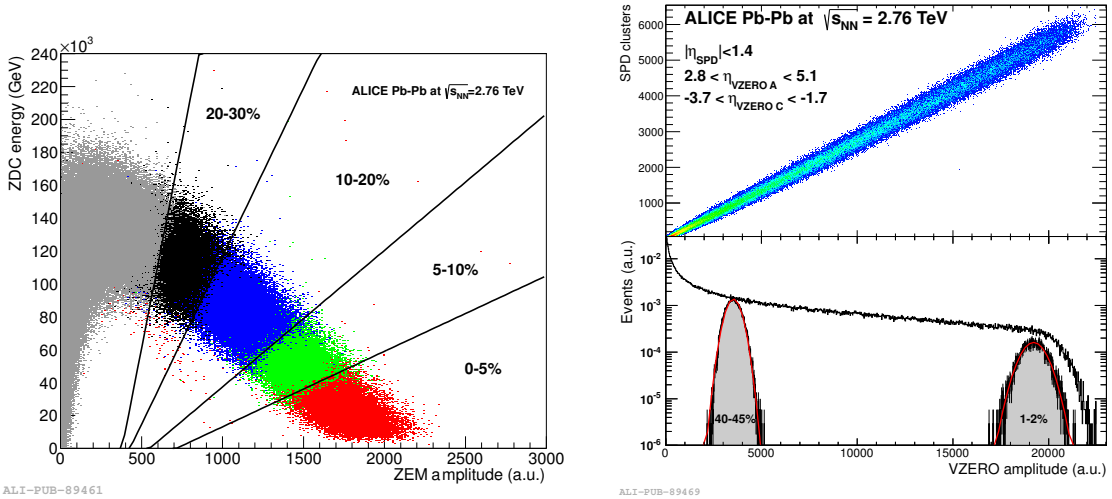

FIGURE 3.1: Left: Energy deposit of the spectators in the ZDCs as a function of the ZEMs signal amplitude. The coloured areas represent the corresponding distribution using given V0 signal amplitudes. Right: In the top panel, the SPD multiplicity is shown as a function of the V0 amplitude. The total V0 signal amplitude distribution is compared with two distributions for given centrality values selected using the SPD detector in the bottom panel. Both figures can be found in [185].

The left figure represents the correlation between the energy deposit of the nucleons escaping the collision and the energy of the particles emitted in the forward direction. The latter increases with the collision centrality and is used to distinguish between central and very peripheral events, since in both cases few spectators are detected. Figure 3.1 right shows instead the correlation between the multiplicity measured by the V0 detector, which is given by the sum of the signals from the V0A and V0C, and by the SPD, in the top panel. In the bottom panel, their estimations are compared.
The number of nucleons that underwent a binary collision, *i.e.* participant nucleons or N_{part}, is obtained from the number of spectator nucleons. The dependence of the impact parameter on N_{part} is then modelled with a Glauber Monte Carlo simulation.
The Glauber model [36] used by ALICE allows to describe the geometry of the nuclear collisions and access the impact parameter. The model treats the nuclear collision as a superposition of independent inelastic binary nucleon-nucleon collisions, with each one independent and unaffected by the others. It relies on the impact parameter and purely geometrical quantities such as the number of participant nucleons (N_{part}) and of colliding nucleons (N_{coll}) to give a consistent picture in all colliding systems.
In the simulation, the nuclei are composed of nucleons stochastically positioned according to the nuclear density function

$$\rho(r) = \rho_0 \frac{1 + W(r/R)^2}{1 + \exp\frac{r-R}{a}} \tag{3.1}$$

where $R = (6.62 \pm 0.06)$ fm is the radius of the ^{208}Pb nucleus, $a = (0.546 \pm 0.010)$ fm is the nuclear skin thickness and ρ_0 is the nucleon density, obtained from the normalisation condition $\int \rho(r)\mathrm{d}r = A$, with A the mass number.
The nuclear collisions are simulated randomly selecting the impact parameter up to a maximum value of $2R$. For a binary nucleon-nucleon collision to take place, the distance between the nucleons has to be $d < \sqrt{\sigma_{\mathrm{NN}}^{\mathrm{inel}}/\pi}$, where $\sigma_{\mathrm{NN}}^{\mathrm{inel}}$ is the inelastic nucleon-nucleon cross section. Elastic processes are not included in the model calculations. Furthermore, a black-disk nucleon-nucleon overlap function is assumed, but it has been shown that also a Gaussian overlap function delivers consistent results [186].
The values of b and N_{part} extracted from the Glauber model are shown in Figure 3.2.
The simplification that equates the collision centrality to the nuclear overlap is justified because the former is expressed as a percentage of the total nuclear interaction cross section,

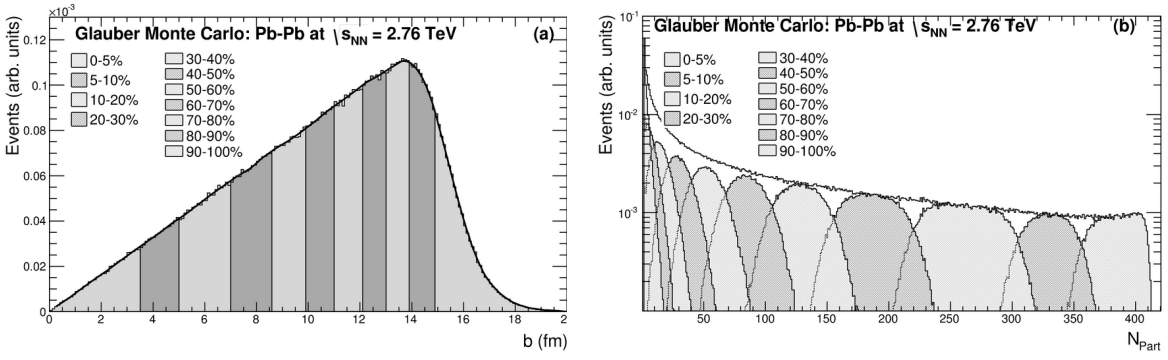

FIGURE 3.2: Impact parameter b (left) and number of participant nucleons N_{part} (right) in slices of percentiles of the hadronic cross section and corresponding centralities, respectively. These quantities are extracted from Glauber Monte Carlo simulations for Pb–Pb collisions at $\sqrt{s_{\mathrm{NN}}} = 2.76$ TeV [185].

σ_{AA}. The centrality percentile for an impact parameter b is obtained integrating the impact parameter distribution $\mathrm{d}\sigma/\mathrm{d}b'$:

$$c(b) = \frac{\int_0^b \frac{\mathrm{d}\sigma}{\mathrm{d}b'}\mathrm{d}b'}{\int_0^\infty \frac{\mathrm{d}\sigma}{\mathrm{d}b'}\mathrm{d}b'} = \frac{1}{\sigma_{AA}}\int_0^b \frac{\mathrm{d}\sigma}{\mathrm{d}b'}\mathrm{d}b'. \tag{3.2}$$

Considering how centrality is measured in ALICE [185], this becomes the fraction of nuclear cross section above a certain value of charged particle multiplicity,

$$c(b) \approx \frac{1}{N_{event}}\int_{N_{ch}}^{\infty} \frac{\mathrm{d}n}{\mathrm{d}N'_{ch}}\mathrm{d}N'_{ch}, \tag{3.3}$$

where the nuclear cross section is substituted with the number of observed events, corrected for trigger efficiency. As illustrated above, the charged particle multiplicity is measured by the V0 detector. The multiplicity distribution of Figure 3.3 shows a rise towards small amplitudes, visible in the inlaid panel, originating from trigger inefficiencies and electromagnetic background from interaction between the ions. The coincidence of the V0 signal and of a hit in the SPD, as well as signals in the ZDCs are required to suppress this background.
For larger V0 amplitudes, the multiplicity distribution shows a plateau region and then an edge corresponding to the most central collisions, sensitive to the detector acceptance and to fluctuations in the charged particle density. The V0 amplitude distributions are fitted with a convolution of a negative binomial distribution (NBD) fit to the detector amplitude in the elementary collision system, shown with the red line in Figure 3.3. The good description of the V0 distribution is achieved considering the number of "ancestors" in the characterisation of the relation between N_{coll}, N_{part} and the multiplicity. The "ancestors", defined as an independent source of particles, can be parametrised with $N_{ancestors} = f \cdot N_{\mathrm{part}} + (1-f)\, N_{\mathrm{coll}}$, where f takes into account the fraction of particles produced due to soft processes.

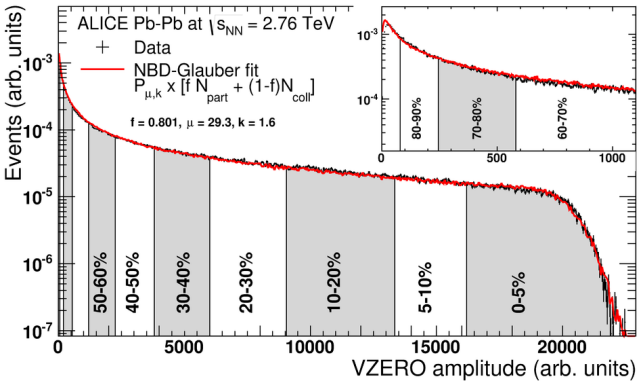

FIGURE 3.3: Distribution of the V0 amplitude (summed signals from the two scintillators). The red line represents the fit with the NBD-Glauber distribution [185]. The centrality classes are indicated with alternating grey and white areas. The leftmost region is zoomed in the inlaid pad.

As mentioned in Section 3.1, centrality triggers were used during the data taking of the Pb–Pb run in 2011. It has to be noted that the centrality of the trigger selection and the event centrality shown, for example, in Figure 3.3 are not the same. Applying a centrality trigger does not mean cutting on the V0 amplitude distribution but setting a certain threshold level on the signals detected in the V0, based on which the events are classified on-the-fly,

at the time of the data recording. The V0 distributions for the separate centrality classes are obtained offline, a posteriori.
The centrality distribution specific to this work, *i.e.* after all the analysis selection criteria are applied (see Section 5.2 for details), is shown in Figure 3.4. It is based on the multiplicity measured by the V0 detector.

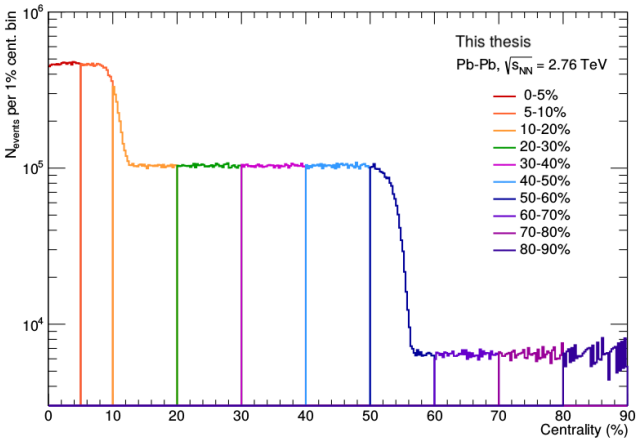

FIGURE 3.4: Centrality distribution for the 2011 Pb–Pb run after all the analysis selection criteria are applied (see Section 5.2). Different colours indicate different centrality classes.

3.2 Monte Carlo simulations

Monte Carlo simulations, relying on the variety of event generators available, are a useful tool for physics analyses. They can be used to understand the eventual unexpected behaviour of the observables and improve the data analysis, studying the effects of certain selection cuts. Moreover, the selection criteria themselves can introduce inefficiencies that need to be corrected for. The corrections also account for detector effects and acceptance at the moment of data taking, for the reconstruction efficiency and knowledge of the background of the measurement.
The simulations are composed of two parts, event generation and detector response. Particles are generated using an event generator, their interactions and momentum distributions are simulated. Subsequently, the generated particles are propagated through the experiment, simulating the detector response and the particle interactions with the detector material (*e.g.*, ionisation) and their effects on the particle trajectory (*e.g.*, multiple scattering).
The produced sample is then reconstructed with the same algorithm and analysis procedures and selection used for the data reconstruction. It is necessary to verify that the simulation gives a good description of the data, checking that data and MC are matching. If not, the simulation needs to be tuned to the data until a satisfying matching level is reached. The tuning can be done using certain high quality data sample subsets as anchors, whose characteristics will be mimicked in the simulation. Once a good level of agreement between data and MC is reached, the MC can be used to extract the efficiency, acceptance and other correction factors to obtain the final results.
In Aliroot, various event generators are available, such as PYTHIA [187], DPMJET [188], PHOJET [189], HIJING [61] and several others. For Pb–Pb collisions, HIJING is typically

used as event generator, and it is also used for this work. The particle transport through the detector is done with GEANT [190, 191].
Moreover, the PYTHIA decayer is used to produce the hadron cocktail simulation needed to extract the secondary pion correction and the electromagnetic cocktail to estimate the decay photon contribution to the direct photon background.

3.2.1 HIJING

HIJING (Heavy Ion Jet Interaction Generator) is a Monte Carlo event generator used to describe jet and particle production in high energy collisions of different systems (pp, p–A, A–A). Particular emphasis is given to multiple mini-jet production, a phenomenon whose importance grows in high energy hadron and nuclear interactions. The model, designed for pA and A–A collisions, but also describing pp events, is based on pQCD and the Lund string model, accounting for soft interactions and jet production and fragmentation. In particular, the Lund FRITIOF [192, 193] and Dual Parton [194] models are used. HIJING is then extended to heavy-ion collisions assuming a Glauber model geometry description of the collision and nuclear effects such as parton shadowing [195] and final state interactions [61]. The nuclear interaction is simplified as binary nucleon-nucleon interaction, where the interacting nucleons are treated as strings excited along the beam axis in the Lund model. The strings, resulting from scattered partons associated with the corresponding valence quark in the nucleon, interact before fragmenting into particles.
The event generator version used for the simulations in this thesis is the 2.0, where the parton distribution functions and the gluon shadowing description are updated to compare with LHC data. In particular, the Gluck-Reya-Vogt parametrisation [196] of the nucleon PDFs, updated using global fits to the LHC data available at the time, is adopted together with other parameter modifications to account for the higher energies, such as a larger minimum p_{T} for the jets (cut-off scale). The jet quenching description implemented in this version is still a schematic one, thus it will not fully reproduce the data, as shown in Section 5.3.2.

3.2.2 GEANT

GEANT (Geometry And Tracking) is a set of tools for simulating the passage of particles through matter, in particular the detectors and their responses. The complexity of this tool has increased with the complexity of the experiments and with the need of increasing accuracy of the simulation.
Basic elements of the software comprise the geometry of the experiment and the materials that compose the detectors, the particles most likely to be produced, their tracking in the detector and the effects of the electromagnetic fields and physics phenomena on them, the detector behaviour and how the signals from the particles are registered as data. The Monte Carlo simulations used in this work are produced with GEANT3, though now GEANT 4 is also available.

3.2.3 PYTHIA

PYTHIA is a general purpose event generator for high-energy collisions of elementary particles. The version used in this work is the 6.4. The generator can describe '2 → 1', '2 → 2' (for which it is optimised) and certain '2 → 3' scatterings, though the higher number of final state particles also entails a more complicated generation procedure. The processes considered include hard and soft QCD processes and those induced by photons. Resonance decays are also part of the generation chain, with the possibility of activating only certain decays channels, thus making the calculation of the cross section less complicated if wanted. Initial and final state radiation as well as multiple parton interactions are included. The hadronisation is described by the Lund fragmentation model, as in HIJING.
Only the PYTHIA decayer will be used in this work, to generate the cocktail simulation for the direct photon measurement background estimation.

3.2.4 Monte Carlo simulations for the 2011 Pb–Pb run

For the analysis of the 2011 Pb–Pb data, three Monte Carlo simulations were produced using HIJING and GEANT3. In order to have better agreement with the data, the simulation are based, or "anchored", on individual data runs and produced with the same settings and detector conditions. In particular, changes in the TPC chambers voltage with respect to the nominal values need to be reflected in MC, since they affect the TPC-based analyses.
The simulations correspond to three different intervals of impact parameter or centrality class. The ranges are $0 < b < 5$ fm, for centralities in the range 0–10%, $5 < b < 11$ fm for 10–50% and $11 < b < 15$ fm, valid in the centrality range 50–90%. This last simulation is not used because the statistics in the measured data sample is not enough for a neutral meson measurement better than the already existing one obtained with the 2010 data, where the statistics for peripheral collisions was higher. In addition to the standard HIJING event, additional π^0 and η mesons are generated in order to increase the statistics at high-p_{T} and enhance the signals for photon physics. This is a required procedure in order to have small statistical uncertainties at high-p_{T} and keep the CPU time for the simulation production reasonable. The additional particles have been generated in the acceptance of the central barrel and of the PHOS and EMCal calorimeters, flat as a function of p_{T}, from 0 to 30 GeV/c, and flat with respect to the azimuthal angle ϕ and in the rapidity range -1.2 $< y <$ 1.2.
The number of additional π^0 and η mesons is dependent on the centrality of the event, according to the function

$$N_{\pi^0,\eta}(b) = 30 + 30 \times \exp(-0.5 \cdot b^2/(5.12)^2) \tag{3.4}$$

where b is the impact parameter in fm. This dependence, of empirical origin, is motivated by the necessity of having enough added signals for the most central events, without biasing the semi-central and peripheral ones with too many signals.
The jet quenching phenomenon is not included in the HIJING description of the event. Therefore, in order to have a data-like (steeply falling) transverse momentum spectrum, the MC input spectra need to be weighted with respect to the data ones. This procedure, described in Section 5.3.2, is iterative and ensures a realistic efficiency. Furthermore, a correction for the track density in MC, where the number of TPC tracks is higher than data,

is needed since the reconstruction efficiency depends on the multiplicity. In order for the MC to reflect the data track multiplicity, the crossing points between two classes of the data distributions of the TPC tracks passing the basic quality criteria (explained in Section 5.2) are taken as limits for the number of MC TPC tracks of the corresponding centrality classes. The data distributions of the "good" TPC tracks taken as template are shown in Figure 3.5.

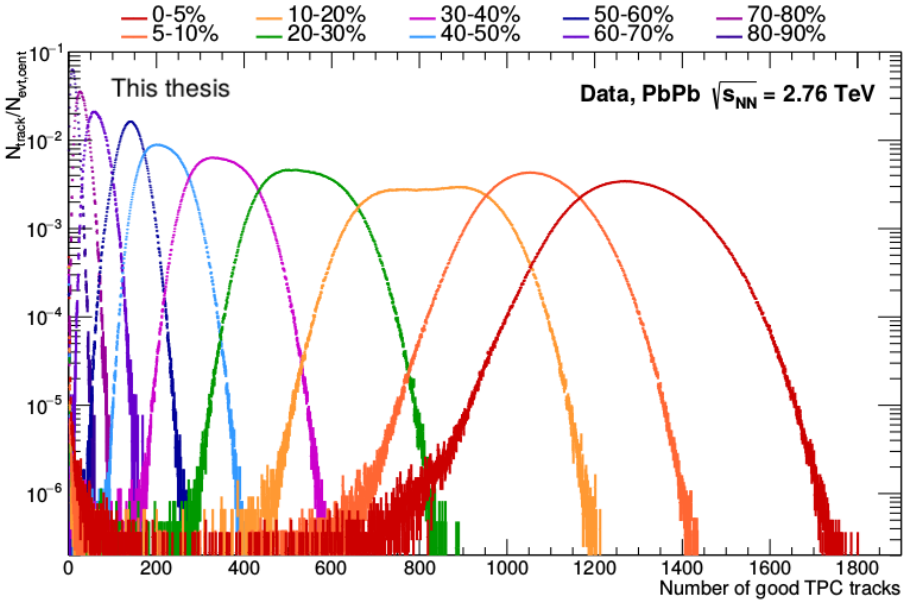

FIGURE 3.5: Good TPC track multiplicity distributions in centrality slices from 0 to 90%. The distributions are normalised to the number of events in the respective centrality class.

The number of events for the data sample and for each MC simulation after all the selection criteria are applied is reported in Table 3.1.

	Period	Centrality	N_{event} accepted
Data	LHC11h	0–5%	9.8×10^6
		5–10%	9.8×10^6
		0–10%	2.7×10^7
		20–40%	8.5×10^6
		20–50%	1.3×10^7
Simulation	LHC14a1a	0–5%	9×10^5
		5–10%	4.1×10^5
		0–10%	1.3×10^6
	LHC14a1b	20–40%	2.1×10^6
		20–50%	2.7×10^6

TABLE 3.1: Number of events passing the event, track and photon selection criteria for the 2011 Pb–Pb data and the two MC simulation used in this thesis work.

The neutral meson analysis has been carried out in parallel for all the centrality classes listed above. However, the 0–10% and 20–50% centralities have been taken to represent the neutral meson measurements, given their higher statistics. In the main text, the results shown will refer to these two centrality classes only. The performance and final results for the other centralities are reported in Appendix C.

Chapter 4

Particle reconstruction in ALICE

Two methods are mainly employed to reconstruct photons in experiments at accelerators. Photons can be reconstructed with electromagnetic calorimeters, exploiting the full photon energy deposition and measuring the subsequent electromagnetic shower in the calorimeter. The ALICE calorimetry system is composed of two different detectors, EMCal and PHOS, described in Section 2.2. They use different technology and are placed in complementary position to each other, in order to cover a larger acceptance and give independent measurements. Photons can also interact with the nuclei of the detector material. At the energies investigated here, pair production is the dominant process. Photons that convert in the detector material can be reconstructed via the electron-positron pairs using the central barrel detectors and a secondary vertex finding algorithm. This is referred to as Photon Conversion Method (PCM).
For the analysis presented in this thesis, the PCM was used. Therefore, the ALICE tracking system will be introduced in this chapter, together with the secondary vertex finder algorithm and the particle identification process of the central barrel detectors.

4.1 ALICE central barrel tracking system

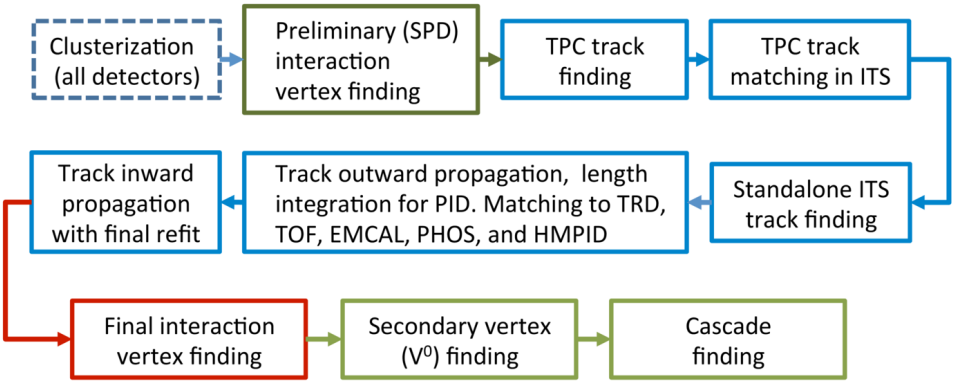

FIGURE 4.1: The ALICE event reconstruction workflow [169].

The workflow of the ALICE event reconstruction system is illustrated in Figure 4.1.
The first step of the event reconstruction procedure is carried out independently for each of the detectors and consists in grouping the data according to the detector signals, based on the channel information in space and time. Detector data with signals having, for example, similar timing and positions compose together a cluster. Once the clusterisation is done, the tracking system proceeds from the inside-out of the experiment in finding the collision vertex and reconstructing the particle tracks [169].
The SPD, the two innermost layers of the ITS, is used to find the interaction vertex. The basic unit in this step is a SPD-tracklet: each cluster on the first SPD layer is associated with one on the second layer and the line passing through two clusters, within an azimuthal window of about 0.5 rad with respect to the nominal beam axis, is called tracklet. The tracklets are considered "good" when the distance of closest approach (DCA) between a tracklet pair is small (less than 1 mm) and they point towards the beam pipe; they are otherwise rejected by the primary vertex finder algorithm. The primary vertex is thus defined as the space point with the maximum number of good tracklets associated, as represented in Figure 4.2, left. This first estimation of the primary vertex candidate is used to build again the tracklets, with respect to the beam position given by this estimation and within an azimuthal window of 0.01 rad. Once the primary vertex is updated with the new tracklet sample, it will be used during the track finding and further updated with the global tracking information. The primary vertex reconstruction is done in three dimensions. In case this fails because of insufficient information, the z-coordinate only of the vertex is estimated.
The next step is the track finding and fitting, consisting of three phases and using the Kalman filter algorithm [197].

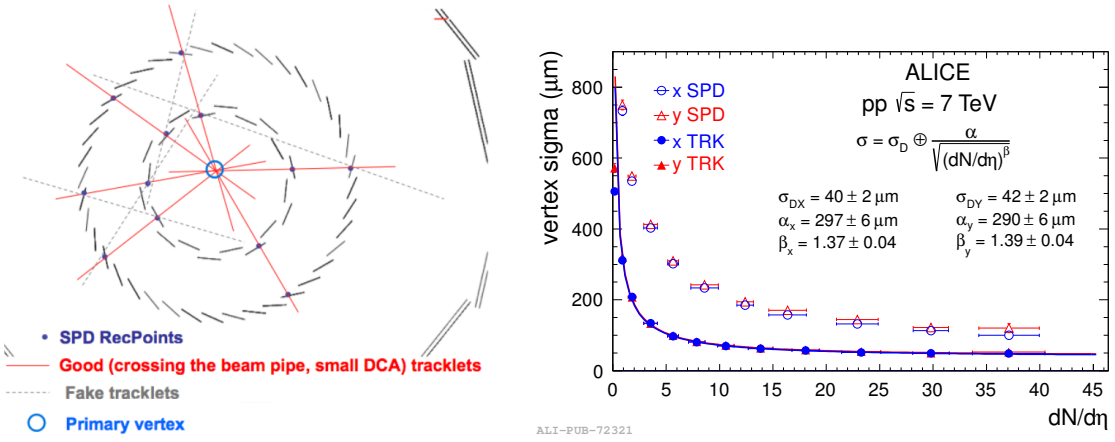

FIGURE 4.2: Left: Schematic representation of the primary vertex reconstruction. The blue dots represents the SPD clusters, the red line are good tracklets, the grey dashed lines are the fake ones. The primary vertex is highlighted with the blue circle [198]. Right: Comparison of the transverse width of the final vertex distribution (full symbols), obtained with global tracks, to the preliminary one (open symbols), obtained with the SPD, as a function of the charged particle multiplicity in pp collisions [169]. The total resolution is composed of the finite size of the luminous region, σ_D, and the vertex resolution, $\alpha/\sqrt{(\mathrm{d}N/\mathrm{d}\eta)^{\beta}}$.

The first phase of the central barrel tracking starts from the outermost radius of the TPC. The track seeds are built either using two TPC clusters and the vertex or without the vertex and with only three TPC clusters. The seed propagation moves inwards until the inner TPC radius, updating each time a cluster satisfying a proximity cut is found. The reconstructed TPC tracks that do not satisfy quality criteria, such as a minimum number of associated

clusters, are discarded while the accepted ones become seeds at the outermost ITS layer. The propagation and cluster association is repeated, again with the seeding starting with and without the vertex constraint and using the surviving clusters. The seeding procedure is repeated in order to increase the tracking efficiency. For the clusters that were not used in the ITS-TPC combined tracking, a reconstruction using only the ITS is done. Before the final step, all the track hypotheses are fitted with a Kalman filter. If they are accepted, their clusters will be removed from the search.

All the reconstructed tracks are extrapolated towards the preliminary primary vertex for the second phase of the tracking procedure. As done in the previous step, the tracks are refitted with a Kalman filter, but in the outgoing direction and using the clusters already found. A tentative matching is done first when the track reaches the TRD and the TOF, respectively with TRD tracklets or TOF clusters, and then again with the EMCal, PHOS and HMPID detectors. At the time of the data taking concerning this work, the information from these detectors was not used to update the track kinematics, but it was stored for later use in particle identification. Since 2016, the TRD is actively used for the fitting procedure and is essential for a good calibration of the tracking detectors.

In the last phase of the tracking procedure, the tracks are again refitted inwards and their final covariance matrix is stored for each track in the reconstructed event. Once the global tracking is completed, the reconstructed tracks are used to determine the primary vertex with higher precision. The primary vertex resolution in the transverse plane is shown in Figure 4.2, right, showing the dependence on the multiplicity in pp collisions. It is evident how the final resolution obtained with global tracks is much improved compared to the initial estimation using only the SPD.

More details on the tracking procedure can be found in [169, 199], while in Figure 4.3 examples of the ALICE tracking performance are shown. In the left figure, the TPC tracking efficiency is shown. The drop at low-p_{T} is given by the energy loss of the particles in the detector material while the higher p_{T} shape is due to the loss of clusters for particles passing in the read-out dead-zones. It can also be observed that the tracking efficiency does not depend on the detector occupancy. The right figure shows the resolution for the inverse transverse

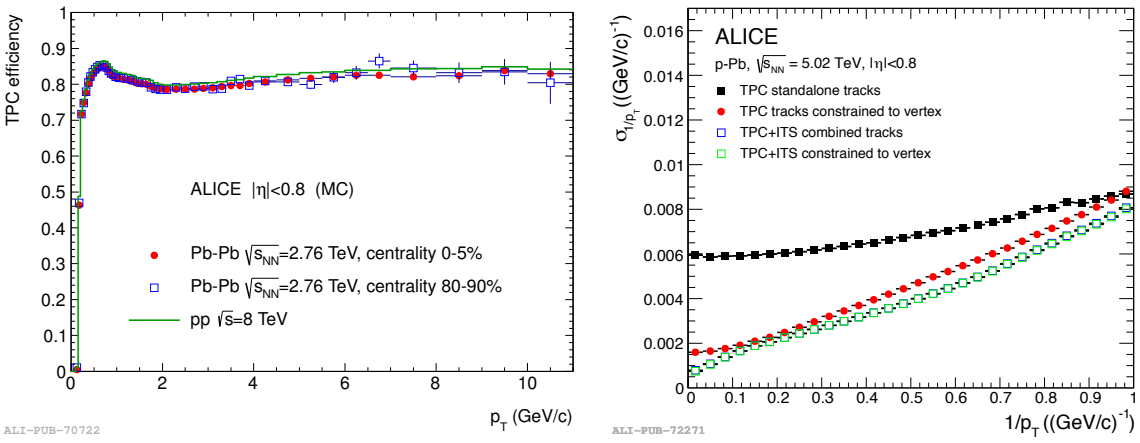

FIGURE 4.3: ALICE tracking performance plots [169]. Left: ALICE TPC track finding efficiency estimated from Monte Carlo simulations for primary particles in pp and Pb–Pb collisions. Right: Inverse transverse momentum resolution for TPC and ITS–TPC combined tracking in p–Pb collisions.

momentum, related to the relative transverse momentum resolution by $\sigma_{p_T}/p_T = p_T\sigma_{1/p_T}$, for TPC and ITS–TPC combined tracking in p–Pb collisions. The resolution at high-p_T is expected to be ∼10–15% worse for central Pb–Pb collisions due to the loss of clusters on the ion tails and fake or overlapping clusters.

4.2 Secondary vertex finder

After the interaction vertex and the primary tracks are identified, the tracking system proceeds to finding secondary vertices (V^0), attributed to particle decays and photon conversions. The algorithm used is of the same kind used for the primary vertex finder. The initial selection for the secondary tracks requires their distance of closest approach from the primary vertex to be more than 1 mm in Pb–Pb collisions (0.5 mm in pp). Each pair of unlike-sign tracks is a V^0 candidate. The successive selection asks for the DCA between the two tracks to be less than 1.5 cm, for their point of closest approach to be closer to the primary vertex than any of the tracks inner points and for the cosine of pointing angle (angle between the total momentum of the pair and the line connecting primary and secondary vertex) to be greater than 0.9, as shown in Figure 4.4.

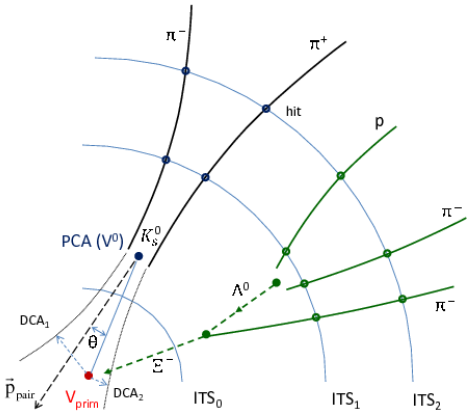

FIGURE 4.4: Schematic representation of the a secondary vertex, with example decays from K^0_S and Ξ^- particles [169]. The angle indicated with θ is the angle between the vector connecting the primary to the secondary vertex and the V^0 particle momentum, called pointing angle.

Two methods are available for the vertex reconstruction: On-the-Fly and offline V^0 finder. The first, as the name suggests, finds the secondary vertex and selects the secondary tracks at the same time of the data processing, when all the information about the tracks are still available. The latter is applied on the already reconstructed data, when the track cluster information are not available anymore. Given the higher precision and efficiency of the On-the-Fly method, this is the secondary vertex finder used in this work.

4.2.1 Recalculation of the conversion point

As mentioned above, the secondary vertex finder is meant to find particle decays, but it is also used for conversions. The conversion point is recalculated offline to improve its

resolution [200]. It is assumed that the opening angle between the e^+e^- pairs is small, given that the photon is massless, so the electron and positron momenta have to be roughly parallel at their origin. The recalculation is done first in the xy-plane. The z coordinate is recalculated last. A mathematical description of this method and illustrative sketches can be found in [200].

4.3 Particle identification

Particle identification in ALICE is provided by several sub-detectors with different methods. The ITS and the TPC measure the charge deposit and do particle identification via the $\mathrm{d}E/\mathrm{d}x$ measurement. The first is especially useful for low-p_{T} primary tracks (below 1 GeV/c) while the latter gives a measurement with good resolution on a wider transverse momentum range (from 0.05 GeV/c up to 20 GeV/c). Particle identification with the TOF detector and the HMPID (ring-imaging Cherenkov detector) allows a good separation of kaon and protons up to 4–5 GeV/c. Likewise, the electromagnetic detectors (EMCal and PHOS) and the TRD can be used for particle identification at higher p_{T}.
More details on the PID with the TPC detector, essential for the electron identification, will be given in the next section.

4.3.1 Identification with the TPC

The TPC measures the specific energy loss of a particle per unit length ($\mathrm{d}E/\mathrm{d}x$). The mean energy loss of a particle of charge z and velocity $\beta = v/c$ traversing a medium of atomic number Z and mass number A is described by the Bethe-Bloch formula [9]:

$$-\left\langle \frac{\mathrm{d}E}{\mathrm{d}x} \right\rangle = Kz^2 \frac{Z}{A} \frac{1}{\beta^2} \left[\frac{1}{2} \ln \frac{2m_e c^2 \beta^2 T_{\mathrm{max}}}{I^2} - \beta^2 - \frac{\delta(\beta\gamma)}{2} \right] \tag{4.1}$$

where T_{max} is the maximum kinetic energy that can be transferred in a single collision and I is the mean excitation energy of the medium. The density effects due to the polarisation of the medium when traversed by a charged particle are considered in the term $\delta(\beta\gamma)$. More details on this term and on the factors used in the formula are given in [9]. Particles traversing the medium can be distinguished because the energy loss is proportional to their velocity β: different particles will give different specific energy loss for a given momentum. The particle identification is then achieved with the combined information from the $\mathrm{d}E/\mathrm{d}x$, estimated from the charge deposit from the clusters associated with a track, the charge and the particle momentum. The specific energy loss in the TPC for Pb–Pb collisions is shown in Figure 4.5, left.
The best particle separation is achieved at low momentum, below 1 GeV/c, where a track-by-track identification is possible. The separation is also good above 2 GeV/c, in the relativistic raise, where the truncated mean method is applied to the signal to get rid of the Landau tail and a statistical method employing multi-Gaussian fits for the particles separation is adopted, as shown in Figure 4.5, right. The energy loss resolution in 0–5% central Pb–Pb collisions is 6.5% [169].
For the analysis of experimental data, the parametrisations already introduced by the ALEPH

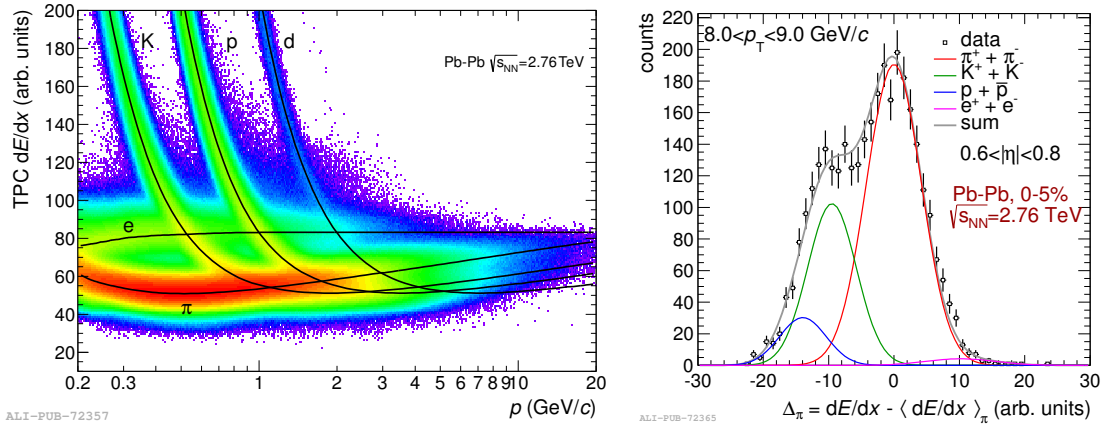

FIGURE 4.5: ALICE TPC specific energy loss, $\mathrm{d}E/\mathrm{d}x$, as a function of the particle momentum in Pb–Pb collisions (left). The black lines represent the mean energy loss parametrisations. In the right figure, the energy loss distributions assuming the mean pion energy loss are shown together with the multi-Gaussian fits [169].

collaboration [201] are used to describe the energy loss distributions and extract their mean value. These parametrisations, indicated with the black curves in Figure 4.5, left, are optimised for each set of data recorded, in order to reproduce at best the TPC performance at the time of data taking. In addition, parametrisations for the Monte Carlo simulations are also produced, tuned to the data distributions for a better rendering. In both data and MC, corrections for multiplicity or pseudorapidity dependence can also be applied.

Chapter 5

Neutral meson measurements with the Photon Conversion Method in Pb–Pb collisions

This chapter will illustrate the technical details of the analysis, such as the quality and selection criteria, the detector efficiencies and the method performance.
The first step in obtaining reliable results is to establish the quality of the data sample used. At this stage, issues for which a correction may be needed are also identified. Afterwards, the selection cuts are carried out in a natural flow: event selection, acceptance and geometrical cuts, electron identification, photon reconstruction. Last, the cuts to improve the meson significance are applied. While the initial set of selection criteria is the result of the experience gathered from the analysis of previous data samples, it is in no way the final one. Several iterations of fine tuning are required to extract the best results for the specific sample and available statistics.

5.1 Quality assurance and detector conditions

The quality of the recorded and reconstructed data has to be verified in a procedure called Quality Assurance (QA). To do so, quantities characterising the measurement and essential to the analysis method are studied in more detail on a run-by-run basis (where a run is the unit of continuous recording time during a period of data taking), or focusing on specific runs, when deemed necessary. Only the runs where all the detectors relevant to the analysis are flagged with good performance are taken.
The most relevant quantities monitored are the mean value of the specific energy loss ($\mathrm{d}E/\mathrm{d}x$) for electrons and positrons, the integrated number of reconstructed photons per event and their azimuthal and pseudorapidity distributions. The momentum calibration is cross checked studying the mesons width and mass position. Moreover, these quantities are compared in data and MC to verify the level of agreement and that there are no detector issues. In case of deviation from the average behaviour, it is considered whether to reject or correct the affected data. The selection criteria used for the QA are less strict than those used in the analysis in order to have a feeling of the overall behaviour of the data while still having the

possibility to improve on it.

An example of QA study is given in Figure 5.1. The integrated number of photons N_γ, reconstructed from electron and positron pairs identified with the TPC, is shown versus run number, for data and MC simulation. In the top plot, N_γ at positive pseudorapidity (A-side of the detector) is reported. Likewise, the bottom plot shows the same quantity at negative pseudorapidity (C-side of the detector, where the muon arm also sits). A deviation from the standard behaviour can be seen in the C-side, affecting the centrality class 0–10%. There is a drop in the number of photons in data (full markers) that is not reproduced by the MC simulation (empty markers) in the second half of the runs. The cause was identified further detailing the study and looking at the N_γ in the azimuthal regions corresponding to the TPC chambers. It was observed that the loss of photons, appearing in specific azimuthal areas, corresponds to TPC chambers that were turned off or at a reduced working voltage as they were known to be affected by discharges in this data taking period. The effects of these conditions have not been properly ported to the MC simulations. The adopted solution is a geometrical cut on the affected azimuthal areas, explained in the next section.

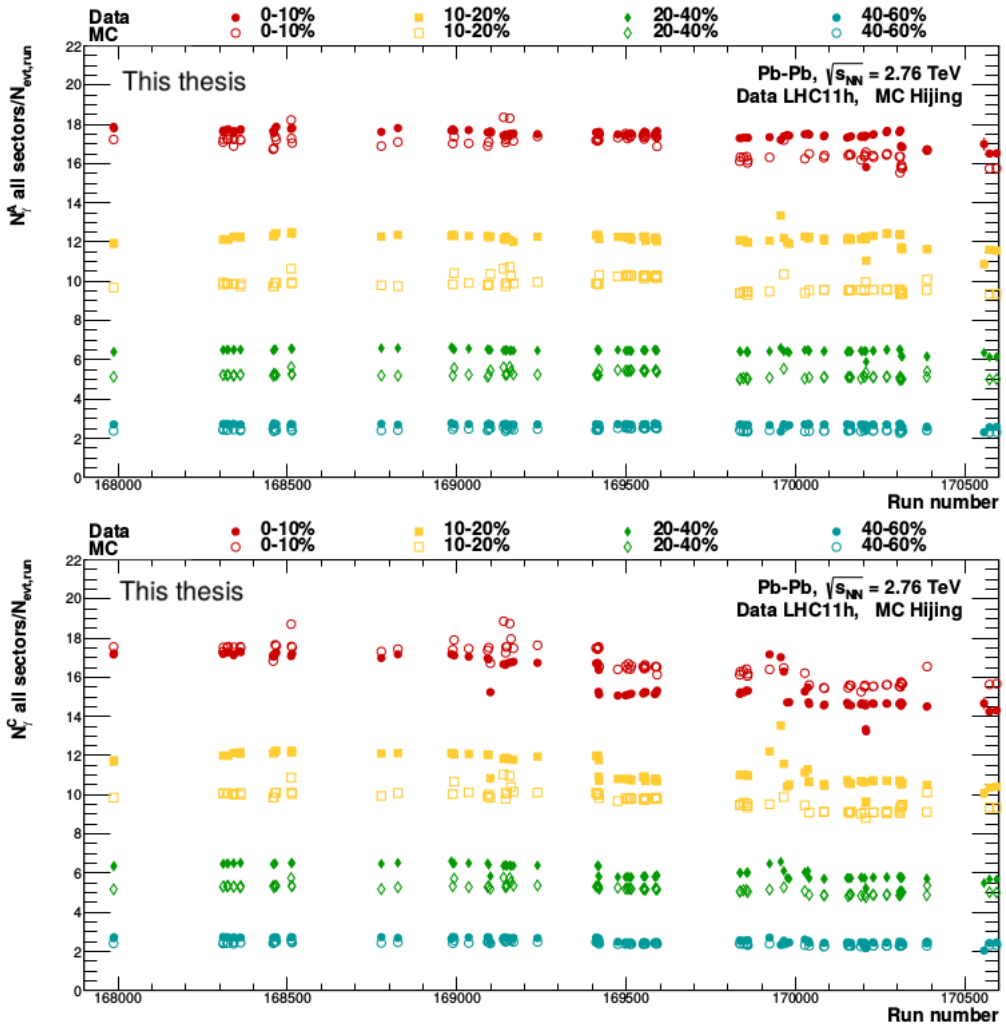

FIGURE 5.1: Integrated number of photons, N_γ, per run number, normalised to the respective number of events. The distribution is show for the A-side (positive pseudorapidity, $\eta > 0$, top) and C-side (negative pseudorapidity, $\eta < 0$, bottom) of the detector. Data is represented by the full markers, MC by the empty ones.

5.1.1 Azimuthal cut for problematic TPC chambers

From the QA, it emerges that a smaller number of photons is reconstructed for the second half of the runs of the 2011 period. As mentioned in the previous section, the loss is due to several chambers of the TPC with working condition different from the standard ones. The effects of this deviation on the reconstructed data and in the MC simulation has been studied for each run individually. Given that the problem is mainly localised at negative pseudorapidity, only the figures for $\eta < 0$ will be shown here. In the top panels of Figure 5.2, the number of photons N_γ, normalised to its integral, is shown as a function of the azimuthal angle φ for a few runs of the data sample.

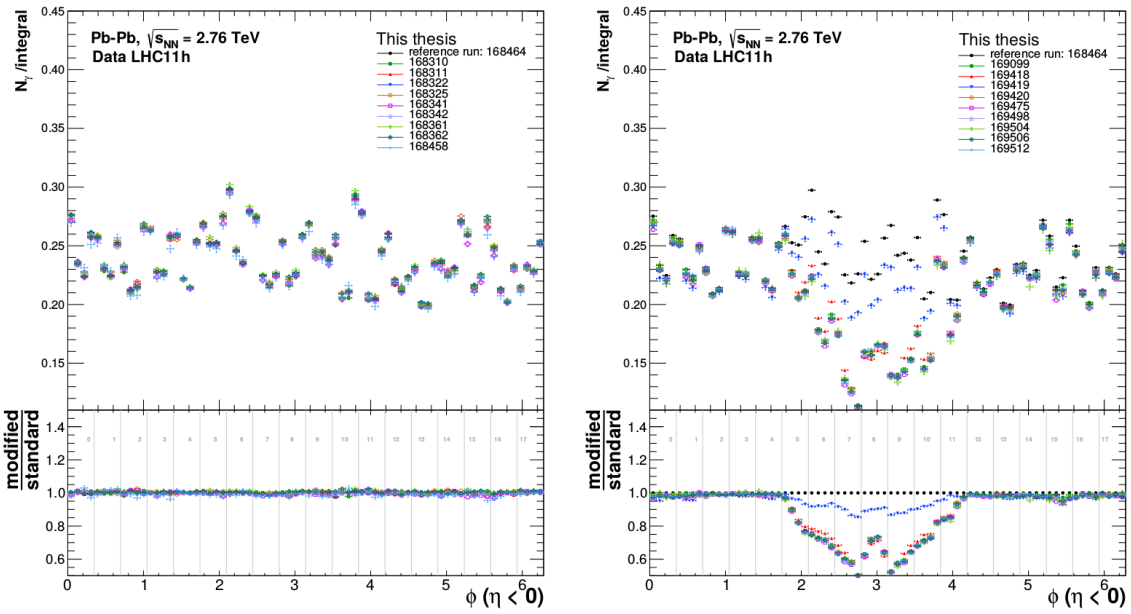

FIGURE 5.2: Distribution of the number of photons versus the azimuthal angle φ, normalised to its integral, for the 0–10% centrality class of the data sample from the runs listed in the legend. The bottom panel shows the ratio of these runs to a reference run with good quality. The light grey lines indicate the TPC sector boundaries, identified by the numbers. Left: sample of standard runs. Right: sample of runs with a problematic TPC chamber.

The ratio of the distribution of this sub-sample to a reference run with good quality is shown in the bottom panels. Figure 5.2, left, illustrates a sample of run with standard conditions, while some of the runs with identified problematic chambers are in the right figure. The peculiar shape of the ratio is peaked in the azimuthal region of the TPC chamber with non-standard conditions, but not completely understood. In fact, the effect is not localised, spreading to the neighbouring areas and much wider than expected.
The same distributions have been studied in the MC simulation. It is observed that for some of the runs the MC actually follows the data behaviour. No action is thus taken in these cases. On the other hand, where it was necessary to account for the difference between data and MC, a geometrical cut has been implemented in order to reject the photons from the affected φ region. Figure 5.3 has been used to determine the optimal rejection window. The double ratio of the problematic to standard distribution for MC over data is plotted as a function of the azimuthal angle φ. The azimuthal interval of the rejection cut has been chosen considering the range in which the data to MC ratio deviates more than 5% from

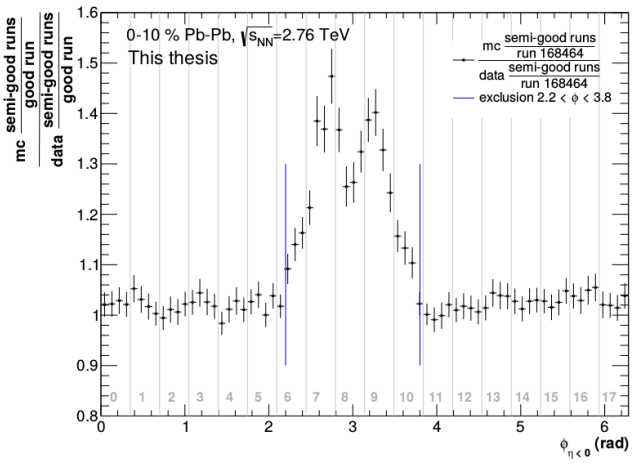

FIGURE 5.3: Double ratio of the distribution of the N_γ of problematic over standard behaviour, for MC simulation over data, as a function of the azimuthal angle φ. The light grey lines indicate the TPC sector boundaries, identified by the numbers. The blue lines indicate the boundaries of the rejection window.

unity. The photons that are rejected with this geometrical cut are around 6% of all the reconstructed photons.

5.1.2 Parametrization of the expected mean energy loss in the TPC

As mentioned in Section 4.3.1, the energy loss distribution in the TPC is parametrised in order to obtain the mean energy loss for a given particle type at a given momentum. These parametrisations, called splines after the type of function used, are loaded during the data analysis to ensure a good description of the TPC detector response and tune the MC simulation to the data. The set of functions are produced for each reconstructed period and on demand for specific sets of data if it is needed, as it was the case for the 2011 Pb–Pb run. The 2011 specific parametrisations have been produced using a sample of runs with particularly good and stable characteristics. A correction for the pseudorapidity dependence of the mean $\mathrm{d}E/\mathrm{d}x$ was also applied, not present in the previous version. The description of the mean $\mathrm{d}E/\mathrm{d}x$ is therefore improved, at low momentum and in the relativistic rise.

5.2 Electron and photon selection for the neutral meson measurement

The first selection the data undergoes, independently of the nature of the analysis, is the Physics Selection (see Chapter 3): events that do not fulfil the central barrel trigger conditions, calibration and beam-gas interactions are rejected. The reconstructed primary vertex is required to be within $|z_{\mathrm{vtx}}| < 10$ cm from the centre of the detector while the On-the-Fly V^0 finder is used to reconstruct the secondary vertex from γ conversions and K^0_S, Λ and $\bar{\Lambda}$ decays. The secondary tracks are required to have opposite charge and the TPC refit (see Chapter 4). Those with kink topology, that would hint to a decay and not a conversion, are rejected. A good track quality is ensured asking for a minimum track momentum of

0.05 GeV/c and for a percentage of the associated TPC clusters over the total number of theoretically findable clusters larger than 60%. A pseudorapidity fiducial cut is applied with respect to the origin of the detector geometric system. Since the V^0s are displaced from the centre of the detector, it is possible that tracks lying outside of this fiducial region are accepted too. To overcome this, the condition

$$R_{\text{conv}} > |Z_{\text{conv}}| \cdot \tan(2 \arctan(\exp(-\eta_{\text{fiducial}}))) - Z_0 \tag{5.1}$$

has to be fulfilled. The value for Z_0 is set to 7 cm, while R_{conv} and Z_{conv} are required to be less than 180 cm and 240 cm, respectively. A minimum value of $R_{\text{conv}} > 5$ cm helps rejecting Dalitz decays ($\pi^0(\eta) \to \gamma^*\gamma \to e^+e^-\gamma$), where the virtual photon responsible for the lepton pair could be reconstructed as a real one.
The track selection cuts are summarised in Table 5.1.

Track & V^0 cuts

V^0-finder	On-the-Fly
minimum track-p_{T}	$p_{\text{T,track}} > 0.05$ GeV/c
$N_{\text{cluster TPC}}/N_{\text{findable clusters}}$	$> 60\%$
η-cut for tracks & V^0	$\lvert\eta_{\text{track, V}^0}\rvert < 0.9$
Cut on R_{conv}	5 cm $< R_{\text{conv}} <$ 180 cm
Cut on Z_{conv}	$\lvert Z_{\text{conv}}\rvert <$ 240 cm
Fiducial volume cut	(see text for values)
Cut on φ (only for problematic TPC chambers and runs, for $\eta < 0$)	2.2 rad $< \phi <$ 3.8 rad

TABLE 5.1: List of track selection cuts applied in the analysis.

Once the track cuts have been applied, the selection focuses on the remaining sample of secondary tracks, aiming at identifying electrons and positrons and rejecting pions and protons. The electron selection is based on the energy loss distribution in the TPC. All the tracks with energy loss within -3σ and 5σ from the expected electron dE/dx are accepted. Moreover, a p_{T}-dependent rejection cut is applied to improve the electron sample purity in the region where the pion energy loss distribution merges with the electron one at about 2 GeV/c. As pions are one of the highest background sources in this region, the cut on the pion line is tuned to maximise the rejection. The pion dE/dx hypothesis is taken as a reference in this case and the tracks within $\pm3\sigma$ from 0.4 to 2 GeV/c and $\pm1\sigma$ from 2 GeV/c are discarded. The p_{T}-dependent cut is adopted in order to have an effective rejection at lower momentum, where electron and pion line are closer together, while it is released at higher momentum where the signal to background ratio is larger. Figure 5.4 shows the energy loss distribution of the electron candidates before (left) and after (right) all the analysis cuts are applied.
Similarly as in the TPC case, the difference between the measured and expected time-of-flight of the electron in the TOF can be used as a selection criteria. The cut on the TOF electron hypothesis is only applied when the signal from TOF is present, *e.g.* when the track has been successfully matched with a TOF cluster during the tracking. The acceptance region for the electron hypothesis in the TOF is $\pm5\sigma$. Though the cut does not improve much the quality of the electron sample, it is anyway kept.
The electron identification cuts are summarised in Table 5.2.
At this point of the selection process, the V^0 candidates sample still contains combinatorial

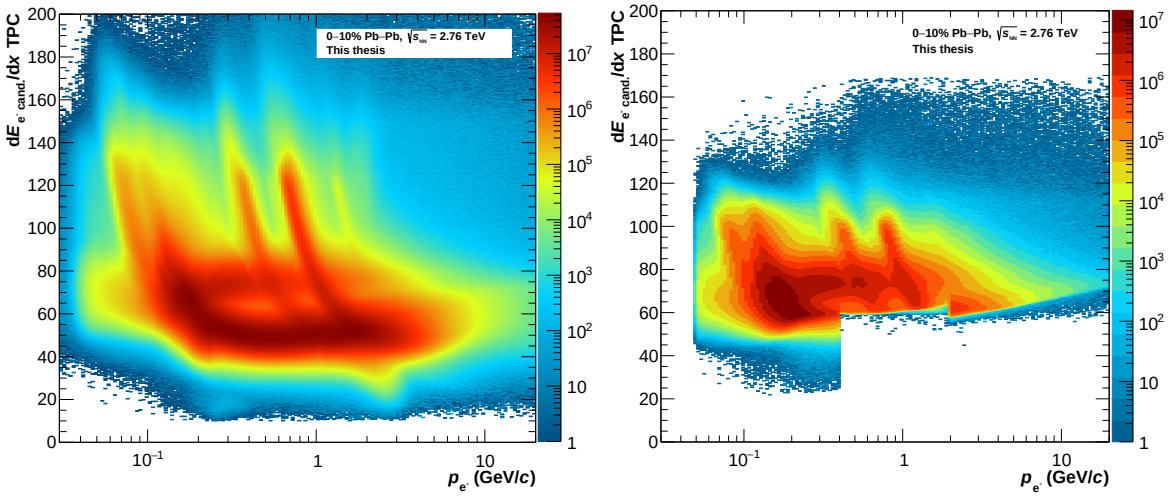

FIGURE 5.4: TPC $\mathrm{d}E/\mathrm{d}x$ for electron candidates of the PCM analysis before (left) and after (right) all the selection cuts are applied.

PID cuts	
σ_e TPC $\mathrm{d}E/\mathrm{d}x$ (accept)	$-3 < \sigma_e < 5$
σ_π TPC $\mathrm{d}E/\mathrm{d}x$ (reject)	0.4 GeV/c $< p_e <$ 2 GeV/c: $\sigma_\pi > 3$
	$p_e >$ 2 GeV/c: $\sigma_\pi > 1$
σ_e TOF (accept, if available)	$-5 < \sigma_e < 5$

TABLE 5.2: List of electron identification cuts applied in the analysis.

background contamination (mainly from electrons, pions and electron-pion random combination) and from particle decays. These contaminations are reduced exploiting the topology characteristic of conversion photons.

In Figure 5.5 the longitudinal momentum asymmetry between the secondary tracks ($\alpha_{V^0} = (p_L^{e^+} - p_L^{e^-})/(p_L^{e^+} + p_L^{e^-})$ is shown, with p_L being the longitudinal momentum of the positive/negative particle) versus the projection of the momentum of the daughter particle (e^+ and e^-) with respect to the mother particle (V^0 candidate) in the transverse direction ($q_\mathrm{T} = p_e \times \sin\theta_{\mathrm{V}^0,e}$). This characteristic distribution, called Armenteros-Podolanski plot, allows for a good separation of the photons from the other V^0 candidates. In fact, in the laboratory frame, the $\mathrm{e}^+\mathrm{e}^-$ pair from the photon conversion fly, within a very small opening angle, in the same direction as the photon. The q_T of the real photons is thus close to zero. Moreover, the distribution is symmetric in α, as the conversion products have the same mass. For heavier particles the opening angle is larger and, therefore, the q_T is larger. The photon selection is done adopting a 2-dimensional (elliptic) cut:

$$\left(\frac{\alpha_{V^0}}{\alpha_{V^0_{\max}}}\right)^2 + \left(\frac{q_\mathrm{T}}{q_{\mathrm{T,\,max}}}\right)^2 < 1, \tag{5.2}$$

with $\alpha_{V^0_{\max}} = 0.95$ and $q_{\mathrm{T,\,max}} = 0.05$ GeV/c. In Figure 5.5, right, the distribution after the cut is shown.

To reject as much as possible of the combinatorial background, the next cuts will focus on the conversion point topology and its relation to the primary vertex, since this kind of

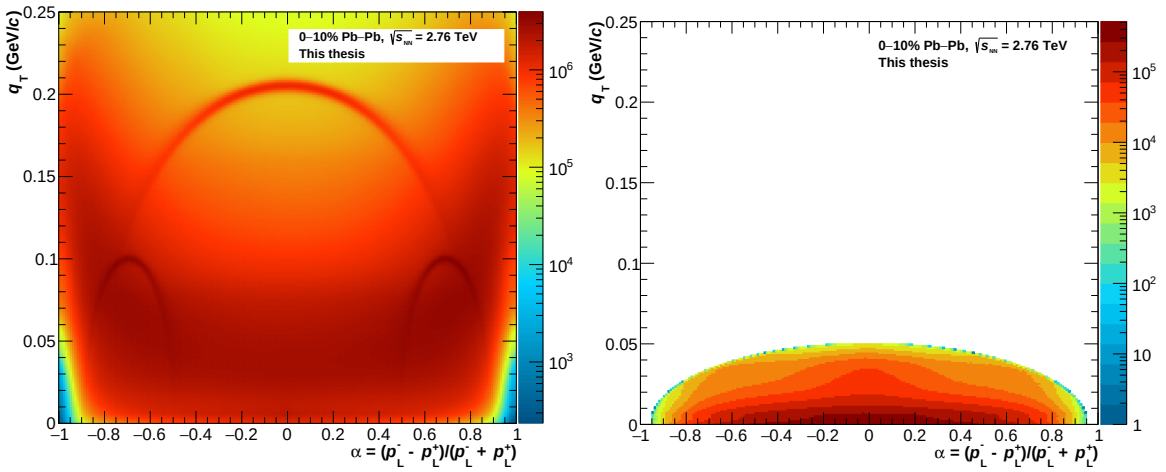

FIGURE 5.5: Armenteros-Podolanski distribution for V^0 candidates of the PCM analysis before (left) and after (right) all the selection cuts are applied.

background comes from wrongly reconstructed secondary verteces. First, the invariant mass of the V^0 candidate is set to zero. It is also assumed that the cosine of the angle between the vector connecting the primary to the secondary vertex and the V^0 particle momentum, called cosine of the pointing angle, shown in the previous chapter in Figure 4.4, is close to 1. The cut is then set to $cos(\theta_{\mathrm{P.A.}}) > 0.85$. The reconstruction algorithm, based on the Kalman filter (see Chapter 4) associates a certain χ^2 and number of degrees of freedom (NDF) to quantify the goodness of the track hypotheses. Photon candidates are accepted if they have χ^2/NDF smaller than 20. Moreover, the opening angle between tracks coming from the secondary vertex, which should tend towards zero for the photon hypothesis, can be also considered. The angle ξ_{pair} between the track pairs is defined by the track momenta as

$$\xi_{\mathrm{pair}} = \arccos\left(\frac{\vec{p}_{e^-} \cdot \vec{p}_{e^+}}{|\vec{p}_{e^-}| \cdot |\vec{p}_{e^+}|}\right). \tag{5.3}$$

The relation of the plane defined by this angle with the plane perpendicular to the beam axis, *i.e.* the xy-plane for the ALICE coordinate system, is given by the difference between the polar angles of the secondary tracks: $\Delta\theta = \theta_{e^-}$ - θ_{e^+}. Considering two secondary tracks, the polar angle difference remains constant while the opening angle increases due to the bending in the magnetic field. A representation of the angles and pair plane is given in Figure 5.6. The quantity on which the V^0 candidates are selected is the ψ_{pair} angle, defined as

$$\psi_{pair} = \arcsin\left(\frac{\Delta\theta}{\xi_{pair}}\right). \tag{5.4}$$

A vanishing opening angle also implies a ψ_{pair} angle close to zero, or smaller than 0.1 rad, as it is assumed in this work. To further improve the rejection power for contaminations, this quantity is put in relation with the χ^2 in a two-dimensional cut:

$$|\psi_{pair}| < \frac{-\psi_{pair,cut}}{\chi^2_{\gamma,cut} \cdot \chi^2_{\gamma}} + \psi_{pair,cut}, \tag{5.5}$$

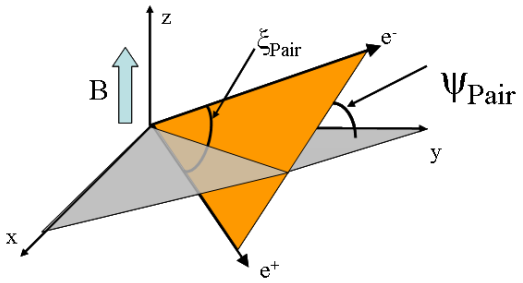

FIGURE 5.6: Sketch of the ψ_{pair} angle as the angle between the plane of the electron and positron pair (coloured in orange) and the bending plane of the magnetic field (in grey) [202].

where the index *cut* indicates the value applied during the cut selection.
The last selection considered is based on the photon energy asymmetry distribution, $\alpha = |E_{\gamma_1} - E_{\gamma_2}|/(E_{\gamma_1} + E_{\gamma_2})$, versus the meson transverse momentum. The cut applied is a p_{T}-dependent one, modelled on the function $f(p_T) = a \cdot \tanh(b \cdot p_T)$, with $a = 0.65$, $b = 1.2$ and the meson transverse momentum p_{T} given in GeV/c.
The photon selection cuts are summarised in Table 5.3.

Photon cuts

Armenteros-Podolanski (2D cut): $\left(\frac{\alpha_{V^0}}{\alpha_{V^0_{\text{max}}}}\right)^2 + \left(\frac{q_{\text{T}}}{q_{\text{T, max}}}\right)^2 > 1$	$\alpha_{V^0_{\text{max}}} = 0.95$, $q_{\text{T, max}} = 0.05$ GeV/c
χ^2_γ/ndf & ψ_{pair} (2D cut): $\lvert\psi_{pair}\rvert < \frac{-\psi_{pair,cut}}{\chi^2_{\gamma,cut}\cdot\chi^2_\gamma} + \psi_{pair,cut}$	$\chi^2_{\gamma,cut}/\text{ndf} < 20$, $\psi^{cut}_{pair} < 0.1$ rad
Cosine of pointing angle	$\cos\theta_{\text{P.A.}} > 0.85$ rad
Photon energy asymmetry, p_{T}-dependent: $\alpha < f(p_T)$, $f(p_T) = a \cdot \tanh(b \cdot p_T)$	$a = 0.65$, $b = 1.2$

TABLE 5.3: List of photon selection cuts applied in the analysis.

5.3 Neutral mesons reconstruction

The π^0 and η meson decay into two photons with branching ratio $(98.823 \pm 0.034)\%$ and $(39.41 \pm 0.20)\%$, respectively. Thus, they are reconstructed combining two photons from the selected sample. The invariant mass of the photon pairs is calculated as

$$M_{\gamma\gamma} = \sqrt{2E_{\gamma_1}E_{\gamma_2}(1 - \cos\theta_{12})} \tag{5.6}$$

where $E_{\gamma_{1,2}}$ is the energy of the photons and θ_{12} is the opening angle between them. The invariant mass distribution is sliced according to the reconstructed meson transverse momentum. The width of the slices is chosen such that there is enough statistics in each interval to allow for a reliable meson analysis.

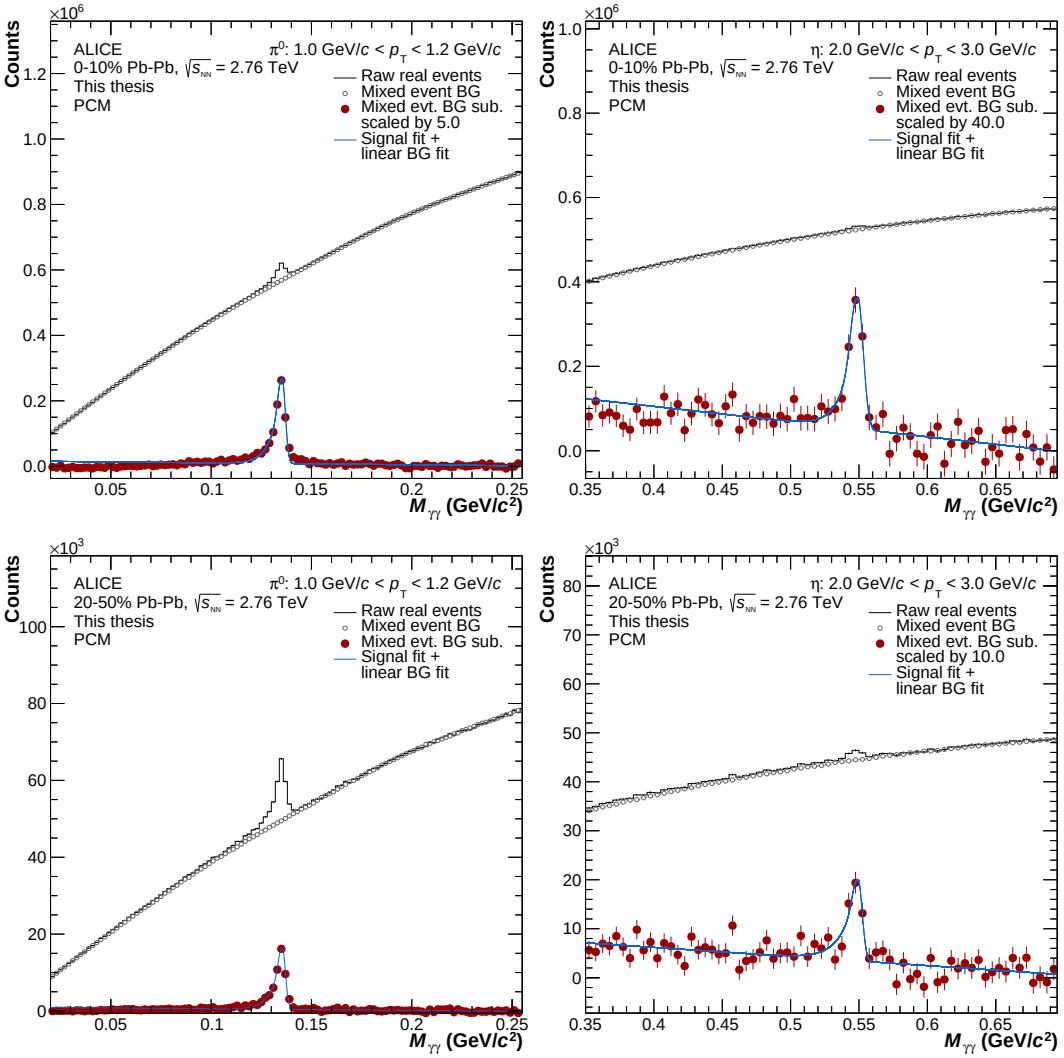

FIGURE 5.7: Invariant mass distribution of reconstructed photon pairs $M_{\gamma\gamma}$ around the neutral pion mass (0.135 GeV/c^2), left column, and the η meson mass (0.548 GeV/c^2), right column, in a selected p_T slice in Pb–Pb collisions at $\sqrt{s_{NN}}$ = 2.76 TeV for the centrality classes 0–10% (top) and 20–50% (bottom). The black histogram shows the data before combinatorial background subtraction (grey circles). The red bullets show the data after background subtraction. The cyan line is the fit to the invariant mass spectrum after background subtraction using Equation 5.7.

In Figure 5.7, the reconstructed invariant mass for the π^0 (left column) and η (right column) meson are shown in the transverse momentum interval $1 < p_T < 1.2$ GeV/c and $2 < p_T < 3$ GeV/c, respectively, for central (top) and semi-central (bottom) collisions. The black histogram represents the total reconstructed invariant mass distribution. The photon pairs coming from a neutral meson decay appear as an excess around the expected mass of the meson on top of the combinatorial background. The expected mass is 0.135 GeV/c^2 for the π^0 mesons and 0.548 GeV/c^2 for the η meson [9]. The distribution also shows a large background (grey circles), with a sloping shape rising towards higher mass values. This background originates from randomly associated photon pairs. In order to subtract this combinatorial background, an estimation using the event mixing technique is done. The event mixing technique combines photons from different events, thus uncorrelated. For a better description, the events to be combined are required to have similar topological characteristics:

primary vertex position on the z-axis and the reaction plane angle. The angle with respect to the reaction plane is obtained as explained in Section 1.3.3, relying on the VZERO detector estimation of the flow vector. Seven and eight bins are considered for these two quantities, respectively. The collision centrality is implicitly accounted for with the event selection and would result in one single bin being filled. The photons coming from the same bins are combined together when estimating the combinatorial background. The depth of the event pool considered for the estimation is 50. Since this gives an event multiplicity higher than the measured one, the event mixing background is normalised to the invariant mass distribution at the right of the meson peak for each p_{T}-bin. Once the combinatorial background has been subtracted, the distributions shown with the red bullets in Figure 5.7 are obtained. The complete set of figures for each p_{T}-interval is shown in Appendix A. The tail on the left-hand side of the peak is due to electron/positron Bremsstrahlung. The invariant mass peak fit shown in Figure 5.7 is a Gaussian function modified with an exponential to account for the Bremsstrahlung tail that is switched off on the right-hand side of the peak by the Heavyside function:

$$y = A \cdot \left(G(M_{\gamma\gamma}) + \exp\left(\frac{M_{\gamma\gamma} - M_{\pi^0,\eta}}{\lambda} \right) (1 - G(M_{\gamma\gamma}))\theta(M_{\gamma\gamma} - M_{\pi^0,\eta}) \right) + B + C \cdot M_{\gamma\gamma} \quad (5.7)$$

where λ is the inverse slope parameter of the exponential function, and $G(M_{\gamma\gamma})$ is the Gaussian term

$$G(M_{\gamma\gamma}) = \exp\left(-0.5 \left(\frac{M_{\gamma\gamma} - M_{\pi^0,\eta}}{\sigma_{M_{\gamma\gamma}}} \right)^2 \right). \quad (5.8)$$

The linear function term $B + C \cdot M_{\gamma\gamma}$ accounts for the residual background left after the combinatorial background subtraction. The fit of equation Equation 5.7 is not used to obtain the meson yields but only to estimate the mass peak position and width, used to determine the integration window of the meson peaks. These are shown in Figure 5.8 for the π^0 (left) and η (right) mesons. The full markers represent the values of mass width or position obtained from data, while the empty markers are the corresponding values estimated from the validated MC simulation. The notation "validated" MC represents the simulated signal which has been verified as coming from a real neutral pion or η meson. Given the "truth" of the MC information, the comparison of the data and MC mass peak information gives an estimate of the goodness of our measurement. The difference between the mass position in data and in MC, relative to the expected mass, is taken as mass resolution uncertainty and will be included in the systematic uncertainties estimation, in Section 5.4.

5.3.1 Yield extraction

The π^0 and η meson yields are obtained integrating the invariant mass peak after the event mixing background subtraction in an asymmetric mass window, necessary to include the Bremsstrahlung tail. The mass integration ranges are reported in Table 5.4.

Meson	Lower integration range (M_{low})	Upper integration range (M_{high})
π^0	M_{π^0} - 0.035 GeV/c^2	M_{π^0} + 0.010 GeV/c^2
η	M_{η} - 0.047 GeV/c^2	M_{η} + 0.023 GeV/c^2

TABLE 5.4: Mass integration ranges for the π^0 and for the η mesons.

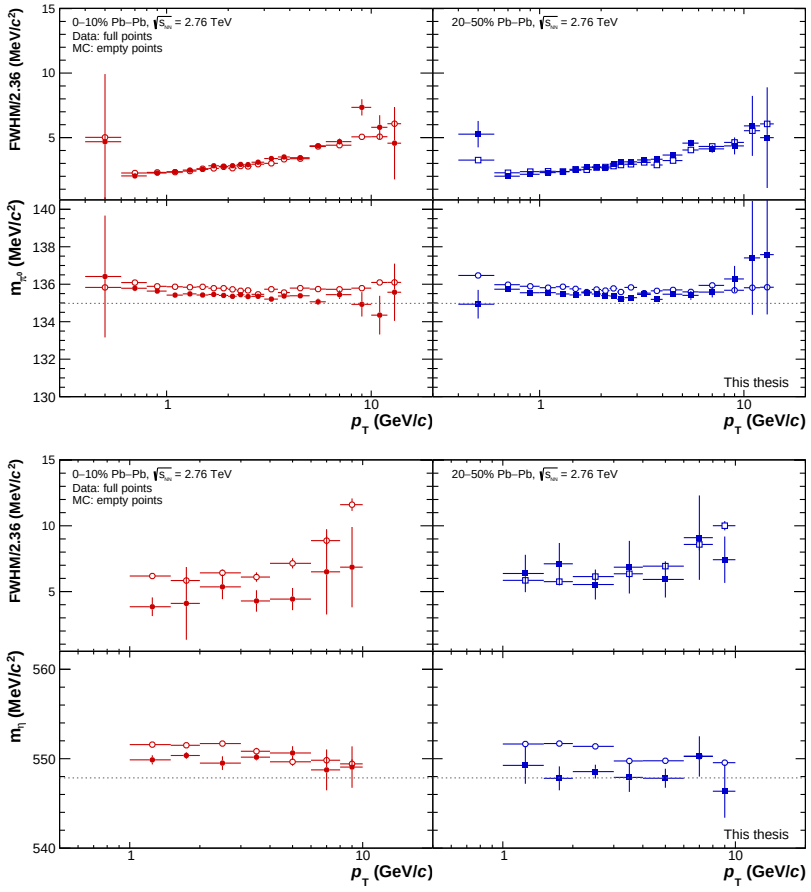

FIGURE 5.8: Reconstructed mass resolution (σ = FWHM/2.36, top panels) and mass (bottom panels) for the π^0 (top figure) and η (bottom figure) mesons as a function of the transverse momentum for centrality classes 0–10% (left) and 20–50% (right). The points for both data (full markers) and simulation (empty markers) are extracted using Equation 5.7.

As mentioned in the previous section, the linear part of the fit accounts for the residual background. This is integrated and subtracted from the meson signal integral. The final raw yields are thus obtained in the following way:

$$N^{\pi^0,\eta}_{\text{raw}} = \int_{M^{\pi^0,\eta}_{low}}^{M^{\pi^0,\eta}_{high}} (N^{\gamma\gamma} - N^{\text{comb. BG}}) dM_{\gamma\gamma} - \int_{M^{\pi^0,\eta}_{low}}^{M^{\pi^0,\eta}_{high}} (B + C \cdot M_{\gamma\gamma}) dM_{\gamma\gamma}. \tag{5.9}$$

The p_{T}-differential raw yield distributions for the π^0 and η mesons are shown in Figure 5.9 for the centrality classes 0–10% and 20–50%.

5.3.2 Monte Carlo weighting

The HIJING Monte Carlo event generator describes initial and final state effects of a nucleus-nucleus collision. Unfortunately, the simulation fails in taking into account the full effect of the jet quenching on the meson yields. As it can be seen in Figure 5.10, the MC input yields for the neutral mesons do not fully match the particle production in data. The fit function indicated in Figure 5.10 with the red line is a QCD inspired power-law. To compensate for

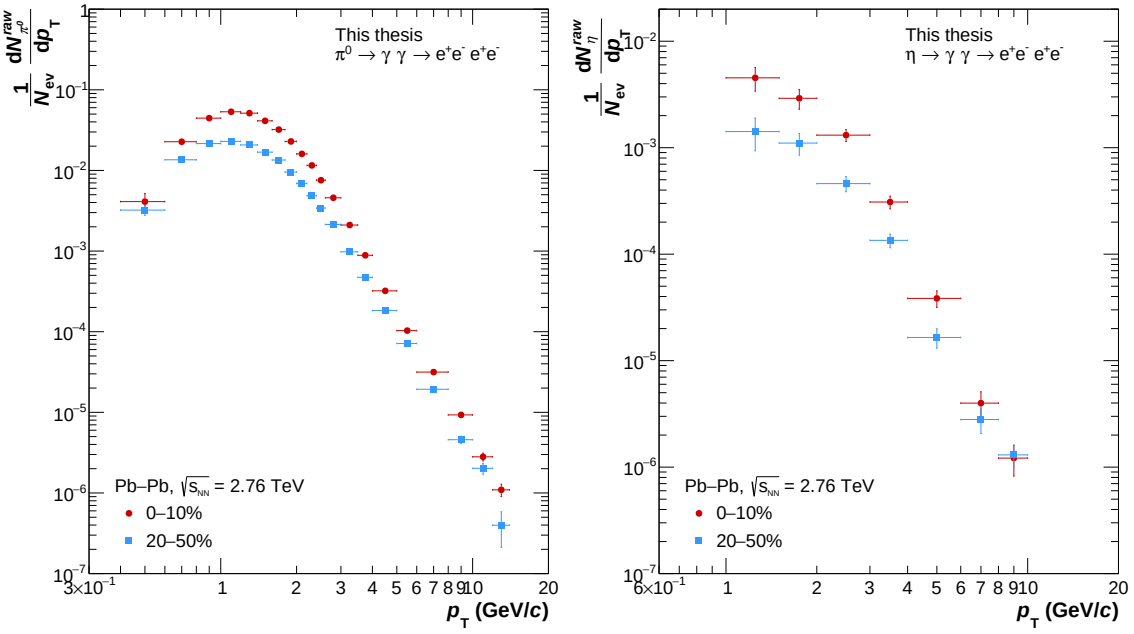

FIGURE 5.9: Raw yields for the neutral pion (left) and η meson (right) in the centrality classes 0–10% and 20–50%. Vertical bars indicate the statistical uncertainties.

the missing jet quenching, the MC input is weighted using the fit to the data as reference. Moreover, the MC simulation used in this work contains additional π^0 and η particles, to provide enough statistics at high-p_T, with a flat meson distribution versus transverse momentum (described in Section 3.2.4). This input is weighted in the same way as the standard one. The weighting procedure is done separately for the central and semi-central productions, and also for each centrality class, given that the quenching has different magnitude in central and peripheral events and that the number of added mesons is made to be dependent on the impact parameter. The weighting is also iterative, and it is repeated until the fluctuations of the weighted spectra stay well within the statistical error of the data points.
Figure 5.11 shows the ratio of the first, orange points, and last, red points, iteration for the

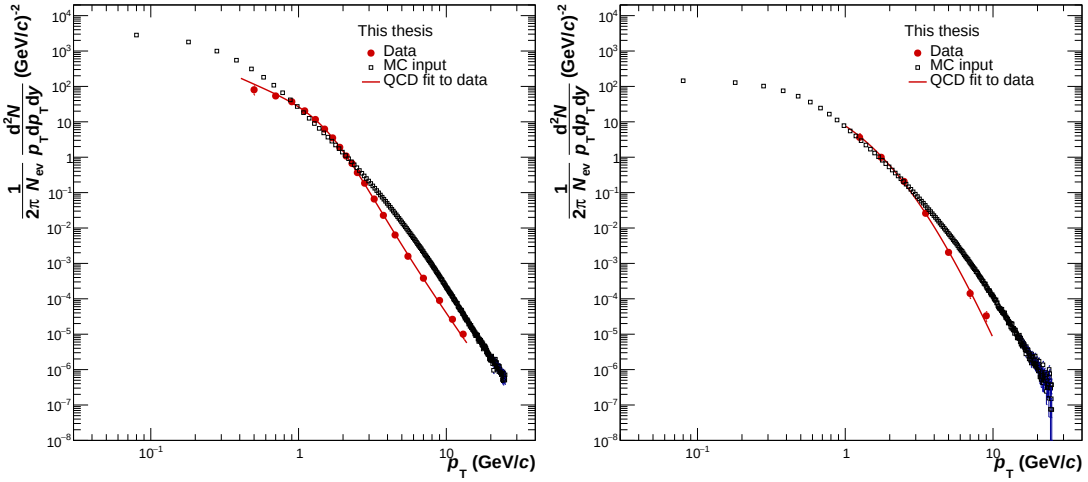

FIGURE 5.10: Comparison of the neutral pion (left) and η meson (right) spectra to the respective MC input yields for the centrality class 0–10%. The red line indicates a QCD inspired power-law fit to the data.

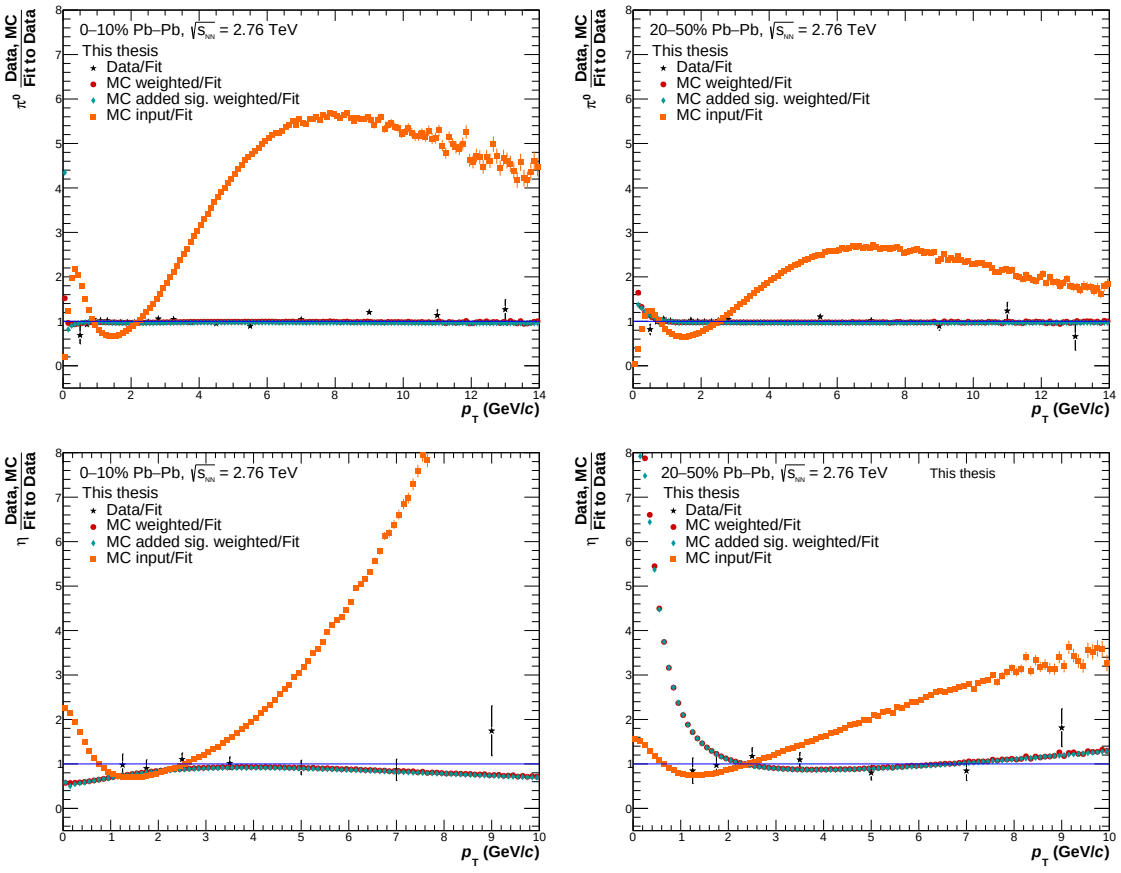

FIGURE 5.11: Ratio to the fit to the data of the unweighted MC (orange), weighted standard (red) and added signal (cyan) MC neutral meson spectrum after the 4^{th} iteration for 0–10% (left) and 20–50% Pb–Pb collisions at $\sqrt{s_{\mathrm{NN}}} = 2.76$ TeV. The ratio of the data points to the fit itself is indicated with the black markers. The π^0 meson is shown on the top row, while the η meson is on the bottom row.

standard MC simulation to the fit to the data spectra, for π^0 (top row) and η (bottom row) mesons. The added signals final iteration is indicated with the cyan points. The data points ratio, in black, are also shown for reference. Once the last iteration has given satisfying results, the MC simulations can be used to extract the corrections to apply in order to obtain the meson invariant yields. The reconstruction efficiency from the standard MC simulation and from the added signals are first extracted separately and then merged according to their statistical errors. The final efficiency is given by the standard MC efficiency as long as its statistical error is smaller than the added signals efficiency statistical error. When this is not true above a certain p_{T}, the added signals efficiency is taken.

5.3.3 Corrections to the raw neutral meson spectra

The sample of reconstructed neutral mesons selected with the analysis cuts is the optimal one, considering good background rejection, good agreement between data and MC while, at the same time, preserving the significance of the measurement.
To obtain the meson invariant yields, it is necessary to subtract the residual contaminations from particles coming from bunches other than the one of the actual collision event (pile-up)

and, for the neutral pion, from contamination due to pions from secondary particle decays. Furthermore, the spectra also need to be corrected for the detector response and acceptance.

5.3.3.1 Correction for contamination from pile-up verteces

In a high multiplicity collision such as a Pb–Pb one, there can be more than one collision vertex at a time. Given that the TPC drift time is about 94 μs, it could happen that not all the particles detected come from the same vertex. Moreover, the vertexing algorithm reconstructs only one vertex at a time, being then temporarily blind to the others. The verteces displaced from the centre of the experiment, not coming from the primary collision, are called pile-up verteces and need to be rejected. It is helpful that, by definition, the pile-up event has a vertex with a larger value of the z-coordinate. This makes their identification possible studying the distance of closest approach distributions in the z-direction (DCA_z) of the photon candidates, that will be wide around zero. The p_{T}-integrated DCA_z distribution for data and validated MC sources is shown in Figure 5.12 for the centrality class 20–50%. The pile-up is not simulated in MC and it can be seen that its DCA_z distribution is not as broad as in data. Moreover, this correction is estimated only for events with centrality larger than 20% (classes 20–50% and 20–40%): the number of neutral mesons is much higher in central collisions and as it is unlikely to have two consecutive central collisions, thus contributions from pile-up. In addition, the photon misidentification is also much higher in central collisions, given the higher multiplicity.

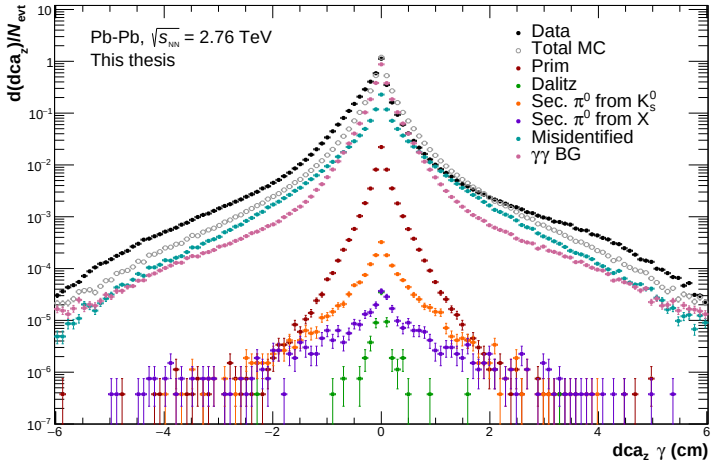

FIGURE 5.12: Comparison of integrated γ DCA_z distribution in 20–50% Pb–Pb collisions in data (black markers) and in MC (grey markers). The contamination in MC is shown decomposed into the separate contributions.

The typology of photons and mesons to be taken into account in the DCA analysis can be classified in three and six categories, respectively.
The photon categories are:

1. both electron and positron tracks are TPC-only tracks (no ITS hits), which happens for all the photons with $R_{\mathrm{conv}} > 50$ cm;
2. one of the tracks has at least two ITS hits;
3. both tracks have each two ITS hits minimum.

In the meson case, the classification is based on the photons category:

1. both photon belong to category 1;
2. one photon from category 1, one from category 2;
3. one photon from category 1, one from category 3;
4. both photons belong to category 2;
5. one photon from category 2, one from category 3;
6. both photons belong to category 3;

The largest contribution to the pile-up will come from the first category. Conversely, the last meson category, being constrained to having multiple ITS hits on both photons, will be basically without pile-up.
To extract the correction, the DCA_z distribution for photons from pairs within the meson mass region and in the separate categories are analysed in p_{T}-bins. These distributions are collected in Appendix B. The pile-up background under the DCA_z peak is estimated using the ROOT function *Showbackground*, with iterative steps. The pile-up contamination fraction for both mesons is shown in Figure 5.13. Together with the standard method used (method A for separate categories), other extraction methods with different settings for the *Showbackground* function or evaluating the categories all together are shown. These methods are used as systematic variations. Moreover, since the statistic runs out at a smaller transverse momentum compared to the meson analysis, the contamination is fitted with a power-law to extend it at high-p_{T}, where the contribution is anyway negligible.
The correction at 1 GeV/c is of the order of 2% for both mesons.

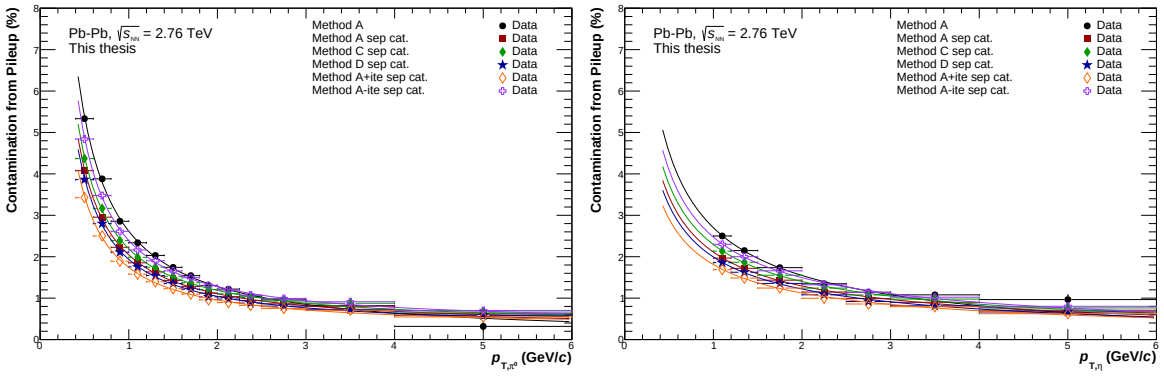

FIGURE 5.13: Contamination from pile-up verteces for the neutral pion (left) and η meson (right) in 20–50% Pb–Pb collisions shown with the different estimation methods.

5.3.3.2 Correction for contamination from secondary neutral pions

Following the ALICE definition of primary particle as coming from the primary vertex, the neutral pions we want to measure correspond to the primary ones, not coming from weak decays. The largest secondary pion contribution comes from $\mathrm{K}^0_{\mathrm{S}}$ decays into two neutral pions, followed by the Λ decay in a much smaller fraction and by the $\mathrm{K}^0_{\mathrm{L}}$ decays that are negligible. In addition, pions coming from interaction with the detector material should also be taken into account.
In order to only have pions coming from the primary vertex in the sample, the secondary neutral pions are subtracted after the contamination has been estimated via MC simulation. The contributions from secondary pions are obtained from the MC simulation checking the

identity of the particle mother. While this is a reasonable procedure for the contribution from interactions in the material, it is not acceptable for the K^0_S case, that has large fluctuations at high-p_T, and for K^0_L and Λ, that are affected by an overall lack of statistics. In order to compensate for the the inadequate MC statistics, a hadronic cocktail simulation based on the parametrisations of the measured (when available) spectra of K^0_S, K^0_L and Λ is produced. The mother particles are generated flat in p_T, pseudorapidity η and azimuthal angle φ, within the same rapidity interval of the neutral meson analysis ($|y| < 0.85$). The parametrised transverse momentum distributions are then used to weight the produced sample. The particles are decayed with the PYTHIA6 decayer, which follows the branching ratios given in [9]. The secondary π^0 obtained from the cocktail are based on the parametrisations of the fully corrected spectra, meaning that they need to be reverted to the raw yields before it is possible to use them for correcting the primary pions. Therefore, the cocktail yields are multiplied with the secondaries acceptance and reconstruction efficiency for K^0_S, K^0_L, Λ, extracted from the standard MC simulation. In this case, the efficiency fluctuations that would propagate to the yields and make the use of the cocktail less effective, are overcome fitting the ratio of the secondary to the primary efficiency and using the fit to scale the primary pion efficiency and obtain a secondary pion efficiency without fluctuations. The final step is the subtraction of the raw secondary yields from the primary neutral pion raw yields.

In Figure 5.14 the fraction of secondary pions is shown separately for each contribution. The examples provided here are for the centrality 0–10%, left, and 20–50%, right. The correction at 1 GeV/c is 2.4% for central and 2.7% for semi-central collisions, and then decreases towards high-p_T. The contributions from Λ and K^0_L are negligible.

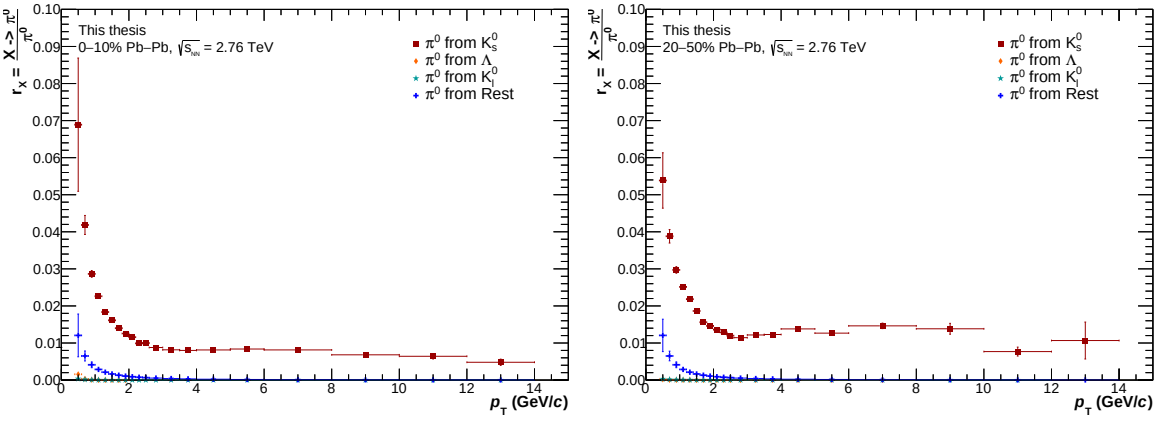

FIGURE 5.14: Correction factor for the secondary neutral pions shown separately for each contribution in 0–10% (left) and 20–50% (right) Pb–Pb collisions.

5.3.3.3 Correction for detector effects and acceptance

The corrections for the detector acceptance and reconstruction efficiencies are extracted from the Monte Carlo simulations. The geometrical acceptance is defined as

$$A_{\pi^0(\eta)}(p_T) = \left. \frac{N^{\text{daughters in acceptance}}_{\pi^0,\eta}(p_T)}{N^{\text{all}}_{\pi^0,\eta}(p_T)} \right|_{|y|<y_{max}} \tag{5.10}$$

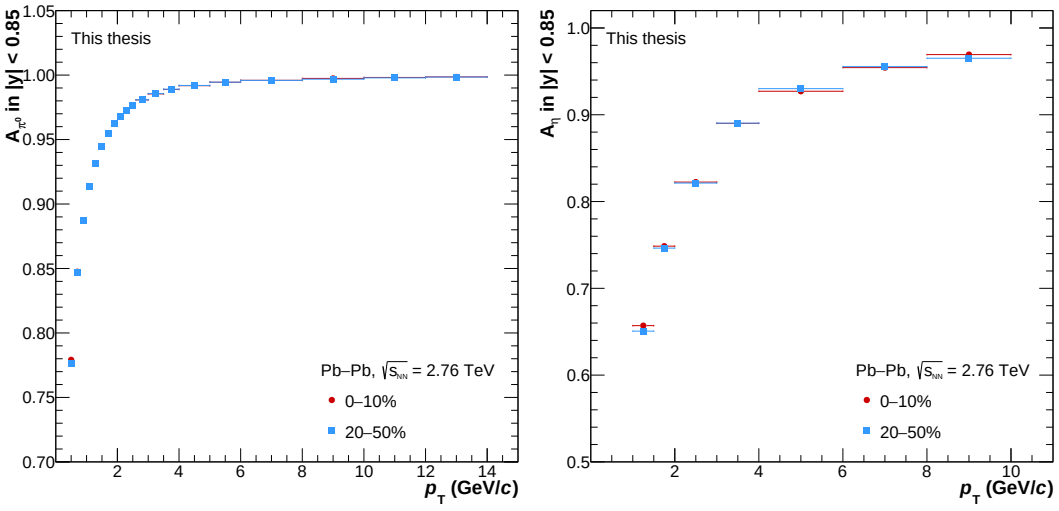

FIGURE 5.15: Geometrical acceptance of the π^0 (left) and η (right) meson in Pb–Pb collisions at $\sqrt{s_{\mathrm{NN}}} = 2.76$ TeV in the centrality classes 0–10% and 20–50%.

where the numerator is the number of primary π^0 or η mesons generated in MC in the fiducial acceptance ($|y| < 0.85$) with daughters also within the acceptance ($|\eta| < 0.9$), and the denominator is the number of all the primary π^0 or η mesons generated in the fiducial region ($|y| < 0.85$). Figure 5.15 shows the geometrical acceptance for π^0 and η mesons in the centrality classes 0–10% and 20–50%. For both mesons, the acceptance does not depend on the particle multiplicity of the collision. The slower rise to unity for the η meson is due to the higher mass compared to the π^0, resulting in a wider opening angle between the daughter particles.

The meson reconstruction efficiency is extracted analysing the MC simulations after validating that the reconstructed photon pair comes from a real (and the same) neutral pion or η meson. The analysis selection cuts are the same ones used for the data. This correction, which also includes the photon conversion probability, is expressed as

$$\epsilon_{\pi^0(\eta)}(p_{\mathrm{T}}) = \frac{N^{\text{validated}}_{\pi^0,\eta}(p_{\mathrm{T}})}{N^{\text{daughters in acceptance}}_{\pi^0,\eta}(p_{\mathrm{T}})} \tag{5.11}$$

where the numerator is the number of meson reconstructed and validated with the Monte Carlo truth, and the denominator is the same as the acceptance numerator. Differently from the acceptance, the reconstruction efficiency depends on the collision centrality: the single particle reconstruction efficiency is lower in central collisions due to the higher multiplicity. Figure 5.16 shows the reconstruction efficiency for the π^0 and η mesons in the two centrality classes of interest.

5.3.3.4 Correction for finite bin width

An additional correction not related to the detector or event characteristic is the finite bin width correction. The meson spectrum as a function of the transverse momentum has a steeply falling slope, meaning that the bin centre value will not reflect correctly the value of the yield at the given p_{T}. To overcome this, the spectrum is shifted either in the x- or y-axis direction according to the Lafferty-Wyatt method [203].

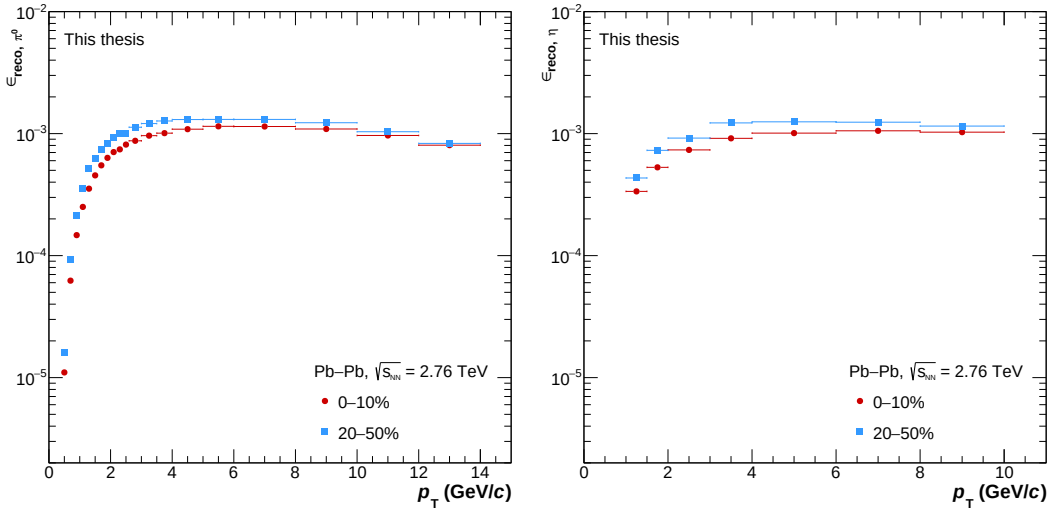

FIGURE 5.16: Reconstruction efficiency of the π^0 (left) and η (right) mesons in Pb–Pb collisions at $\sqrt{s_{\mathrm{NN}}} = 2.76$ TeV in the centrality classes 0–10% and 20–50%.

The π^0 and η meson invariant yields will be displayed with the x-shift correction, thus the p_{T} shown will indicate the true transverse momentum. In the case of the η to π^0 ratio and of the nuclear modification factor R_{AA}, the y-shift correction will be applied instead. The choice is driven by the fact that the underlying physics is different for the numerator and the denominator and that the x-position of the point has to be the same. The correction will be applied separately in the case of π^0 and η in the ratio, and to Pb–Pb and pp results in the R_{AA} case. For both mesons, the shift is larger for higher p_{T}, with the shift for the η yields being larger compared to the π^0 case. In both cases, the reason is the larger width of the transverse momentum bins.

5.4 Systematic uncertainties for the neutral meson measurement

The systematic uncertainties are estimated by varying each of the selections made in the analysis of the data sample and comparing the results obtained with the standard selection. When possible, a tighter and looser cut selection in comparison with the standard selection will be adopted. Otherwise, two variations in the same direction or just one variation will be considered. The systematic deviations are studied for each transverse momentum bin. The mean of the positive and negative deviations will give the single contribution uncertainty, while the total systematic uncertainty will result from the squared sum of all the single contributions. The cross correlation between the selection cuts, especially when they are p_{T}-dependent, has been checked, and special care is taken to avoid that the statistical fluctuations influence the systematic uncertainty estimation.
In this section, the systematic selection cut variations and the single systematic uncertainty contributions will be illustrated.

5.4.1 Material budget

The material budget uncertainty depends solely on the current knowledge of the ALICE detector material and is p_{T}-independent. The mapping of the material is done studying the photon conversions in all the geometrical coordinates, obtaining a radiography of the detector. The procedure is explained in detail in [169].
During the detector assembly the materials used and their relative positions in the experiment were recorded. This knowledge has been implemented in the geometry inputs used in GEANT Monte Carlo simulations. However, the composition and design is known only to a certain precision and some simplification have been done. The uncertainty is estimated comparing the results from a MC simulation to the data. The error, which takes into account the rapidity range, the event generators used and the secondary vertex reconstruction efficiency, amounts to 4.5% for a single photon. Therefore, this is doubled for the neutral meson spectra, while it is not considered in the ratios (η to π^0 ratio and nuclear modification factor) systematic uncertainty, as it cancels out.

5.4.2 Meson reconstruction

The uncertainties deriving from the selection cuts used to reconstruct the neutral mesons are grouped according to what they are acting upon.

Track reconstruction: the number of TPC clusters over findable clusters and the minimum electron transverse momentum give a systematic uncertainty larger at lower p_{T} (below 1 GeV/c), where the tracks are shorter and the reconstruction efficiency drops sharply.

Electron identification: affects the selection based on the particle identification in the TPC and TOF. This includes also the pion rejection cuts. As the variations on the TOF cut are negligible, these are not included in the systematic uncertainty.

Photon reconstruction: gives one of the largest contributions to the final systematic uncertainty, it includes the error from the azimuthal angle φ rejection, the q_{T}, ψ_{pair} and χ^2 photon cuts. The cosine of pointing angle is also excluded from the estimation as negligible.

The complete list of the systematic variations for the meson reconstruction selection cuts is reported in Table 5.5.

5.4.3 Signal extraction

As explained in Section 5.3.1, the raw meson yields are extracted integrating, in each p_{T}-bin, the invariant mass distribution after the combinatorial and residual backgrounds have been subtracted. The systematic uncertainty related to the signal extraction depends on the background estimation and integration window. To estimate it, the range in which the invariant mass distribution is integrated is varied according to the values in Table 5.6 and an alternative normalisation region is considered, on the left side of the meson peak.
Under the signal extraction systematic error, the uncertainty coming from the cut on the photon energy asymmetry is also added (last line of Table 5.5). The mass resolution uncertainty, given by the discrepancy between the data and MC estimation of the meson mass

Quantity	Standard	Variation 1	Variation 2
TPC cluster ratio	> 0.6	> 0.7	> 0.35
Min. p_{T} $e^{\pm}$	> 0.05 GeV/c	> 0.075 GeV/c	> 0.1 GeV/c
dE/dx e-line $\sigma_{\mathrm{d}E/\mathrm{d}x,e}$	$-3 < n_\sigma < 5$	$-4 < n_\sigma < 5$	$-2.5 < n_\sigma < 4$
dE/dx π-line in momentum range	[0.4, 2.0] GeV/c	[0.4, 2.0] GeV/c	[0.4, 100] GeV/c
π rej. low p $\sigma_{\mathrm{d}E/\mathrm{d}x,\pi}$	< 3	< 2	< 2.5
π rej. high p $\sigma_{\mathrm{d}E/\mathrm{d}x,\pi}$	< 1	< 1	< -10
$p_{\mathrm{min},\ \pi\ \mathrm{rej}}$	0.4 GeV/c	0.3 GeV/c	–
$p_{\mathrm{max},\ \pi\ \mathrm{rej}}$	2.0 GeV/c	3.0 GeV/c	–
χ^2 γ	< 20	< 50	< 30
ψ_{pair} γ	< 0.1 rad	< 0.2 rad	< 0.05 rad
$q_{\mathrm{T,max}}$	< 0.05 GeV/c	< 0.03 GeV/c	< 0.06 GeV/c
Cut on φ	[2.2, 3.8] rad	[2.0, 4.0] rad	[2.4, 3.6] rad
α meson	$< f(p_T)$, $f(p_T) = a \cdot \tanh(b \cdot p_T)$ with $a = 0.65$ and $b = 1.2$	< 0.75	< 1.0

TABLE 5.5: Complete list of the selection criteria and their variations to evaluate the meson reconstruction systematic uncertainty. Only one of these cuts is varied at a time to estimate the systematic uncertainty.

	π^0	η
	Normalization window	
Right side (standard)	[0.17, 0.3] GeV/c^2	[0.58, 0.8] GeV/c^2
Left side	[0.05, 0.08] GeV/c^2	[0.35, 0.48] GeV/c^2
	Integration range	
Standard	[0.1, 0.145] GeV/c^2	[0.5, 0.57] GeV/c^2
Narrow	[0.12, 0.14] GeV/c^2	[0.52, 0.56] GeV/c^2
Wide	[0.08, 0.16] GeV/c^2	[0.48, 0.58] GeV/c^2

TABLE 5.6: Variations of the normalisation range and integration windows for the evaluation of the signal extraction systematic uncertainty.

position, is weakly dependent on the transverse momentum, thus a constant uncertainty of 1.4% is assumed for both mesons. The mass resolution uncertainty is not considered for the η to π^0 ratio. The total and single contributions systematic uncertainties on the yields for the two meson in the two centrality classes considered are shown in Figure 5.17.
For the η to π^0 ratio, the systematic uncertainties are evaluated directly on the ratio, in order to cancel out the common deviations. A systematic uncertainty about 10% smaller is obtained compared to what is estimated from the separate meson uncertainties. The total and single contribution systematic uncertainties for the η to π^0 ratio are shown in Figure 5.18.
The systematic uncertainty associated with the pile-up contribution and evaluated using

different functions to calculate the background, is negligible (less than 1%) and it is not considered.

For the π^0 measurements, it was chosen to make public only the results for p_{T} above 1 GeV/c. The excluded data points have rapidly decreasing efficiency (2×10^{-4} just below 1 GeV/c, 1×10^{-5} in the first bin) and large statistical and systematic uncertainties compared to the other p_{T}-bins, thus do not allow for a significant/reliable measurement.

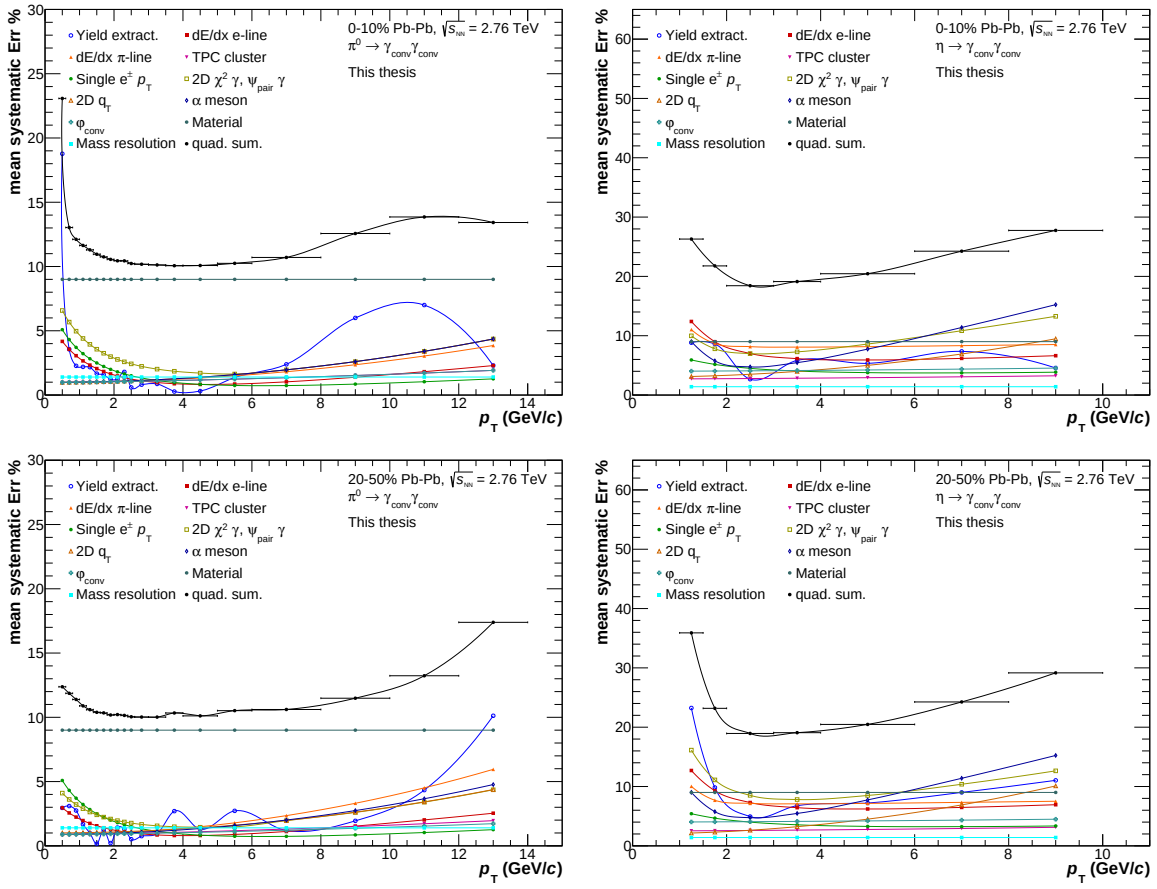

FIGURE 5.17: Systematic uncertainties of the π^0 (left) and η (right) mesons in Pb–Pb collisions at $\sqrt{s_{\mathrm{NN}}} = 2.76$ TeV in the centrality classes 0–10% (top) and 20–50% (bottom).

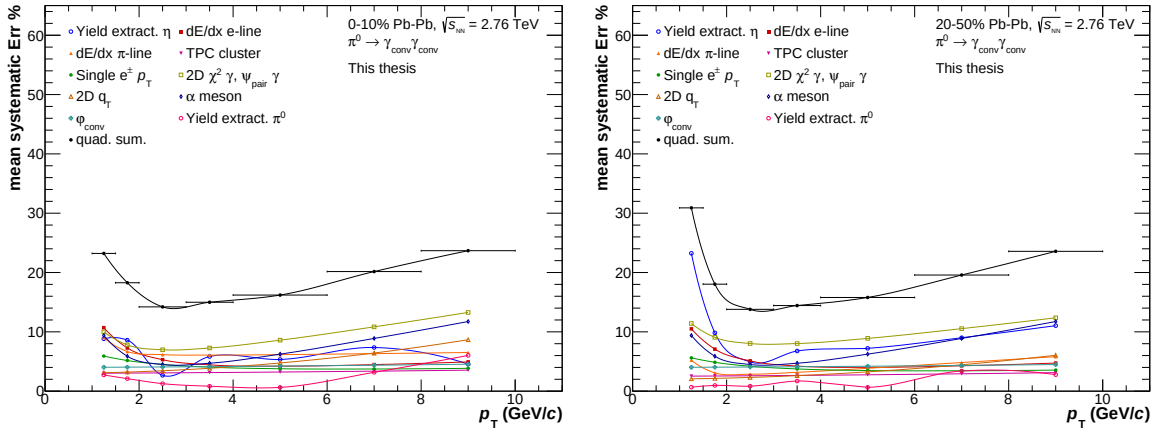

FIGURE 5.18: Systematic uncertainties of the η/π^0 ratio in Pb–Pb collisions at $\sqrt{s_{\mathrm{NN}}} = 2.76$ TeV in the centrality classes 0–10% (left) and 20–50% (right).

Chapter 6

Results on the neutral meson measurements in Pb–Pb collisions

This chapter illustrates the neutral meson measurements obtained in this thesis from the analysis of the 2011 Pb–Pb run. First, the results obtained using only the PCM method will be shown. Then, the combination of the PCM results with the EMCal and PHOS neutral meson measurements will be introduced and used to compare with the theoretical models.

6.1 Neutral meson transverse momentum spectra

The differential invariant yield is calculated, for each centrality class, with

$$E\frac{\mathrm{d}^3N}{dp^3} = \frac{\mathrm{d}^3N}{p_{\mathrm{T}}\mathrm{d}p_{\mathrm{T}}\mathrm{d}y\mathrm{d}\varphi} = \frac{1}{2\pi}\frac{1}{p_{\mathrm{T}}}\frac{\mathrm{d}^2N}{\mathrm{d}y\mathrm{d}p_{\mathrm{T}}} = \frac{1}{2\pi N_{\mathrm{ev}}}\frac{1}{\epsilon_{\pi^0(\eta)}A_{\pi^0(\eta)}\mathrm{BR}}\frac{1}{p_T}\frac{N_{\mathrm{raw}}^{\pi^0,\eta}}{\Delta y\Delta p_{\mathrm{T}}} \tag{6.1}$$

where N_{ev} is the number of events in the different centrality classes, reported in Table 3.1, $\epsilon_{\pi^0(\eta)}$ is the reconstruction efficiency and $A_{\pi^0(\eta)}$ is the acceptance for each meson in the respective centrality class, as defined in Section 5.3.2. BR is the branching ratio of the decay $\pi^0(\eta) \rightarrow \gamma\gamma$ and $N_{\mathrm{raw}}^{\pi^0,\eta}$, from Equation 5.9, the measured raw yield for the π^0 (η) meson within the rapidity range $|y| < 0.85$ and the transverse momentum bin Δp_{T}. Even though not explicitly written in the equation here, $N_{\mathrm{raw}}^{\pi^0,\eta}$ has also been corrected for pile-up and, in the case of the π^0, for the secondary pion contamination.
The spectra are shown in Figure 6.1 for the π^0 (left) and η (right) meson. Statistical uncertainties are represented by the vertical bars, systematic uncertainties by the boxes. The π^0 differential invariant yields obtained in this work have been compared to the published π^0 measurement in Pb–Pb collisions at the same centre-of-mass energy (2010 Pb–Pb run) [90]. The consistency of the two measurements has been confirmed within uncertainties [1]. The increased luminosity of the 2011 Pb–Pb run improves both the transverse momentum reach and the statistical uncertainties of the neutral meson measurement, as it can be seen in Figure 6.2. Here, the statistical errors versus transverse momentum are shown in percentage for the 2010 and 2011 results, for the centrality classes common to both measurements. The

[1] Different selection criteria have been applied in this work compared to [90].

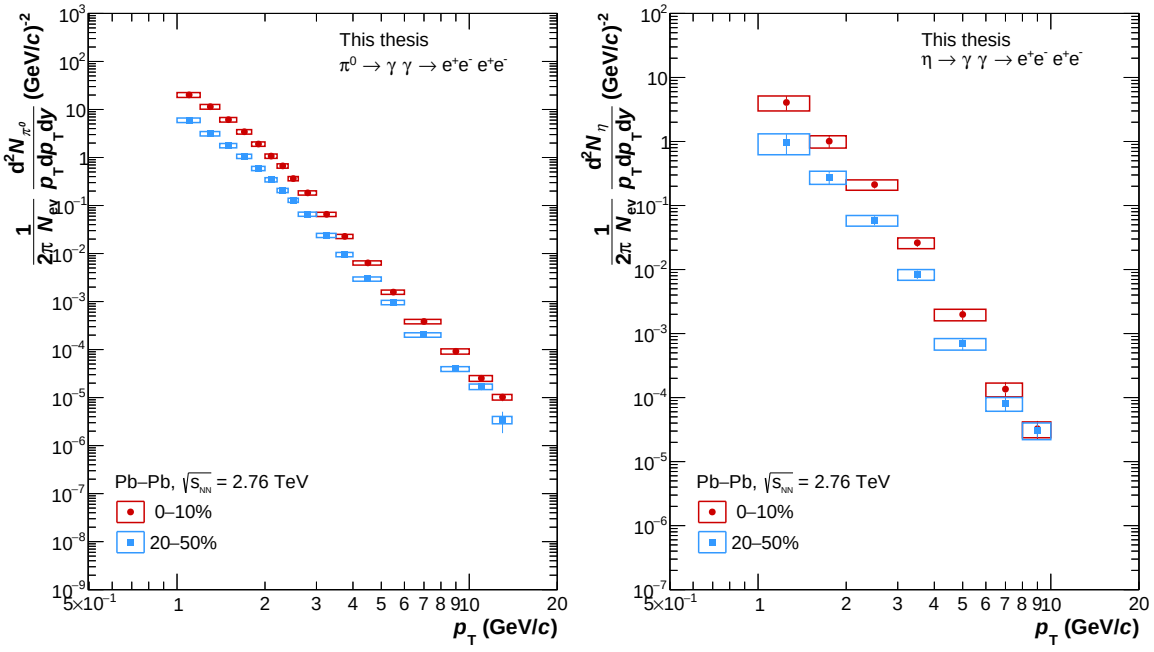

FIGURE 6.1: Differential invariant yields for the π^0 (left) and η (right) meson for the centrality classes 0–10% (red) and 20–50% (azure) in Pb–Pb collisions at $\sqrt{s_{\rm NN}} = 2.76$ TeV measured with the PCM. The statistical uncertainties are represented by the vertical bars, the systematic uncertainties by the boxes.

statistical uncertainty decreases from 8% to 2.5% below 5 GeV/c in the central class, and from 5% to 3% in the 20–40% centrality class for $p_{\rm T}$ <4 GeV/c. Moreover, the increased statistics of 2011 allows for the η meson measurement, which was not possible before.

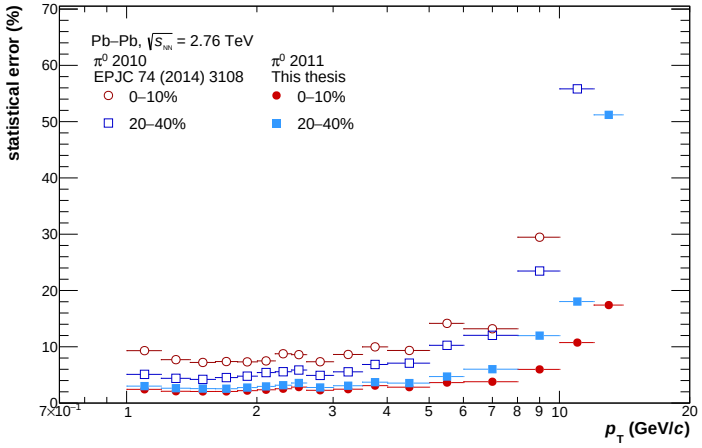

FIGURE 6.2: Percentage of the differential invariant yield statistical errors for the π^0 meson in 0–10% (round markers) and 20–40% (square markers) Pb–Pb collisions at $\sqrt{s_{\rm NN}} = 2.76$ TeV. Open markers represent the 2010 measurement [90], full markers the results of this thesis.

6.1.1 Comparison of the neutral and charged meson spectra

The fully corrected spectra of the π^0 and η meson have been compared, respectively, with the charged pion and kaon spectra in Pb–Pb collisions at the same centre-of-mass energy [204]. The pion comparison is motivated by the fact that, due to isospin symmetry, the ratio of π^0 to $(\pi^+ + \pi^-)/2$ is expected to be one, in the transverse momentum region of interest. In Figure 6.3, the comparison of the measurements of the neutral to charged pion are shown for the centralities 0–10% and 20–40%. The charged pion spectra are measured via a combined ITS, TPC and TOF analysis [204] for the low-p_{T} part while the high momentum part is measured via the particle fractions in the relativistic rise of the TPC $\mathrm{d}E/\mathrm{d}x$ [205]. The ratios are consistent with unity.

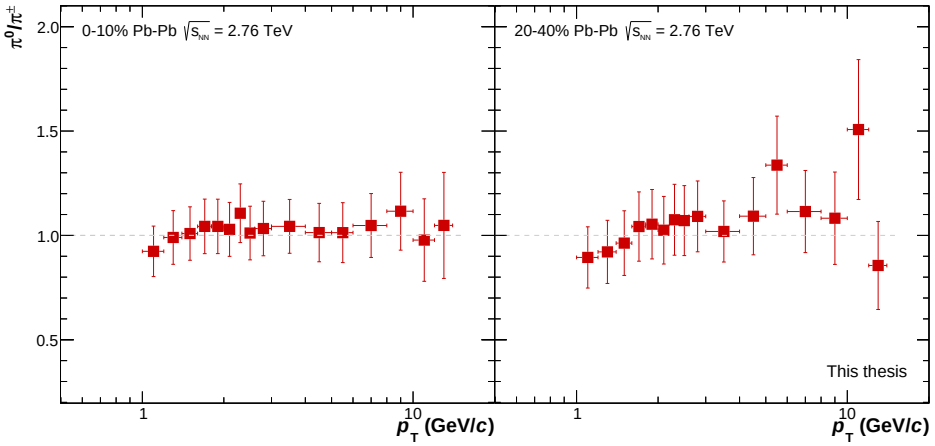

FIGURE 6.3: Ratio of the π^0 to $(\pi^+ + \pi^-)/2$ spectrum [204, 205] in 0-10% and 20–40% Pb–Pb collisions. The error bars represent the quadratic sum of systematic and statistical uncertainties.

The η meson is compared to the charged kaon spectrum because the two mesons have similar masses and both contain strangeness. In addition, the parallel comparison of the ratio of charged pion to kaon and of the η meson to the neutral pion, shown in the next section, helps in discerning whether there is a difference in the radial flow of the considered particles.

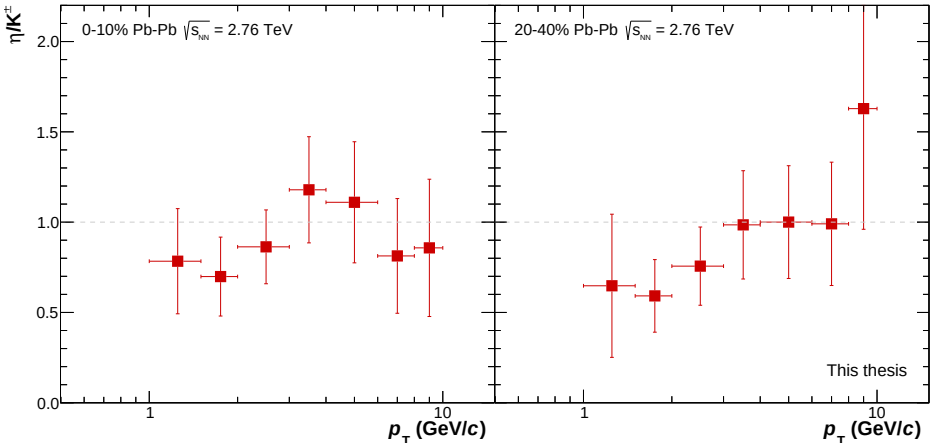

FIGURE 6.4: Ratio of the η to $(K^+ + K^-)/2$ spectrum [204, 205] in 0-10% and 20–40% Pb–Pb collisions. The error bars represent the quadratic sum of systematic and statistical uncertainties.

Figure 6.4 illustrates the ratio of η to $(K^+ + K^-)/2$ in 0–10% and 20–40% Pb–Pb collisions. The charged kaons are measured together with the charged pions in the same analysis. The η to $(K^+ + K^-)/2$ ratio tends to values below unity at low-p_{T}. In this transverse momentum region, the trend of the ratio could hint at a difference in the radial flow of the kaons compared to the η meson. Unfortunately, the total uncertainties are too large to consider this deviation as significant.

6.2 η/π^0 ratio

The study of the η/π^0 ratio can give information about the particle production mechanisms in the medium. Moreover, the comparison of this quantity to the theory models and to other experimental results of similar nature adds to this knowledge and helps the study of the characteristics of the particles involved.
In order to compute the η to π^0 ratio, the π^0 analysis is carried out also in the same transverse momentum binning used for the η meson. The η/π^0 ratio is calculated using the fully corrected yields. Moreover, the systematic uncertainties are evaluated directly on the ratio, once the common errors have been excluded, to further reduce them (see Section 5.4).
In Figure 6.5, left, the η/π^0 ratio is shown for the centrality classes 0–10% and 20–50%.

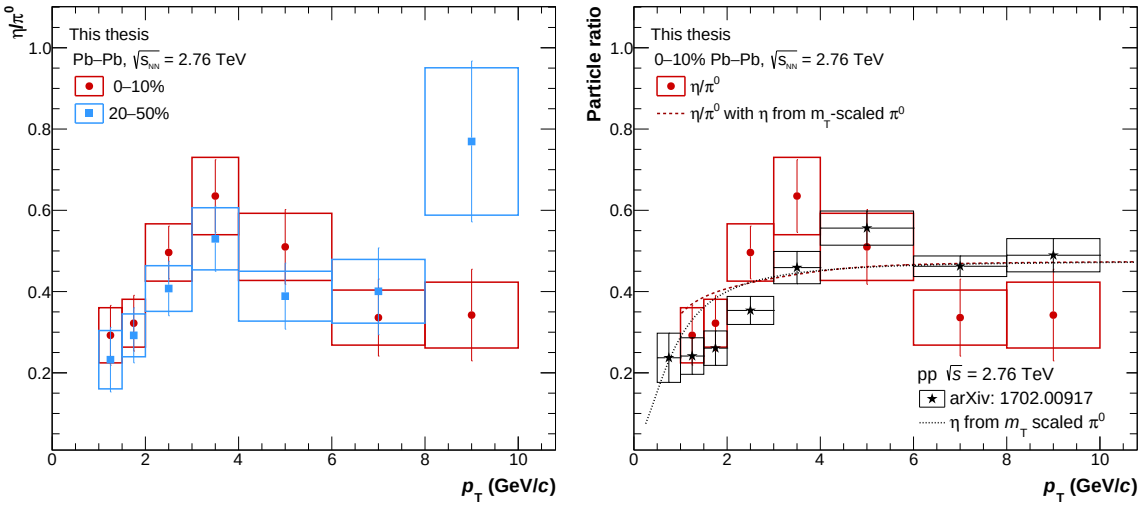

FIGURE 6.5: Left: Ratio of the η to π^0 meson for the centrality classes 0–10% and 20–50% in Pb–Pb collisions at $\sqrt{s_{\mathrm{NN}}} = 2.76$ TeV. Right: The ratio in the centrality 0–10% is compared to the same measurement in pp collisions at $\sqrt{s} = 2.76$ TeV [206]. Vertical bars represent statistical uncertainties, boxes the systematic uncertainties. The dashed lines represent the η/π^0 ratio with the η obtained from the m_{T}-scaling of the π^0 meson spectrum measured in the respective systems.

The ratio is also very important to verify the assumptions on the particle spectra when using the m_{T}-scaling, where m_{T} is the transverse mass $m_{\mathrm{T}} = \sqrt{m^2 + p_T^2}$ [207]. The scaling is often adopted to obtain the transverse momentum invariant yields of the desired particles, using the well measured reference of the charged pion, kaon and proton spectra. The underlying assumption is that p_{T}-dependent invariant yields can be expressed as a function of m_{T}, whose shape is common to all particle species, via a normalisation factor. It has been observed that the scaling is violated in the low-p_{T} region of the particle spectra for pp [208] and p–A [209]

results at RHIC and LHC, as opposed to what was observed at lower energies [210]: the deviation is attributed to the emergence of radial flow [208]. Nonetheless, the m_{T}-scaling is often used in direct photon measurements and in similar cases, such as the low mass dileptons measurement or the study of electron from heavy flavour decays. In these measurements, the scaling is used to describe the p_{T}-spectra of particles with electromagnetic decays necessary for the background subtraction, via cocktail simulation (Chapter 7), but that are not yet experimentally available. In this direction, the η meson measurement of this work, first of its kind in Pb–Pb collisions at the LHC, will help in reducing the uncertainties on the cocktail and therefore on the background estimation.
The η/π^0 ratio is a tool to study and quantify the magnitude of the m_{T}-scaling violation, not only with the direct comparison to the scaling results but also with the comparison to the pp η/π^0 measurement at the same centre-of-mass energy. Figure 6.5, right, shows these results together. The η/π^0 ratio in 0–10% Pb–Pb collisions is compared to the one in pp collisions [206]. The ratio computed using the η meson input from the m_{T}-scaled π^0 spectra is also reported here with the dashed line. It can be observed that while the m_{T}-scaling result is in agreement with the data points at high-p_{T}, it fails to follow both Pb–Pb and pp at low-p_{T}.

Comparison to the pp η/π^0 ratio. Additional remarks to the Pb–Pb to pp collisions comparison can be made considering that the latter represents the baseline (vacuum) behaviour. While the uncertainties of the Pb–Pb measurement are such that they do not allow for a more certain statement, nevertheless, in Figure 6.5 (right), there seems to be an enhancement over the pp measurement at intermediate p_{T} (2–4 GeV/c) in the centrality class 0–10%. In 20–50%, the enhancement in the same transverse momentum region is smaller. As mentioned above, a deviation in this region could be attributed to the radial flow, more pronounced in central than in semi-central collisions and absent in the pp case.

Comparison to the charged kaon over pion ratio. The enhancement of the spectra in the intermediate p_{T} region due to radial flow can also be observed in the comparison of this thesis results to the ALICE ratio of charged kaon to charged pions [204]. It was mentioned earlier that such a comparison is justified by the similar characteristics of kaon and η mesons (mass, strangeness) and the expectation that they should behave in the same way. The study of the two ratios would verify this assumption. In Figure 6.6, the η/π^0 ratio is plotted together with the $\mathrm{K}^{\pm}/\pi^{\pm}$ ratio measured at the same centre-of-mass energy. Above 4 GeV/c, the data ratios and the m_{T}-scaled lines are all in agreement at 0.47, which is the m_{T}-scaled normalisation factor. However, at intermediate p_{T}, the data points reach higher above the scaling line. The enhancement is more pronounced in central collisions, consistent with a larger radial flow due to higher multiplicity and energy density. Below 2 GeV/c, the same deviation between kaons and η meson observed in Figure 6.4 is visible here too. Again, the uncertainties are large and no definite conclusion can be reached here. Nevertheless, such a difference could be explained given the larger mass of the η meson and the influence of radial flow: the heavier particle momentum has a larger shift towards higher-p_{T} compared to the lighter one, following the mass ordering already observed in Section 1.3.3.

Comparison with results from other experiments. The results obtained in this thesis with ALICE are compared with the PHENIX results measured in Au–Au collisions at $\sqrt{s_{\mathrm{NN}}} = 200$ GeV [211], as shown in Figure 6.7. Both measurements are in agreement in the

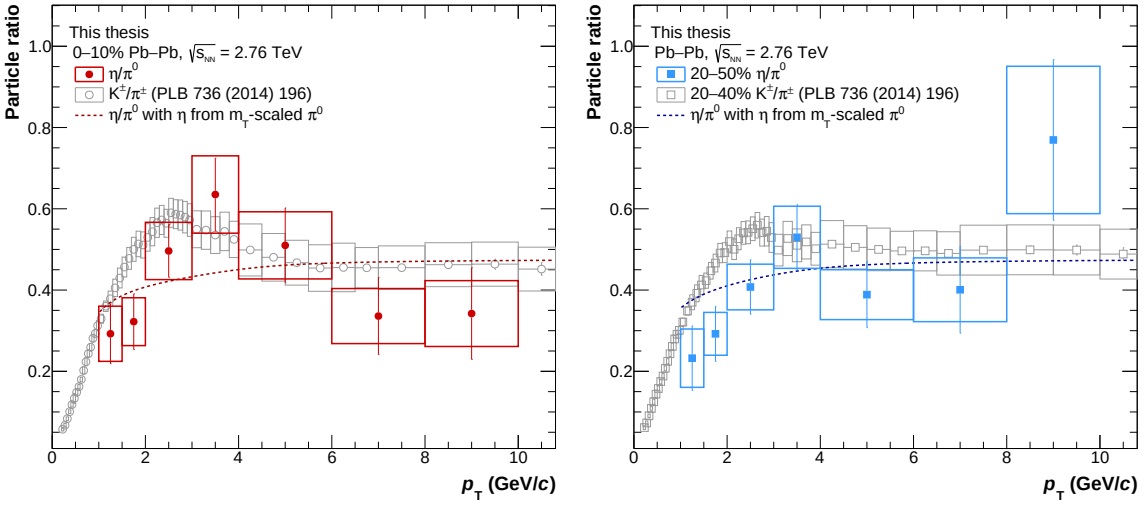

FIGURE 6.6: The η/π^0 ratio for 0–10% (left) and 20–50% (right) Pb–Pb collisions at $\sqrt{s_{\mathrm{NN}}} = 2.76$ TeV is compared to the ALICE kaon to pion ratio at the same centre-of-mass energy [204], in the centrality classes 0–10% and 20–40%, respectively. The dashed lines represent the ratio obtained using the π^0 meson measured in the respective centrality classes to m_{T}-scale the η meson spectrum.

two corresponding centrality ranges, with the ratio constant at the m_{T}-scaling factor starting at 2 GeV/c for PHENIX and at 4 GeV/c for ALICE. For the former results, the enhancement around 2-4 GeV/c observed in this thesis work for central collisions is not visible.

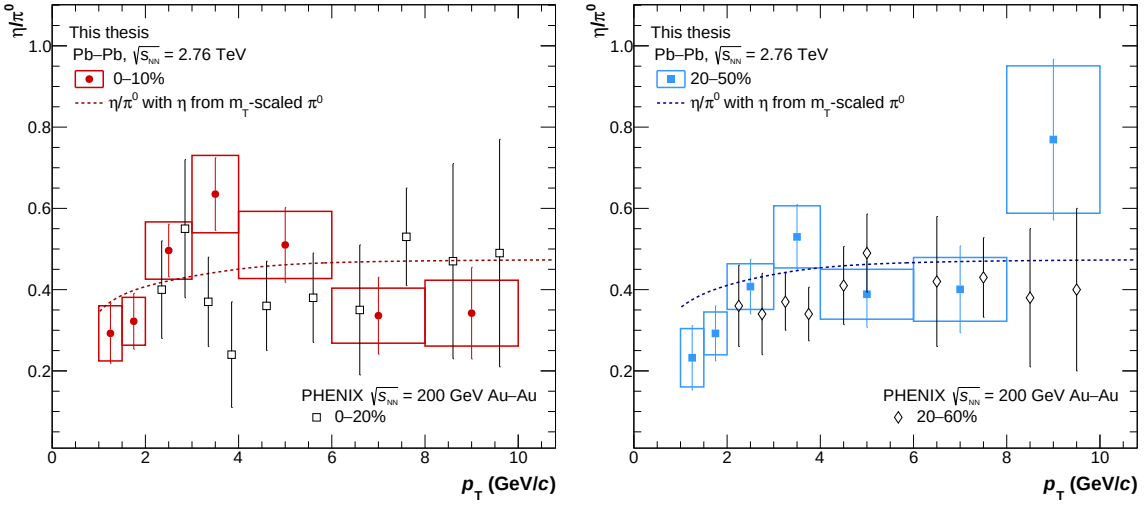

FIGURE 6.7: The η to π^0 ratio for the centrality classes measured in Pb–Pb collisions at $\sqrt{s_{\mathrm{NN}}} = 2.76$ TeV is compared to the PHENIX results from 0–20% (left) and 20–60% (right) Au–Au collisions at $\sqrt{s_{\mathrm{NN}}} = 200$ GeV [211]. The error bars for the PHENIX points represent the total uncertainty.

6.3 Neutral meson nuclear modification factor

The nuclear modification factor, R_{AA}, gives insights into the suppression of the particle spectra at high-p_{T} in heavy-ion collisions. The formula used is:

$$R_{\mathrm{AA}} = \frac{\mathrm{d}^2 N^{\mathrm{AA}}/\mathrm{d}y\mathrm{d}p_{\mathrm{T}}}{\langle T_{\mathrm{AA}} \rangle \times \mathrm{d}^2\sigma/\mathrm{d}y\mathrm{d}p_{\mathrm{T}}}, \tag{6.2}$$

where $\mathrm{d}^2 N^{\mathrm{AA}}/\mathrm{d}y\mathrm{d}p_{\mathrm{T}}$ are the differential yields in Pb–Pb, the nuclear overlap function $\langle T_{\mathrm{AA}} \rangle$ is related to the mean number of inelastic nucleon-nucleon collisions as $\langle T_{\mathrm{AA}} \rangle = \langle N_{\mathrm{coll}} \rangle / \sigma^{\mathrm{pp}}_{\mathrm{inel}}$ and $\mathrm{d}^2\sigma/\mathrm{d}y\mathrm{d}p_{\mathrm{T}}$ is the pp invariant differential cross section. The pp reference for π^0 and η is taken from [206], while T_{AA} and N_{coll} are taken from [185]. The R_{AA} is used to quantify the suppression of the high-p_{T} particles due to their energy loss in the medium. Taking the pp reference as the vacuum scenario, one expects that the absence of a strongly interacting medium returns a nuclear modification factor equal to one. This was the case for the neutral meson nuclear modification factor in p–Pb collisions [212], where the R_{pPb} is consistent with unity for $p_{\mathrm{T}} > 2$ GeV/c. Conversely, as introduced in Section 1.3.2, hadron spectra in A–A collisions display a strong suppression, whose magnitude increases with the collision centrality.

The neutral meson R_{AA} shown in this section relies on the pp reference obtained with PCM only. Given that the π^0 and η spectra measured with PCM in pp collisions do not have the same p_{T} reach as for the Pb–Pb case (a maximum of 10 GeV/c and 6 GeV/c, respectively), an extrapolation is used to cover the missing transverse momentum bins. The extrapolation is based on the fit to the meson yield measurements from [206], where the combination of PCM with the calorimeter results gives a higher reach in p_{T}. The variation of the fit range and of the fit function is used to estimate the related systematic uncertainty. In Figure 6.8, the R_{AA} for the π^0 (left) and η (right) mesons are shown for the centrality classes 0–10% and 20–50%. For both mesons, a centrality dependent suppression, expected from the parton

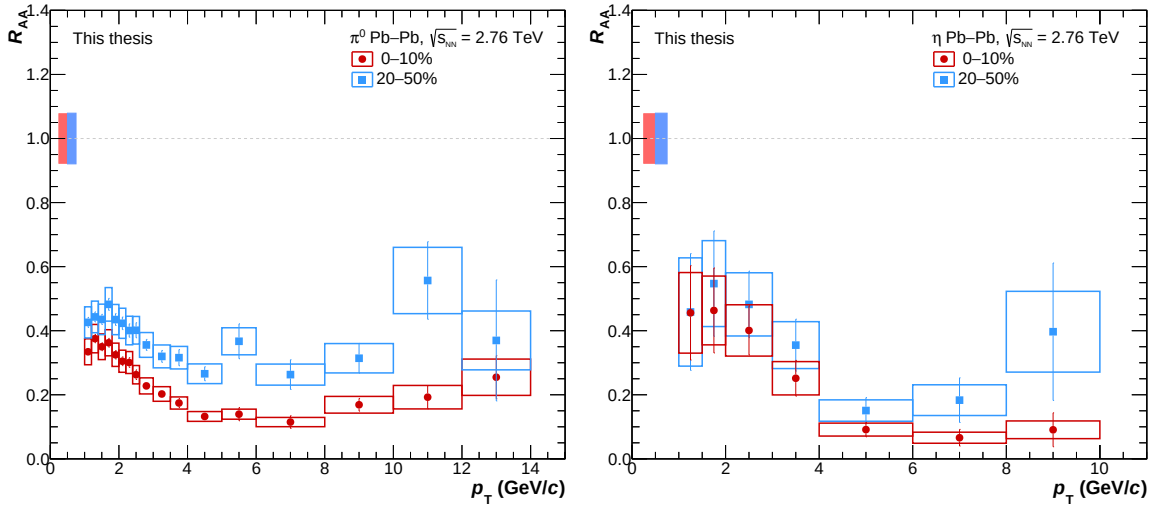

FIGURE 6.8: Nuclear modification factor for the π^0 (left) and η (right) meson in the centrality classes 0–10% and 20–50%. Statistical uncertainties are given as vertical bars, systematic uncertainties as boxes. The coloured boxes around unity reflect the uncertainty of the average nuclear overlap function (T_{AA}) and the normalisation uncertainty of the pp spectrum added in quadrature.

energy loss in the medium, can be observed. A higher energy density is reached in central collisions, inducing a larger energy loss on the partons traversing the medium [82].

Comparison to the charged pion and charged kaon R_{AA}. As for the η/π^0 ratio, the neutral meson measurements of the nuclear modification factor in Pb–Pb are compared to the charged pion and kaon R_{AA} at the same centre-of-mass energy, in Figure 6.9. The expectation that neutral and the respective charged particles must behave similarly is confirmed here: the data points fall on top of each other and agree within the uncertainties.

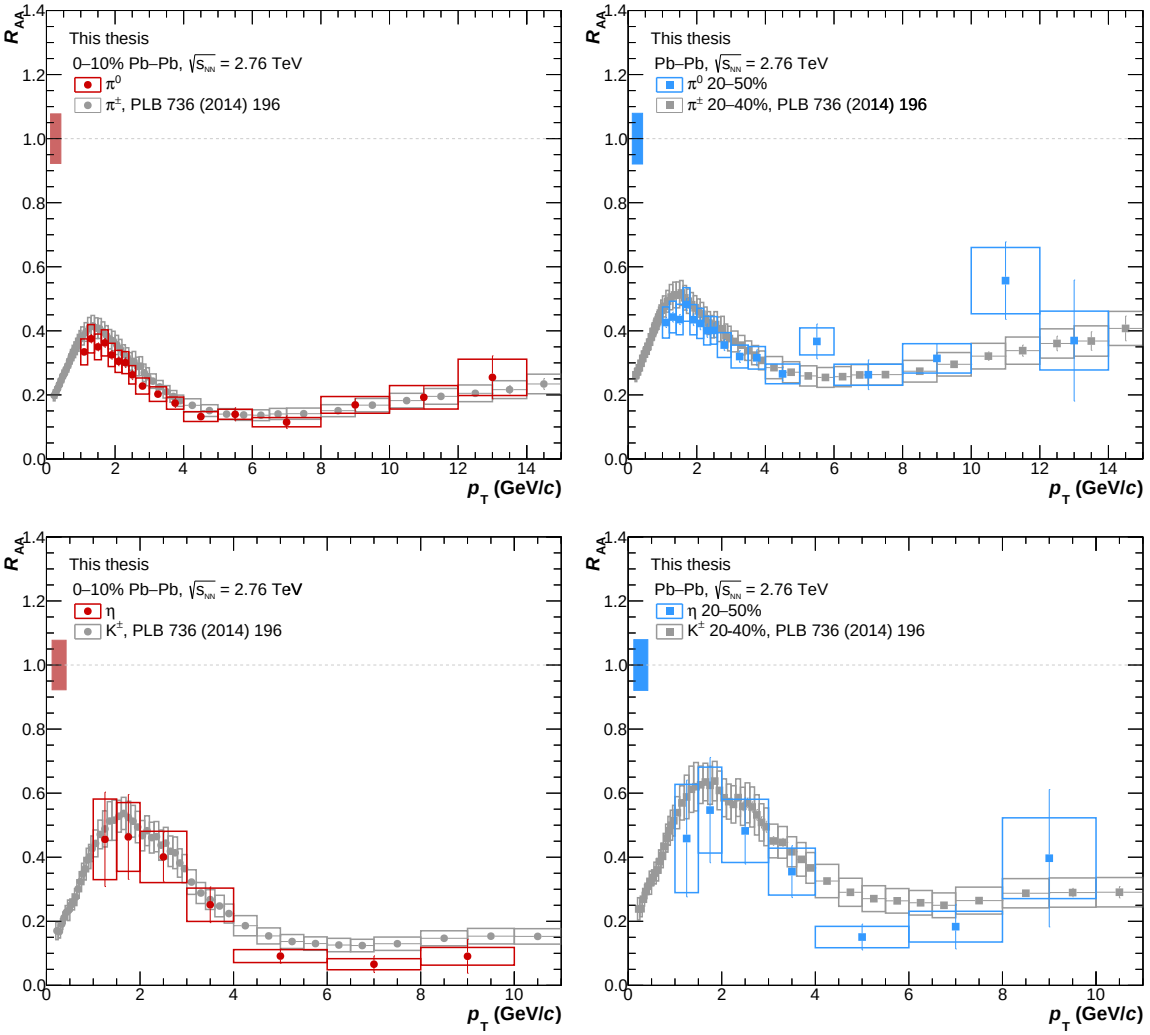

FIGURE 6.9: Nuclear modification factor for the π^0 (top row) and η (bottom row) meson in the centrality classes 0–10% (left) and 20–50% (right), compared to the charged pion and kaon R_{AA}, respectively, in the same centrality classes, both measured in Pb–Pb collisions at $\sqrt{s_{\mathrm{NN}}} = 2.76$ TeV [204].

Comparison with results from other experiments. Figure 6.10 compiles a summary of the available π^0 R_{AA} results in Pb–Pb collisions at $\sqrt{s_{\mathrm{NN}}} = 2.76$ TeV (this thesis) and from measurements at lower energies, from the CERN SPS [93] and RHIC [91, 92]. This figure is derived from Figure 1.12, right, where the ALICE data points have been substituted with the newer ones from this work. As it was commented in Section 1.3.2, the "turn on" of the suppression is clearly visible going from lower to higher centre-of-mass energies. However, the higher statistics of the data sample used in this work shows that at high-p_{T} the suppression

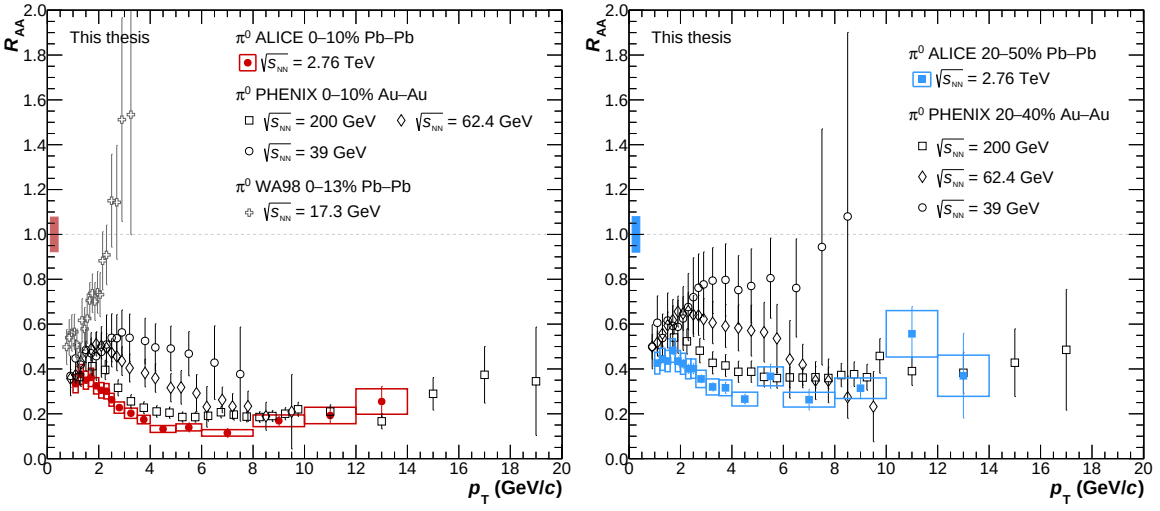

FIGURE 6.10: Neutral pion nuclear modification factor R_{AA} in Pb–Pb collisions at $\sqrt{s_{\mathrm{NN}}}$ for the 010% (left) and 20–50% (right) centrality classes is compared to the results from colliders at lower energies: from Au–Au collisions at $\sqrt{s_{\mathrm{NN}}} = 39$, 62.4 [91], and 200 GeV [92] at RHIC and, for 0–10% only, the result from the CERN SPS [93] are shown.

gets smaller, hinting to a change of the underlying energy loss mechanisms where the hot medium effects vanish in favour of a pure parton radiative energy loss mechanism [213]. In Figure 6.11, an analogous comparison for the η meson is shown, with the η R_{AA} measured at RHIC [211]. The lack of results from other energies for this meson and the fewer data points for the ALICE measurement do not give the same broad overview as it is the case for the neutral pion. However, it can still be observed that the ALICE points are consistently below the PHENIX data, following the energy dependent scaling of the suppression.

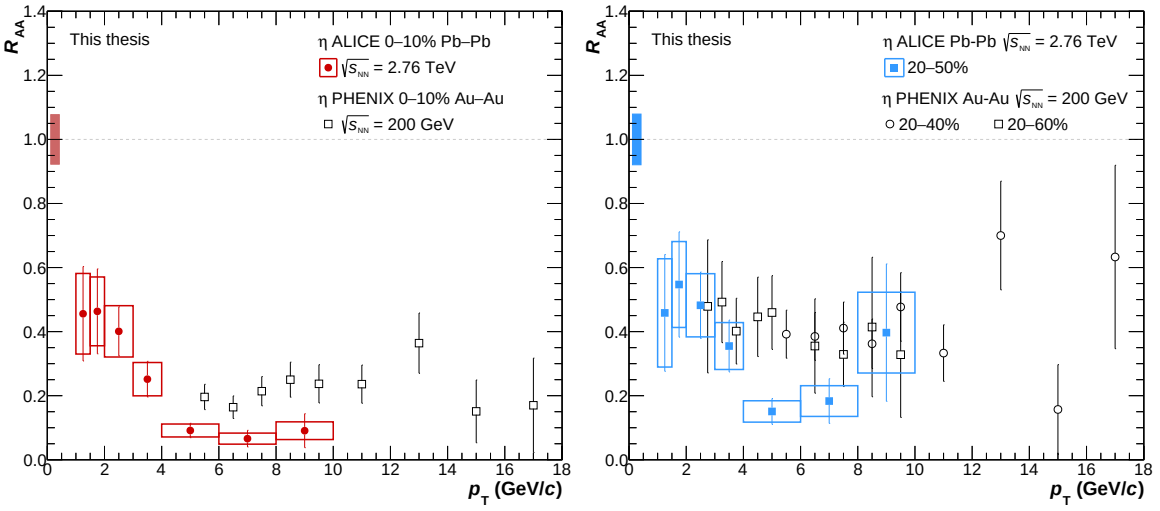

FIGURE 6.11: Nuclear modification factor R_{AA} of the η meson in Pb–Pb collisions at $\sqrt{s_{\mathrm{NN}}} = 2.76$ TeV for the centrality classes 0–10% (left) and 20–50% (right), compared to results from Au–Au collisions at $\sqrt{s_{\mathrm{NN}}} = 200$ GeV measured at RHIC [211].

These comparisons have been repeated with the combined PCM, PHOS and EMCal measurements, introduced in the next section. The higher p_{T} reach of the combined measurement confirms the conclusions reached here (the figures are reported in Appendix D).

6.4 Combined PCM, PHOS and EMCal analysis

Neutral mesons are also measured in ALICE with the two electromagnetic calorimeters, PHOS and EMCal. While the analysis of the 2011 Pb–Pb data was not pursued with the PHOS calorimeter, it was completed using the EMCal for minimum bias events. The neutral meson analyses using PHOS or EMCal alone are not part of this thesis work. More details on both can be found in [90, 214].
The p_{T} range of the PCM π^0 meson goes from 1 to 14 GeV/c, while the EMCal π^0 measurement extends from 4 to 20 GeV/c. Moreover, as it is already published in [90], the π^0 measurement obtained from the 2010 Pb–Pb data with the PHOS calorimeter is also included, further reducing the π^0 total uncertainties. This addition is valid only for the π^0 spectrum and R_{AA} in the centrality class 0–10%, since this is the only centrality class common to all three methods. The 2010 PCM π^0 meson measurement is not included because it is consistent with the 2011 measurement and has larger statistical uncertainties, as shown in Figure 6.2. Similarly to the π^0, the η meson measurements from PCM and EMCal are combined, while no η meson measurement exists for the PHOS calorimeter. The p_{T} reach in this case is 1–10 GeV/c and 4–20 GeV/c for PCM and EMCal, respectively. The transverse momentum ranges for the neutral meson combined analysis are summarised in Table 6.1.

	π^0			η	
	PCM	EMCal	PHOS	PCM	EMCal
0–10%	1 – 14 GeV/c	4 – 20 GeV/c	1 – 12 GeV/c	1 – 10 GeV/c	4 – 20 GeV/c
20–50%	1 – 14 GeV/c	4 – 20 GeV/c	–	1 – 10 GeV/c	4 – 20 GeV/c

TABLE 6.1: Transverse momentum ranges for the π^0 and η meson measurement. The combination is between PCM and EMCal for the η meson in both centralities and for the π^0 in the centrality class 20–50%. For π^0 in 0–10%, the combination is done among PCM, EMCal as well as previously published results using the PHOS detector [90].

The invariant yields, the η/π^0 ratio, the R_{AA} of the combined PCM and EMCal analysis are computed separately for each of the methods. In particular, the choice of combining the ratios instead of calculating them with the combined spectra is driven by the possibility of cancelling the common errors in the respective analysis, reducing the systematic uncertainties. The results of the different methods are combined in the common p_{T} region with a weighted average, where the weights are given by the statistical and systematic errors [9]. The formula used for the combination is

$$\bar{x} \pm \delta\bar{x} = \frac{\sum_i w_i x_i}{\sum_i w_i} \pm \left(\sum_i w_i\right)^{-1/2}, \tag{6.3}$$

where $w_i = 1/(\delta x_i)^2$ is the weight associated to the value x_i of error δx_i of the ith measurement (PCM, EMCal or PHOS), all summed over the total number of measurements.
The combined neutral meson invariant yields are plotted together for the centrality classes 0–10% and 20–50% in Figure 6.12. The black dashed line indicates the fit to the data using the two-component model (TCM) proposed by A.A. Bylinkin and A.A. Rostovtsev [215, 216]:

$$E\frac{\mathrm{d}^3N}{\mathrm{d}p^3} = A_e \exp\left(-\frac{\sqrt{p_{\mathrm{T}}^2 + M^2} - M}{T_e}\right) + \frac{A}{\left(1 + \frac{p_{\mathrm{T}}^2}{T^2 n}\right)^n} \tag{6.4}$$

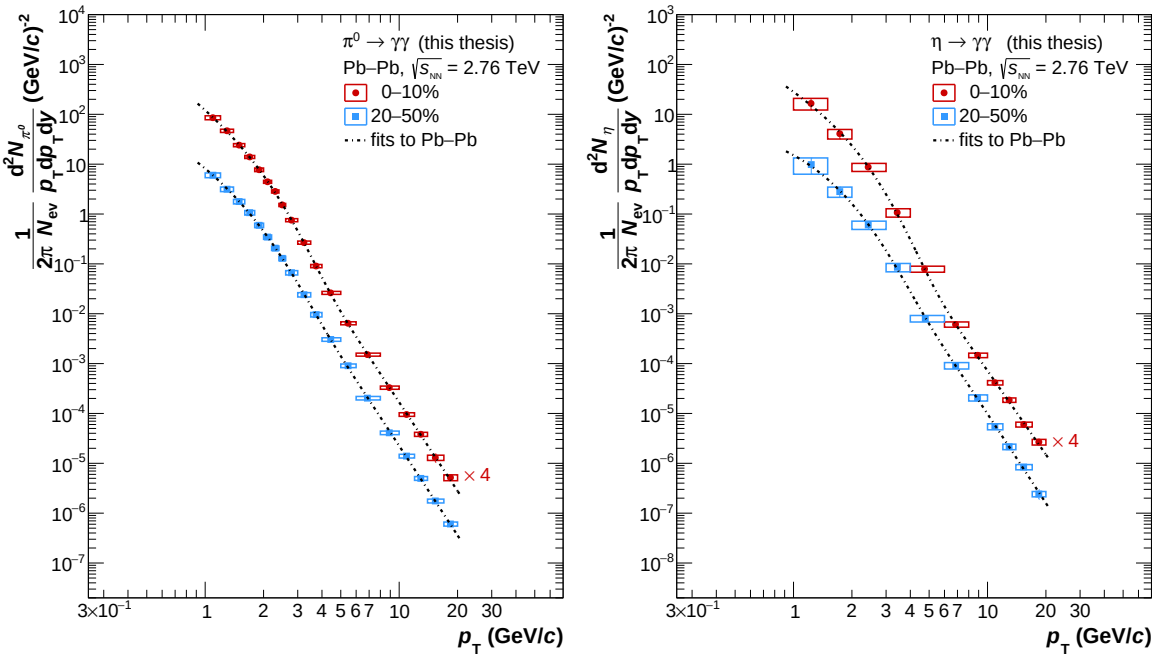

FIGURE 6.12: Differential invariant yields of the π^0 (left) and η (right) meson in the centrality classes 0–10% and 20–50% from the combined PCM, PHOS (for the π^0 0–10% only) and EMCal analysis. The dashed black lines correspond to the fits to the data with the Bylinkin-Rostovtsev two-component model from Equation 6.4.

where A_e and A are the normalisation factors (in GeV$^{-2}c^3$), T_e and T (in GeV) are temperature-like parameters, n is the power-law order and M the meson mass (in GeV/c^2). The parameters extracted from the fit to the combined spectra are reported in Table 6.2. To ensure the convergence of the fits, the normalisation parameter A is fixed to a value resulting from a systematic study of the parameters of the two separate components of the TCM function and their variation within different constraining values.

	π^0		η	
	0–10%	20–50%	0–10%	20–50%
A_e (GeV$^{-2}c^3$)	170 ± 21	34 ± 7	15.6 ± 5.4	4.0 ± 2.5
T_e (GeV)	0.37 ± 0.01	0.38 ± 0.02	0.43 ± 0.03	0.42 ± 0.06
A (GeV$^{-2}c^3$)	840 fixed	80 fixed	100 fixed	2 fixed
T (GeV)	0.34 ± 0.01	0.47 ± 0.01	0.37 ± 0.03	0.76 ± 0.05
n	3.00 ± 0.05	3.00 ± 0.05	2.7 ± 0.1	3.0 ± 0.1

TABLE 6.2: Parameters of the fits to the differential invariant yields of π^0 and η mesons from the combined PCM, PHOS (for the π^0 0–10% only) and EMCal analysis, using the Bylinkin-Rostovtsev two-component function from Equation 6.4.

Figure 6.13 shows the ratio of the spectrum for each individual method over the fit of the combined spectrum for the π^0 (left) and η (right) meson in the centrality class 0–10% (top panels) and 20–50% (bottom panels). The fit to the combined spectrum is also used for the bin-shift correction of the steeply falling spectrum, applied to the individual measurements to set the data point at the true yield value in each p_T-bin, introduced in Section 5.3.3.4. Appendix D contains a compilation of figures showing the separate PCM, PHOS and EMCal results prior combination, as well as the final combined results. The same physical conclusions reached for the PCM only measurements in Section 6.1, Section 6.2 and Section 6.3 are

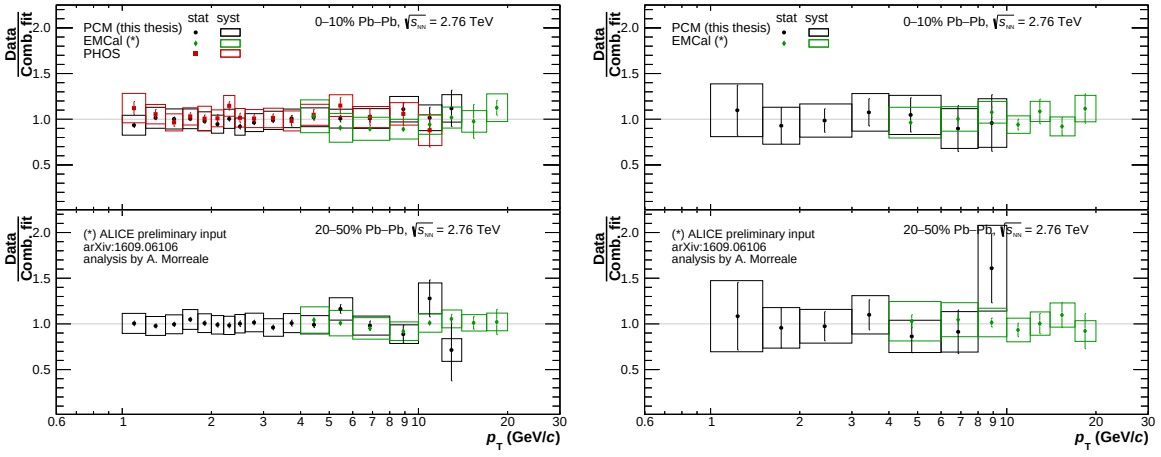

FIGURE 6.13: Ratio of the spectrum of the individual measurements to the fit of the combined spectrum for the π^0 (left) and η (right) meson in 0–10% (top panels) and 20–50% (bottom panels) Pb–Pb collisions. The EMCal measurement is the input of a ALICE preliminary results [214]. The statistical uncertainties are represented by the vertical bars, the systematic uncertainties by the boxes, as also noted in the legend.

valid also for the combined results. The inclusion of the combined results has been considered helpful within this thesis work, given the higher p_{T} reach and smaller uncertainties of the measurement.

6.5 Comparison of the results with models

In the following paragraphs, the combined PCM and EMCal (and PHOS, when available) measurements will be compared to the latest theoretical predictions.

Invariant yield of the π^0 and η meson

Figure 6.14 shows the comparison of the π^0 and η meson spectra to a (non)equilibrium statistical hadronisation model, (N)EQ SHM [217, 218], and to the EPOS2 event generator [219]. Both versions of the statistical hadronisation model (SHM), the equilibrium and the non-equilibrium one, focus on the low-p_{T} region (below 3 GeV/c). The two predictions are based on the Cracow single-freeze-out model [220], which assumes a simultaneous chemical and kinetic freeze-out (no rescattering after freeze-out) and adopts a hydrodynamical description with longitudinal and transverse flow. The feed-down from resonance decays is also properly integrated. The (N)EQ model uses the single-freeze-out model that is implemented in THERMINATOR, a Monte Carlo event generator for particle production in heavy-ion collisions following the thermal model description [221]. The thermodynamic parameters (temperature, quark occupancy, etc.) are taken from [222, 223]. The NEQ model differs from the EQ one for the quark phase-space occupancy, which is larger than unity. This entails a lower temperature and/or a smaller volume of the system. Two other parameters are also considered: the transverse size, r_{max}, and the invariant time of the freeze-out, τ_f. These are extracted from the fit to the measured charged pion and kaon spectra.
The equilibrium model gives a good description of the charged pion, kaon and proton results from RHIC, as shown in [220]. This is not the case for the LHC data. An enhancement of the pion spectra for $p_{\mathrm{T}} < 0.3$ GeV/c is observed with respect to the model, while the

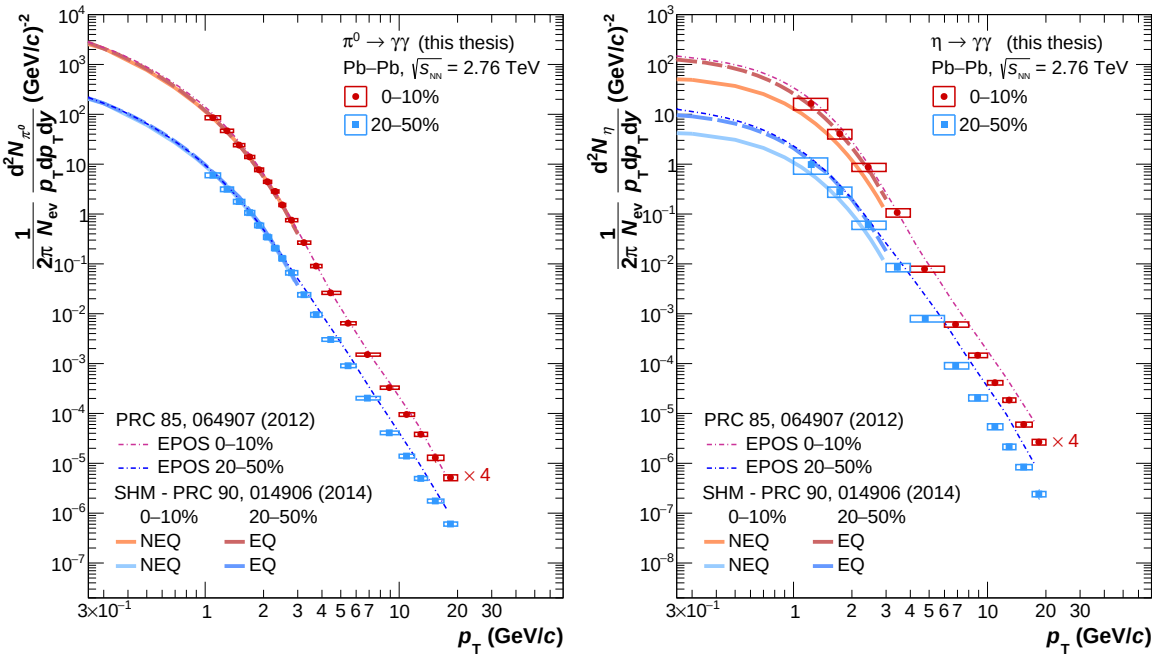

FIGURE 6.14: Combined PCM and EMCal differential invariant yields for the π^0 (left) and η (right) meson for the centrality classes 0–10% and 20–50% in Pb–Pb collisions at $\sqrt{s_{\rm NN}}$ = 2.76 TeV compared to the EQ SHM [218], NEQ SHM [217] and EPOS2 [219] predictions for the respective centralities.

proton-antiproton yields are lower than expected, anomaly also present in the comparison to other statistical models. Conversely, the non-equilibrium model successfully describes not only the pion and kaon but also the proton spectrum, even if the latter is excluded from the fitting procedure. The NEQ model shows good agreement also with strange particles such as K^0_S, $K^*(892)^0$ and ϕ [224].

EPOS2 is an event generator that aims at having a full description of the event and particle production, from soft to hard regime, in order to have generated events as similar as possible to real experimental events. To do so, the soft processes and jets are treated together, controlling the underlying event. A hydrodynamic evolution is also implemented.

EPOS2 has a multiple scattering approach that relies both on the Gribov-Regge theory and on pQCD. A hard scattering is accompanied by the emission of off-shell partons (initial state space-like cascade), each of which will give further parton emission (final state time-like cascade). This is referred to as a single, elementary object called parton ladder. The multiple scattering is thus interpreted as the exchange of several parton ladders in parallel. In the final state, parton ladders are identified with flux tubes and particle production is described by the Lund String Model [225]. Once the strings are broken, they will contribute either to the bulk matter, which will evolve hydrodynamically, or to the jets. Depending on the string position in the medium and on its energy loss, a different classification is done. One can assign strings to the bulk matter if they are produced far from the surface and if they have energy loss larger than their total energy ($\Delta E \geq E$, for details see [219] and references therein). If the string is produced outside of the matter and outside of the hadronisation surface, its segment will escape untouched (hadron jets). Lastly, if the string is produced inside the matter but it still has energy large enough to escape, it will form a hadron jet but its properties will be modified by the interaction with the flowing matter, *e.g.* the string breaking will involve also quark and anti-quark of the fluid, thus carrying a certain flow velocity. The end result

is a prediction extending from low-p_{T} up to about 20 GeV/c, where the particle production at low-p_{T} is driven by hydrodynamics while hard scatterings are dominating at high-p_{T}. The comparison of the ratios of data and theoretical predictions to the data fit, shown in Figure 6.15, gives a clearer image of the agreement of the different theory models with the neutral mesons results. The EQ and NEQ SHM models, indicated with the cyan and green line respectively, show a similar, overall good agreement with the π^0 points in both centralities, with a slight overestimation of the π^0 meson yields at low-p_{T} in semi-central collisions. Analogous behaviour can be observed for the EQ SHM comparison to the η meson. Surprisingly though, in this case, the NEQ SHM prediction underestimates the yields by about 2.5 and 1.5σ in the 0–10% and 20–50% central class, respectively. Several iterations with the theory colleagues seem to suggest it could be attributed to an earlier freeze-out for the η meson, being a heavier particle, also considering that the model reproduces well the charged kaon yields. In addition to the η meson, the ρ^0, $\Sigma(1385)$, $\Lambda(1520)$ and $\Xi(1530)$ predictions for this model also show significantly different results in the two versions [218]. The EPOS2 prediction, lilac dashed line in the figure, agrees with the π^0 meson data in the low and intermediate p_{T} region for central collisions and at low-p_{T} for semi-central collisions. However, it overestimates the yields above 4 GeV/c in both centralities, even if by a different magnitude. The agreement between the η meson yields and EPOS2 is partial at low and intermediate p_{T}, but the data is by far overestimated above 4 (3) GeV/c in central (semi-central) collisions. Also in the case of this model prediction, the divergence between η meson data and theory has been widely discussed. It is understood that the wave function assumed for the η meson is a simplification, and a better prediction could be delivered with a more sophisticated treatment.

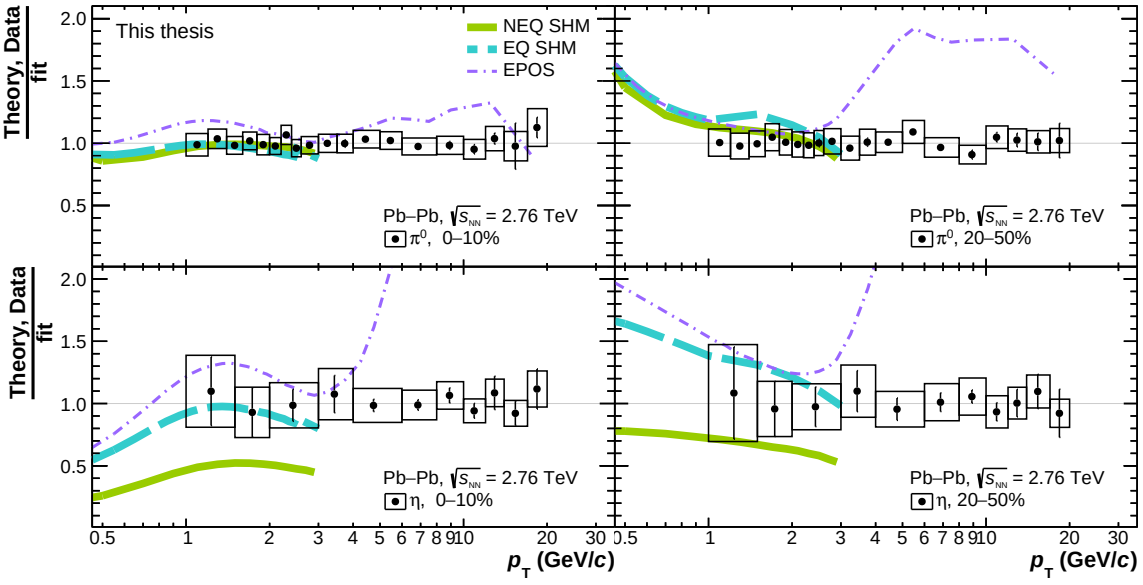

FIGURE 6.15: Ratio of the combined PCM and EMCal differential invariant yields to their fit for the π^0 (top row) and η (bottom row) meson for the centrality classes 0–10% (left panels) and 20–50% (right panels) in Pb–Pb collisions at $\sqrt{s_{\mathrm{NN}}} = 2.76$ TeV compared to the ratio of the EQ SHM [218], NEQ SHM [217] and EPOS2 [219] predictions to the same fit, for the respective centralities.

η/π^0 ratio

In Figure 6.16 the combined PCM and EMCal η/π^0 ratio is compared to the EQ SHM [218],

NEQ SHM [217] and EPOS2 [219] predictions, introduced in the previous section, and to the DCZW pQCD [226] calculation. The NLO pQCD calculation of DCZW focuses on the η meson production at large p_{T} and in high energy environment (RHIC and LHC). It is assumed that the parent parton undergoes multiple scatterings in the QCD matter, losing energy via gluon emission before hadronisation (higher-twist approach). The parton energy loss and the modifications it induces in the parton fragmentation functions (FFs) will depend on the jet transport parameter, which characterises the medium properties. The FFs for π^0 and η meson adopted are the AKK [227, 228] and AESSS [229], respectively, while EPS09 [230] is taken as NLO nuclear PDF. The medium evolution is then treated with an ideal hydrodynamics description. With the initial time of the QGP medium fixed at $\tau_0 = 0.6$ fm, the only parameter left free to vary is the initial value of the jet transport parameter, $\hat{q}_0$. The strength of the jet-medium interaction is directly proportional to $\hat{q}_0$. The higher-twist approach together with NLO pQCD is used to describe the π^0 and η meson production both in pp and A–A collisions.

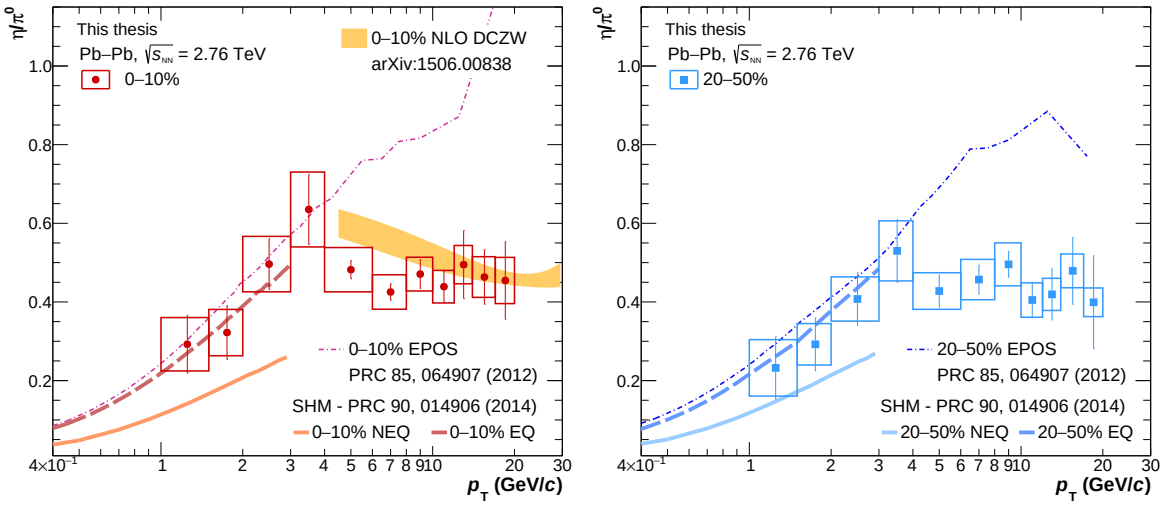

FIGURE 6.16: Comparison of the combined PCM and EMCal η/π^0 ratio for the centrality classes 0–10% (left) and 20–50% (right) in Pb–Pb collisions at $\sqrt{s_{\mathrm{NN}}} = 2.76$ TeV to the EQ SHM, NEQ SHM [217], EPOS2 [219] and pQCD DCZW [226] theory calculations.

From Figure 6.15, it is clear that the conclusions reached regarding the comparison of the (N)EQ SHM and EPOS2 predictions to the η meson spectra can be repeated here. While EQ SHM gives a good description of the η/π^0 ratio, NEQ SHM underestimates it by about 2.5σ. EPOS2 describes the data in both centralities at low-p_{T}, but largely overestimates them above 3–4 GeV/c. DCZW provides their calculation only for the 0–10% centrality class. The flavour dependent energy loss (jet quenching) will lead to a stronger suppression for gluons than for quarks and this suppression is stronger for the π^0 than for the η meson. The final effect is an enhancement of the η/π^0 at intermediate p_{T}. These conclusions are in agreement with the experimental data, even though the enhancement seems to be slightly overestimated. In particular, in the region from 4 to 10 GeV/c, the ratio is especially sensitive to $\hat{q}_0$, as it can be observed in Figure 5 of [226]. The values of $\hat{q}_0$ assumed for the calculation shown here are $\hat{q}_0 = 2.2 \pm 0.4$ GeV^2/fm. Therefore, given the comparison to the data points, smaller values of $\hat{q}_0$ seem to be favoured.

Nuclear modification factor of the π^0 and η mesons

The NLO pQCD calculation by DCZW is compared to the nuclear modification factor of the π^0 and η meson, together with the predictions from the WHDG model [231–233] and the Djordjevic *et al.* model [234–236].

The WHDG model includes elastic and inelastic parton energy loss and jet path length fluctuations into the standard treatment of jet quenching with pQCD. In particular, the combination of elastic and path length fluctuations gives a more realistic geometric description. Already for a fixed value of path length they observe that the inclusion of the elastic energy loss increases the quenching for every flavour and that highly quenched gluons reduce the pion R_{AA}. These observations are confirmed when considering path length fluctuations. This effect is explained by the difference between the elastic and inelastic energy loss fluctuations. The latter are dependent on the number of gluons radiated, whose fluctuations lead to significant modification of the radiative energy loss. On the other end, elastic energy loss fluctuations depend on the number of collisions, whose fluctuations are small if compared with the path length considered, thus not influencing the nuclear modification factor suppression as much as the inelastic energy loss.

The prediction by Djordjevic *et al.* has basic assumptions similar to those of the WHDG model. A generic pQCD approach is used for the quenching description and path length fluctuations are taken into account in the calculations. In addition, radiative and collisional energy loss are treated separately, given the assumption that the amount of energy lost is small (soft-gluon approximation), and the running of the coupling constant is also factorised separately. Furthermore, the jet to hadron fragmentation functions [237] are taken to be the same in Pb–Pb and e^+e^- collisions, assuming the presence of a deconfined QCD medium. In [236], the resulting calculations are compared to several independent nuclear modification measurements from ALICE, showing good agreement in all of them and giving confirmation of the reliability of the theoretical framework.

Figure 6.17, left, shows the comparison of the NLO DCZW, WHDG and Djordjevic predictions to the nuclear modification factor of the π^0 meson in 0–10% and 20–50% centrality class.

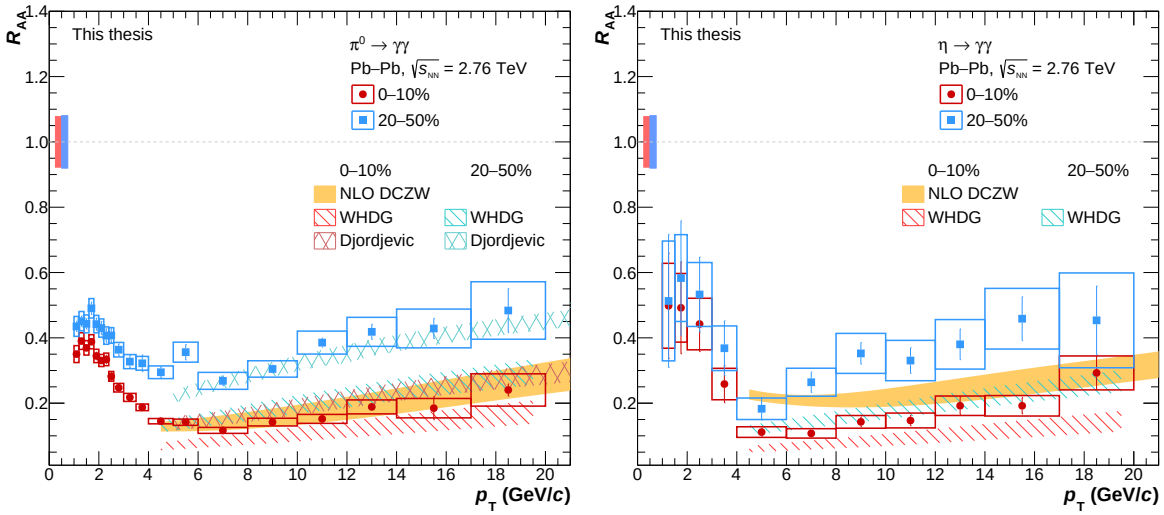

FIGURE 6.17: Comparison of the combined PCM, PHOS (only for the π^0 in 0–10%) and EMCal R_{AA} for the π^0 (left) and η (right) meson in the centrality classes 0–10% and 20–50% in Pb–Pb collisions at $\sqrt{s_{\mathrm{NN}}}$ = 2.76 TeV to the NLO pQCD calculation by DCZW [226], WHDG [231–233] and Djordjevic *et al.* [234–236] (only for the π^0 in 0–10%) predictions.

It can be observed that the NLO DCZW model shows a good agreement with the most central result over all the transverse momentum range. The WHDG and Djordjevic predictions, instead, are respectively overestimating and underestimating the suppression of the π^0 meson R_{AA} by about 1σ. On the other end, the Djordjevic model predicts the right amount of suppression for the R_{AA} in 20–50%, while in the WHDG model the quenching is strongly overestimated ($\sim 4\sigma$).
Similar observations can be done for the comparison to the η meson R_{AA}, in Figure 6.17, right. The WHDG model predicts an R_{AA} suppression stronger than observed in data for both centralities (3σ and 2σ in 0–10% and 20–50%, respectively). The NLO pQCD calculation by DCZW overlaps with the experimental data only above 12 GeV/c. The expectation of a smaller suppression of the η meson R_{AA} is in agreement with the conclusions reached for the comparison of this same model to the η/π^0 ratio results, where the enhancement at intermediate p_{T} is also overestimated. In Figure 6.17 it emerges that the calculation for the η meson is at the origin of the discrepancy. This measurement could help improve the DCZW model, since its calculations are based on fragmentation functions that are little constrained for the η meson.

Chapter 7

Cocktail simulation

The photons coming from particle decays constitute the largest background for the direct photon measurement. A Monte Carlo simulation called "cocktail" is employed to quantify which fraction of the total measured photon yield is due to decays, basing this estimation on the yields of hadrons which decay in one or more photons. In this chapter, the steps for the production of a cocktail will be described.

7.1 Input parametrisations for the cocktail simulation

In Section 1.3.6.2 the main sources of decay photons are described. The MC simulation from which the decay photon spectrum is estimated is called "cocktail simulation". The particles of interest are generated flat in p_{T}, rapidity and azimuthal angle and are then decayed using the PYTHIA6 decayer and according to the stored branching ratios, listed fully in Table E.1. When available, the measured yields of decay photon sources are parametrised and the parametrisations are used to properly weight the generated p_{T} distribution. When measured yields are not available, the m_{T}-scaling approximation is used to estimate the yields of the missing particle, taking as reference the π^0 or the proton in the case of a meson or a baryon, respectively. Being an approximation, the m_{T}-scaling approach is subject to biases, since it has been observed it is slightly violated below 2 GeV/c.
In an effort to generalise the cocktail simulation and make it available to all the ALICE analyses requiring it (direct photons, dileptons and electrons from heavy flavour decays), measured particle spectra, particle ratios and their parametrisations have been collected in a common framework. Part of this thesis work is the documentation and the parametrisation of the existing ALICE measurements of decay photon sources for Pb–Pb collisions at $\sqrt{s_{\mathrm{NN}}} = 2.76$ TeV. These particles are: π^0, η, $\pi^{\pm}$ and $\mathrm{K}^{\pm}$ (not used for the photon decays but as placeholder or cross-check for π^0 and η), protons (for the baryons m_{T}-scaling), ϕ, ρ^0, K^0_{S} and Λ. Figure 7.1 illustrates the particle spectra and ratio measurements that are available for the centrality class 0–10%. The collected inputs are converted, when needed, in yields ($\mathrm{d}^2N/\mathrm{d}p_{\mathrm{T}}\mathrm{d}y$) and fitted separately for the available analysis methods and for each centrality class. Even though for the interest of this section the focus will be on the centrality classes 0–10%, 20–40% and 20–50%, the input spectra are available also in 0–5%, 5–10%, 10–20%, 40–60% and 60–80%.

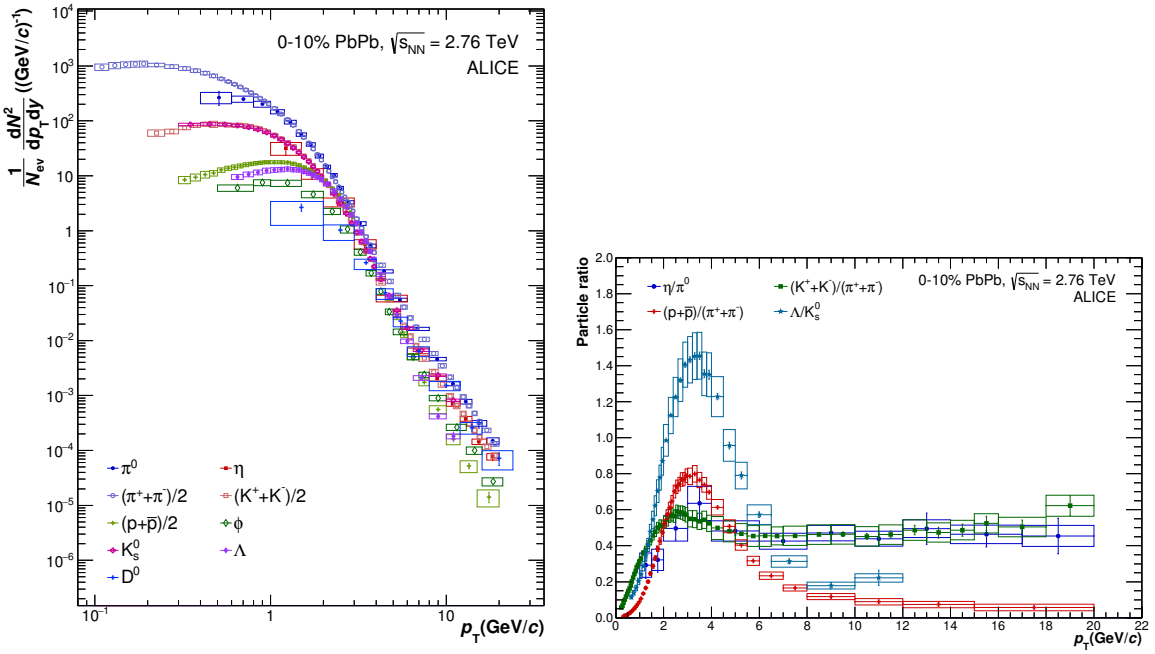

FIGURE 7.1: Collection of the available measurements for the production of the cocktail simulation input parametrisations in the centrality class 0–10% [90, 204, 238, 239].

The two largest contributions to the decay photon spectrum, π^0 and η mesons, are studied in the first part of this thesis with PCM. For the same particles, the measurements with PHOS and EMCal, separate and combined, are also included. The results for the remaining particles are provided by other ALICE measurements, summarised in Table 7.1 for the relevant centralities. Moreover, K^0_S and Λ are also reported here because they are produced in the same environment, to provide the reference for the secondary photons (Section 8.2.2) and secondary pion (Section 5.3.3.2) correction. The full list of particles with photon decays used as sources in the cocktail simulation can be found in Table E.1.

Particle	Centrality			Ref.
	0–10%	20–40%	20–50%	
π^0	✓(PCM, EMCal, PHOS)	✓(PCM, PHOS)	✓(PCM, EMCal)	this thesis, [214], [90]
η	✓(PCM, EMCal)	✓(PCM)	✓(PCM, EMCal)	this thesis, [214]
η/π^0	✓(PCM, EMCal)	✓(PCM)	✓(PCM, EMCal)	this thesis, [214]
ϕ	✓	✓	–	[238]
K^0_S	✓	✓	–	[239]
Λ	✓	✓	–	[239]
K^0_S/Λ	✓	✓	–	[239]
ρ^0	–	✓	–	–
p	✓	✓	–	[204]

TABLE 7.1: List of the available measurements for the production of the cocktail simulation input parametrisations. The check-mark in the centrality column indicates available measurements. The missing references are due to unpublished results.

Given the variety of transverse momentum ranges and shapes of the particle spectra (and ratios), no unique functional form has been found that could fit all the measurements at the

same time. However, a satisfying fit of most of the particle yields is given by the function [240]

$$f(p_{\mathrm{T}}) = N_0 \frac{\sqrt{p_{\mathrm{T}}^2 + M^2} - p_{\mathrm{T}} \cdot \beta}{\sqrt{1-\beta^2}} \exp\left(\frac{p_{\mathrm{T}} \cdot \beta - \sqrt{p_{\mathrm{T}}^2 + M^2}}{\sqrt{1-\beta^2} \cdot T_{kin}}\right) + N_1 \left(\frac{a}{1+p_{\mathrm{T}}}\right)^{n_1} + N_2 \left(\frac{b}{1+p_{\mathrm{T}}}\right)^{n_2} \tag{7.1}$$

where N_0, N_1 and N_2 are normalisation factors, M is the particle mass (in GeV/c^2), β the flow velocity, p_{T} the transverse momentum (in GeV/c), T_{kin} the kinetic freeze-out temperature (in GeV) while a, n_1, b and n_2 are the parameters of the two Hagedorn functions which constitute the second and third term of this function. The spectrum described by the first term corresponds to an emitting source moving with velocity β towards the detector (similarly to the Blast-Wave function described in Section 1.3.3). The combination of a soft term, the first, with two hard scattering terms, second and third, is responsible for the flexibility of this function and allows for fitting with equally good results particles with different mass and spanning a large p_{T} range (from 0.3 GeV/c up to 21 GeV/c), where the underlying physics changes with increasing p_{T}. In Figure 7.2, an example of the parametrisations of π^0 and η for the combined measurement with Equation 7.1 is shown for 0–10% Pb–Pb collisions.

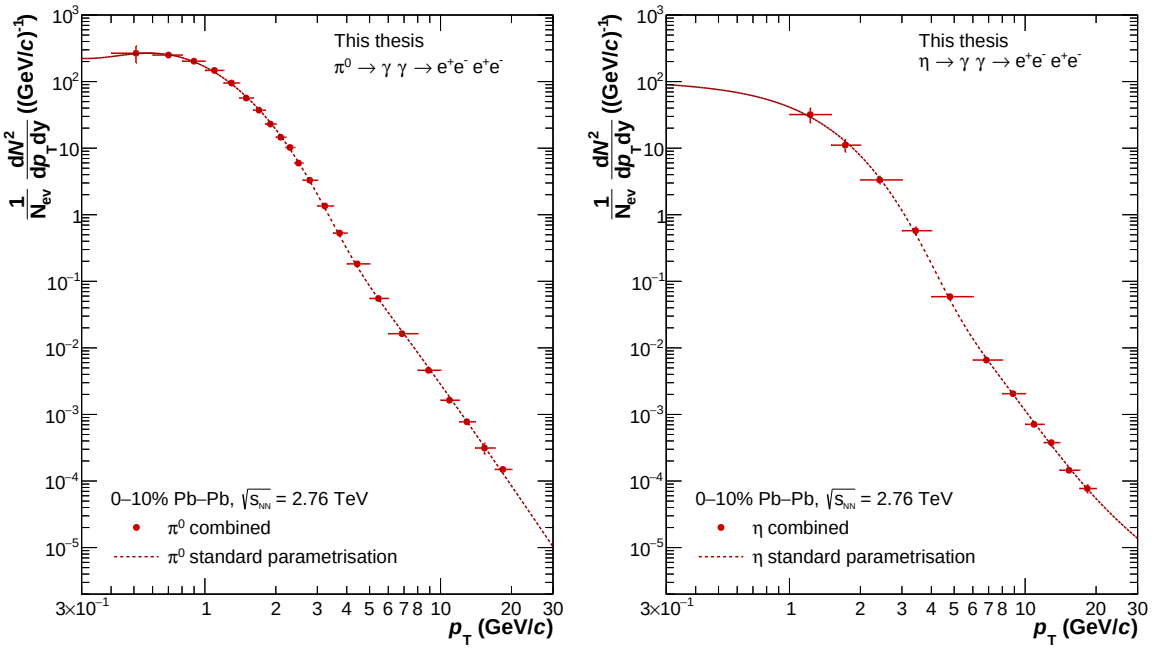

FIGURE 7.2: Combined π^0 (left) and η (right) meson yields for 0–10% Pb–Pb collisions fitted with the function given in Equation 7.1.

For the spectra where the use of Equation 7.1 does not give an optimal result, a modified version of the Hagedorn function, used by PHENIX in Au–Au collisions [241], is adopted:

$$f(p_{\mathrm{T}}) = A\left(\exp\left(-(ap_{\mathrm{T}} + bp_{\mathrm{T}}^2)\right) + \frac{p_{\mathrm{T}}}{p_0}\right)^{-n}, \tag{7.2}$$

where A (in GeV/c) is the normalisation factor and n the power-law order. The parameters a and b are in $(\mathrm{GeV}/c)^{-1}$ and $(\mathrm{GeV}/c)^{-2}$, respectively, and p_0 in GeV/c.
The fit used to parametrise the particle ratios is typically given by the ratio of the two functions used to fit the respective spectra, Hagedorn or a soft and hard scattering combined function, like a simplified version of Equation 7.1.

The fits are varied in order to estimate the related systematic uncertainty. The standard parametrisation is shifted with a linear or second order polynomial, within the yield systematic uncertainty and depending on p_{T}. A cocktail simulation is produced for each parametrisation set, one standard simulation, that will be used to estimate the decay photon spectrum, and four more to estimate the systematic uncertainty: two types of shift in the upward and downward direction with respect to the positive and negative systematic error.

7.2 Output of the cocktail simulation

Figure 7.3 shows the relative contributions to the total decay photon yields resulting from the cocktail simulation for the centrality classes 0–10% and 20–40% (very similar to the contributions in 20–50%, not reported here).

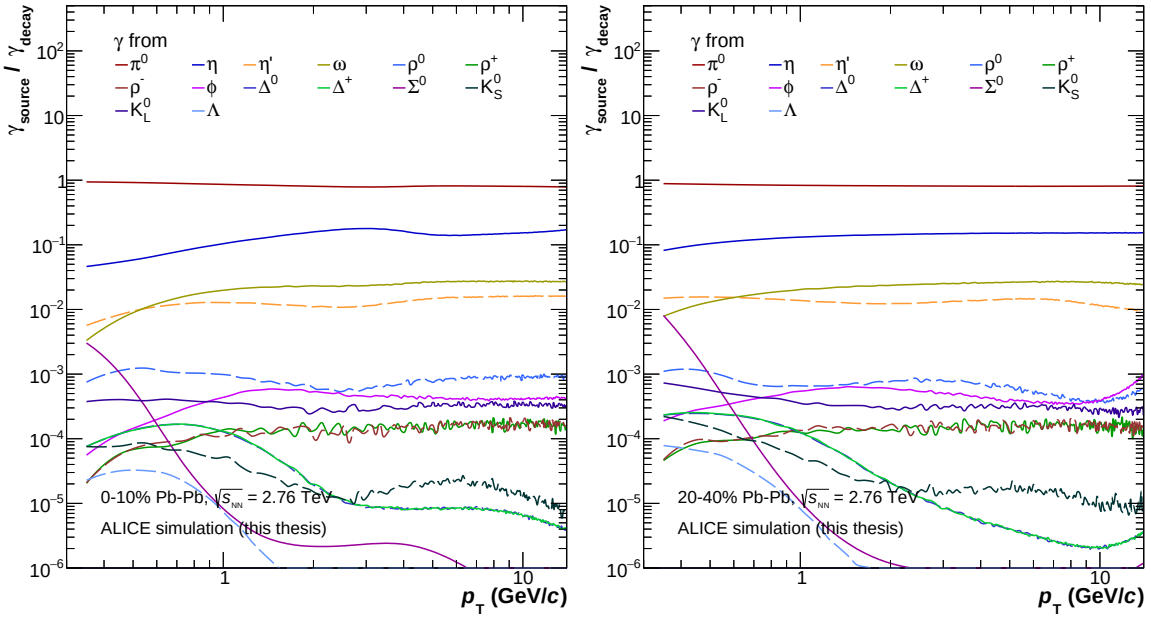

FIGURE 7.3: Relative decay photon contribution to the total decay spectrum yield for the centrality class 0–10% (left) and 20–40% (right).

To cross check that the cocktail simulation is consistent with the neutral meson yields, the π^0 and η spectra obtained from the cocktail are compared to the measured yields, as shown in Figure 7.4 for the 0–10% centrality class. The cocktail simulation is produced with enough events to have small statistical errors, that are of about 1%. The fluctuations visible in the ratio of the data spectrum to the cocktail spectrum are coming from the data and cannot be fully described by the parametrisation.

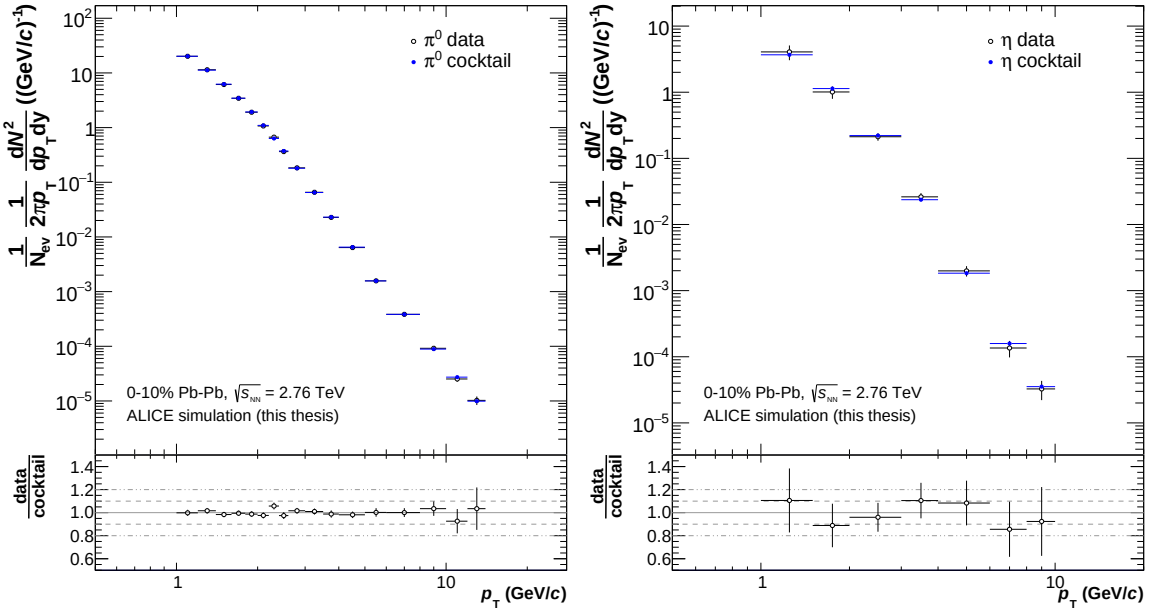

FIGURE 7.4: Comparison of the neutral pion (left) and η (right) meson measured spectra to the yields obtained from the cocktail simulation in 0–10% Pb–Pb collisions. In the bottom panels of each figure, the ratio of the data to the cocktail yield is shown.

Chapter 8

Inclusive and direct photon measurement with the Photon Conversion Method in Pb–Pb collisions

The direct photon analysis follows a similar workflow as the neutral meson analysis. In this chapter, the selection criteria will be redefined when is necessary for the requirements of the direct photon analysis. The corrections to the inclusive photon measurement will then be addressed.
The direct photon analysis is carried out in the centrality classes 0–10%, 20–40% and 20–50%. Only the figures for the first two classes will be shown in this chapter to avoid redundancy between the classes 20–40% and 20–50%, that have very similar behaviour.

8.1 Electron and photon selection for the inclusive and direct photon measurement

The main requirement of the direct photon analysis is to have a high purity of the photon sample, maintaining, at the same time, a high reconstruction efficiency. However, it is also necessary that the neutral pion invariant spectra obtained with the photon analysis selection criteria are consistent with the same measurement derived from the selection criteria of Chapter 5. Keeping these requirements in mind, the latter set differs from the former only in what concerns the pion rejection based on the specific energy loss in the TPC. The rejection, which was less strong at high momentum in the meson analysis, is kept with a rejection of $\pm 3\sigma$ around the pion $\mathrm{d}E/\mathrm{d}x$ hypothesis for the entire electron momentum range. All the other selection criteria are maintained the same.
In Figure 8.1, the decomposition of the residual photon combinatorial background obtained from MC simulations is shown for each identified source over the primary photon signal. The largest overall contamination is due to electron and positron pairs not originating from the same photon, but randomly associated together. Given its nature, this background cannot

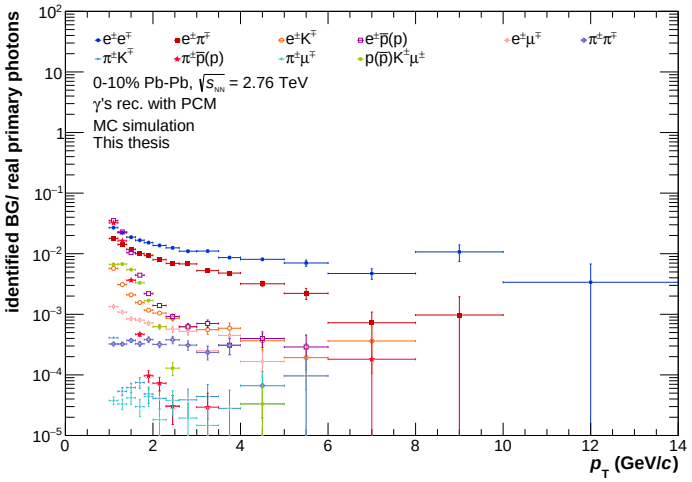

FIGURE 8.1: Ratio of the identified sources of combinatorial background over the primary photon signal in 0–10% Pb–Pb collisions obtained from the MC simulation.

be further reduced without a loss of signal. The e^+e^- contamination can be reduced only using geometrical cuts, such as the χ^2 and ψ_{pair} cuts. This type of geometrical cut strongly affects the yields and the efficiency at low-p_{T}, therefore the optimal values of χ^2 and ψ_{pair} for the photon analysis have been carefully studied to give both good purity and sufficiently high efficiency. The second largest overall combinatorial background is given by electron and pion pairs. At low-p_{T}, a significant contamination is also given by the electron-proton and pion-proton random associations. These contributions can be reduced using PID cuts on the TPC $\mathrm{d}E/\mathrm{d}x$. A rejection cut similar to the one used for the pion signal has been studied also for the proton. Unfortunately, the loss of signal in this case is too large compared to the improvement in the background level, thus the proton rejection has not been adopted as a selection criterion.

The primary photon sample obtained after all the selection cuts have been applied is analysed in transverse momentum bins. The stronger pion rejection results in lower statistics available in the neutral pion invariant mass distributions at intermediate and high-p_{T}. Given that the π^0 measurement is necessary for the direct photon signal extraction, a different binning compared to the neutral meson analysis needs to be adopted. To ensure small fluctuations and the same transverse momentum reach as before, some of the intermediate p_{T} bins have been merged with respect to the meson measurement of Chapter 5.

8.2 Corrections to the inclusive photon spectra

Like in the meson analysis, the inclusive primary photon spectrum needs to be corrected for signal contamination and inefficiencies. The corrections applied are for pile-up, contamination from photons from secondary particles, purity of the photon sample, photon conversion probability and reconstruction efficiency. To avoid repetitions, only essential information and the pertinent figures will be shown here. For details, see Chapter 5.

8.2.1 Correction for photons from pile-up verteces

The estimation of the number of photons from pile-up verteces is obtained studying the z-coordinate of the DCA distribution of photon candidates. Photons from pile-up events have a misplaced vertex, thus give a broad DCA_z distribution. The background is evaluated with the same procedure described in Section 5.3.3.1 from which the correction factor shown in Figure 8.2 is extracted. For both centralities, the correction at $p_{\mathrm{T}} = 1$ GeV/c, where it is largest, is about 1%.

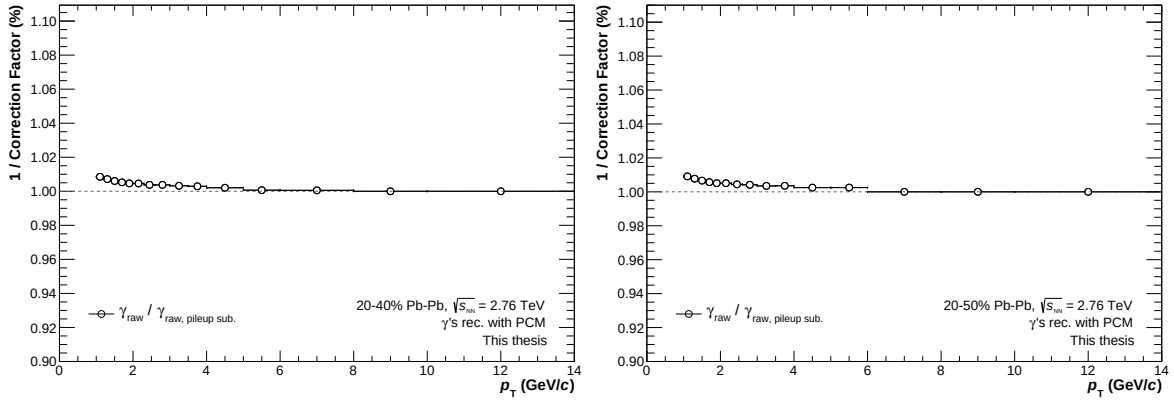

FIGURE 8.2: Inverse of the correction factor for photons from pile-up verteces in 20–40% (left) and 20–50% (right) Pb–Pb collisions.

8.2.2 Correction for contamination from secondary photons

Primary photons are defined as photons coming from the initial collisions or from the decay of primary particles. In order to have a sample with only primary photons, the contributions from weak decays or secondary particle decays need to be subtracted.
The secondary photon contamination is estimated similarly as for the secondary pion contamination (Section 5.3.3.2), relying on a data driven approach using a cocktail simulation together with the validated MC signal to increase the p_{T} reach and have a realistic description. The secondary particle spectra from the cocktail are multiplied by efficiency and conversion probability in order to obtain the raw spectrum for each contamination, to be subtracted from the inclusive primary photon spectrum.
Figure 8.3 shows the fraction of secondary photons for the separate contributions in 0–10% and 20–40% Pb–Pb collisions. The correction at $p_{\mathrm{T}} = 1$ GeV/c is 2.7% for central and about 3–3.5% for semi-central collisions, and then decreases towards higher p_{T}. The fraction of secodaries from $\mathrm{K}^0_{\mathrm{L}}$ and Λ is negligible.

8.2.3 Photon purity

As it can be observed from Figure 8.1, the analysis selection criteria are not able to remove all the combinatorial background from the photon sample. The residual contamination is accounted for with a purity correction. The purity of the photon sample is extracted from

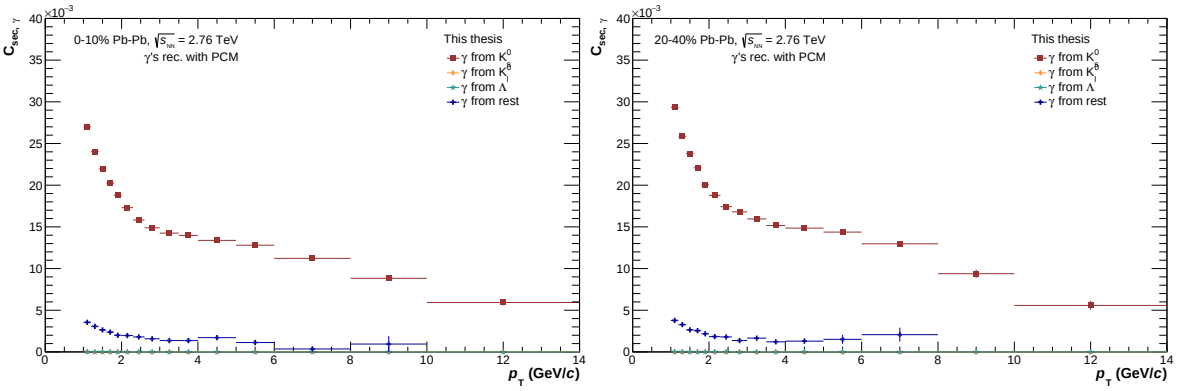

FIGURE 8.3: Fraction of secondary photons shown separately for each contribution in 0–10% (left) and 20–40% (right) Pb–Pb collisions.

the MC simulation and is given by

$$\mathcal{P}_{\gamma}(p_{\mathrm{T}}) = \frac{N_{rec,\gamma}^{\text{validated primary}}(p_{\mathrm{T}})}{N_{rec,\gamma}^{\text{primary}}(p_{\mathrm{T}})}, \tag{8.1}$$

which is the ratio of the reconstructed and validated primary photons over all the primary reconstructed photon candidates. The correction is estimated and applied after the secondary photon contamination has been subtracted from the respective spectra.

The purity for central and semi-central collisions is shown in Figure 8.4. As expected, the purity drops at low-p_{T}, where the higher combinatorial background is located. The largest contribution in this region comes from the random association of $e^{+}e^{-}$ pairs, and is irreducible. The others largest fractions to the combinatorial background are given by $e^{\pm}\pi^{\mp}$ and $e^{\pm}p(\bar{p})$ pairs, which can be partially reduced with rejection cuts on the pion or proton TPC $\mathrm{d}E/\mathrm{d}x$. Moreover, the purity is lower for central than for semi-central collisions because of the higher track multiplicity and therefore higher probability of a random association of the track pairs.

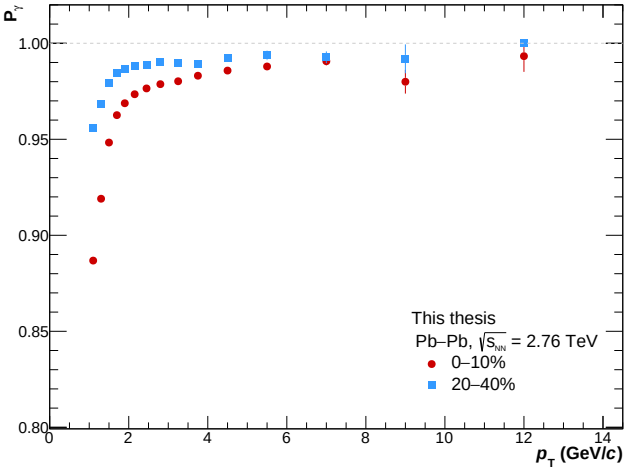

FIGURE 8.4: Purity of the reconstructed photons in 0–10% and 20–40% Pb–Pb collisions.

8.2.4 Efficiency correction

The photon reconstruction efficiency is defined as

$$\epsilon_{\gamma}(p_{\mathrm{T}}) = \frac{N_{rec,\gamma}^{\text{validated primary}}(p_{\mathrm{T}}^{\text{rec.}})}{N_{MC,\gamma}^{\text{converted}}(p_{\mathrm{T}}^{\text{gen.}})} \tag{8.2}$$

where the numerator is the number of reconstructed and validated primary photons and the denominator is the number of generated primary converted photons. The transverse momentum expressed at numerator, $p_{\mathrm{T}}^{\text{rec.}}$, is the momentum with which the photon candidates are reconstructed, while, at denominator, $p_{\mathrm{T}}^{\text{gen.}}$ indicates the momentum with which the conversion photon has been generated in the simulation. The difference between the two is due to the finite resolution of the detector that does not allow for a perfect reconstruction, present also in data. In order to properly account for the detector resolution and efficiency, the inclusive photon spectrum is unfolded with two different techniques, bin-by-bin and iterative or Bayesian [242]. The bin-by-bin unfolding consists in obtaining the efficiency from the ratio between the events in a certain bin of the reconstructed distribution over the events in the same bin of the true distribution, as in Equation 8.2. In both cases, the unfolding is carried out with the RooUnfold ROOT package [243, 244]. The effects due to the finite resolution of the detector are estimated mapping the true, generated p_{T} distribution onto the reconstructed one via a response matrix. The response matrix is shown in Figure 8.5 for the centrality 0–10% and 20–40%.

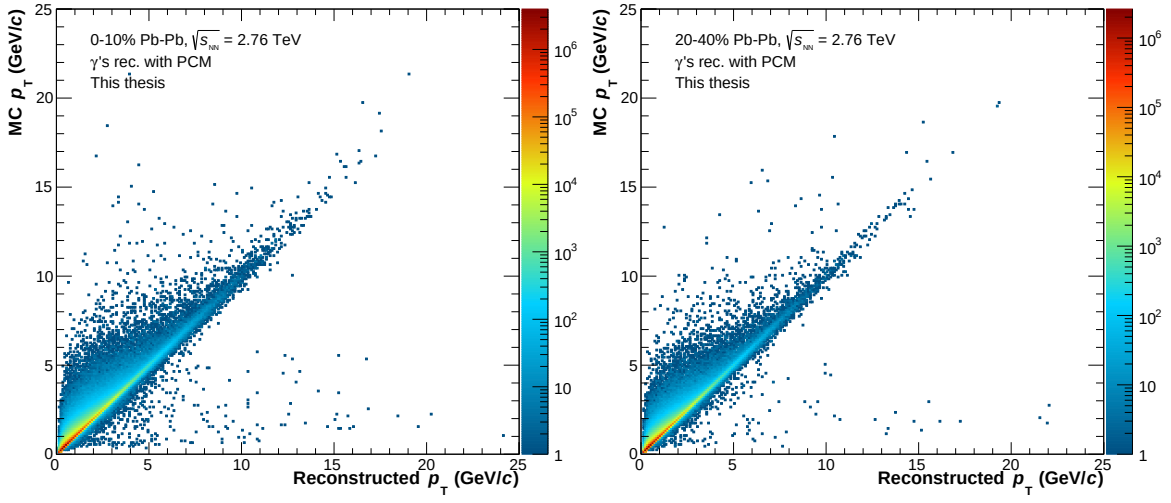

FIGURE 8.5: Response matrix of the reconstructed and generated photon p_{T} for 0–10% (left) and 20–40% (right) Pb–Pb collisions.

The distribution of the photon reconstructed p_{T} is given by the projection of the response matrix on the x-axis, while the true p_{T} distribution is given by the projection on the y-axis. When using the Bayesian unfolding, a regularisation parameter is needed to avoid that statistical fluctuations of the measured distribution are interpreted as real structures of the true distribution. This parameter is given by the number of iterations in which the prior is updated with the information from the previous loop. Given that the difference between the true and reconstructed p_{T} distribution is not large, the number of iterations taken is 4.
In Figure 8.6, the photon reconstruction efficiency estimated with the different methods are compared. The efficiency calculated with Equation 8.2 (yellow points) is to be compared

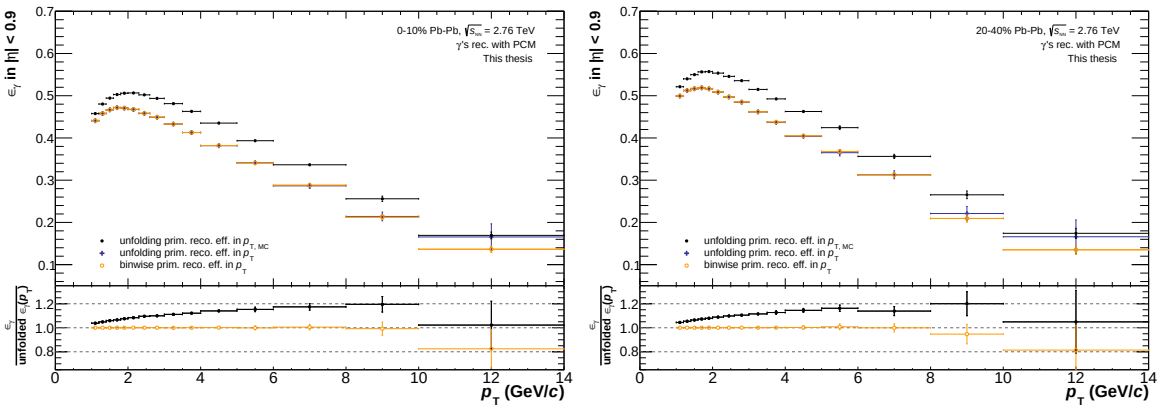

FIGURE 8.6: Photon reconstruction efficiency for the centrality classes 0–10% (left) and 20–40% (right). The efficiency calculated with Equation 8.2 is shown in yellow, while the efficiency without the correction for resolution effects in black and with resolution effects (Bayesian unfolding) in blue.

with the efficiency corrected for finite resolution effects estimated with the Bayesian unfolding (blue points). For comparison, the efficiency without resolution correction is shown with the black markers. To correct the inclusive photon spectra, the efficiency obtained with the Bayesian unfolding is used, while the bin-by-bin one is taken as cross-check.

8.2.5 Conversion probability

The conversion of a photon into an electron-positron pair depends on its transverse momentum, on the material it encounters and with which it may interact. The conversion probability, applied to the inclusive spectrum to account for the detector material budget, is calculated as

$$\mathcal{C}_\gamma(p_\mathrm{T}) = \frac{N^{\mathrm{converted}}_{MC,\gamma}(p_\mathrm{T})}{N^{\mathrm{all}}_{MC,\gamma}(p_\mathrm{T})} \tag{8.3}$$

from MC simulations and is shown in Figure 8.7 for 0–10% collisions.

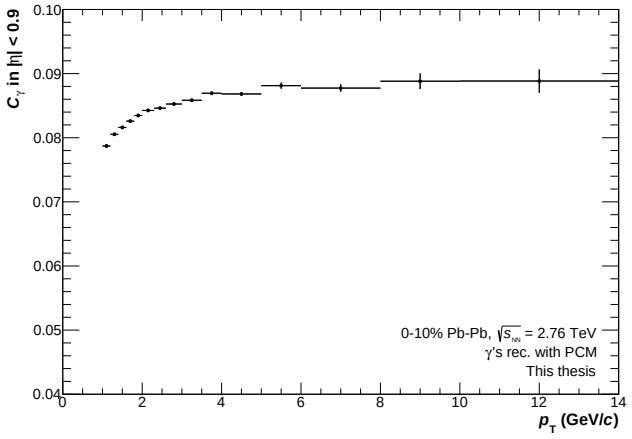

FIGURE 8.7: Photon conversion probability for 0–10% Pb–Pb collisions.

The conversion probability depends on the geometrical region defined by the fiducial cuts (R_{conv}, Z_{conv} and pseudorapidity) that fix the amount of material that the photon traverse.

For the material within $R < 180$ cm and pseudorapidity $|\eta| < 0.9$, the radiation thickness is $11.4 \pm 0.5\%$ X_0 and the conversion probability is $\sim 8.5\%$.

Chapter 9

Results of the direct photon measurement in Pb–Pb collisions

In the following chapter, the inclusive photon measurement in Pb–Pb collisions obtained with PCM will be presented. The systematic uncertainties for all the observables used in the direct photon analysis will also be illustrated here. Then, the extraction of the direct photon signal will be explained and the final results will be compared to the most recent theory models. The results shown in this chapter are obtained in the centrality classes 0–10%, 20–40% and 20–50%.

9.1 Differential inclusive photon spectra and γ/π^0 ratio

The invariant inclusive primary photon spectrum is calculated as

$$E\frac{\mathrm{d}^3N}{dp^3} = \frac{\mathrm{d}^3N}{p_{\mathrm{T}}\mathrm{d}p_{\mathrm{T}}\mathrm{d}y d\varphi} = \frac{1}{2\pi N_{\mathrm{ev}}}\frac{\mathcal{P}_\gamma}{\epsilon_\gamma \mathcal{C}_\gamma}\frac{1}{p_T}\frac{N^\gamma_{\mathrm{raw}}}{\Delta y \Delta p_{\mathrm{T}}}, \tag{9.1}$$

where N_{ev} is the number of events in the different centrality classes, reported in Table 3.1, $\mathcal{P}_\gamma$ and $\mathcal{C}_\gamma$ the photon purity and conversion probability, respectively, and ϵ_γ the reconstruction efficiency, where the finite resolution of the detector is estimated via unfolding as described in Section 8.2.4. The inclusive primary photon raw spectrum, N^γ_{raw}, includes the correction for pile-up and secondary photon contamination. The differential inclusive photon spectrum is shown in Figure 9.1 for the centrality classes 0–10%, 20–40% and 20–50%. The statistical uncertainties are not visible as they are smaller than the marker size. The systematic uncertainties, indicated here with boxes, will be discussed in Section 9.2.
As mentioned in Chapter 8, the π^0 measurement is necessary to extract the direct photon signal. The neutral pion analysis is thus repeated, this time with the selection criteria of the direct photon analysis and in a larger transverse momentum binning. The ratio of the inclusive photon spectrum and of the π^0 spectrum is shown in Figure 9.2. The ratio is useful to reduce the systematic uncertainty because the material budget error partially cancels out. Moreover, to avoid statistical fluctuations for $p_{\mathrm{T}} > 4$ GeV/c, the fit to the π^0 spectrum is used at denominator instead of the data directly. The ratio using the π^0 spectrum itself is shown in Appendix F.

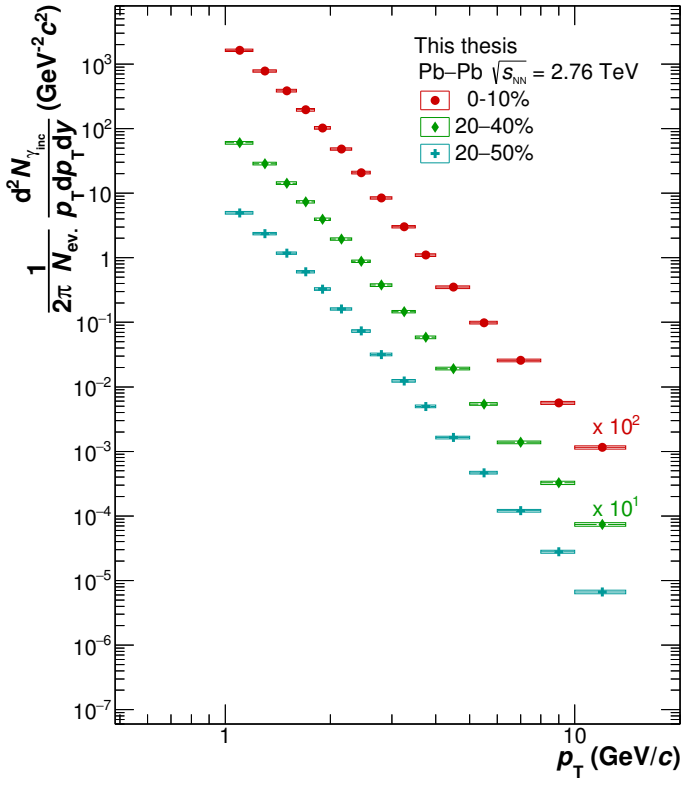

FIGURE 9.1: Differential inclusive photon spectrum measured in Pb–Pb collisions at $\sqrt{s_{\mathrm{NN}}}$ = 2.76 TeV centre-of-mass energy for the centrality classes 0–10%, 20–40% and 20–50%. The statistical uncertainties are smaller than the marker size. The boxes represent the systematic uncertainties (Section 9.2).

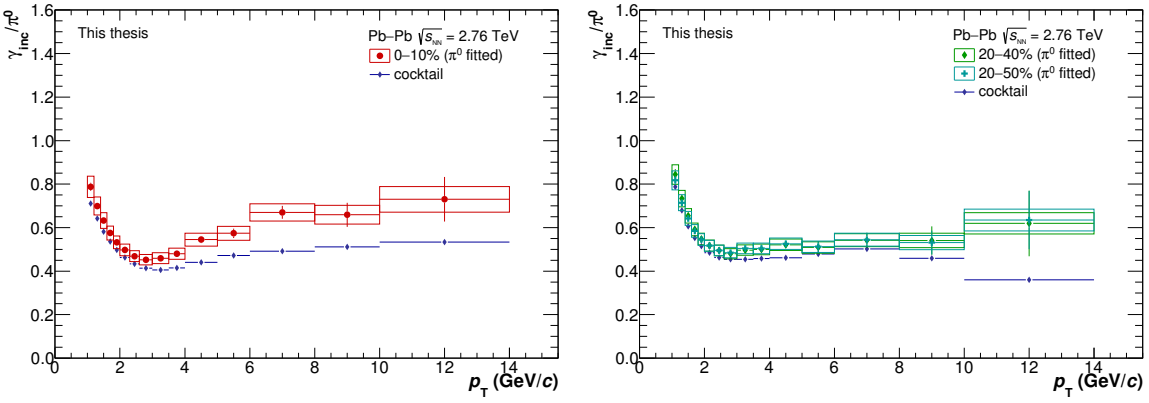

FIGURE 9.2: Ratio of the inclusive photon over the π^0 spectrum measured in 0–10% (left), 20–40% and 20–50% (right) Pb–Pb collisions at $\sqrt{s_{\mathrm{NN}}}$ = 2.76 TeV centre-of-mass energy. The statistical uncertainties are indicated by the vertical bars, the systematic uncertainties by the boxes. The blue histograms represent the $\gamma_{\mathrm{incl}}/\pi^0$ from the cocktail simulation.

9.2 Systematic uncertainties of the photon measurement

The systematic uncertainties of the photon measurement are estimated in the same manner as the meson uncertainties: each of the selections made in the analysis of the data sample are varied and compared to the standard one. When possible, the same variations used in the meson analysis are also used here. The systematic studies consider the mean of the

positive and negative deviations in each transverse momentum bin in order to give a single contribution uncertainty, while the total systematic uncertainty is obtained from the squared sum of all the single contributions. The systematic deviation have been carefully checked to avoid being driven by the statistical fluctuations.
The complete list of systematic variations considered and their values is reported in Table 9.1. The single systematic error component specific of the photon measurements will be explained in the following paragraphs. The other contributions are explained in Section 5.4.
The systematic errors for $\gamma_{\mathrm{incl}}/\pi^0$ and R_γ are estimated directly on the ratio, as it was the case for the η/π^0 ratio, in order to take advantage of the cancellation of common errors. Moreover, with the exclusion of the systematic uncertainties of the π^0 meson, the material budget uncertainty contributes only once.

Quantity	Standard	Variation 1	Variation 2
TPC cluster ratio	> 0.6	> 0.7	> 0.35
Min. p_{T} $e^{\pm}$	> 0.05 GeV/c	> 0.075 GeV/c	> 0.1 GeV/c
dE/dx e-line $\sigma_{\mathrm{d}E/\mathrm{d}x,e}$	-3 $< n_\sigma <$ 5	-4 $< n_\sigma <$ 5	-2.5 $< n_\sigma <$ 4
dE/dx π-line in momentum range π rej. low p	[0.4, 2.0] GeV/c < 3	[0.4, 2.0] GeV/c < 2	[0.4, 100] GeV/c < 2.5
$\sigma_{\mathrm{d}E/\mathrm{d}x,\pi}$ π rej. high p	< 1	< 1	$<$ -10
$\sigma_{\mathrm{d}E/\mathrm{d}x,\pi}$ $p_{\mathrm{min},\ \pi\ \mathrm{rej}}$ $p_{\mathrm{max},\ \pi\ \mathrm{rej}}$	 0.4 GeV/c 2.0 GeV/c	 0.3 GeV/c 3.0 GeV/c	 – –
χ^2 γ	< 20	< 50	< 30
ψ_{pair} γ	< 0.1 rad	< 0.2 rad	< 0.05 rad
$q_{\mathrm{T,max}}$	< 0.05 GeV/c	< 0.03 GeV/c	< 0.06 GeV/c
Cut on φ	[2.2, 3.8] rad	[2.0, 4.0] rad	[2.4, 3.6] rad

TABLE 9.1: Complete list of the selection criteria and their variations used to evaluate the systematic uncertainties of the photon measurement. Only one cut at a time is varied.

9.2.1 Cocktail simulation

The systematic variations of the cocktail simulation consist in producing the decay photon yields using parametrisations of the hadrons with photon decays that are shifted with respect to the standard one with a linear or polynomial function, within the systematic uncertainty of the spectrum. The photon measurements are extracted using the varied simulation and the systematic uncertainties are estimated comparing the final results, as it is done for any other systematic variation.

The photon measurement systematic uncertainties for the centrality classes 0–10% and 20–40% are shown in Figure 9.3, Figure 9.5, Figure 9.4 and Figure 9.6. The total systematic uncertainty as well as the single components are plotted. The uncertainties of the 20–50% centrality class are practically identical to the 20–40% uncertainties and are not shown.

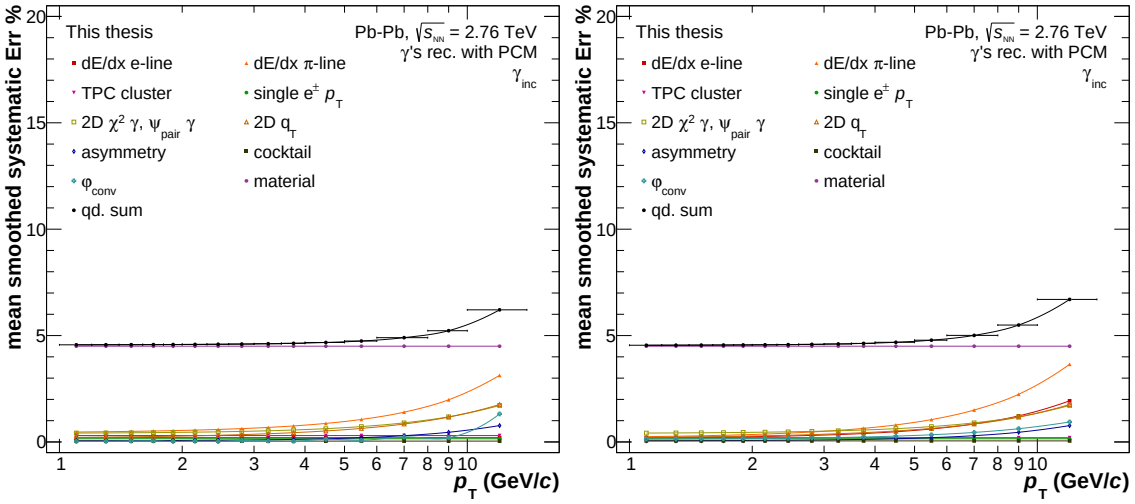

FIGURE 9.3: Systematic uncertainties of the inclusive photon spectrum in Pb–Pb collisions at $\sqrt{s_{\mathrm{NN}}} = 2.76$ TeV in the centrality classes 0–10% (left) and 20–40% (right).

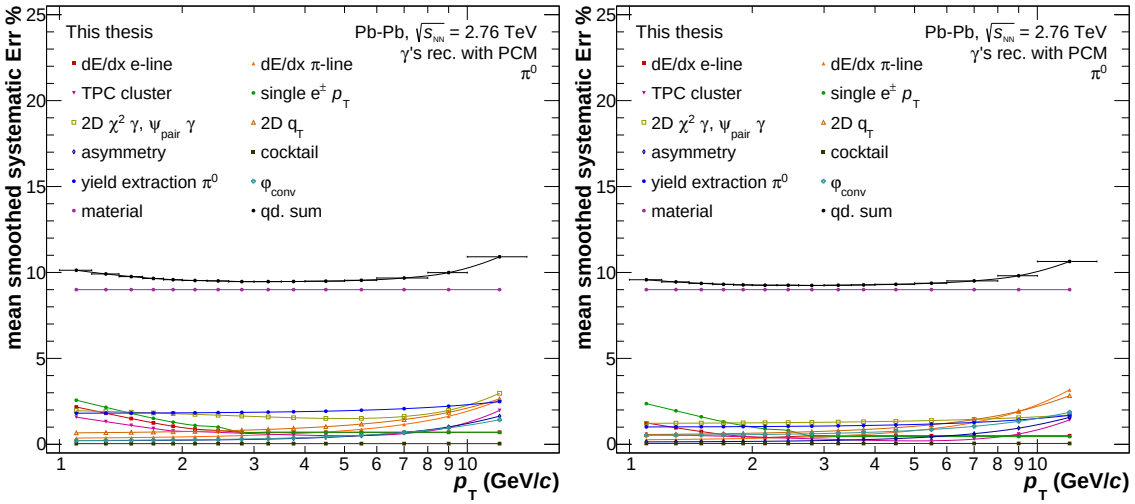

FIGURE 9.4: Systematic uncertainties of the π^0 spectrum in Pb–Pb collisions at $\sqrt{s_{\mathrm{NN}}} = 2.76$ TeV in the centrality classes 0–10% (left) and 20–40% (right).

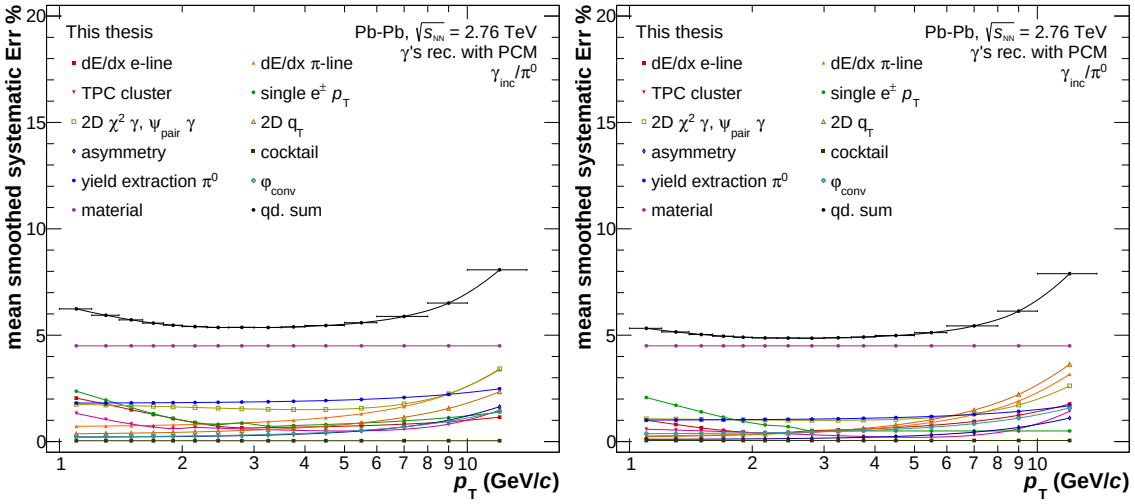

FIGURE 9.5: Systematic uncertainties of the $\gamma_{\mathrm{incl}}/\pi^0$ ratio in Pb–Pb collisions at $\sqrt{s_{\mathrm{NN}}} = 2.76$ TeV in the centrality classes 0–10% (left) and 20–40% (right).

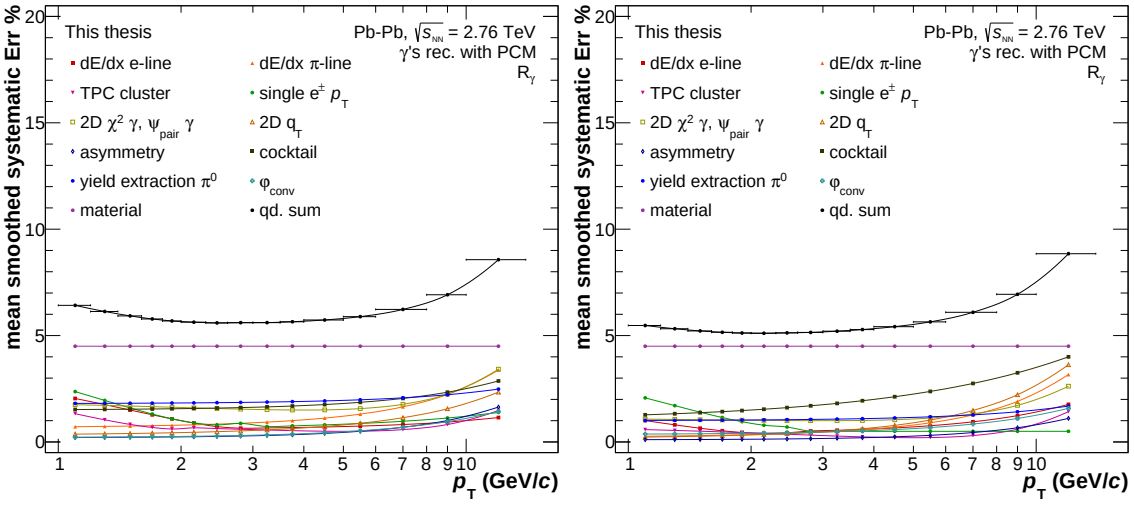

FIGURE 9.6: Systematic uncertainties of the photon double ratio R_γ in Pb–Pb collisions at $\sqrt{s_{\rm NN}}$ = 2.76 TeV in the centrality classes 0–10% (left) and 20–40% (right).

A direct photon measurement in Pb–Pb collisions at $\sqrt{s_{\rm NN}}$ = 2.76 TeV has already been published for the 0-20%, 20-40% and 40-80% centrality classes using the 2010 data [154, 245]. The results illustrated in this publication are the combined PCM and PHOS measurements. The results of this thesis work have been compared with the published ones for the common centrality class (20–40%). Considering that the transverse momentum binning of the latter is finer compared the the binning used in this work and that is optimised for this data, the direct photon analysis of the 2011 Pb–Pb data was repeated in full in a separate instance with the published results $p_{\rm T}$ binning. As additional check, the PCM measurement of this work has been combined with the published PHOS one. In both cases, PCM only with the new binning and PCM and PHOS combined, the R_γ in the 20–40% centrality class is consistent with unity and larger fluctuations are observed at high-$p_{\rm T}$.
It can only be concluded that the two measurements agree within the uncertainties, but the resulting comparison is not shown here.

9.3 Double ratio R_γ

The direct photon signal is extracted using the photon double ratio, R_γ, defined as

$$R_\gamma = \frac{\gamma_{\rm incl}}{\pi^0} \Big/ \frac{\gamma_{\rm decay}^{\rm cocktail}}{\pi^0} \approx \frac{\gamma_{\rm incl}}{\gamma_{\rm decay}^{\rm cocktail}} = 1 + \frac{\gamma_{\rm direct}}{\gamma_{\rm decay}^{\rm cocktail}}. \tag{9.2}$$

Considering that $\gamma_{\rm incl} = \gamma_{\rm decay} + \gamma_{\rm direct}$, the double ratio reveals the presence of a direct photon signal, if $R_\gamma > 1$. If R_γ is consistent with unity, only upper limits can be extracted. The photon double ratio for the centrality classes 0–10%, 20–40% and 20–50% is shown in Figure 9.7, together with pQCD calculations. The photon double ratio calculated using the π^0 spectrum data points instead of the fit to the spectrum is shown in Appendix F.
At low-$p_{\rm T}$, thermal photons are expect to be the dominant component. In the centrality class 0–10%, the R_γ is above unity by about 10% for $p_{\rm T} < 1.6$ GeV/c. In order to calculate

the significance of the direct photon signal, the systematic uncertainties are classified in uncertainties point-by-point uncorrelated (type A), correlated in p_{T} and of p_{T}-dependent magnitude (type B) and constant uncertainties (type C). These uncertainties are considered separately in the significance estimation. The procedure calculates the p-value of the direct photon signal and from here, the number of σ is extracted with respect to "null" hypothesis, *i.e.* $R_\gamma = 1$. The method used to extract the number of sigmas of the direct photon signal is described in more detail in Figure 11 of [245]. The R_γ with the uncertainties represented according to their type is shown in Appendix F. The significance of the direct photon signal has been studied in different transverse momentum ranges. In the range $1 < p_{\mathrm{T}} < 1.6$ GeV/c, the significance is 1.5, 1.3 and 0.9σ for the centrality classes 0–10%, 20–40% and 20–50%, respectively. The values estimated for the other p_{T} ranges are reported in Appendix F.
At high-p_{T}, prompt photons, originating from initial hard parton scatterings, become the dominant component of for the direct photons and can be compared to pQCD calculations. All the pQCD calculations plotted in Figure 9.7 are originally provided as predictions for the direct photon spectrum in pp collisions at the centre-of-mass energy $\sqrt{s} = 2.76$ TeV, $\gamma^{\mathrm{pQCD}}_{\mathrm{direct,pp}}$. The predictions for the Pb–Pb collisions are obtained scaling the original prediction by the number of binary collisions of the appropriate centrality class, N_{coll}, given in [185].

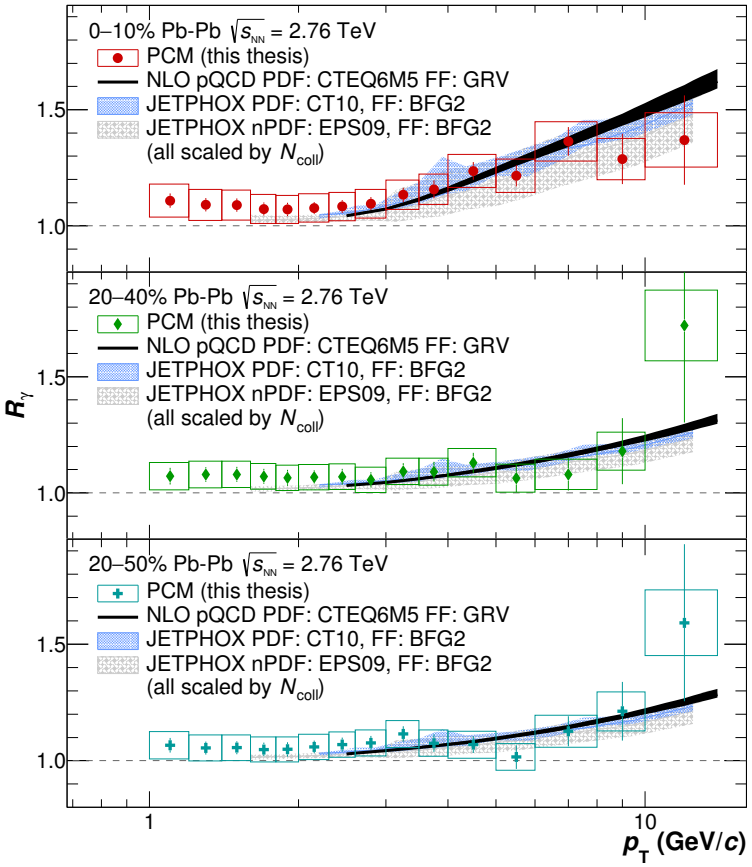

FIGURE 9.7: Photon double ratio, R_γ, measured in 0–10%, 20–40% and 20–50% Pb–Pb collisions at $\sqrt{s_{\mathrm{NN}}} = 2.76$ TeV centre-of-mass energy. The statistical uncertainties are indicated by the vertical bars, the systematic uncertainties by the boxes. The data is compared to NLO pQCD calculations for direct photon in pp collisions, scaled with the appropriate number of binary collisions to match the Pb–Pb data. See text for references.

The R_γ is then calculated dividing the prediction by the fit to the decay photon spectrum

estimated via cocktail simulation, $\gamma_{\text{decay}}^{\text{cocktail}}$:

$$R_{\gamma}^{\text{pQCD}} = 1 + \frac{N_{\text{coll}} \cdot \gamma_{\text{direct,pp}}^{\text{pQCD}}}{\gamma_{\text{decay}}^{\text{cocktail}}}. \tag{9.3}$$

The NLO pQCD calculation shown with the black line in Figure 9.7 follows [144, 246], with the photon fragmentation function GRV from [247]. The width of the line represents the uncertainty of the calculation, which includes factorisation, renormalisation and fragmentation scale uncertainties. The blue and grey bands are JETPHOX calculations [248] using the CT10 [249] and EPS09 [230] parton distribution functions, respectively, and the BFG2 photon fragmentation function from [250]. In this case, the width of the band includes also the parton distribution function uncertainty. It can be observed that for each of the centrality classes shown in Figure 9.7, the excess ratio above unity for $p_{\text{T}} > 3.5$ GeV/c is consistent with the NLO calculations describing an additional contribution, on top of the decay photon one, due to prompt photons.

9.4 Extraction of the direct photon measurement

The direct photon spectrum is obtained using

$$\gamma_{\text{direct}} = \gamma_{\text{incl}} - \gamma_{\text{decay}} = \gamma_{\text{incl}} \cdot \left(1 - \frac{1}{R_{\gamma}}\right) \tag{9.4}$$

and is shown in Figure 9.8 for the centrality classes 0–10%, 20–40% and 20–50%. The arrows indicate upper limits with 90% confidence level. The size of the systematic uncertainties is driven by the uncertainty on the double ratio.
For the direct photon spectrum in the centrality class 20–50%, upper limits are extracted. The different symbols used depend on the double ratio points. An arrow alone is used in the case in which both the data point and the error of the double ratio are consistent with unity, while a point and an arrow in the case in which the point is above one but the error is consistent with unity.
For $p_{\text{T}} > 3.5$ GeV/c, the direct photon spectra can be compared to the NLO pQCD calculations for direct photons in pp collisions, scaled by the number of binary collisions, already shown in Figure 9.7. In this region, the dominant contribution to the spectra is given by prompt photons and it can be observed that the measurements are consistent, within uncertainties, with the predictions. The yellow lines represent a fit to the prompt photon prediction from [156]. The low-p_{T} extrapolation highlights the excess of direct photon yields given by the thermal photon component. This fit will be later used to subtract the prompt photon component from the direct photon spectrum, in order to extract the effective temperature T_{eff} using only the thermal photon signal.
The temperature T_{eff} is given by the inverse slope of the exponential fit to the low-p_{T} part of the direct photon spectrum, where the thermal photon contribution is dominant, as explained in Section 1.3.6. In Figure 9.9, the direct photon spectrum measurements are plotted together with the exponential fit for the centrality class 0–10% and 20–40%. The transverse momentum range of the fit is $1.0 < p_{\text{T}} < 2.2$ GeV/c. It has been observed that the significance of the signal remains about the same for different p_{T} ranges, therefore a larger

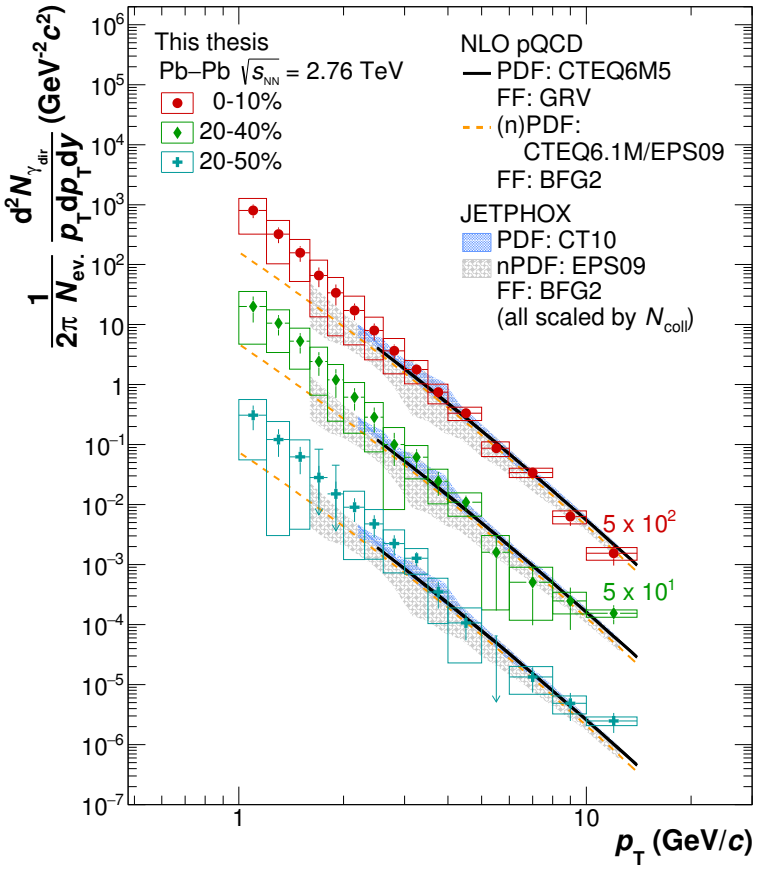

FIGURE 9.8: Differential direct photon spectrum measured in 0–10%, 20–40% and 20–50% Pb–Pb collisions at $\sqrt{s_{NN}}$ = 2.76 TeV centre-of-mass energy. The statistical uncertainties are indicated by the vertical bars, the systematic uncertainties by the boxes. The arrows represent upper limits with 95% confidence level. The data is compared to the same NLO pQCD calculations for direct photons in pp collisions shown in Figure 9.7. The additional yellow lines are a fit to the pQCD calculation for prompt photons from [156]. See text for details.

interval is chosen here to reduce the uncertainties related to the fit. The spectrum of the class 20–50% is not fitted because the data points have upper limits. The values of the effective temperature obtained from the fits are $T_{\text{eff}} = 270 \pm 30^{\text{stat}} \pm 65^{\text{syst}}$ MeV for 0–10% and $T_{\text{eff}} = 294 \pm 45^{\text{stat}} \pm 78^{\text{syst}}$ MeV for 20–40% Pb–Pb collisions.

The spectra shown in Figure 9.9 still contain the prompt photon component. In order to extract the temperature for the pure thermal component, the prompt photons are subtracted using the fit to the NLO pQCD calculation shown in Figure 9.8. The spectrum is then again fitted with an exponential function and the effective temperatures obtained are $T_{\text{eff}} = 245 \pm 23^{\text{stat}} \pm 53^{\text{syst}}$ MeV for 0–10% and $T_{\text{eff}} = 276 \pm 40^{\text{stat}} \pm 66^{\text{syst}}$ MeV. As it was explained in Section 1.3.6, the effective temperature is not the production temperature of the photons, but it is related to the latter through the transverse velocity of the radial flow, as in Equation 1.6: the photons are emitted by an expanding source, thus the measured temperature is blue-shifted with respect to the original emission temperature. Similarly, a smaller T_{eff} is extracted in central compared to semi-central collisions because the higher energy density and temperature of the central nucleus-nucleus collisions require a longer lifetime for the expanding medium before the freeze-out conditions are reached, at a lower temperature [98, 99].

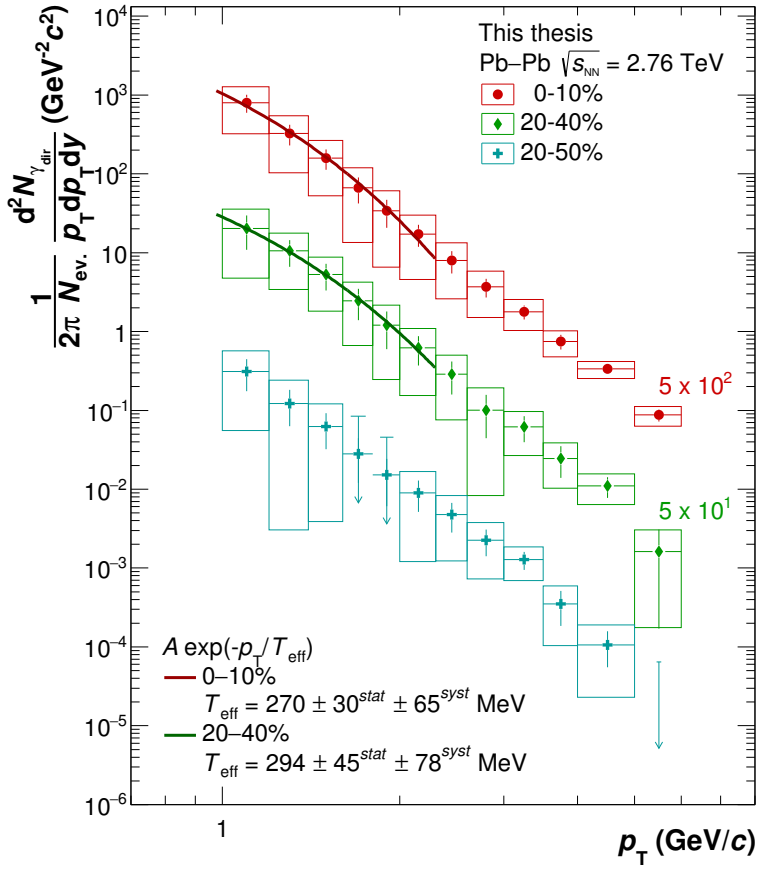

FIGURE 9.9: Differential direct photon spectrum measurements plotted together with the exponential fit to the spectrum of the centrality classes 0–10% and 20–40%. In the legend, the values of the inverse slope parameter, $T_{\rm eff}$ are reported. The x-axis scale is enlarged in order to focus on the thermal part of the spectrum.

The value of the temperature of the thermal emission is also subject to discussion. It is debated that the fact that $T_{\rm eff} > T_{\rm C}$, with $T_{\rm C}$ critical temperature, is not to be interpreted as a photon emission before the QGP phase transition. Instead, the large values of $T_{\rm eff}$ are to be attributed to an emission at a later stage with strong radial flow [251]. The comparison of the measured direct photon spectrum to theoretical predictions is useful in ascertaining the conditions of the system at the time of the photon emission and its (hydrodynamical) evolution. Such comparison will be shown in the next section.

9.5 Comparison to theoretical models

The direct photon spectra in the centrality classes 0–10%, 20–40% and 20-50% are compared with the results from several theory calculations, as shown in Figure 9.10.
The basic assumption in all the models is the formation of a Quark-Gluon Plasma as a result of a heavy-ion collision. The direct photons emitted from this medium are composed of prompt photons, dominant at high-$p_{\rm T}$ and calculable with pQCD, and thermal photons, dominant at low-$p_{\rm T}$ and whose production is dictated by the photon emission rates. What mainly differentiate the models from one another is the treatment of the space-time evolution

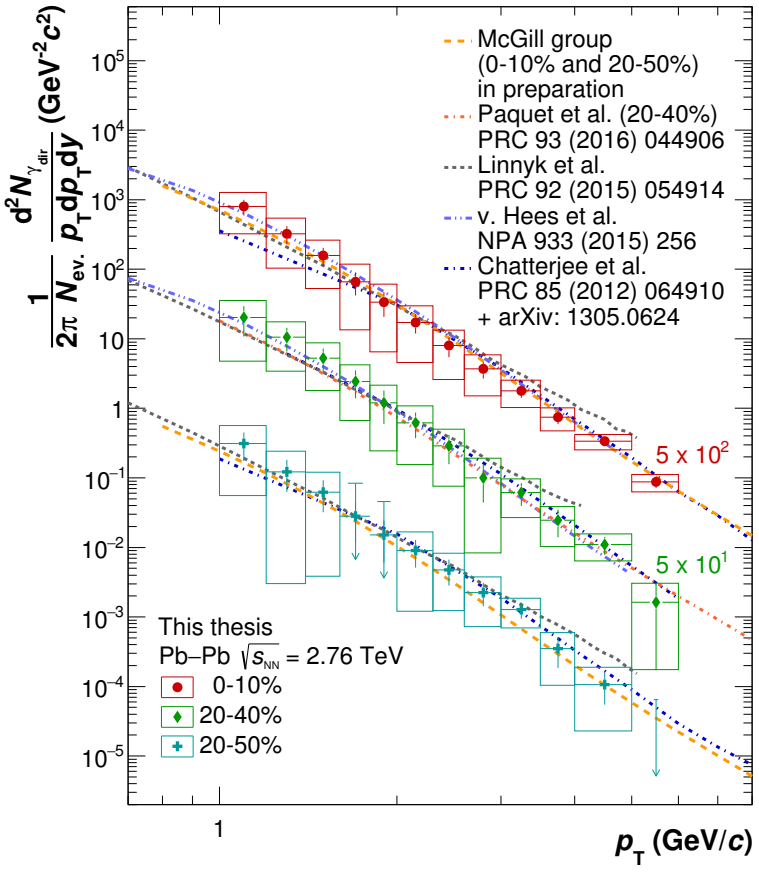

FIGURE 9.10: Comparison of the differential direct photon spectrum measured in 0–10%, 20–40% and 20–50% to several direct photon calculations. See text for references. The x-axis scale is enlarged in order to focus on the thermal part of the spectrum.

of the system.

The system evolution of the Paquet *et al.* [156] approach follows a 2+1D hydrodynamical model, described in [252]. The initial conditions of the collision are built using the IP-Glasma approach [253], with formation time of the plasma set at $\tau_0 = 0.4$ fm/c. Shear and bulk viscosity are also taken into account. To the hydrodynamic phase follows a hadronic phase, in which the particle interactions are modelled by the Ultrarelativistic Quantum Molecular Dynamics (UrQMD) [254]. The photon emission rates from [141, 255, 256] are adopted, with the addition of a viscous correction for each emission channel. The predictions shown for the 0–10% and 20–50% centrality classes are produced with a slightly different underlying hydrodynamical evolution compared to the one used for 20–40%.

The Linnyk *et al.* [153, 257] model uses the off-shell transport approach PHSD [258, 259] to give a microscopic description of the collision evolution. Both partonic and hadronic interactions are considered as sources of photons. The latter involves the production of photons from meson-meson or meson-baryon binary collisions or bremsstrahlung radiation as well as production of photon in hadronic decays. Particular importance is given to the meson-meson and meson-baryon bremsstrahlung, which is the novel feature of this model. In addition, vector meson and nucleon interactions and the Δ resonance decay are also considered. The prompt photon component is the same given in [156].

The van Hees *et al.* [157] calculations (shown only for the centrality classes 0–10% and 20–40%) explore the limits of an ideal hydrodynamic treatment [260]. For a realistic description

of the data, a LQCD equation of state (EoS) is adopted for the QGP phase and it is connected with a hadron gas at the freeze-out. The freeze-out is assumed to be sequential, chemical then kinetic, for the bulk hadrons and simultaneous for multistrange hadrons. Moreover, initial radial and elliptic flow are also included. The photon emission rates are taken from [141].
The Chatterjee *et al.* [158] model employs event-by-event hydrodynamics to better represent the initial inhomogeneities of the energy density profile. The initial formation time adopted is $\tau_0 = 0.14$ fm/c. The 2+1D ideal hydrodynamic evolution is assumed to have longitudinal boost invariance and is solved with the SHASTA algorithm [261]. The EoS is from [262], while the emission rate are taken from [263] for the QGP phase and from [141] for the hadronic phase. The total thermal photon emission rates are calculated integrating over the full fireball space-time evolution. The thermal and prompt component of this model are provided separately and then summed together to obtain the total direct photon yield. The prompt photon contribution becomes dominant for $p_{\mathrm{T}} > 5$ GeV/c.
Figure 9.10 illustrates that the theoretical models all give an equally good description of the measured spectra [1]. In Figure 9.11, the same theory calculations are plotted together with the photon double ratio, R_γ. The theoretical lines for the double ratio are obtained using Equation 9.3, but without the N_{coll} factor, since it is implicit in the calculations. In

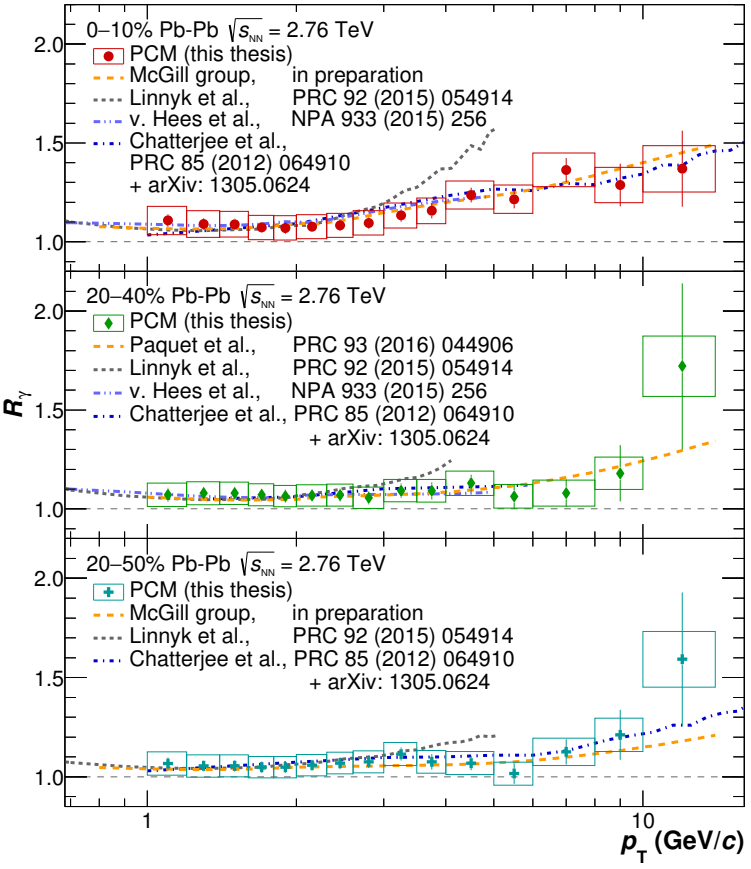

FIGURE 9.11: Comparison of the photon double ratio, R_γ, measured in the centrality classes 0–10%, 20–40% and 20–50% to several direct photon calculations. See text for references.

this representation it is easier to see the thermal and prompt contribution to the excess ratio. The agreement with the models is best at low-p_{T}, while varying levels of accord can be

[1] The theory predictions from Linnyk and Chatterjee for the centrality classes 0–10% and 20–50% have different p_{T} reach compared to the 20–40% centrality class because they are produced at a later time.

observed for $p_{\mathrm{T}} > 3$ GeV/c. In particular, the predictions by Linnyk *et al.* overestimate the data, discrepancy that grows larger in the central class, where it is about 20% at 4 GeV/c. It was mentioned above that in this calculation the photon emission via bremsstrahlung in meson-meson and meson-baryon collisions is considered important, an emission channel that it is not given the same relevance in the other models. On one hand, the meson-meson and meson-baryon bremsstrahlung channels have large uncertainties. On the other hand, it could be that this contribution needs to be fine tuned or reduced in the region where the prompt photons are expected to be dominant, to avoid overestimation.

9.6 Direct photon R_{AA}

The direct photon R_{AA} is another observable that highlights the thermal photon excess. There is no direct photon measurement in pp collisions, only upper limits, thus the reference used to compute the R_{AA} is a NLO pQCD calculation for the direct photons, the same one also used to extract the pure thermal photon spectrum, given by [156]. The resulting R_{AA} is shown in Figure 9.12. The data points are above unity for transverse momentum below 1.6 GeV/c, reaching a maximum of $R_{\mathrm{AA}} \sim 7$. The theory prediction for the 0-10% centrality class are also shown for comparison, while the other centralities are reported in Appendix F.

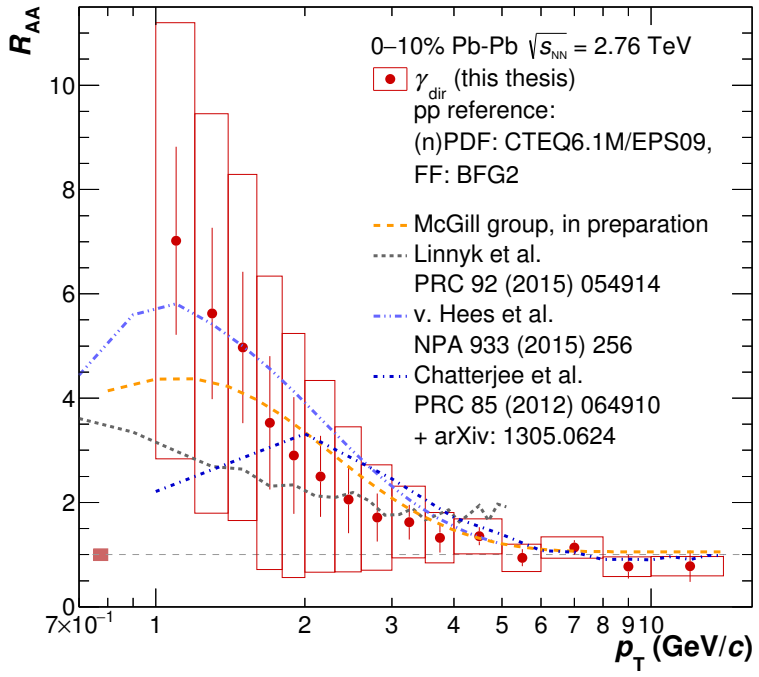

FIGURE 9.12: Comparison of the direct photon R_{AA} for the centrality class 0–10% to several direct photon calculations. See text for references. The coloured box around unity represents the normalisation uncertainty.

In Figure 1.10, the charged hadron nuclear modification factor in Pb–Pb collisions was compared to the same measurement in p–Pb collisions and to the measurement of photon Z and W boson production, also in Pb–Pb collisions. The figure it is interesting because it is immediately clear that in Pb–Pb collisions, with the formation of an hot and dense, strongly interacting medium, the hadron yields are suppressed in the most central collisions due to jet

quenching. However, particles that are not subject to the strong interaction, such as direct photons and the Z and W bosons, are not suppressed are have $R_{\mathrm{AA}} = 1$. In p–Pb collisions instead no medium is expected to form, and thus no jet quenching takes place and the R_{AA} is here, too, equal to one. A similar picture is given in Figure 9.13. The direct photon nuclear modification factor in 0–10% central Pb–Pb collisions is plotted together with the π^0 and η meson R_{AA} in the same centrality class (measured within this thesis work) and with the π^0 R_{AA} in p–Pb collisions at $\sqrt{s_{\mathrm{NN}}} = 5.02$ TeV centre-of-mass energy [212]. The direct photon R_{AA} is plotted only for the data points above 2.3 GeV/c, for visibility. The same figure with also the low-p_{T} data points is shown in Appendix F.

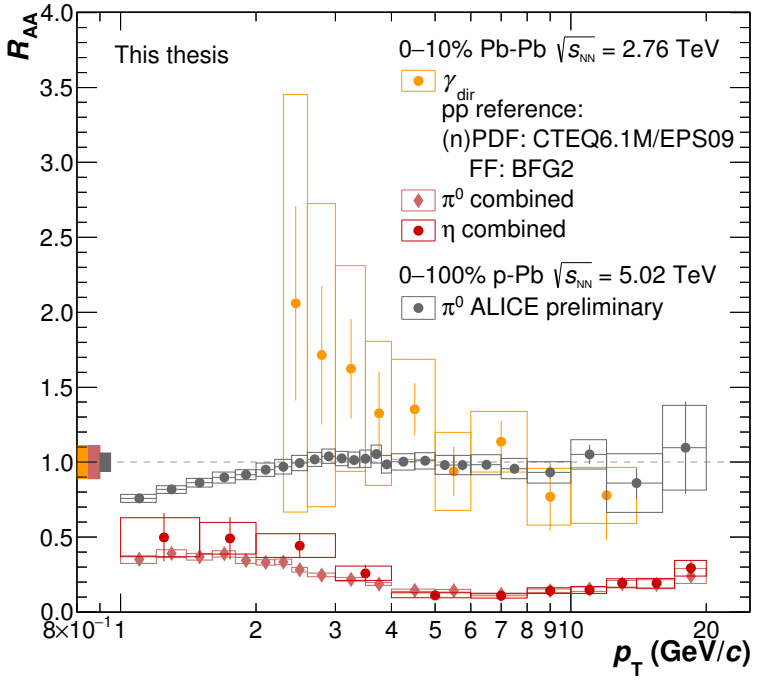

FIGURE 9.13: Direct photon nuclear modification factor R_{AA} in 0–10% Pb–Pb collisions at $\sqrt{s_{\mathrm{NN}}} = 2.76$ TeV compared to the neutral pion and η meson R_{AA}, in the same centrality class and collision energy, and to the neutral pion R_{AA} measured in 0–100% p–Pb collisions at $\sqrt{s_{\mathrm{NN}}} = 5.02$ TeV centre-of-mass energy [212]. The coloured boxes around unity represent the normalisation uncertainty.

For Figure 9.13, the same conclusions are reached as for Figure 1.10. The direct photon R_{AA} is consistent with unity, and similarly is observed also for the neutral pion R_{AA} in p–Pb collisions, while the π^0 and η meson R_{AA} in Pb–Pb collisions shows the typical suppression caused by jet quenching.

Conclusions

The study of the Quark-Gluon Plasma characteristics is performed exploring a variety of observables. Particle production is perhaps the most straight forward of these. The transverse momentum spectrum of the hadrons carries information about the history of the particle. After the liberation of the partonic degrees of freedom in the initial stage of a heavy-ion collision, quarks and gluons interact with each other while expanding, pushed by the pressure gradients between the fireball, in which they collectively move, and the surrounding vacuum. The parton energy loss due to hard and soft scattering translates into a depletion of the measured hadronic invariant yields at high-p_{T} and it clearly emerges in the comparison to hadronic yields measured in pp collisions, assumed as baseline measurement where there is no QGP formation. The collective motion of the particles within the fireball hints at another aspect of the QGP: its similarity to a fluid, not only for the existence of a phase transition between hadronic and partonic phase, but also for the pattern followed in the system evolution. Hydrodynamical models treating the QGP as a viscous fluid, in expansion and going towards thermal equilibrium, give a remarkably good description of the system evolution from the initial fluctuations up to the hadronisation phase, where the analogy with a liquid breaks down. However, the collective flow continues after hadronisation and before freeze-out, and it influences the final hadron yields. The measured hadron transverse momentum spectra are blue-shifted, as expected from an emitting source expanding towards the observer, *i.e.* the detector.

The measurement of neutral pion and η meson in Pb–Pb collisions presented in this thesis contributes to the study of identified particle production in an environment with strongly interacting matter and high energy density. In the low transverse momentum region, for $p_{\mathrm{T}} < 3$ GeV/c, the measured yields are in agreement with hydrodynamical models. At high-p_{T}, the suppression pattern of the hadron yields has been observed in the measurement of the nuclear modification factor R_{AA}. The centrality dependence of the R_{AA} has also been confirmed. This dependence is expected considering that the medium created in central collisions has a much higher energy density compared to what is created in semi-central collisions, where the particle multiplicity is lower. The comparison to theory calculations shows a preference for models relying on a simple LO and NLO pQCD treatment of the parton energy loss. The DCZW model and the Djordjevic *et al.* calculations are in good agreement with the π^0 R_{AA}. DCZW assumes that the parton loses energy via gluon emission, induced by hard scattering with other partons in the dense QCD medium before hadronisation. The suppression due to energy loss is governed by the jet transport coefficient, which is related to the parton density distribution modified by the medium, and is therefore connected to the medium properties. On the other hand, in the Djordjevic *et al.* model the focus is on a separate treatment of the radiative and collisional parton energy loss. This approximation

holds within the ansatz of small energy loss, thus of soft gluon and soft rescattering, respectively. The prediction for the R_{AA} of the η meson partially underestimates the observed suppression. This can be explained considering that the η fragmentation functions are not well constrained because of the few existing measurements at this energy regime. In this regard, the results of both neutral mesons of this thesis work will help improving future calculations.

Modifications of the measured yields by radial flow have also been investigated, using the ratio of the η to π^0 meson as a function of the transverse momentum. The effects of radial flow can be emphasised if compared to the η/π^0 ratio using the m_{T}-scaled approximation. An enhancement of the ratio at intermediate transverse momentum, around 2–4 GeV/c, and depletion at low-p_{T} with respect to the m_{T}-scaling expectation for the ratio could be considered in line with the influence of radial flow on the particle momentum. Moreover, the enhancement at intermediate p_{T} is smaller in the semi-central classes. Again, it could be explained considering that the fireball produced after the semi-central collision is smaller and has a shorter lifetime. Adding to it the observed dependence of the transverse flow velocity on centrality, it follows that the flow does not have time to build up as it happens in central collisions. Last, the mass ordering due to radial flow has been studied comparing the η to π^0 ratio to the charged kaon to pion ratio: the η mass is larger than the kaon mass, enough for a difference to be visible. Taking as reference point the enhancement at intermediate p_{T}, also present in the $\mathrm{K}^{\pm}/\pi^{\pm}$ ratio, a shift towards higher p_{T} is indeed observed for the η/π^0 ratio. This is in agreement with the concept that the mass ordering due to radial flow leads to a larger momentum shift for the heavier particles. Unfortunately, the uncertainties of the η/π^0 ratio are too large to draw clear conclusions.

Going backwards in reconstructing the evolution of the system after the collision, there is a limit beyond which we cannot go with the study of hadron spectra alone. Direct photons are among the probes that allow for the study of the initial stages of the collision. As electromagnetic probes, they are not influenced by the strong interaction that affects hadrons and the information they carry arrives unchanged to us. Unfortunately, the photons originating from the thermal phase of the medium, the one we want to understand better, are to be picked out of a sea of background signal from decay photons which are produced in much larger abundance. Therefore, two key points of the direct photon measurement are, on one hand, to achieve a high purity of the inclusive primary photon sample, on the other hand, to have the best possible description of the decay photon contribution, which is to be subtracted from the former. The photon double ratio R_γ is the observable that immediately reveals the presence of direct photons, when it is above unity. In this thesis work, a thermal photon signal has been observed in the centrality class 0–10% with 1.5σ significance, considering the data points in the transverse momentum range $1 < p_{\mathrm{T}} < 1.6$ GeV/c. The prompt photon contribution, dominant above 3 GeV/c, is consistent with the pQCD NLO calculations for direct photons. The direct photon spectrum is extracted using the inclusive photon spectra and the R_γ, in order to reduce the systematic uncertainties. The effective temperature is extracted as inverse slope of an exponential fit to this spectrum, after subtracting the prompt photon component. It is important to remember that this is not the actual temperature of the source emitting thermal photons: the source is expanding, therefore the radial flow blue-shifts the initial temperature to the measured one. The fit in the range $1 < p_{\mathrm{T}} < 2.2$ GeV/c returns an effective temperature of $T_{\mathrm{eff}} = 245 \pm 23^{\mathrm{stat}} \pm 53^{\mathrm{syst}}$ MeV and $T_{\mathrm{eff}} = 276 \pm 40^{\mathrm{stat}} \pm 66^{\mathrm{syst}}$ MeV for 0–10% and 20–40% central Pb–Pb collisions, respectively. More information on the thermal temperature and on the system evolution can be obtained

with the comparison to models. For this reason, the direct photon spectrum and the photon double ratio are compared to theoretical predictions for the direct photon production. The core assumptions in all of them are the formation of a Quark-Gluon Plasma after a heavy-ion collision and that thermal and prompt photons compose the direct photon signal. Then, the models distinguish themselves from one another by the description of the system evolution, for the initial conditions set for it and for the different sources of photons considered. Despite their diversity, all the predictions show a good agreement with the data. Unfortunately, this similarity across the models does not make possible to narrow down which of these is on the right path: a very high precision measurement and much smaller systematic uncertainties would be needed, especially below 2 GeV/c. On the theory side, an interesting outlook is given by the growing importance of the pre-equilibrium photons, whose contribution could help disentangle between the different descriptions of the origin of the direct photons signal. The two measurements of this thesis, neutral mesons and direct photons, are tied together in one last comparison of the nuclear modification factor of the neutral mesons measured in Pb–Pb and p–Pb collisions with the direct photon R_{AA} for the most central collisions. This result completes this work. In the absence of a hot and dense medium, the neutral pion measurement in non-single diffractive p–Pb collisions demonstrates that there is no modification of the hadron spectrum with respect to the baseline offered by the pp measurement. The energy loss induced on the hadrons appears clear in the suppression of the R_{AA} of the neutral mesons in Pb–Pb collisions, where a strongly interacting system is expected to be formed. It is also shown that in the same environment, a probe not sensitive to strong interaction, such as the direct photon production, is unaffected.

Appendix A

Neutral meson invariant mass in transverse momentum bins

The invariant mass distribution of the π^0 and η mesons is studied in transverse momentum slices. In the following, the distributions before and after the event mixing background subtraction will be shown for the centrality classes 0–10% and 20–50%, that are this thesis work main focus. The distributions for 0–5%, 5–10% and 20–40% central collisions are also reported here for completeness.
The figures are ordered with first all the distribution for the π^0 meson then for the η meson, in the centrality classes 0–10%, 0–5%, 5–10%, 20–40% and 20–50%.

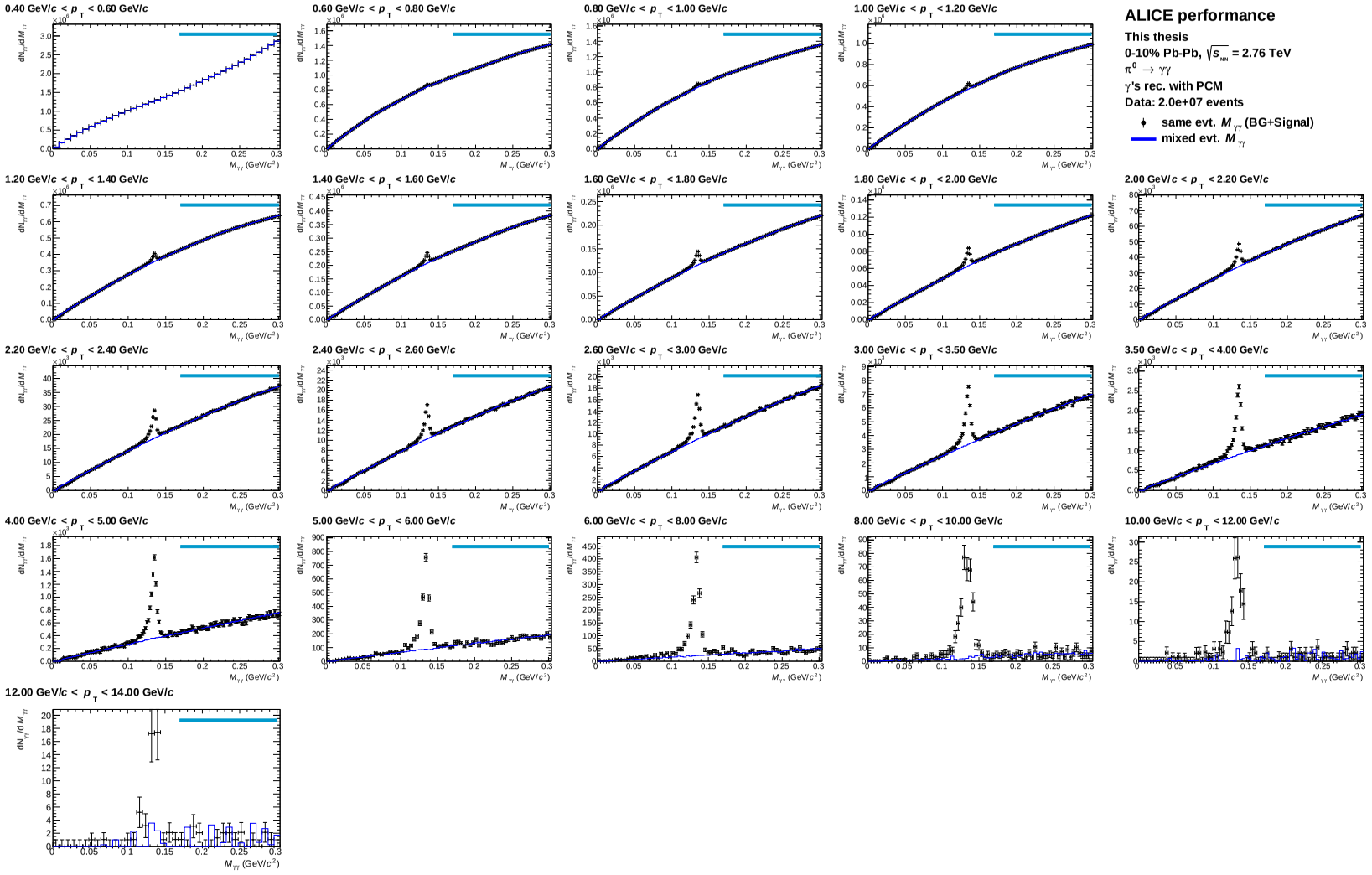

FIGURE A.1: Invariant mass distribution of reconstructed photon pairs $M_{\gamma\gamma}$ around the π^0 meson mass in p_{T} slices in 0–10% Pb–Pb collisions before the background subtraction. The black points show the combined signal and background distribution and the blue histograms show the calculated and normalised mixed event background. The normalisation range, taken from the right side of the peak, is represented by the azure line.

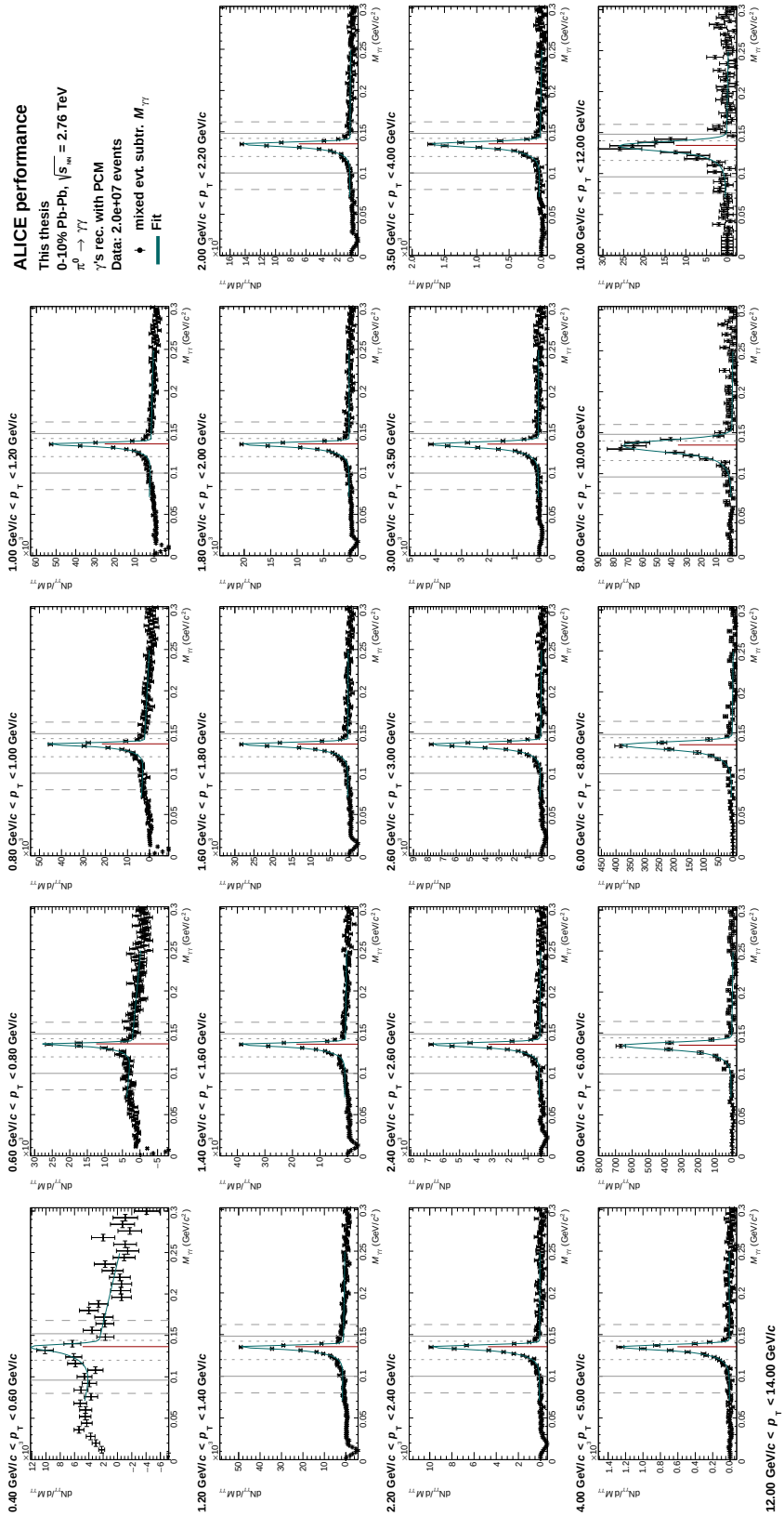

FIGURE A.2: Invariant-mass distribution of reconstructed photon pairs $M_{\gamma\gamma}$ around the π^0 meson mass in p_{T} slices in 0–10% Pb–Pb collisions after the background subtraction (black points). The invariant mass distributions are fitted with Equation 5.7 (cyan line). The black vertical lines represent the standard (solid), narrow (small dashed) and wide (large dashed) integration windows. The red vertical line show the estimated mass position.

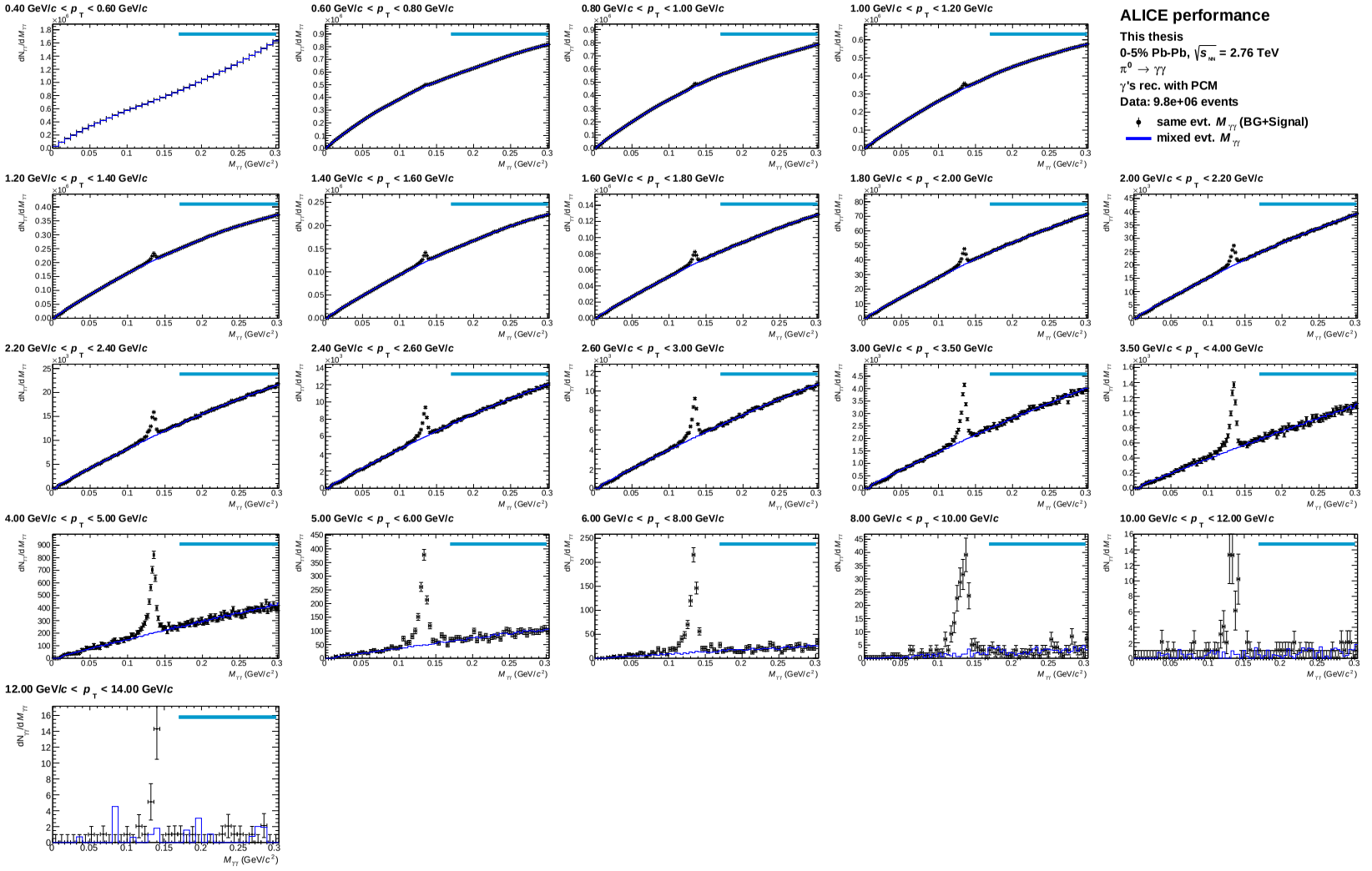

FIGURE A.3: Invariant mass distribution of reconstructed photon pairs $M_{\gamma\gamma}$ around the π^0 meson mass in p_{T} slices in 0–5% Pb–Pb collisions before the background subtraction. The black points show the combined signal and background distribution and the blue histograms show the calculated and normalised mixed event background. The normalisation range, taken from the right side of the peak, is represented by the azure line.

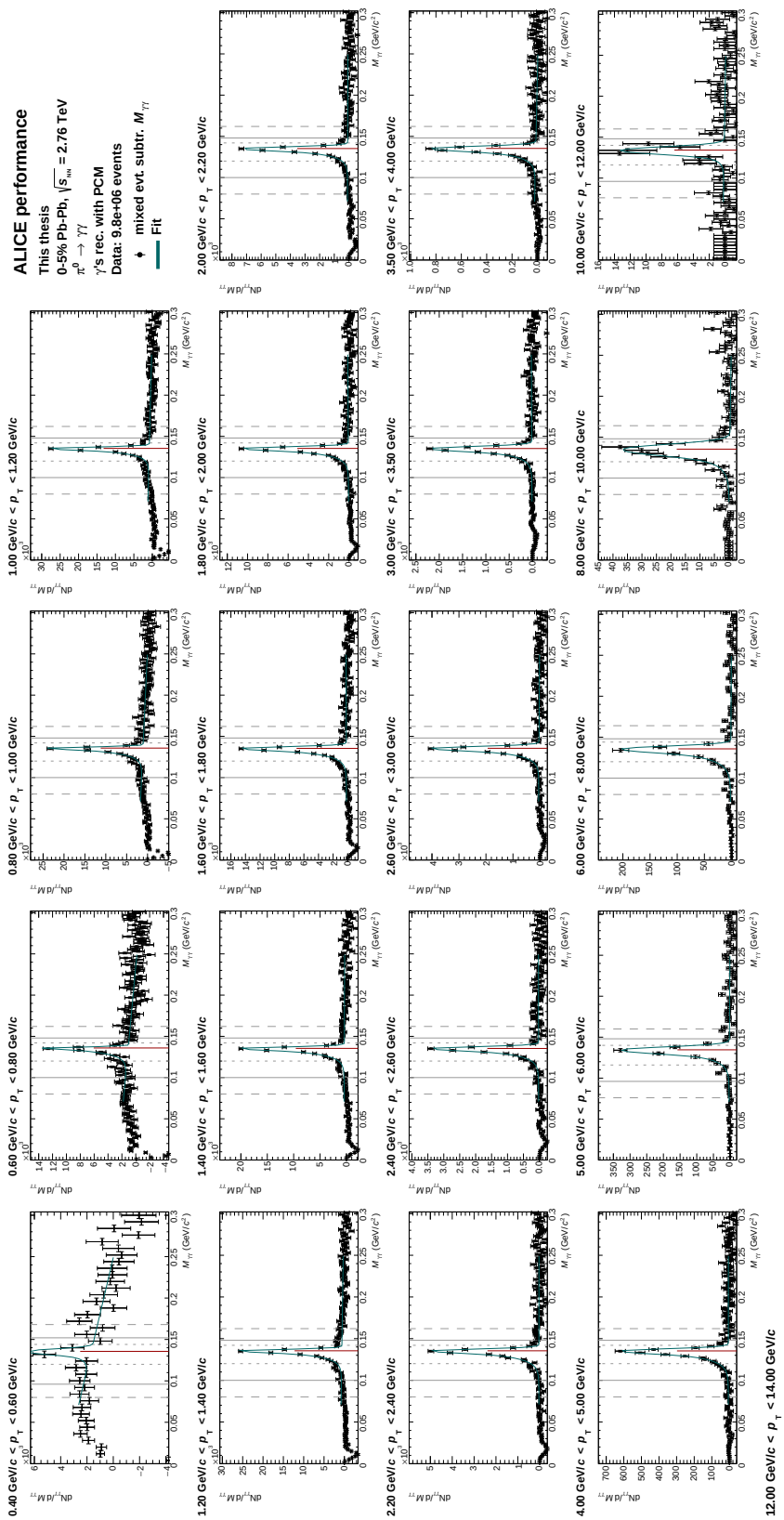

FIGURE A.4: Invariant-mass distribution of reconstructed photon pairs $M_{\gamma\gamma}$ around the π^0 meson mass in p_{T} slices in 0–5% Pb–Pb collisions after the background subtraction (black points). The invariant mass distributions are fitted with Equation 5.7 (cyan line). The black vertical lines represent the standard (solid), narrow (small dashed) and wide (large dashed) integration windows. The red vertical line show the estimated mass position.

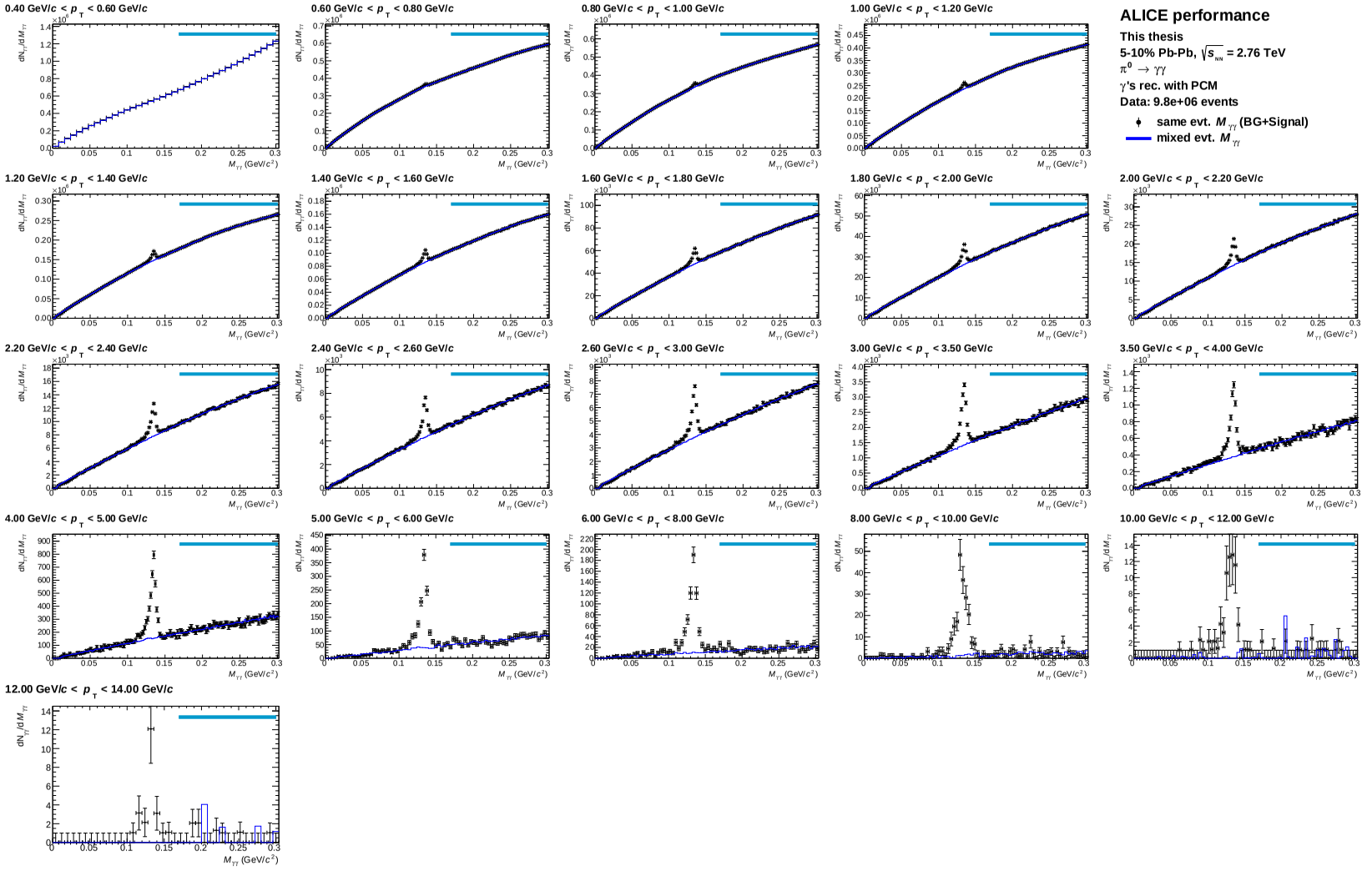

FIGURE A.5: Invariant mass distribution of reconstructed photon pairs $M_{\gamma\gamma}$ around the π^0 meson mass in p_{T} slices in 5–10% Pb–Pb collisions before the background subtraction. The black points show the combined signal and background distribution and the blue histograms show the calculated and normalised mixed event background. The normalisation range, taken from the right side of the peak, is represented by the azure line.

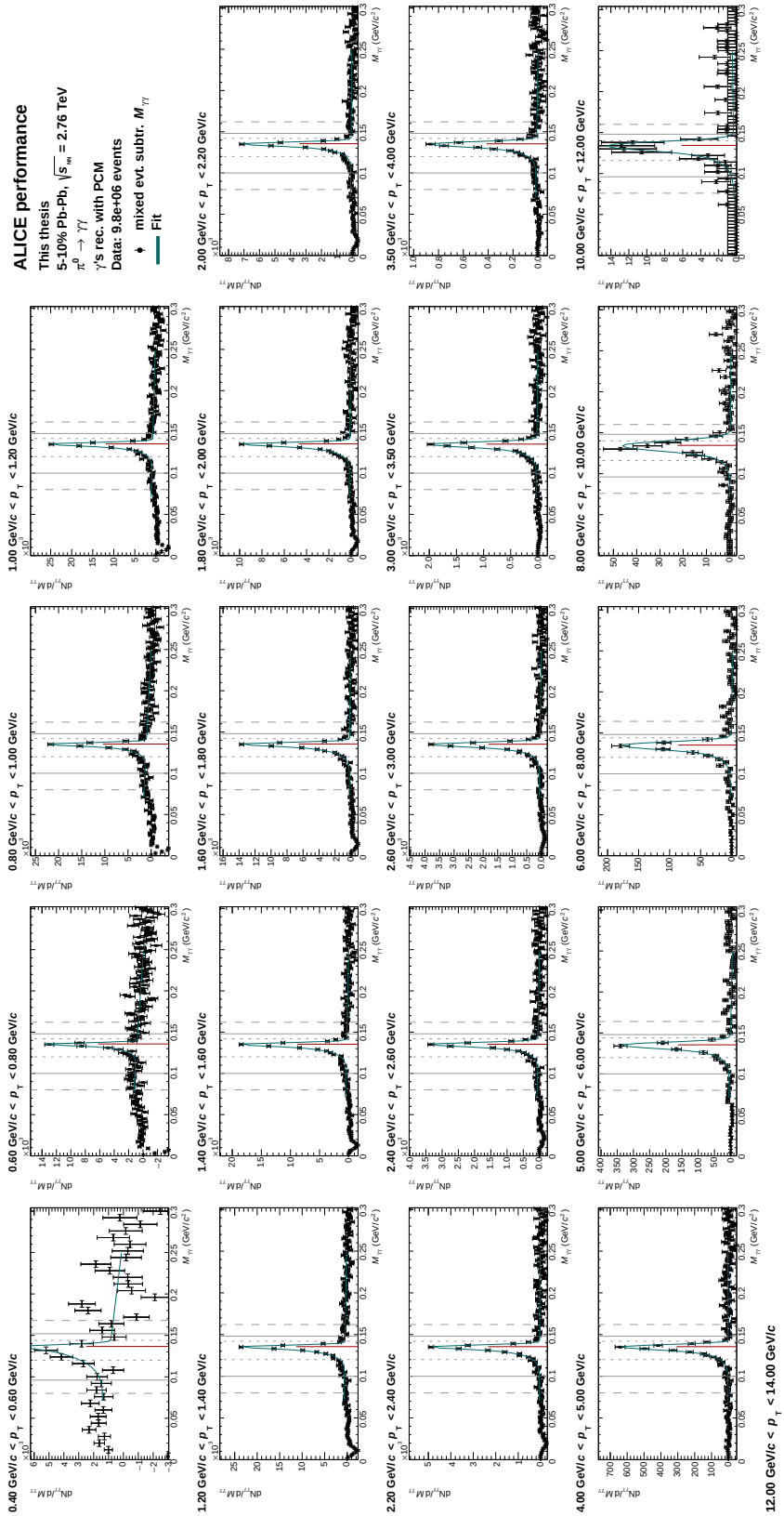

FIGURE A.6: Invariant-mass distribution of reconstructed photon pairs $M_{\gamma\gamma}$ around the π^0 meson mass in p_{T} slices in 5–10% Pb–Pb collisions after the background subtraction (black points). The invariant mass distributions are fitted with Equation 5.7 (cyan line). The black vertical lines represent the standard (solid), narrow (small dashed) and wide (large dashed) integration windows. The red vertical line show the estimated mass position.

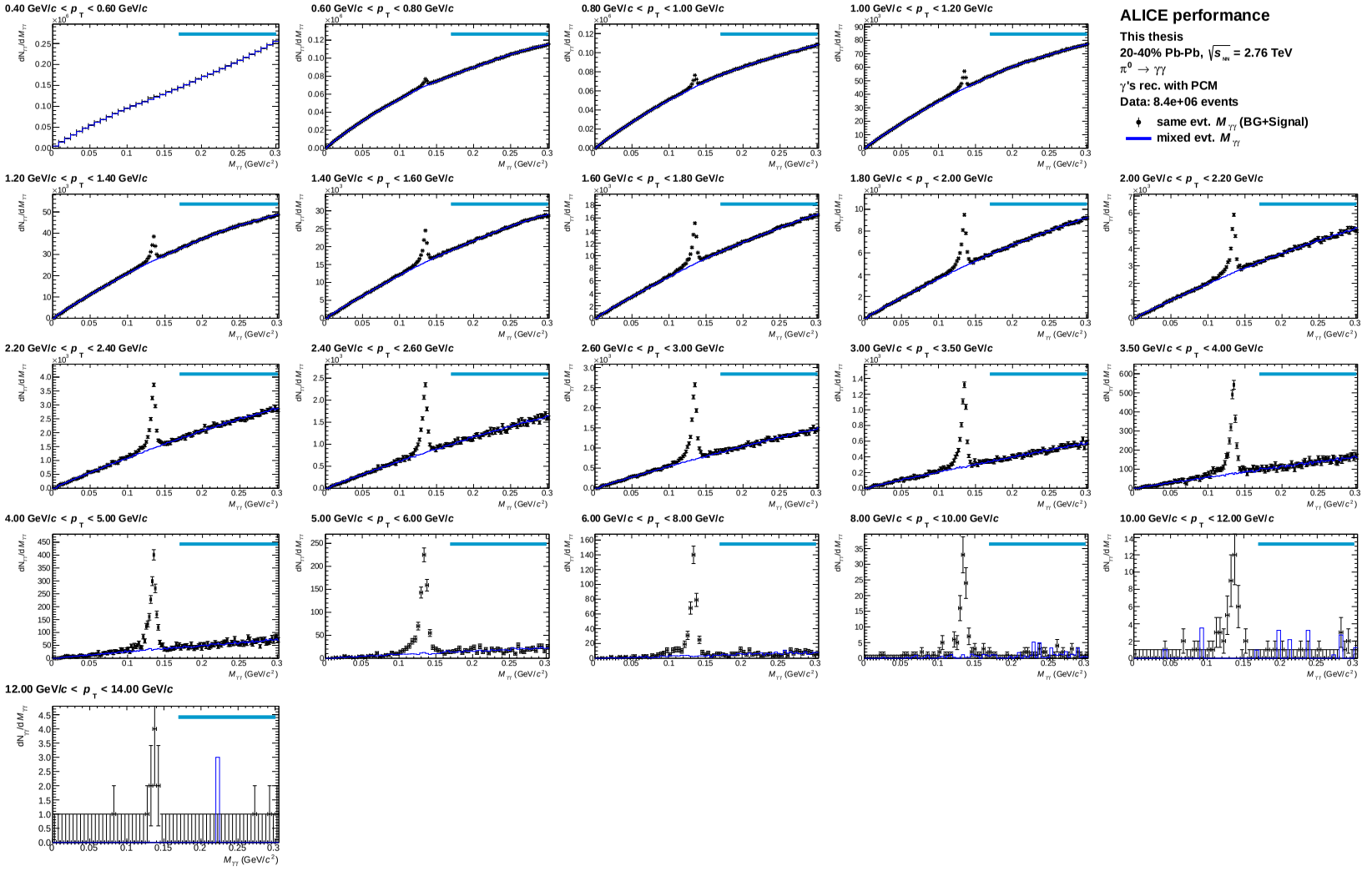

FIGURE A.7: Invariant mass distribution of reconstructed photon pairs $M_{\gamma\gamma}$ around the π^0 meson mass in p_{T} slices in 20–40% Pb–Pb collisions before the background subtraction. The black points show the combined signal and background distribution and the blue histograms show the calculated and normalised mixed event background. The normalisation range, taken from the right side of the peak, is represented by the azure line.

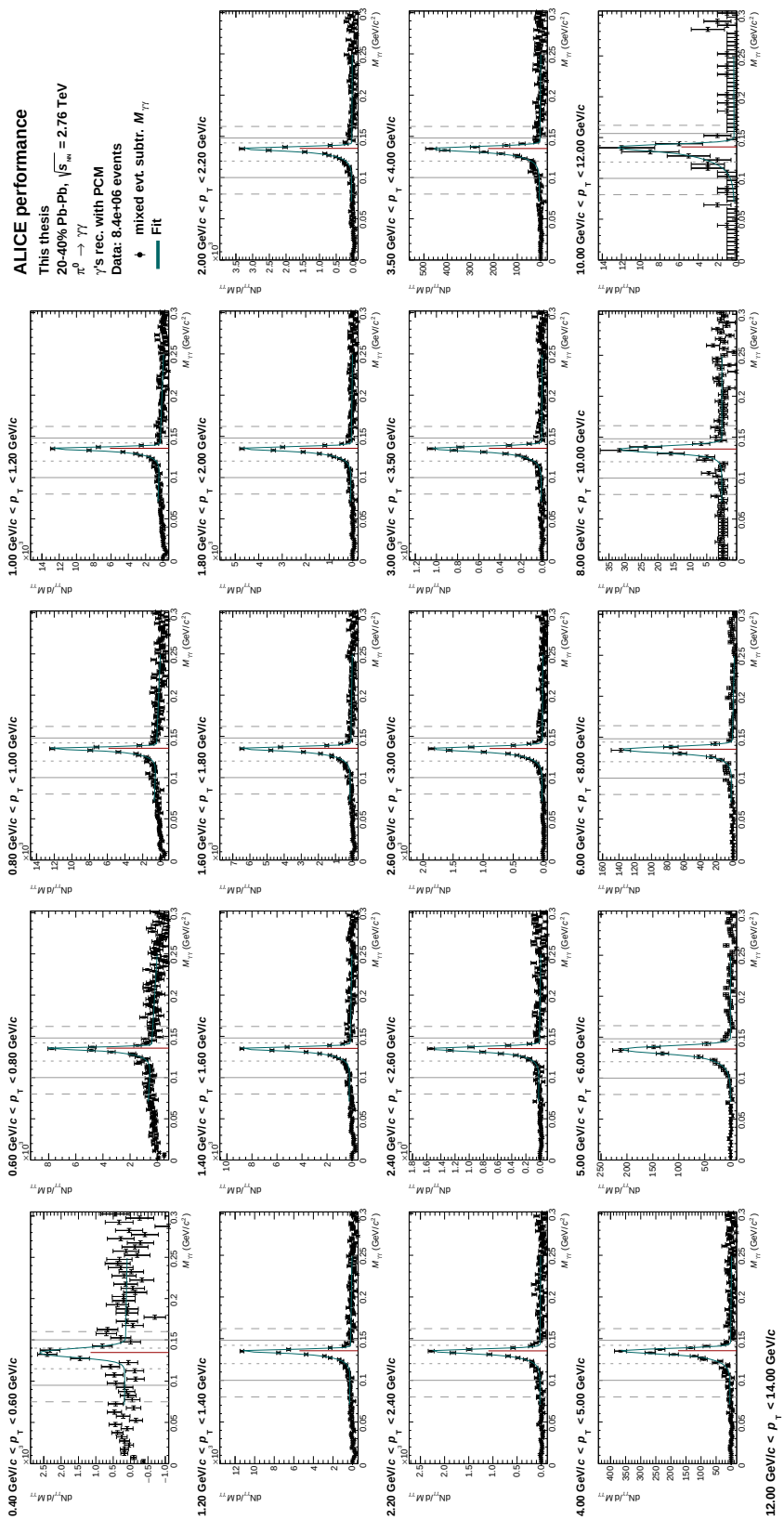

FIGURE A.8: Invariant-mass distribution of reconstructed photon pairs $M_{\gamma\gamma}$ around the π^0 meson mass in p_{T} slices in 20–40% Pb–Pb collisions after the background subtraction (black points). The invariant mass distributions are fitted with Equation 5.7 (cyan line). The black vertical lines represent the standard (solid), narrow (small dashed) and wide (large dashed) integration windows. The red vertical line show the estimated mass position.

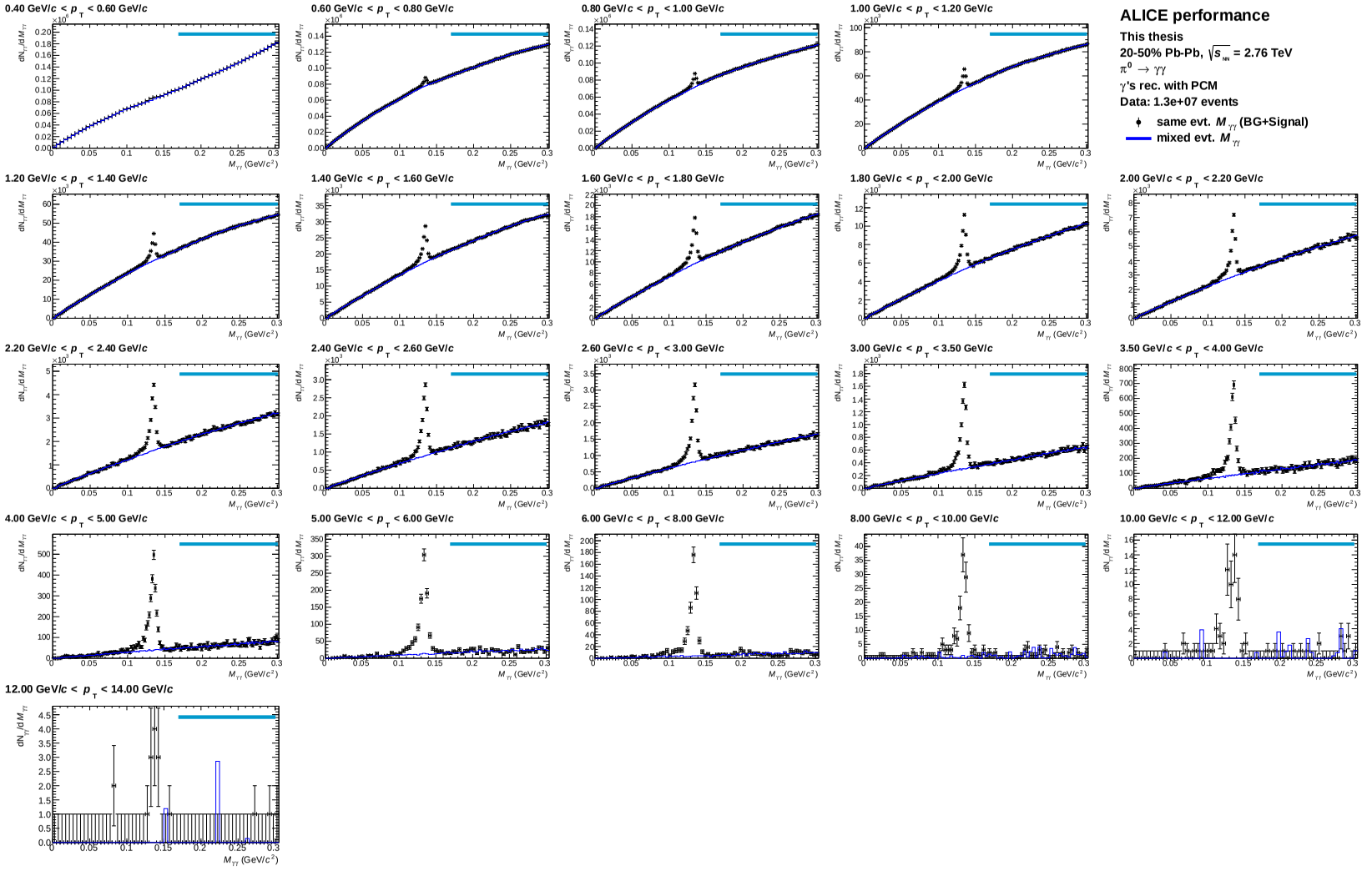

FIGURE A.9: Invariant mass distribution of reconstructed photon pairs $M_{\gamma\gamma}$ around the π^0 meson mass in p_{T} slices in 20–50% Pb–Pb collisions before the background subtraction. The black points show the combined signal and background distribution and the blue histograms show the calculated and normalised mixed event background. The normalisation range, taken from the right side of the peak, is represented by the azure line.

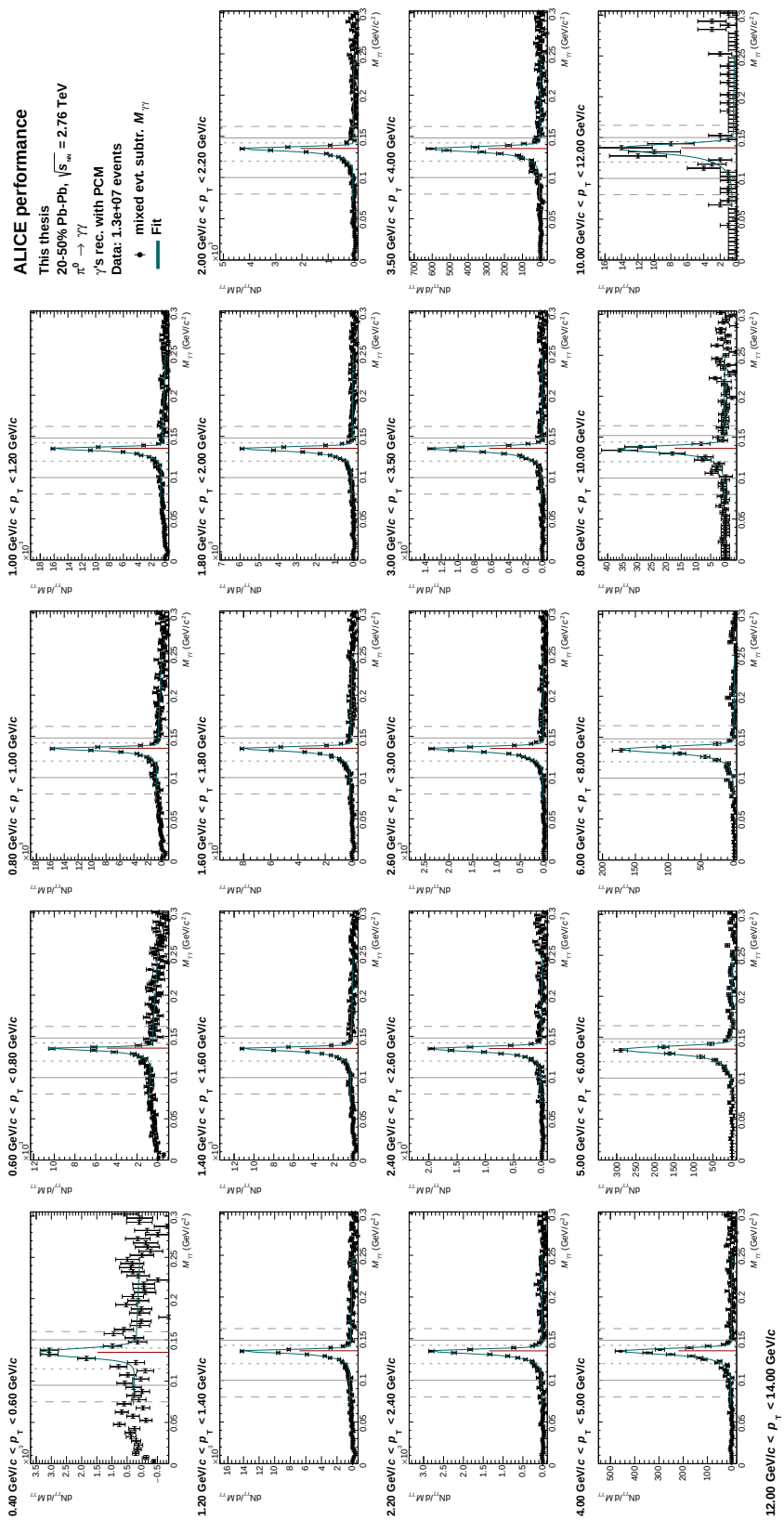

FIGURE A.10: Invariant-mass distribution of reconstructed photon pairs $M_{\gamma\gamma}$ around the π^0 meson mass in p_{T} slices in 20–50% Pb–Pb collisions after the background subtraction (black points). The invariant mass distributions are fitted with Equation 5.7 (cyan line). The black vertical lines represent the standard (solid), narrow (small dashed) and wide (large dashed) integration windows. The red vertical line show the estimated mass position.

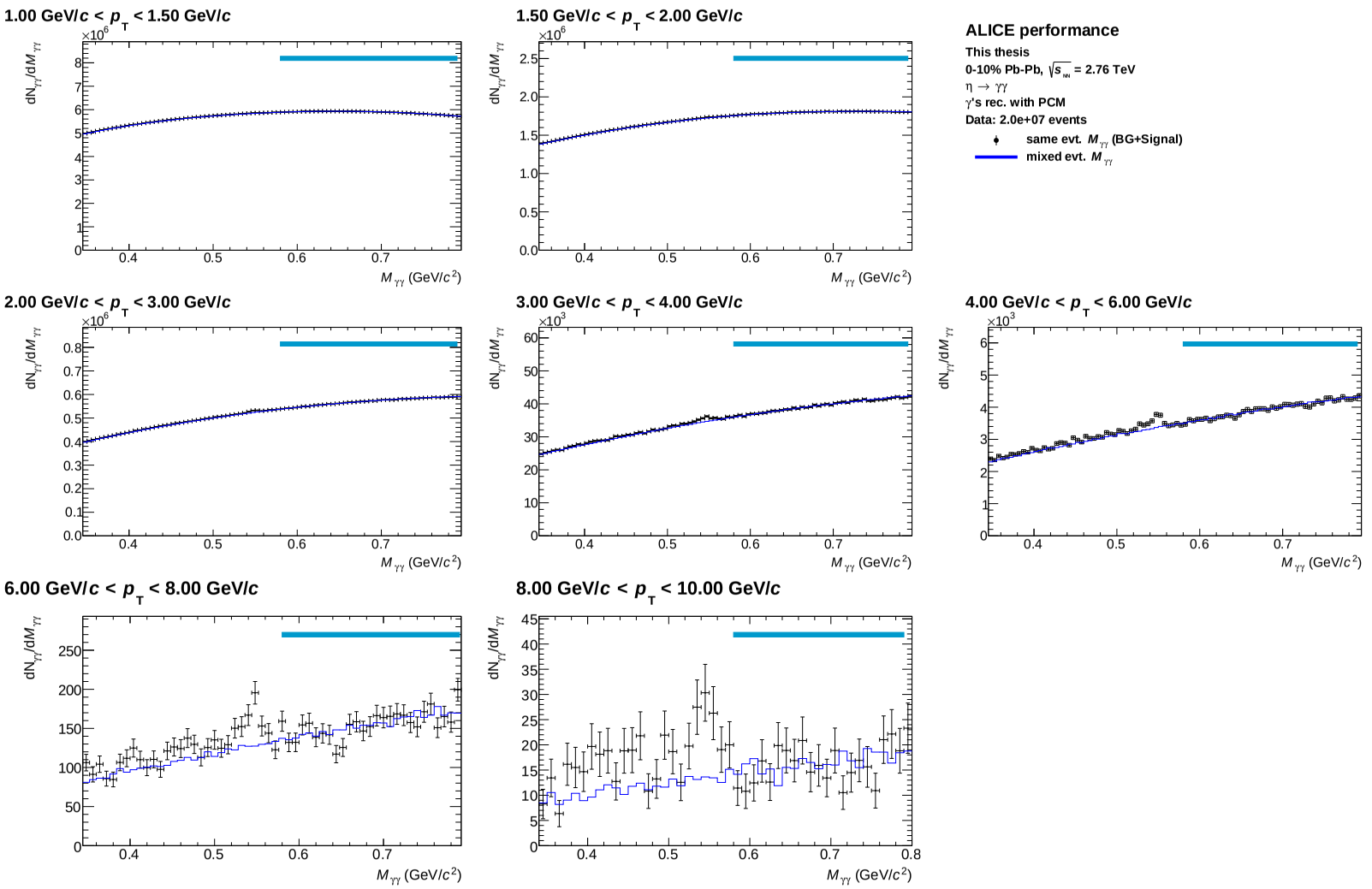

FIGURE A.11: Invariant mass distribution of reconstructed photon pairs $M_{\gamma\gamma}$ around the η meson mass in p_{T} slices in 0–10% Pb–Pb collisions before the background subtraction. The black points show the combined signal and background distribution and the blue histograms show the calculated and normalised mixed event background. The normalisation range, taken from the right side of the peak, is represented by the azure line.

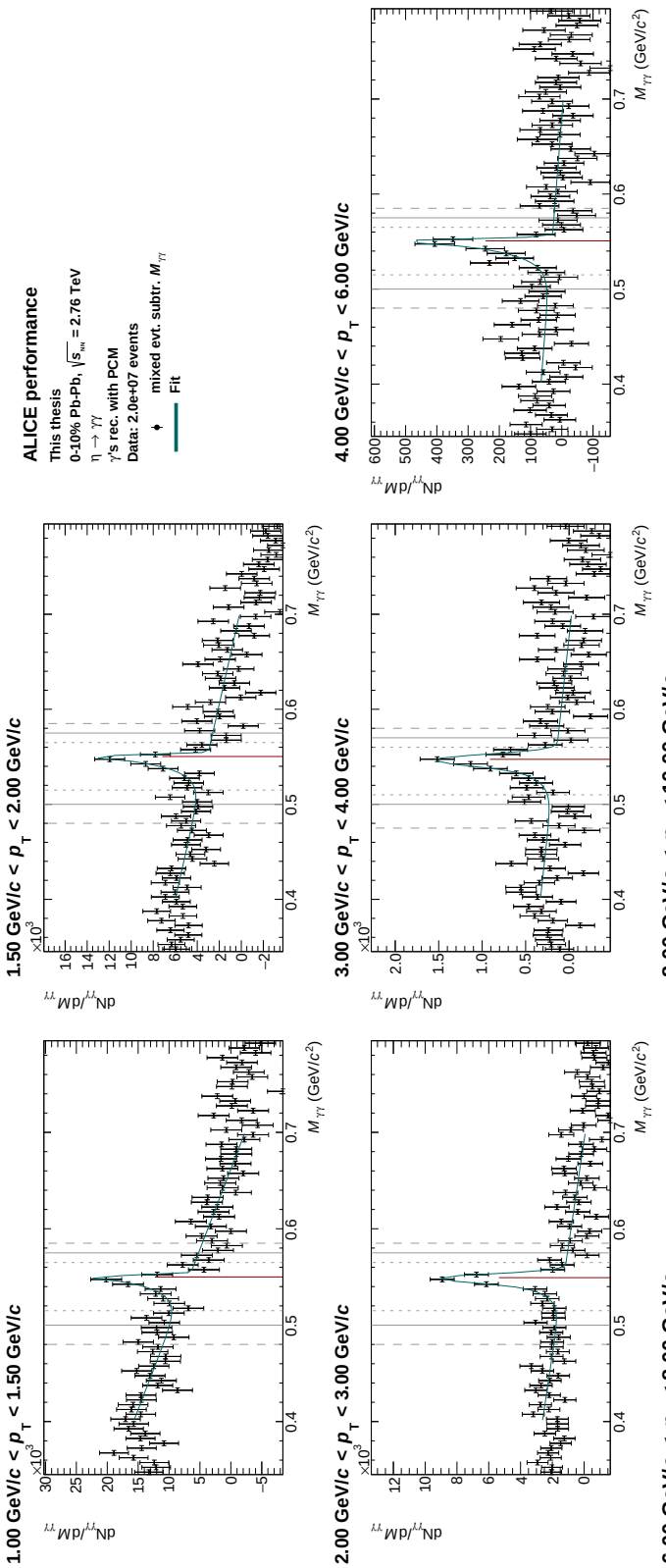

FIGURE A.12: Invariant-mass distribution of reconstructed photon pairs $M_{\gamma\gamma}$ around the η mass in p_{T} slices in 0–10% Pb–Pb collisions after the background subtraction (black points). The invariant mass distributions are fitted with Equation 5.7 (cyan line). The black vertical lines represent the standard (solid), narrow (small dashed) and wide (large dashed) integration windows. The red vertical line show the estimated mass position.

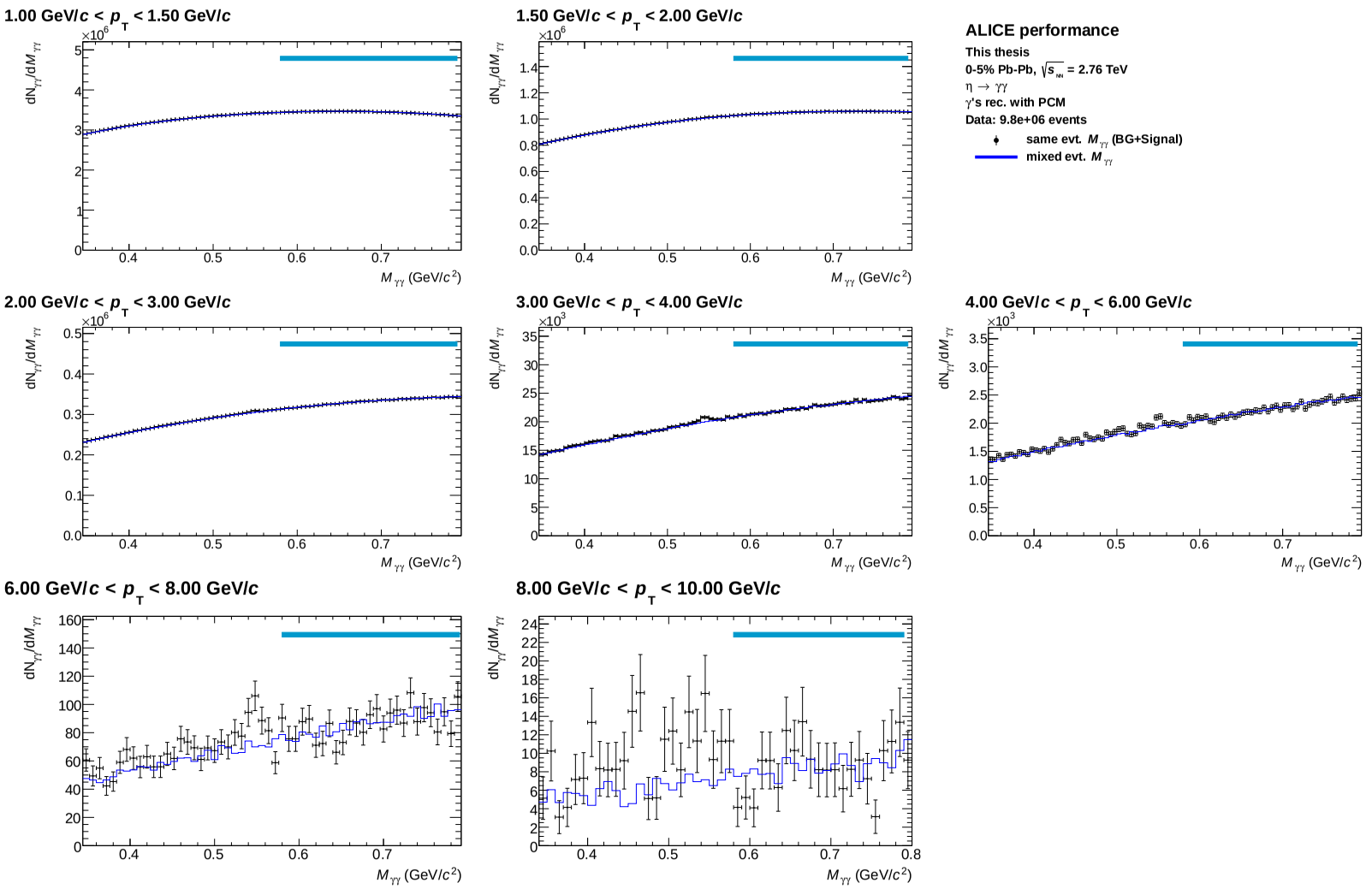

FIGURE A.13: Invariant mass distribution of reconstructed photon pairs $M_{\gamma\gamma}$ around the η meson mass in p_{T} slices in 0–5% Pb–Pb collisions before the background subtraction. The black points show the combined signal and background distribution and the blue histograms show the calculated and normalised mixed event background. The normalisation range, taken from the right side of the peak, is represented by the azure line.

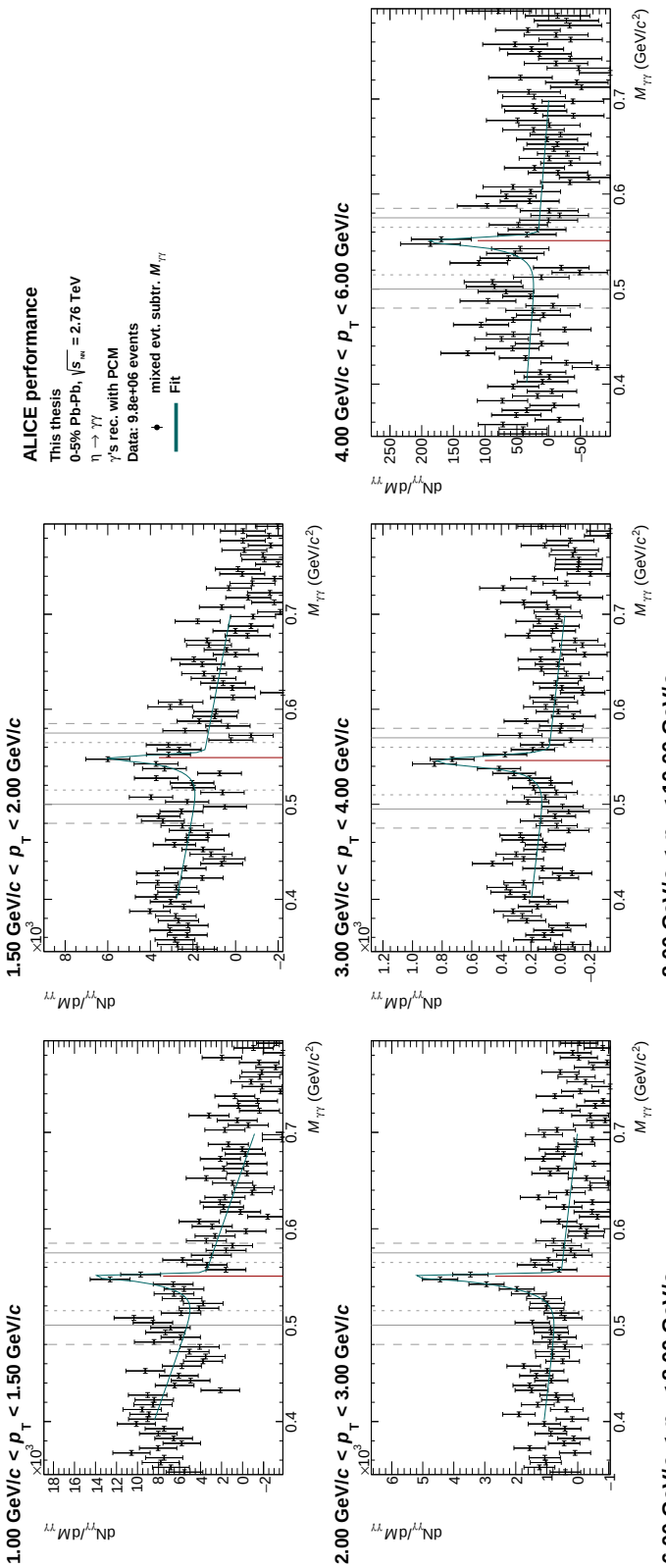

FIGURE A.14: Invariant-mass distribution of reconstructed photon pairs $M_{\gamma\gamma}$ around the η mass in p_{T} slices in 0–5% Pb–Pb collisions after the background subtraction (black points). The invariant mass distributions are fitted with Equation 5.7 (cyan line). The black vertical lines represent the standard (solid), narrow (small dashed) and wide (large dashed) integration windows. The red vertical line show the estimated mass position.

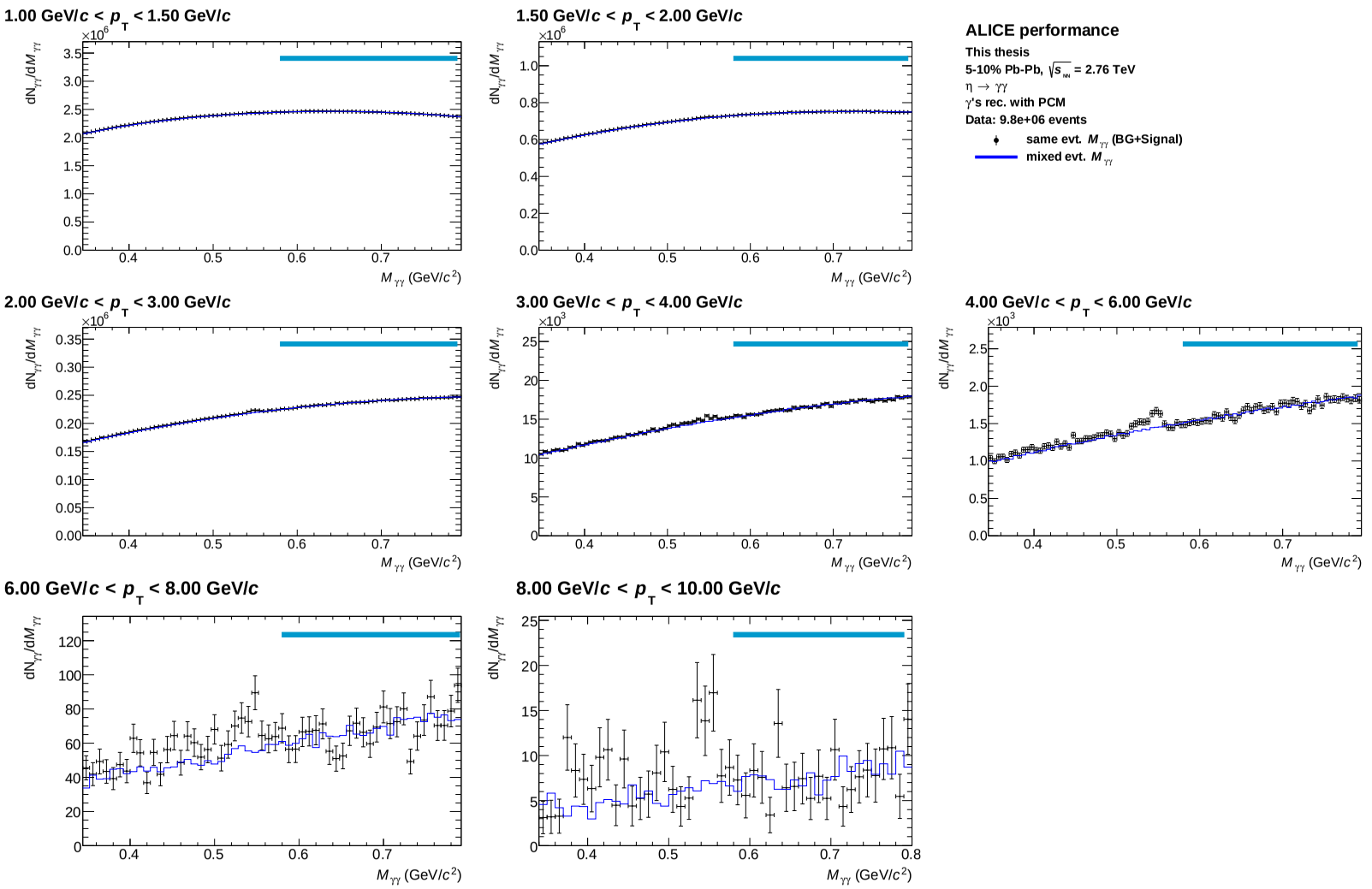

FIGURE A.15: Invariant mass distribution of reconstructed photon pairs $M_{\gamma\gamma}$ around the η meson mass in p_{T} slices in 5–10% Pb–Pb collisions before the background subtraction. The black points show the combined signal and background distribution and the blue histograms show the calculated and normalised mixed event background. The normalisation range, taken from the right side of the peak, is represented by the azure line.

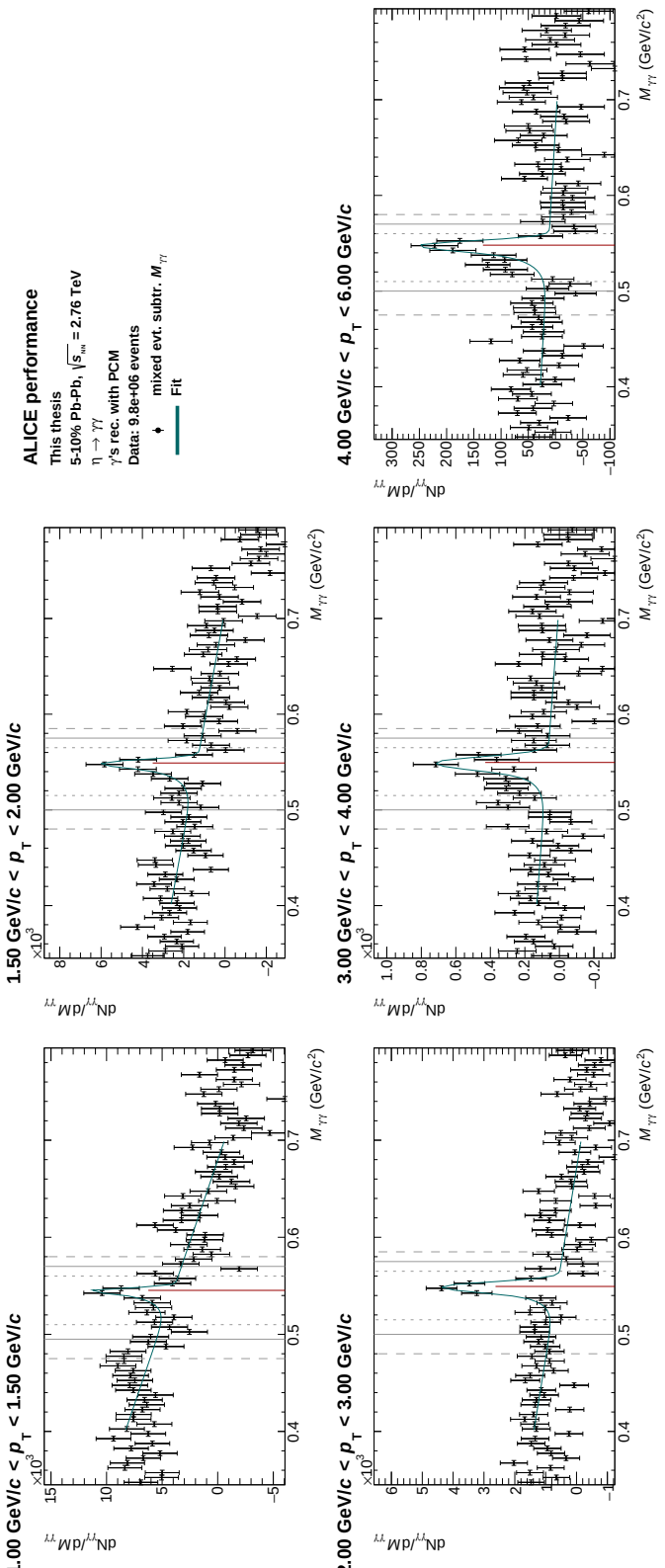

FIGURE A.16: Invariant-mass distribution of reconstructed photon pairs $M_{\gamma\gamma}$ around the η mass in p_{T} slices in 5–10% Pb–Pb collisions after the background subtraction (black points). The invariant mass distributions are fitted with Equation 5.7 (cyan line). The black vertical lines represent the standard (solid), narrow (small dashed) and wide (large dashed) integration windows. The red vertical line show the estimated mass position.

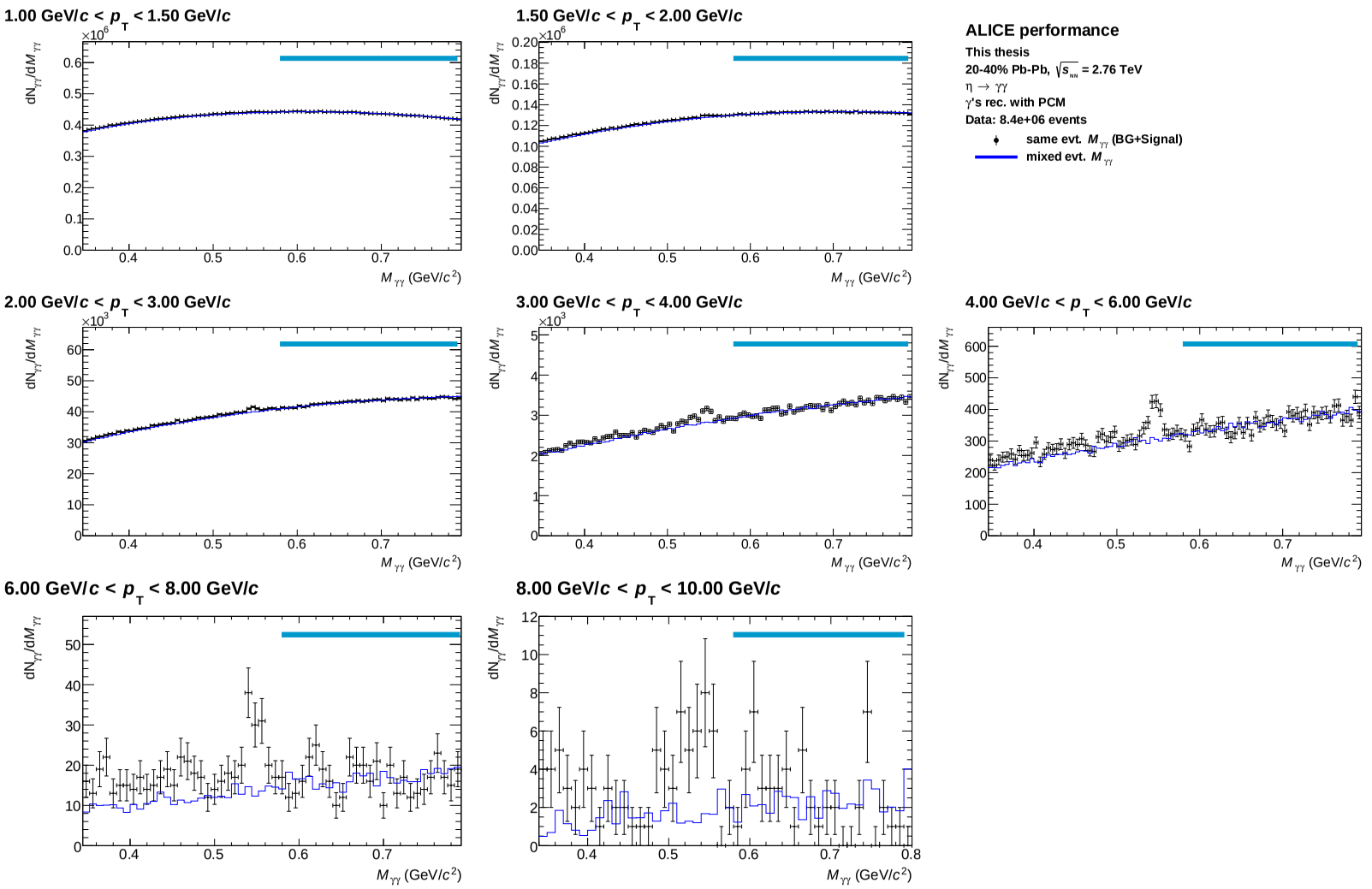

FIGURE A.17: Invariant mass distribution of reconstructed photon pairs $M_{\gamma\gamma}$ around the η mass in p_{T} slices in 20–40% Pb–Pb collisions before the background subtraction. The black points show the combined signal and background distribution and the blue histograms show the calculated and normalised mixed event background. The normalisation range, taken from the right side of the peak, is represented by the azure line.

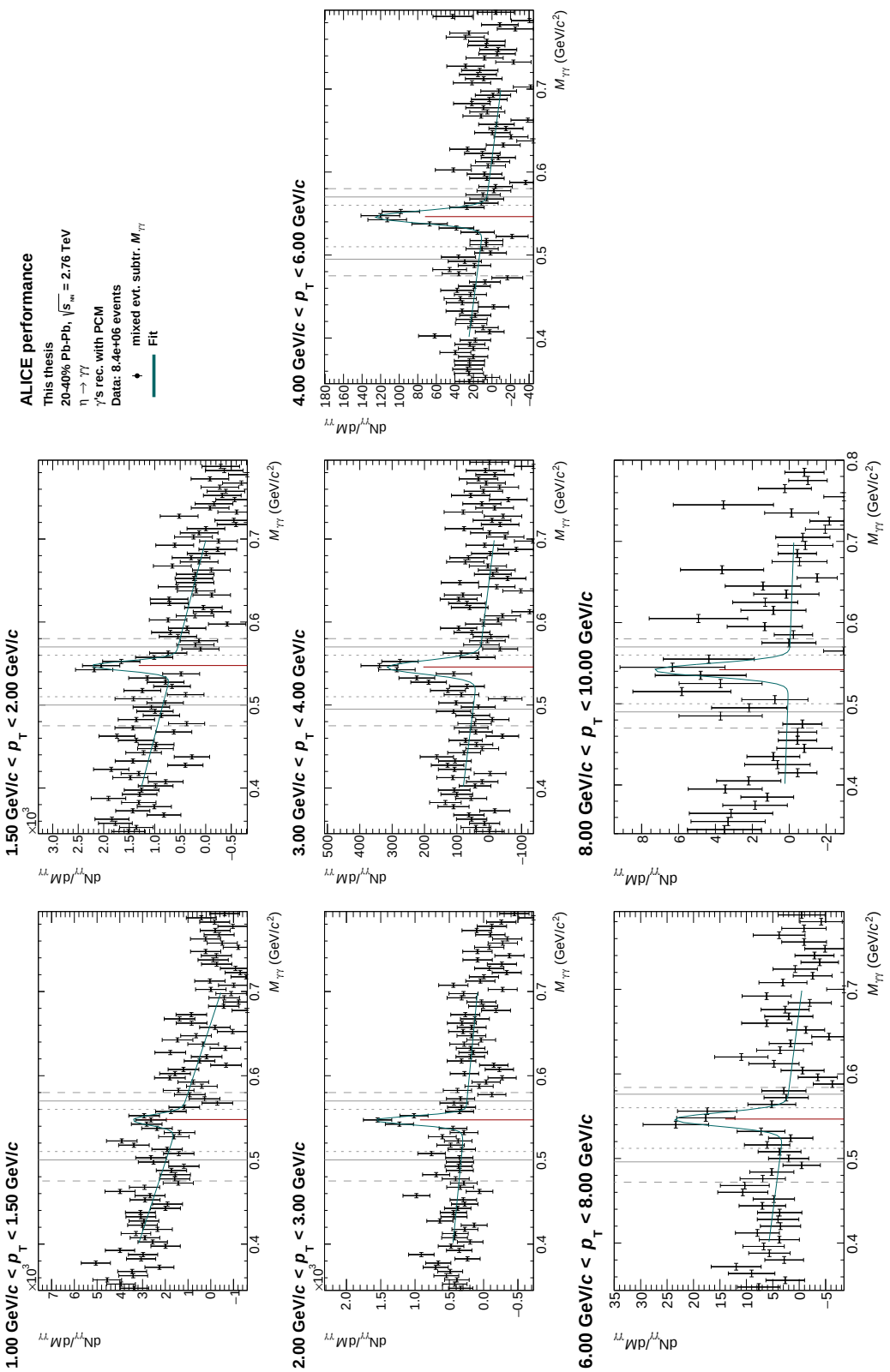

FIGURE A.18: Invariant-mass distribution of reconstructed photon pairs $M_{\gamma\gamma}$ around the η mass in p_{T} slices in 20–40% Pb–Pb collisions after the background subtraction (black points). The invariant mass distributions are fitted with Equation 5.7 (cyan line). The black vertical lines represent the standard (solid), narrow (small dashed) and wide (large dashed) integration windows. The red vertical line show the estimated mass position.

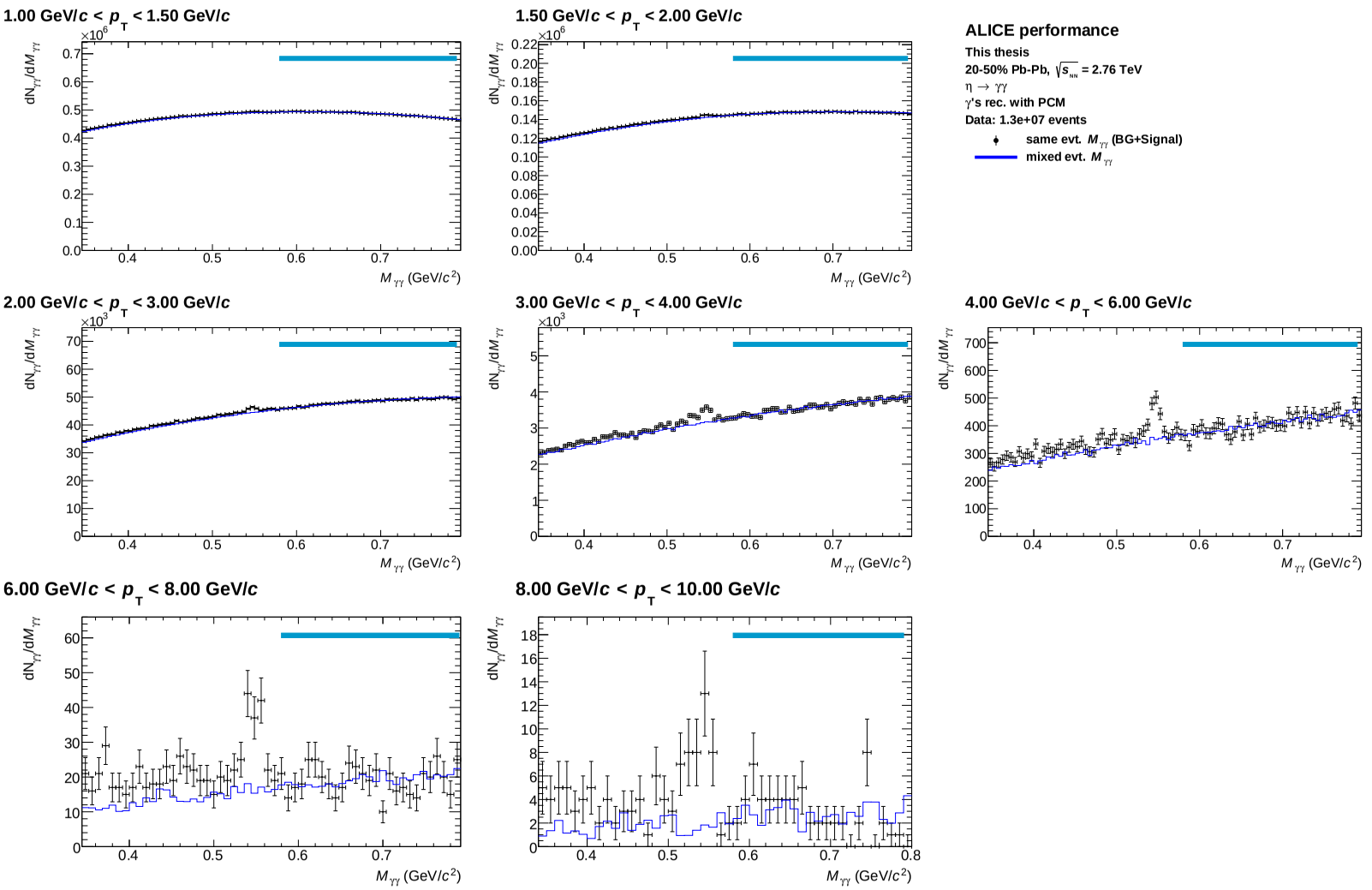

FIGURE A.19: Invariant mass distribution of reconstructed photon pairs $M_{\gamma\gamma}$ around the η mass in p_{T} slices in 20–50% Pb–Pb collisions before the background subtraction. The black points show the combined signal and background distribution and the blue histograms show the calculated and normalised mixed event background. The normalisation range, taken from the right side of the peak, is represented by the azure line.

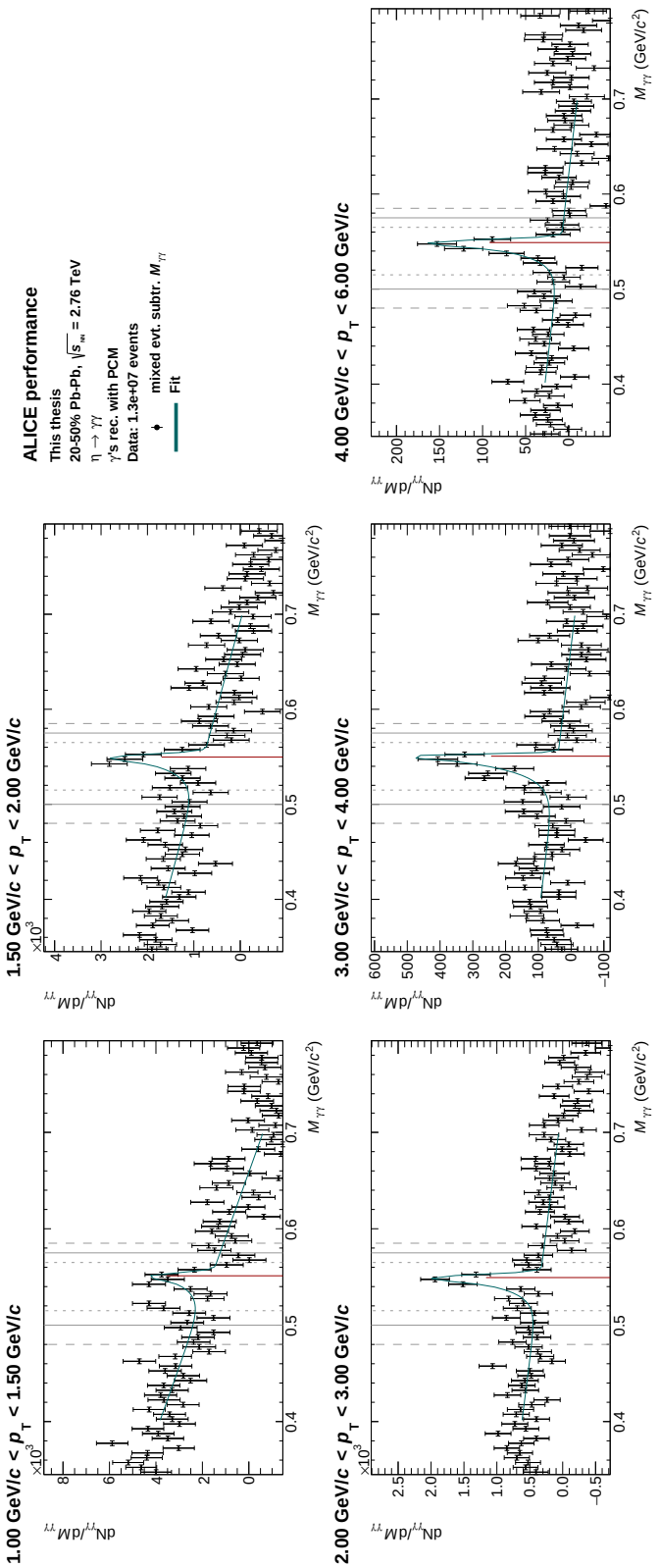

FIGURE A.20: Invariant-mass distribution of reconstructed photon pairs $M_{\gamma\gamma}$ around the η mass in p_{T} slices in 20–50% Pb–Pb collisions after the background subtraction (black points). The invariant mass distributions are fitted with Equation 5.7 (cyan line). The black vertical lines represent the standard (solid), narrow (small dashed) and wide (large dashed) integration windows. The red vertical line show the estimated mass position.

Appendix B

DCA_z distributions for the pile-up contamination

The photon DCA_z distribution from which the pile-up correction is estimated for the π^0 and η meson analysis is studied in the same transverse momentum slices used to extract the meson yields, until it is allowed by the statistics available. In the following, the DCA_z distributions are shown for all the meson categories together and separately, first for the π^0 meson and η meson in the centrality 20–50%, then in the centralities 20–40%.

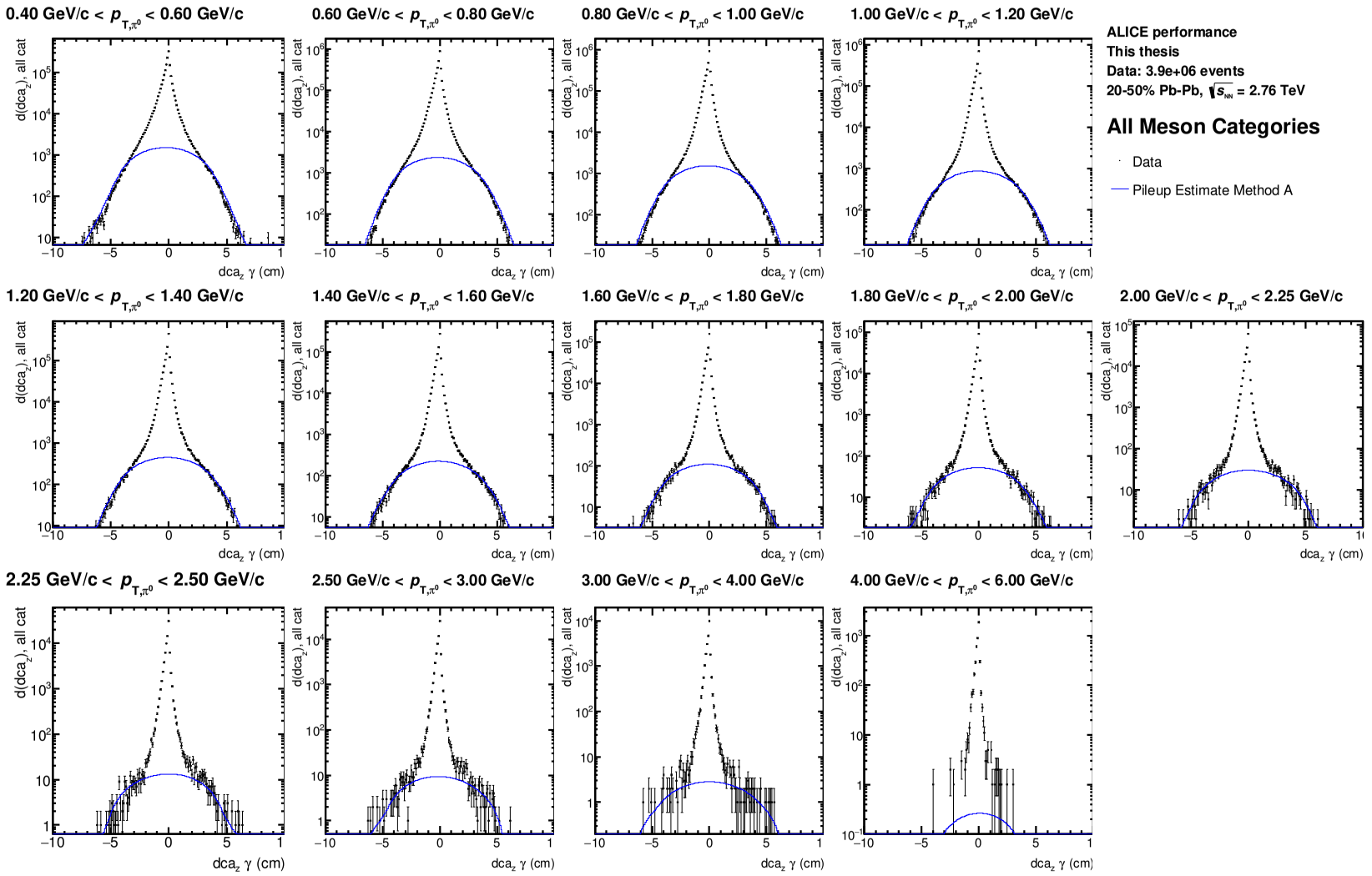

FIGURE B.1: DCA$_z$ distributions for photon from a pair within the π^0 mass region in transverse momentum intervals for the centrality class 20–50%. All the meson categories are shown together.

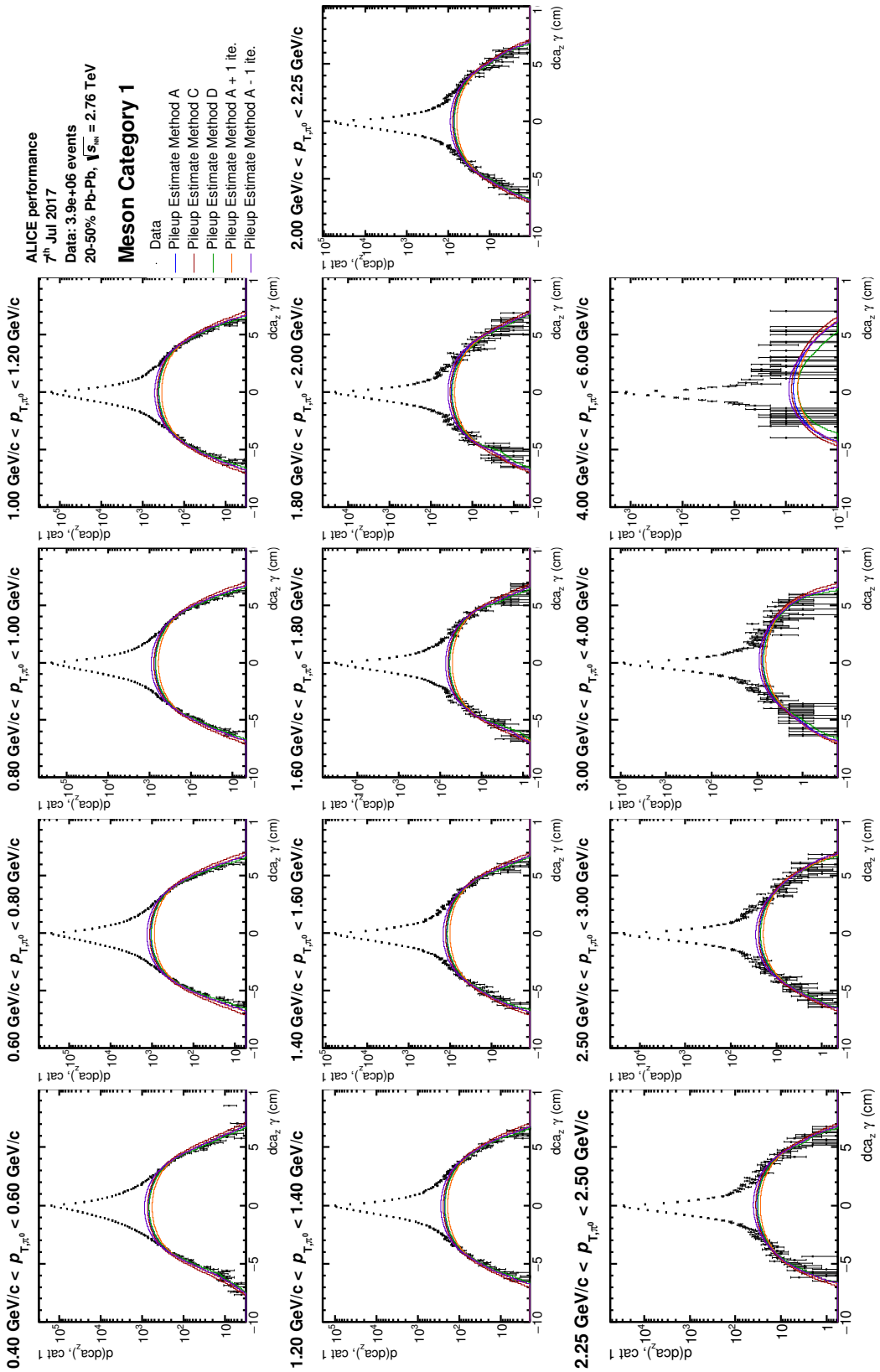

FIGURE B.2: DCA$_z$ distributions for photon from a pair within the π^0 mass region in transverse momentum intervals for meson category one and centrality class 20–50%.

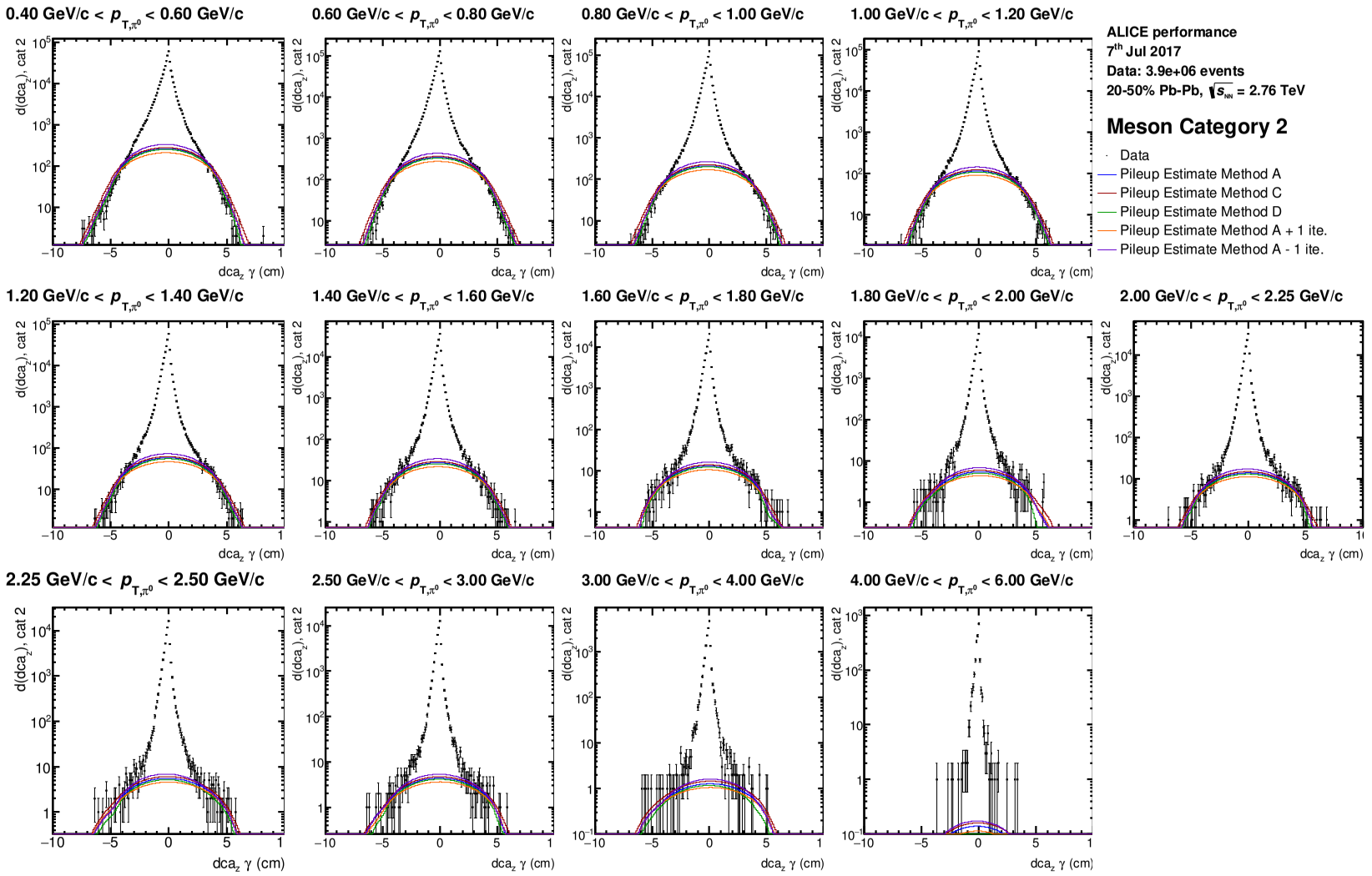

FIGURE B.3: DCA$_z$ distributions for photon from a pair within the π^0 mass region in transverse momentum intervals for meson category two and centrality class 20–50%.

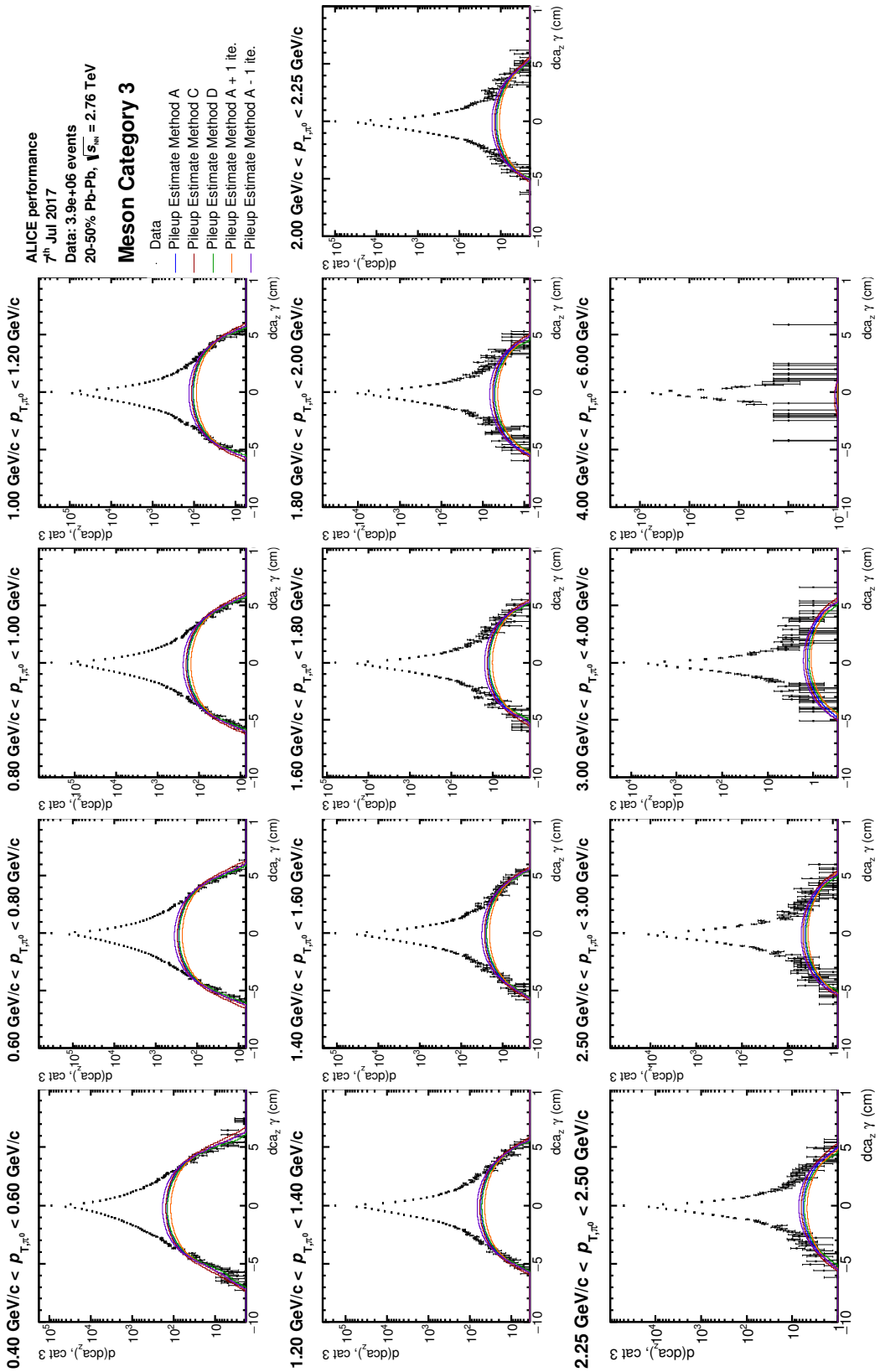

FIGURE B.4: DCA$_z$ distributions for photon from a pair within the π^0 mass region in transverse momentum intervals for meson category three and centrality class 20–50%.

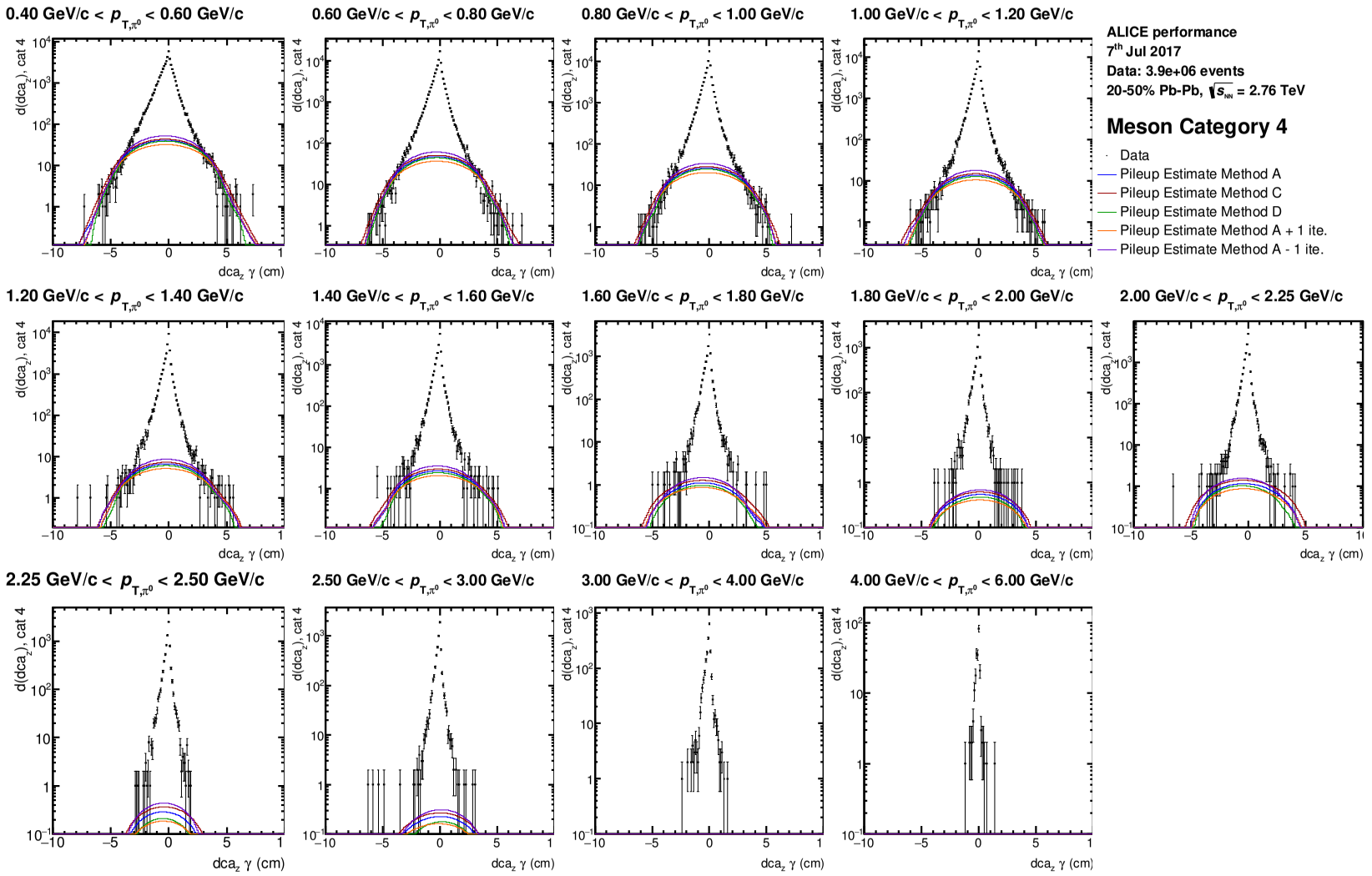

FIGURE B.5: DCA$_z$ distributions for photon from a pair within the π^0 mass region in transverse momentum intervals for meson category four and centrality class 20–50%.

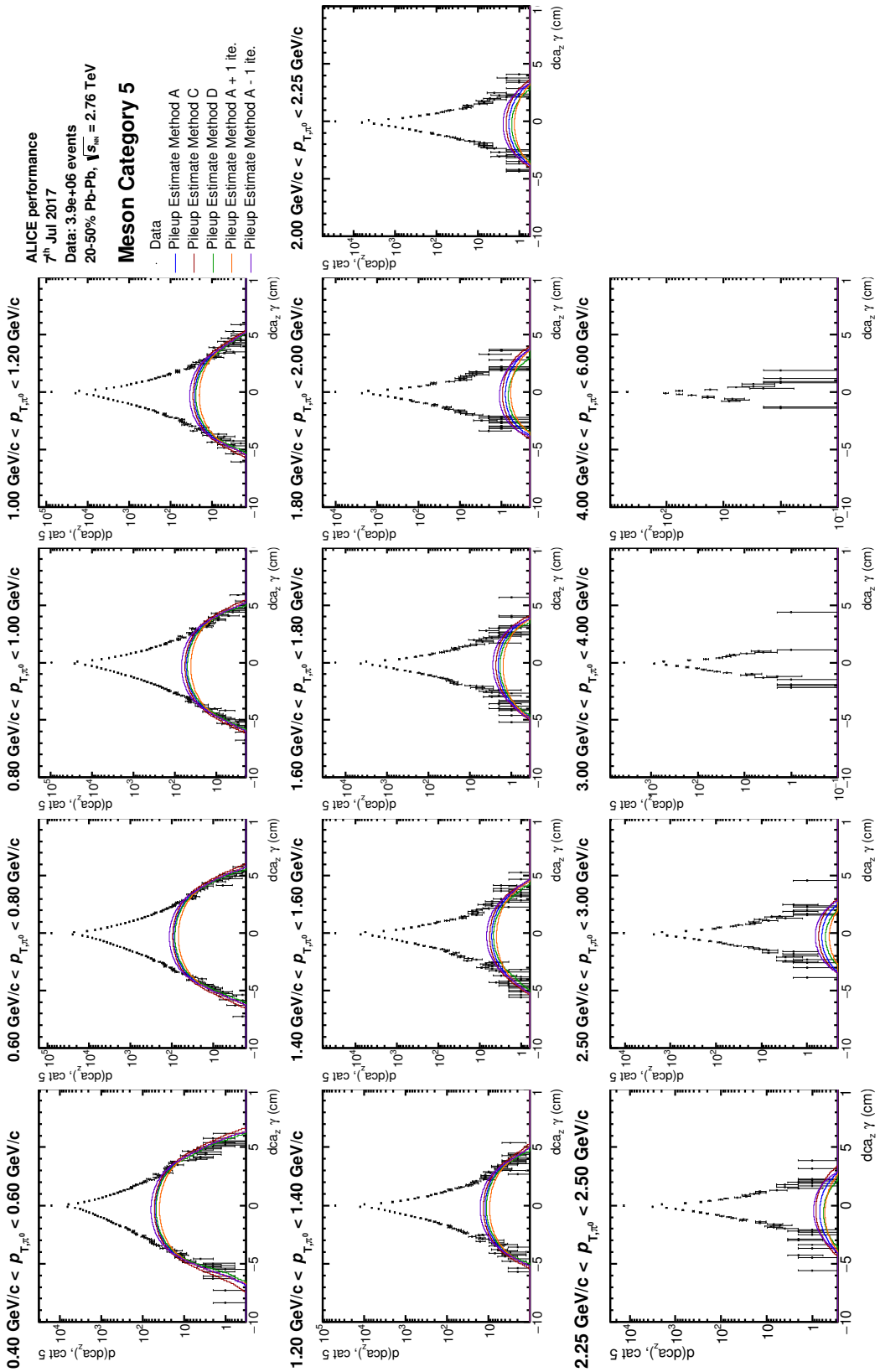

FIGURE B.6: DCA$_z$ distributions for photon from a pair within the π^0 mass region in transverse momentum intervals for meson category five and centrality class 20–50%.

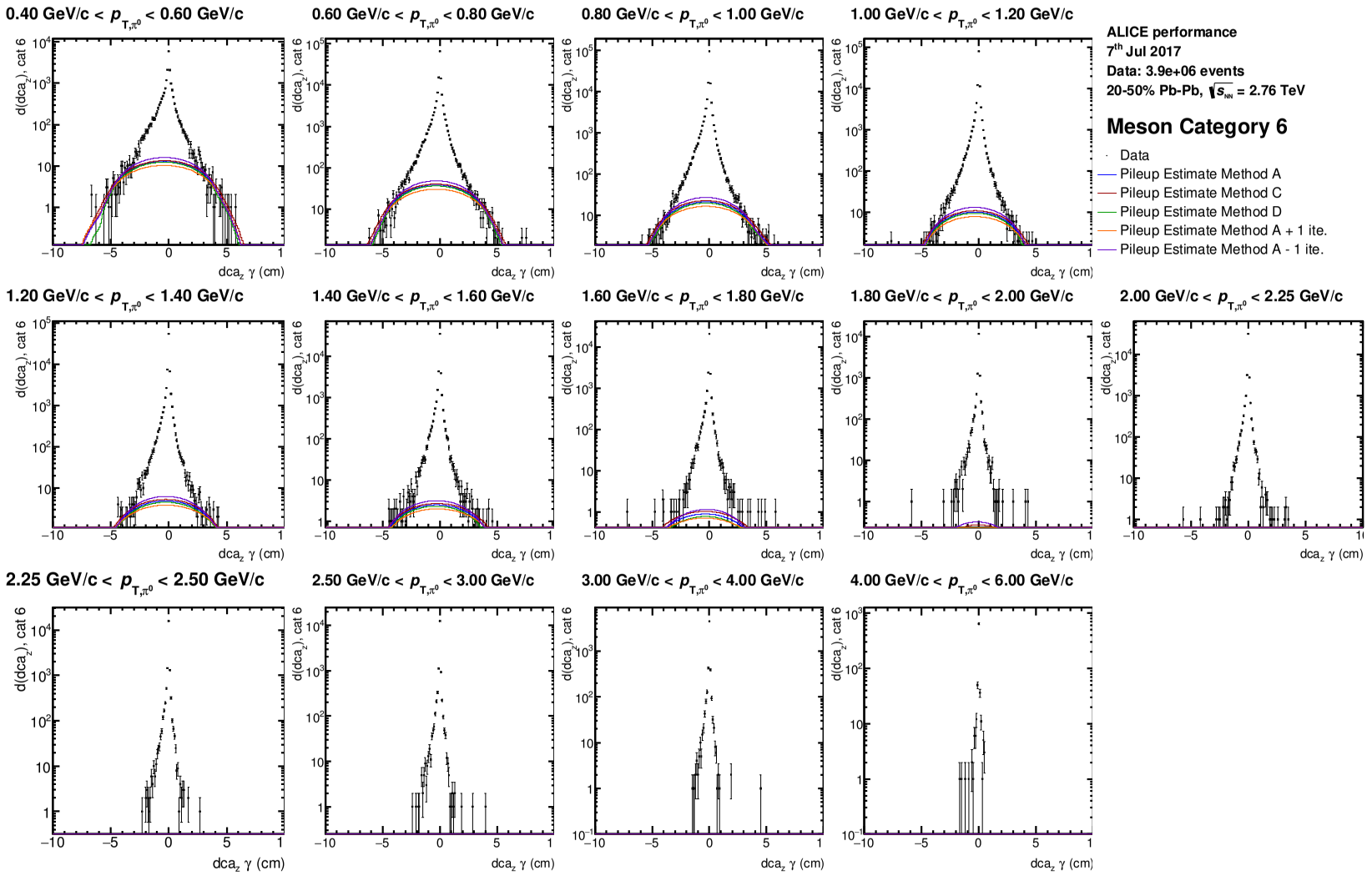

FIGURE B.7: DCA$_z$ distributions for photon from a pair within the π^0 mass region in transverse momentum intervals for meson category six and centrality class 20–50%.

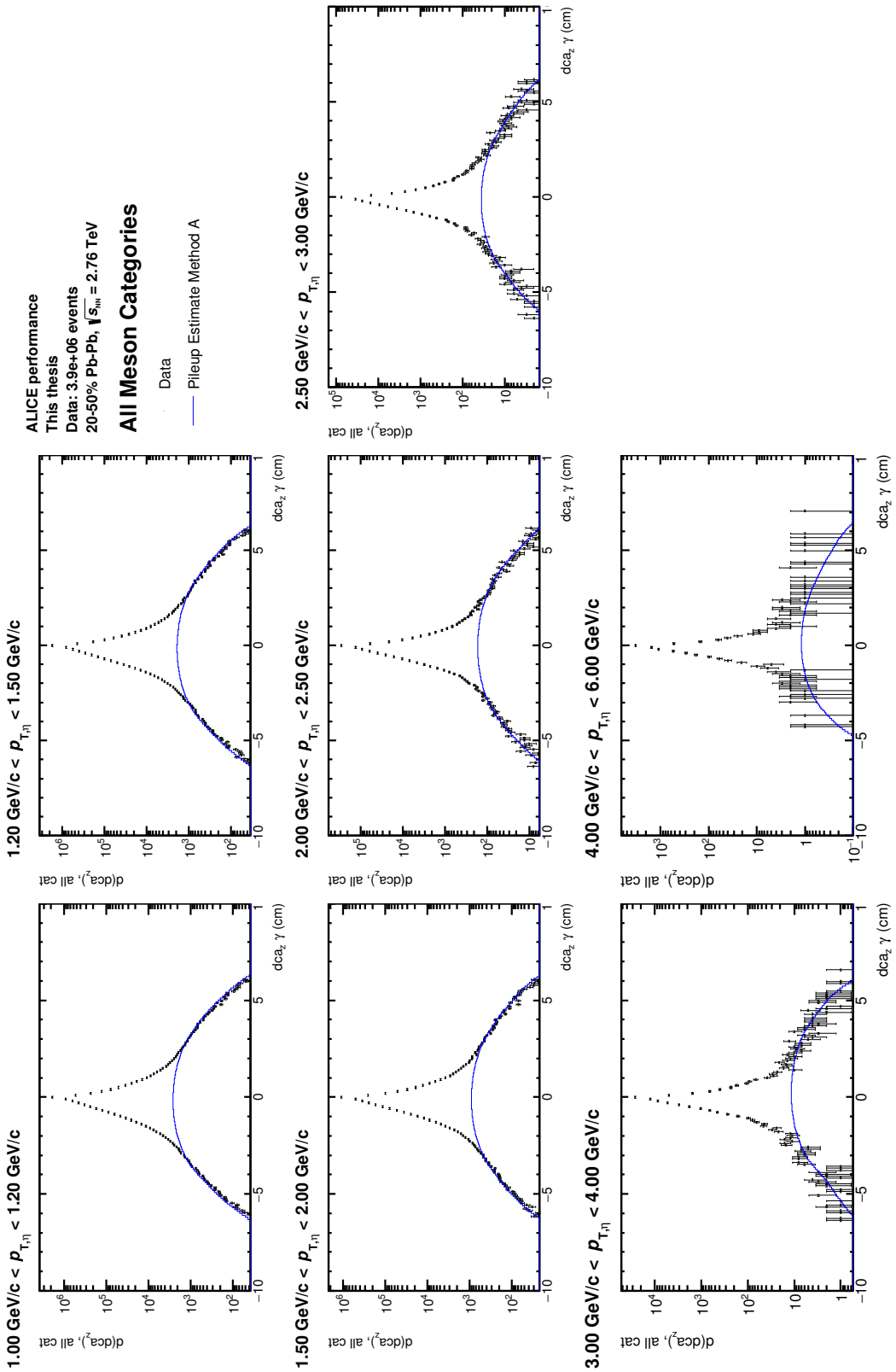

FIGURE B.8: DCA$_z$ distributions for photon from a pair within the η mass region in transverse momentum intervals for the centrality class 20–50%. All the meson categories are shown together.

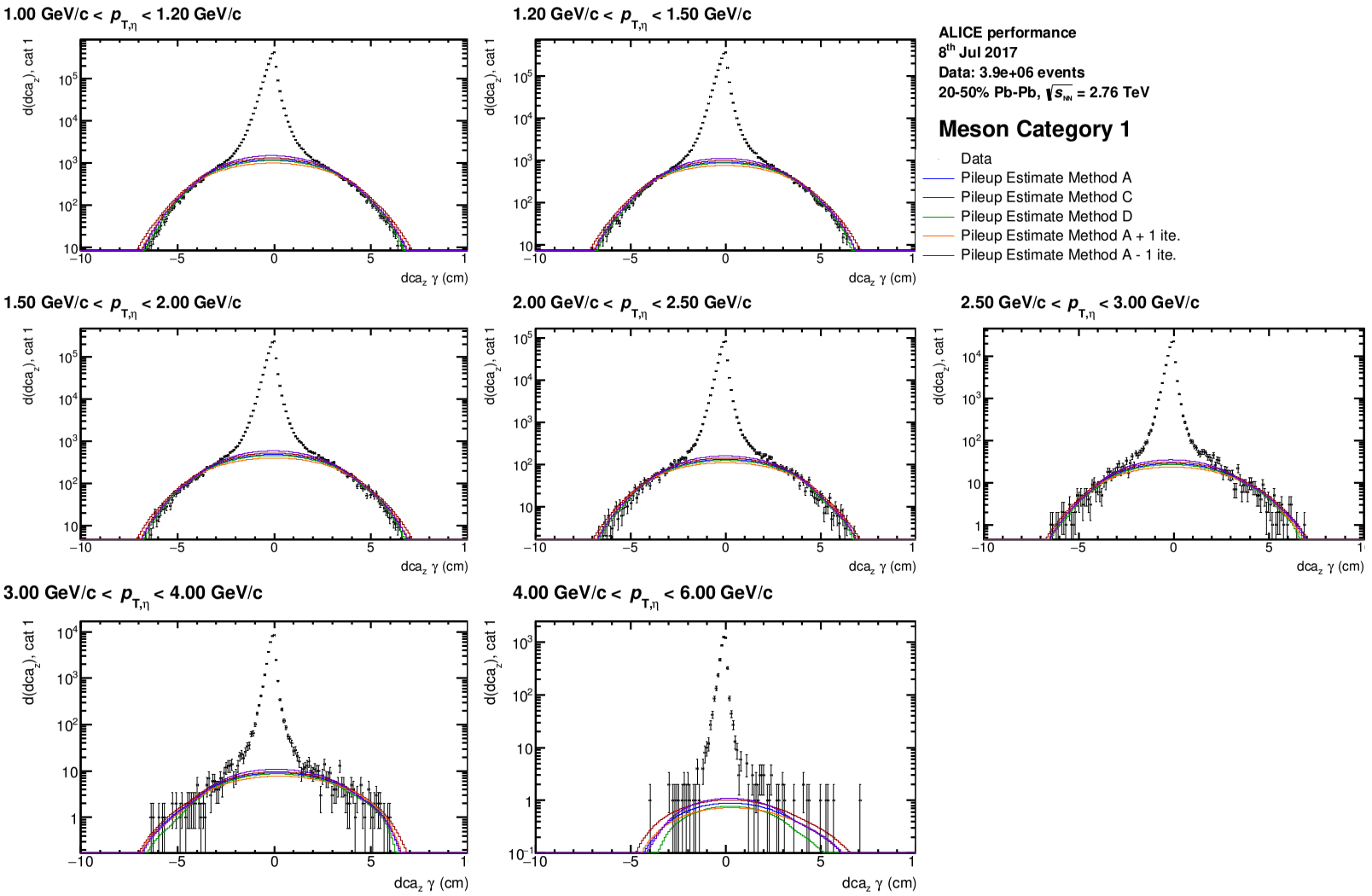

FIGURE B.9: DCA$_z$ distributions for photon from a pair within the η mass region in transverse momentum intervals for meson category one and centrality class 20–50%.

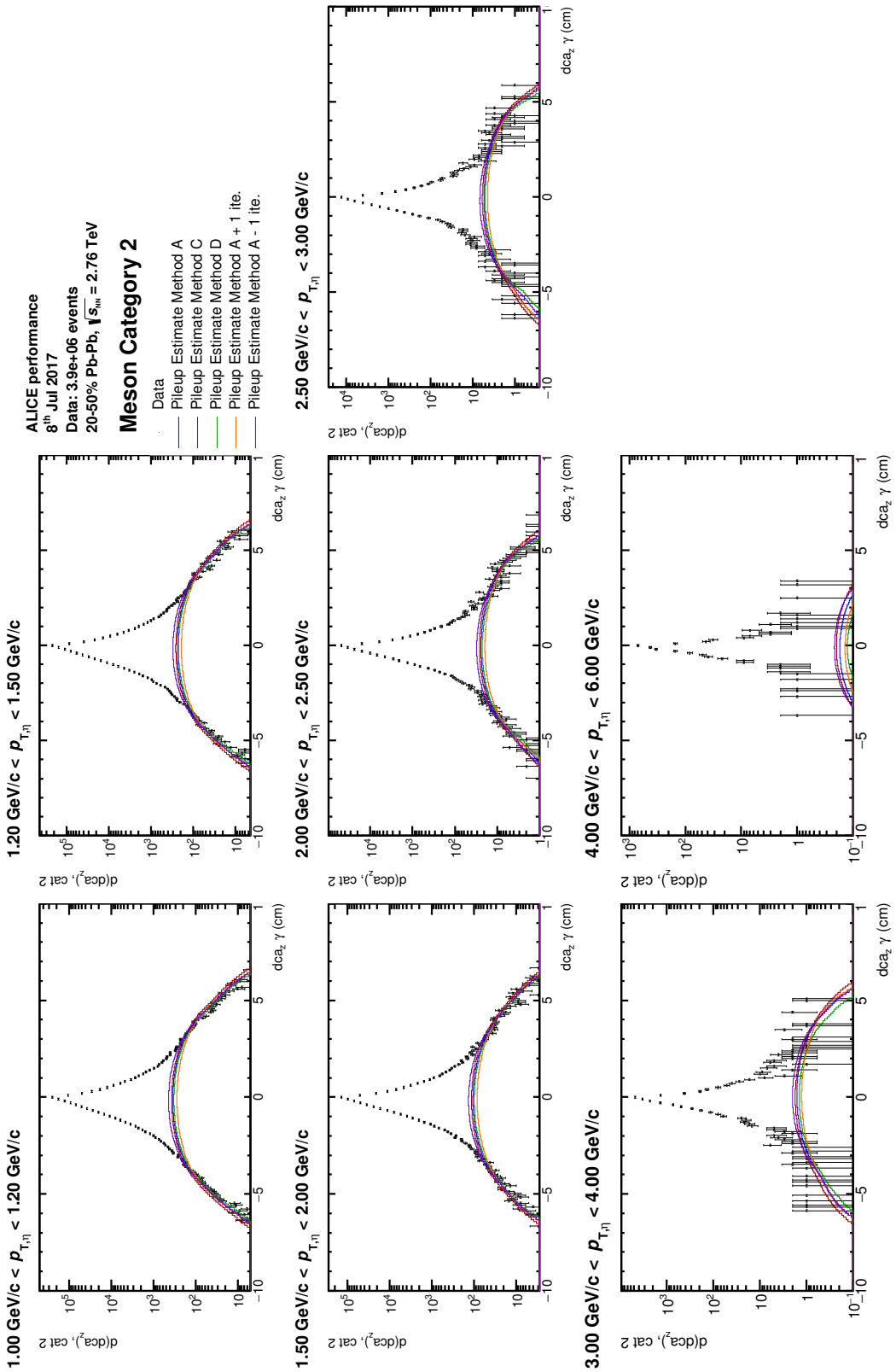

FIGURE B.10: DCA$_z$ distributions for photon from a pair within the η mass region in transverse momentum intervals for meson category two and centrality class 20–50%.

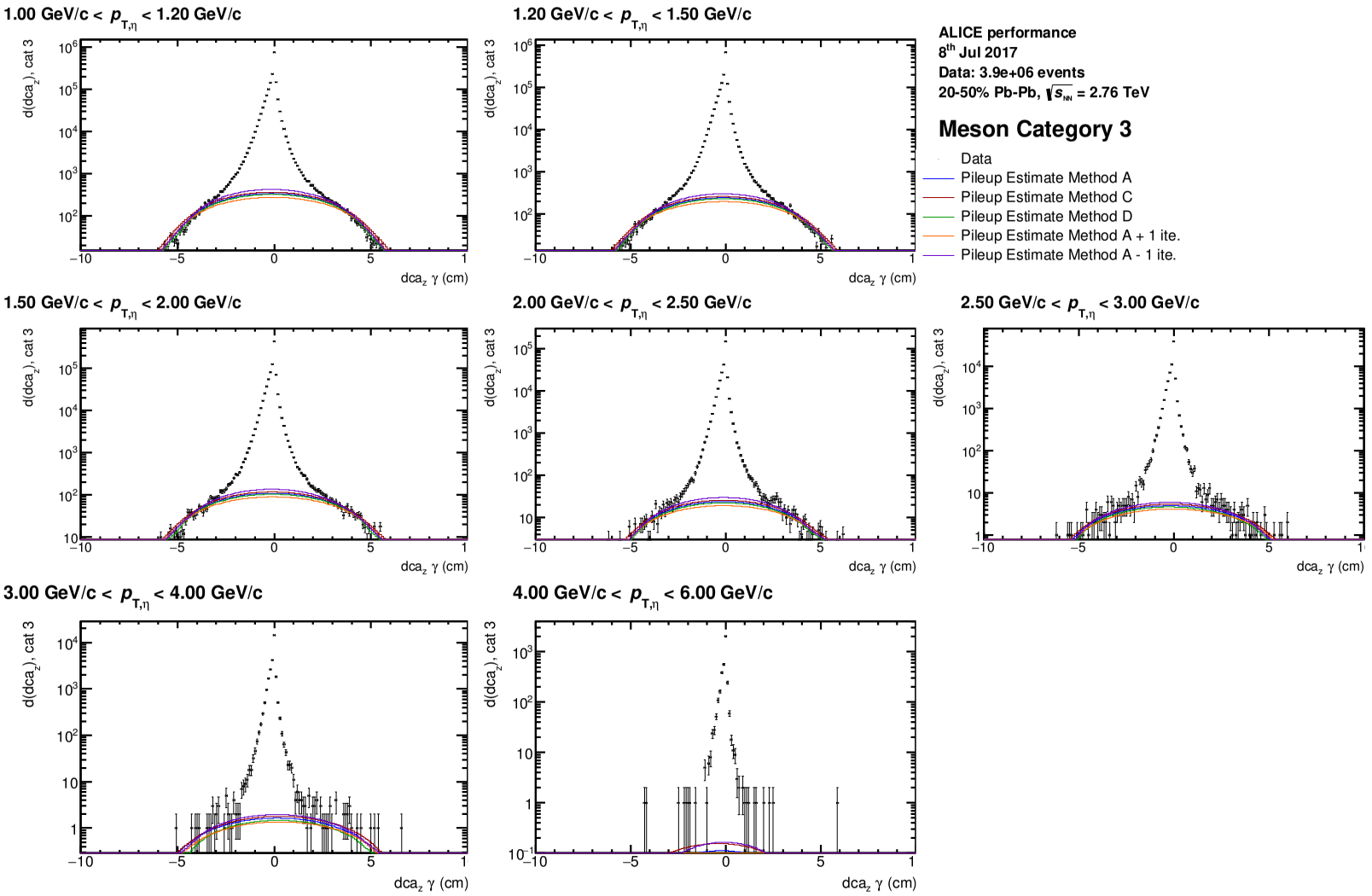

FIGURE B.11: DCA$_z$ distributions for photon from a pair within the η mass region in transverse momentum intervals for meson category three and centrality class 20–50%.

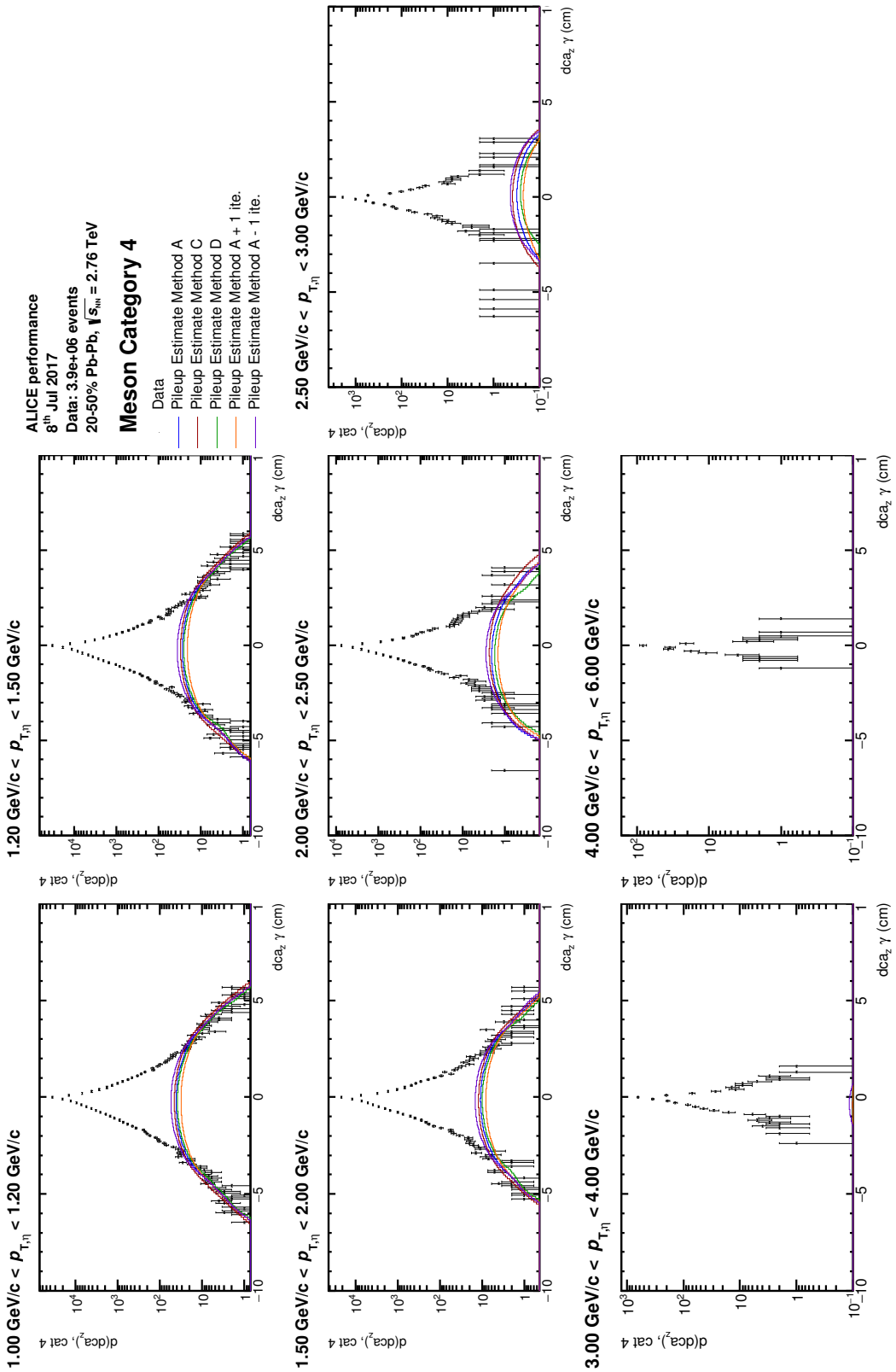

FIGURE B.12: DCA$_z$ distributions for photon from a pair within the η mass region in transverse momentum intervals for meson category four and centrality class 20–50%.

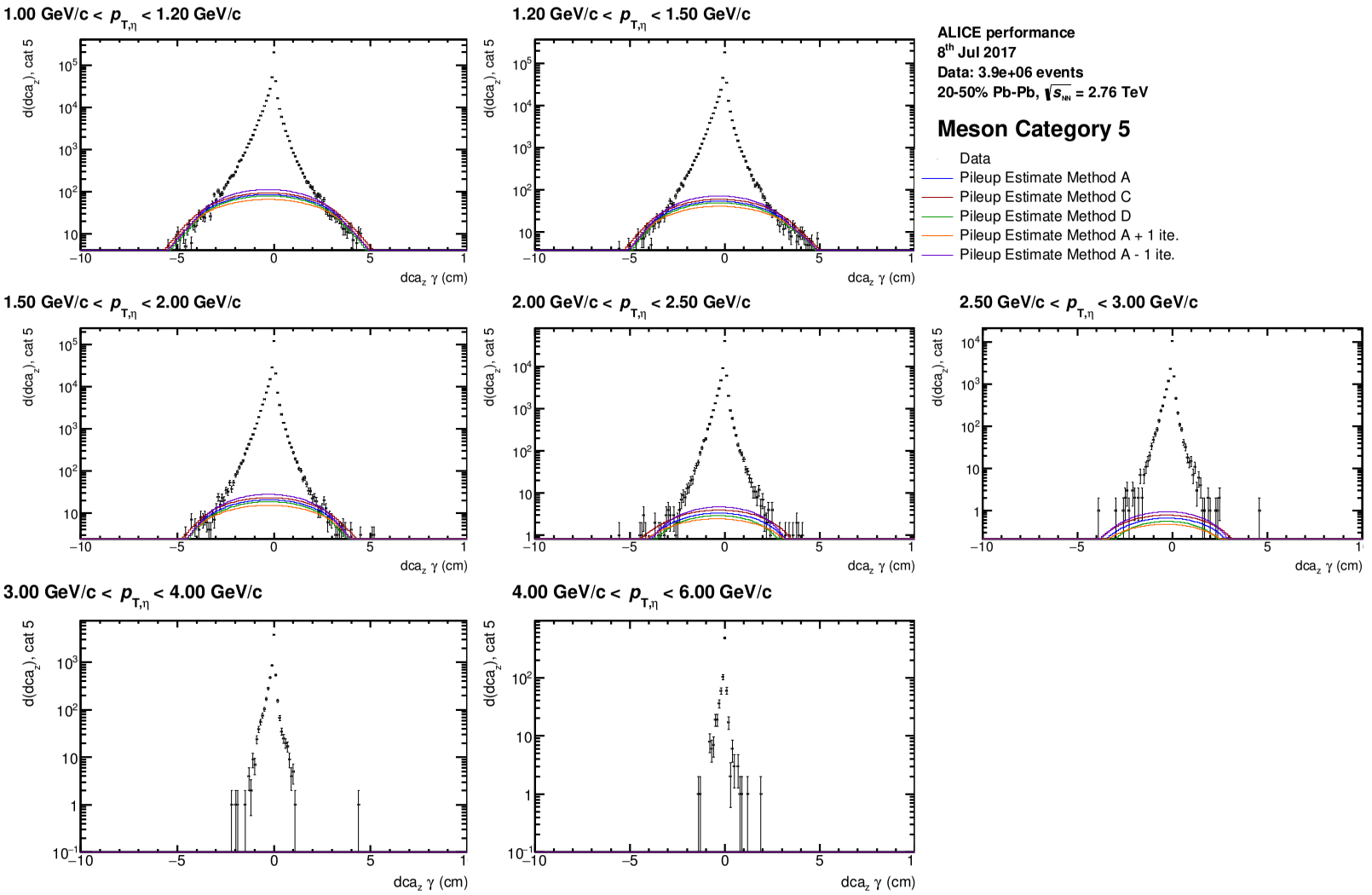

FIGURE B.13: DCA$_z$ distributions for photon from a pair within the η mass region in transverse momentum intervals for meson category five and centrality class 20–50%.

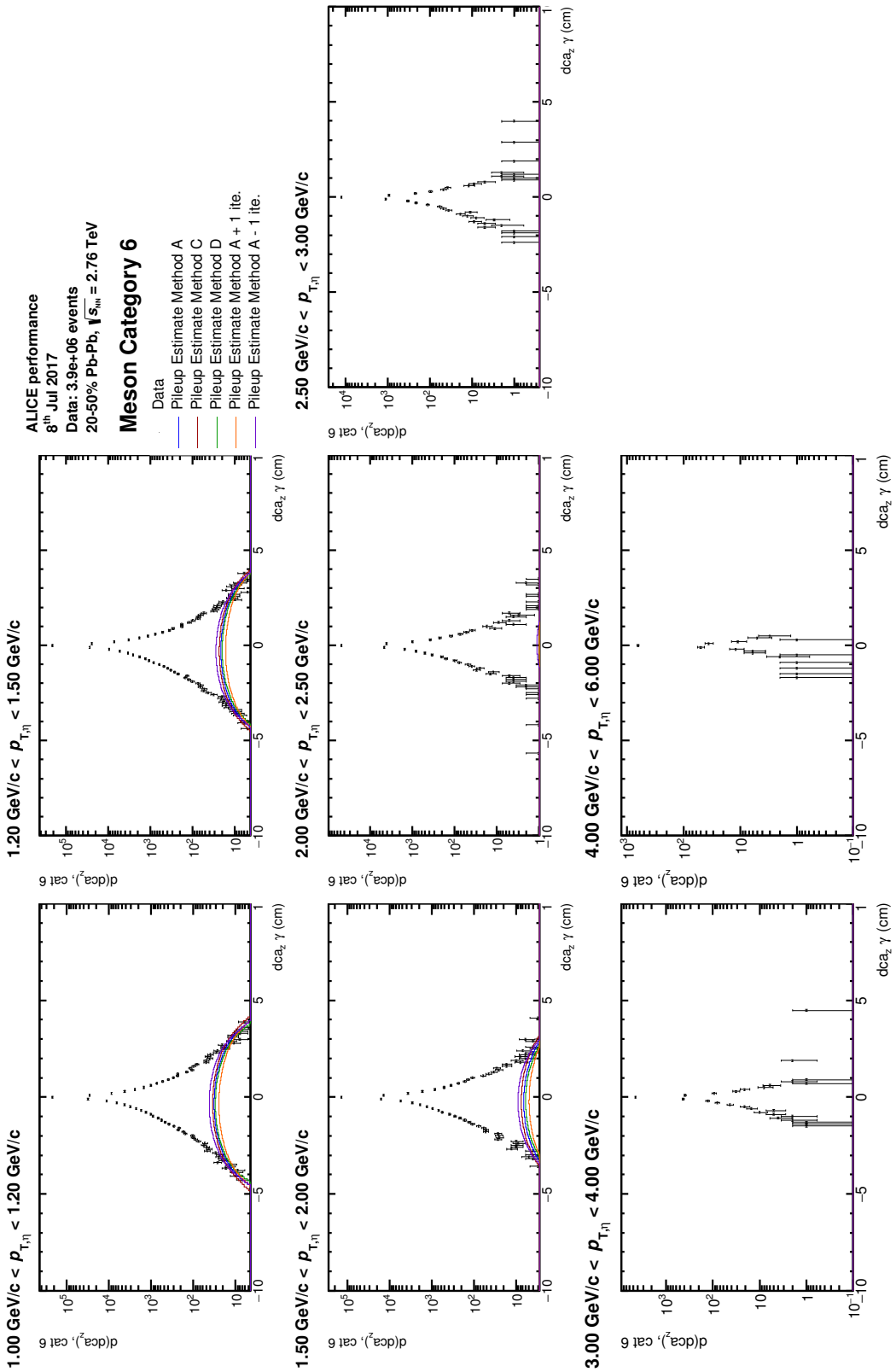

FIGURE B.14: DCA$_z$ distributions for photon from a pair within the η mass region in transverse momentum intervals for meson category six and centrality class 20–50%.

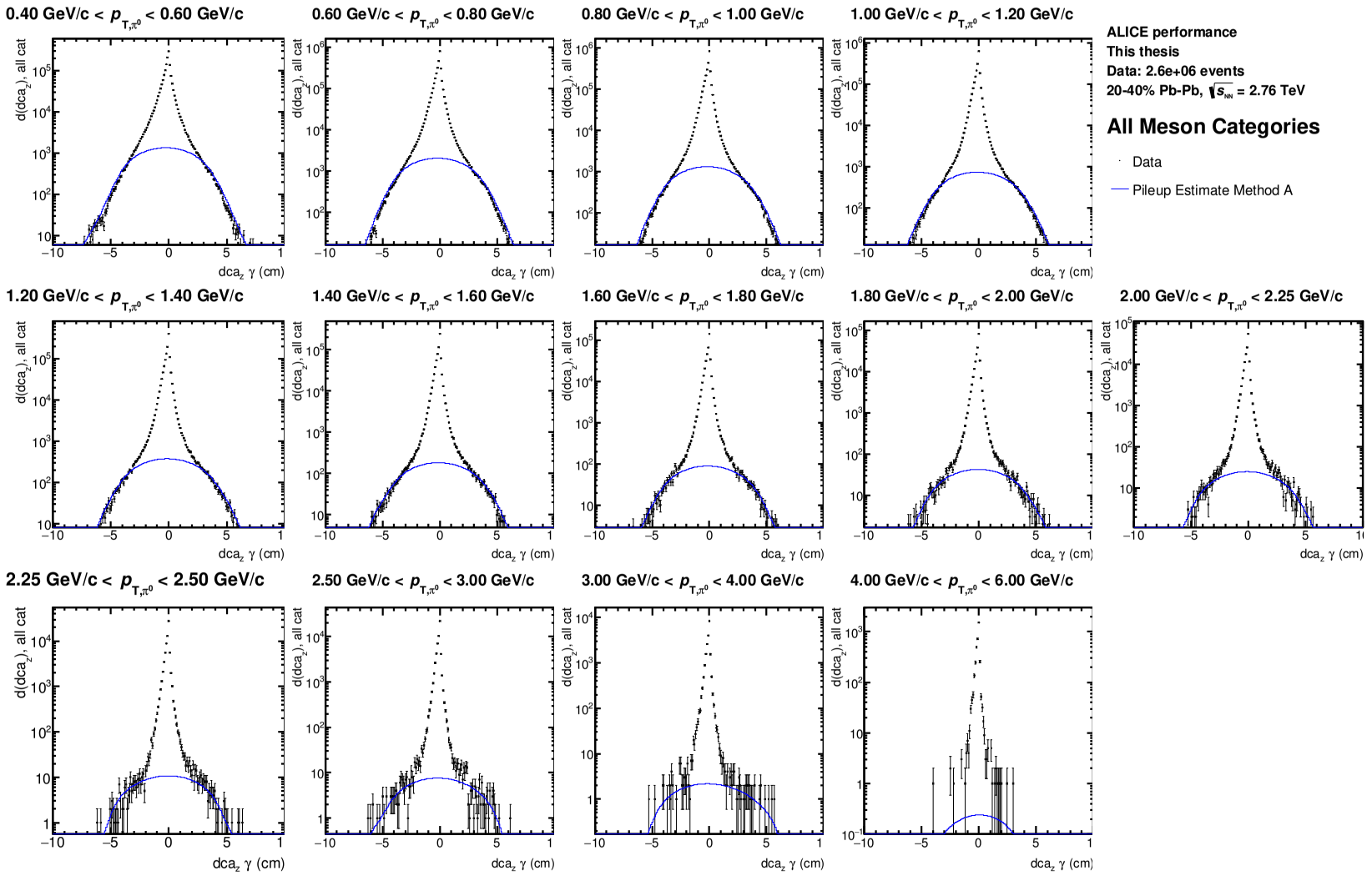

FIGURE B.15: DCA$_z$ distributions for photon from a pair within the π^0 mass region in transverse momentum intervals for the centrality class 20–40%. All the meson categories are shown together.

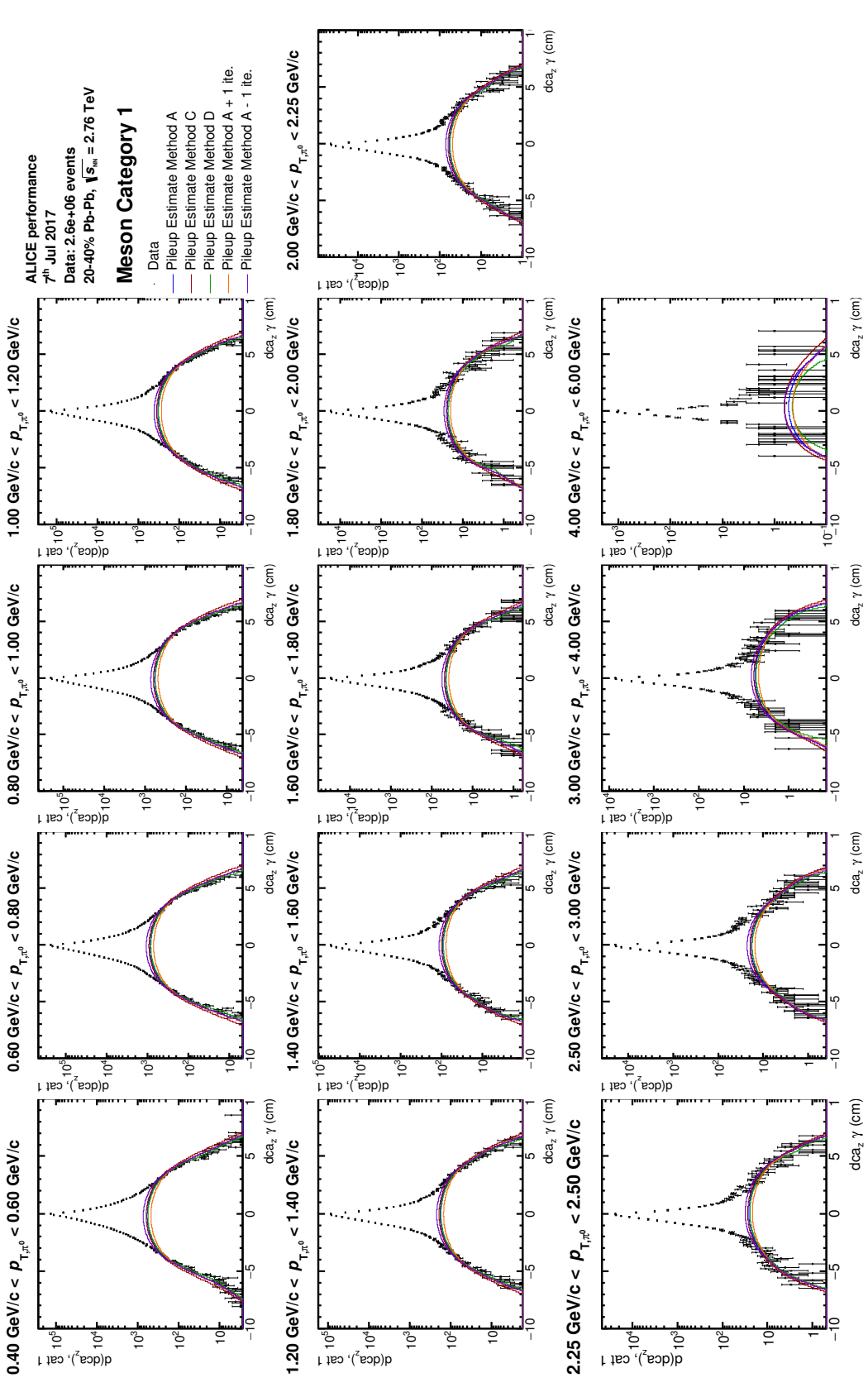

FIGURE B.16: DCA$_z$ distributions for photon from a pair within the π^0 mass region in transverse momentum intervals for meson category one and centrality class 20–40%.

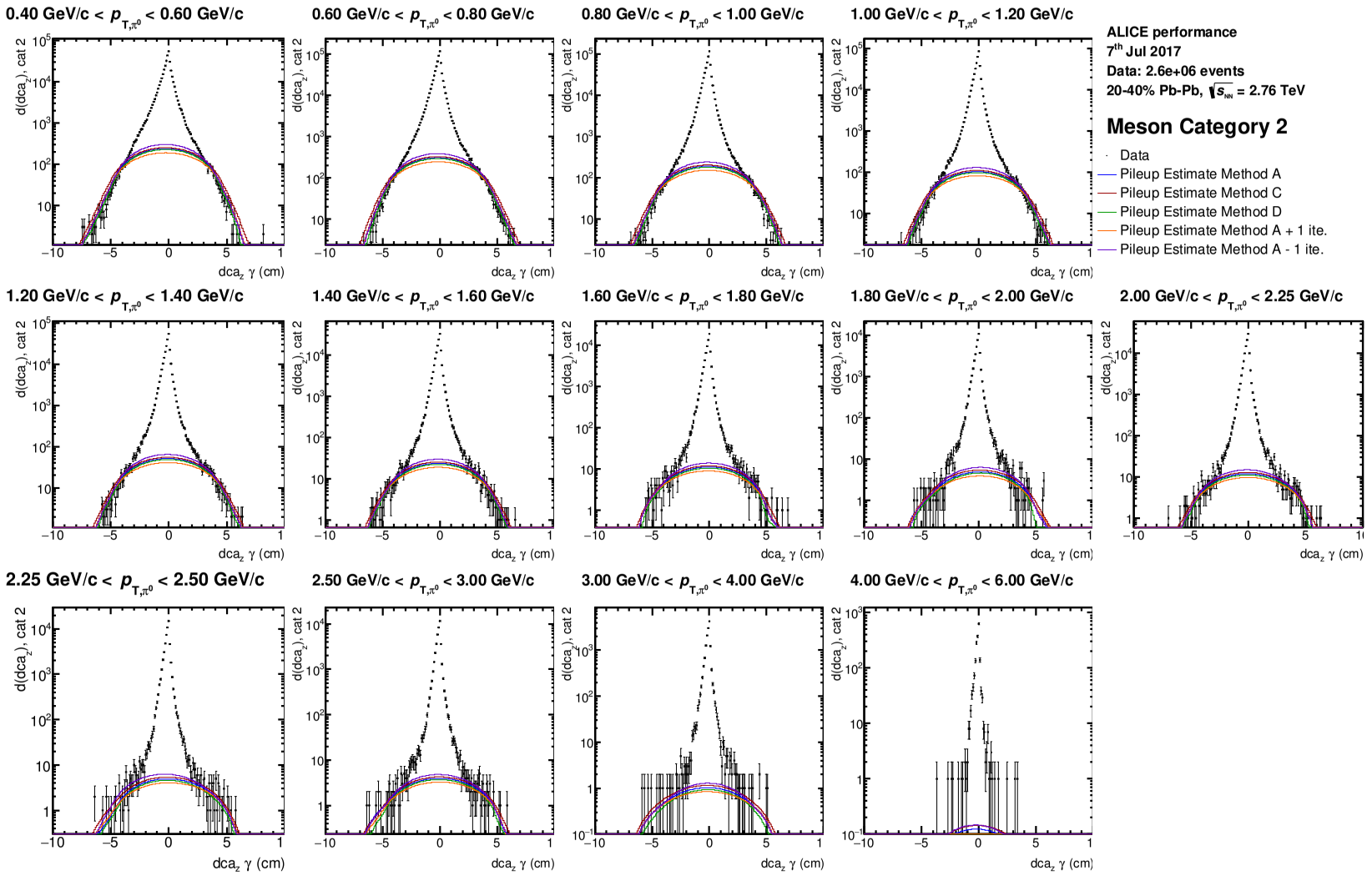

FIGURE B.17: DCA$_z$ distributions for photon from a pair within the π^0 mass region in transverse momentum intervals for meson category two and centrality class 20–40%.

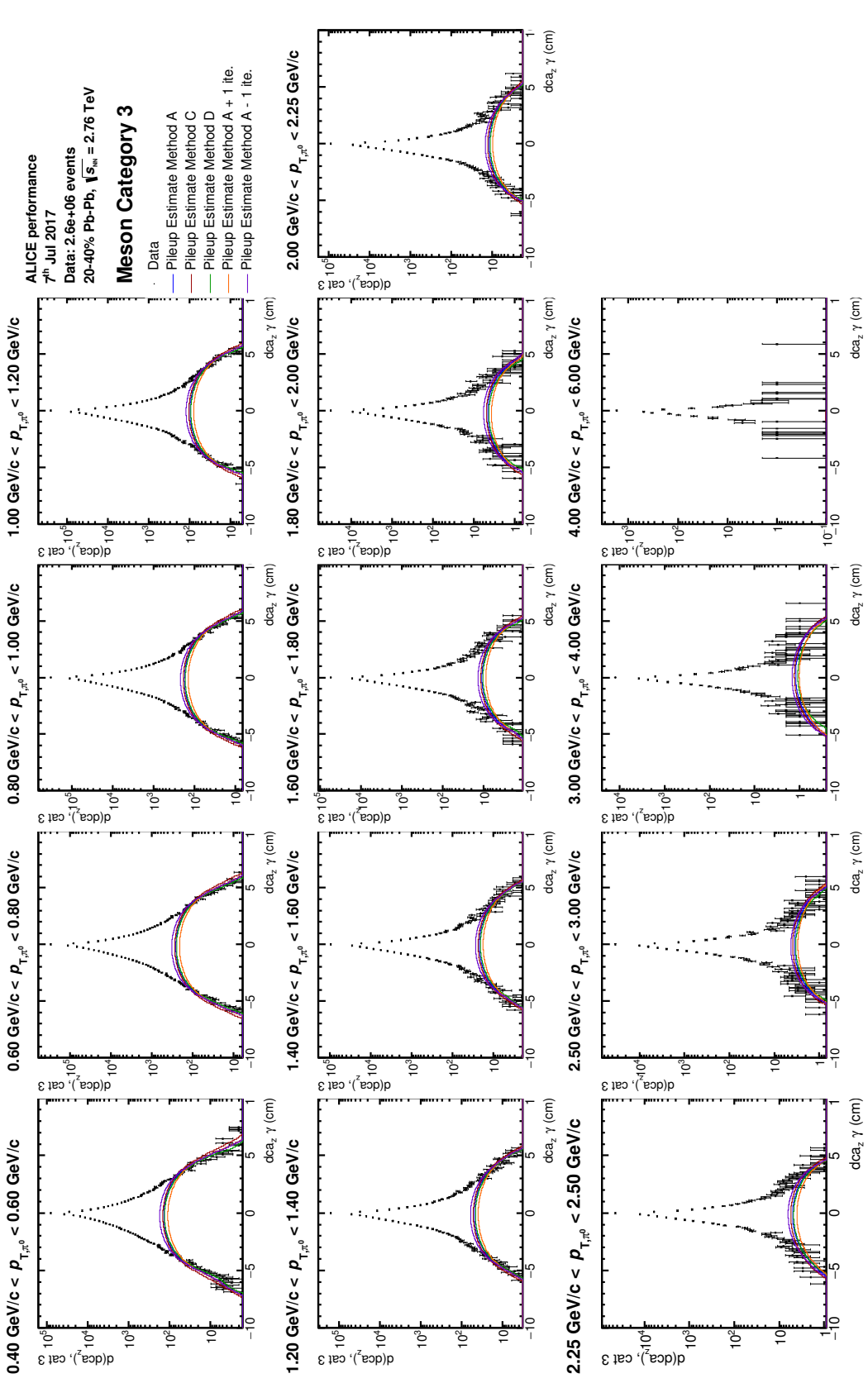

FIGURE B.18: DCA$_z$ distributions for photon from a pair within the π^0 mass region in transverse momentum intervals for meson category three and centrality class 20–40%.

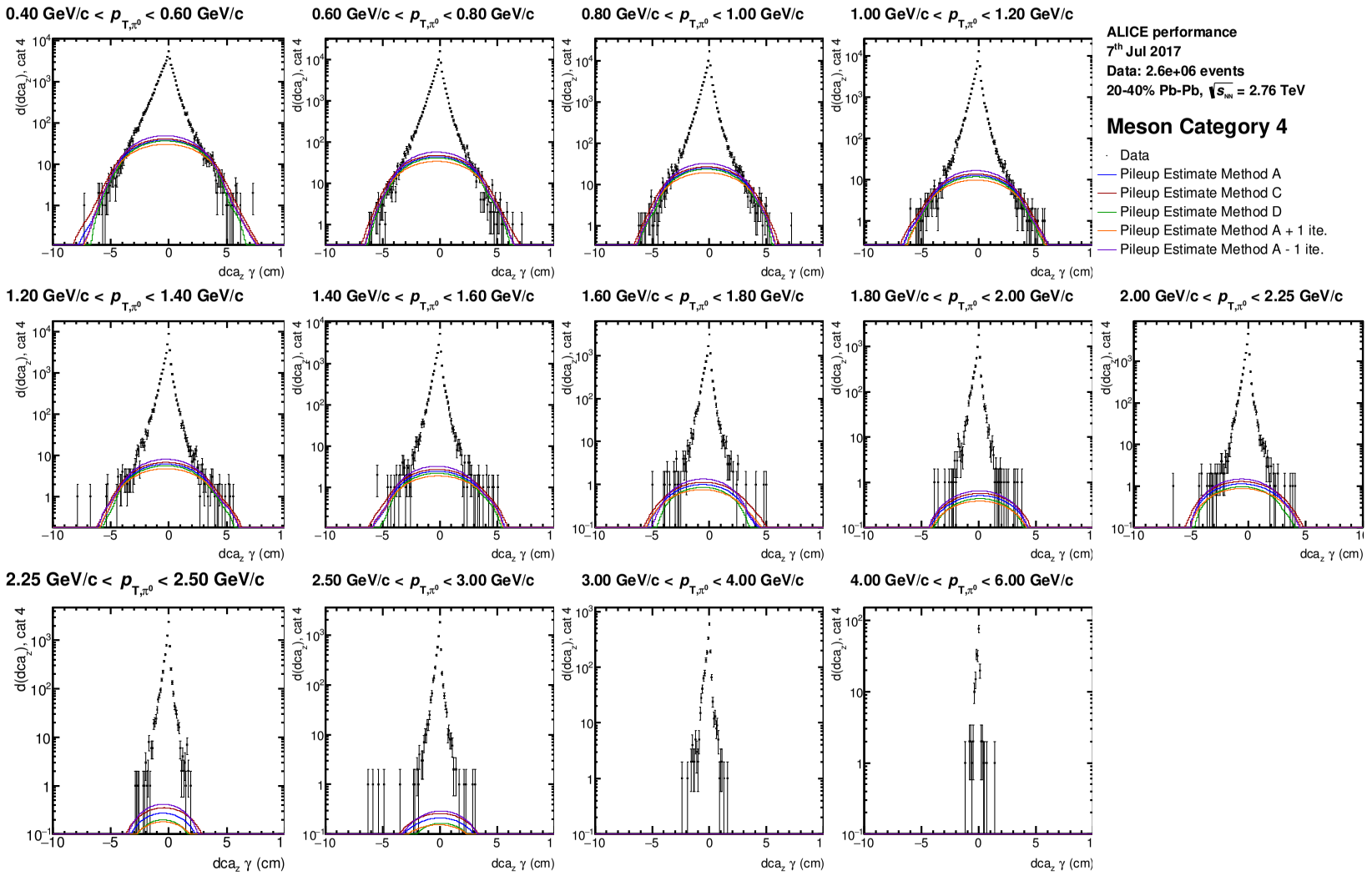

FIGURE B.19: DCA$_z$ distributions for photon from a pair within the π^0 mass region in transverse momentum intervals for meson category four and centrality class 20–40%.

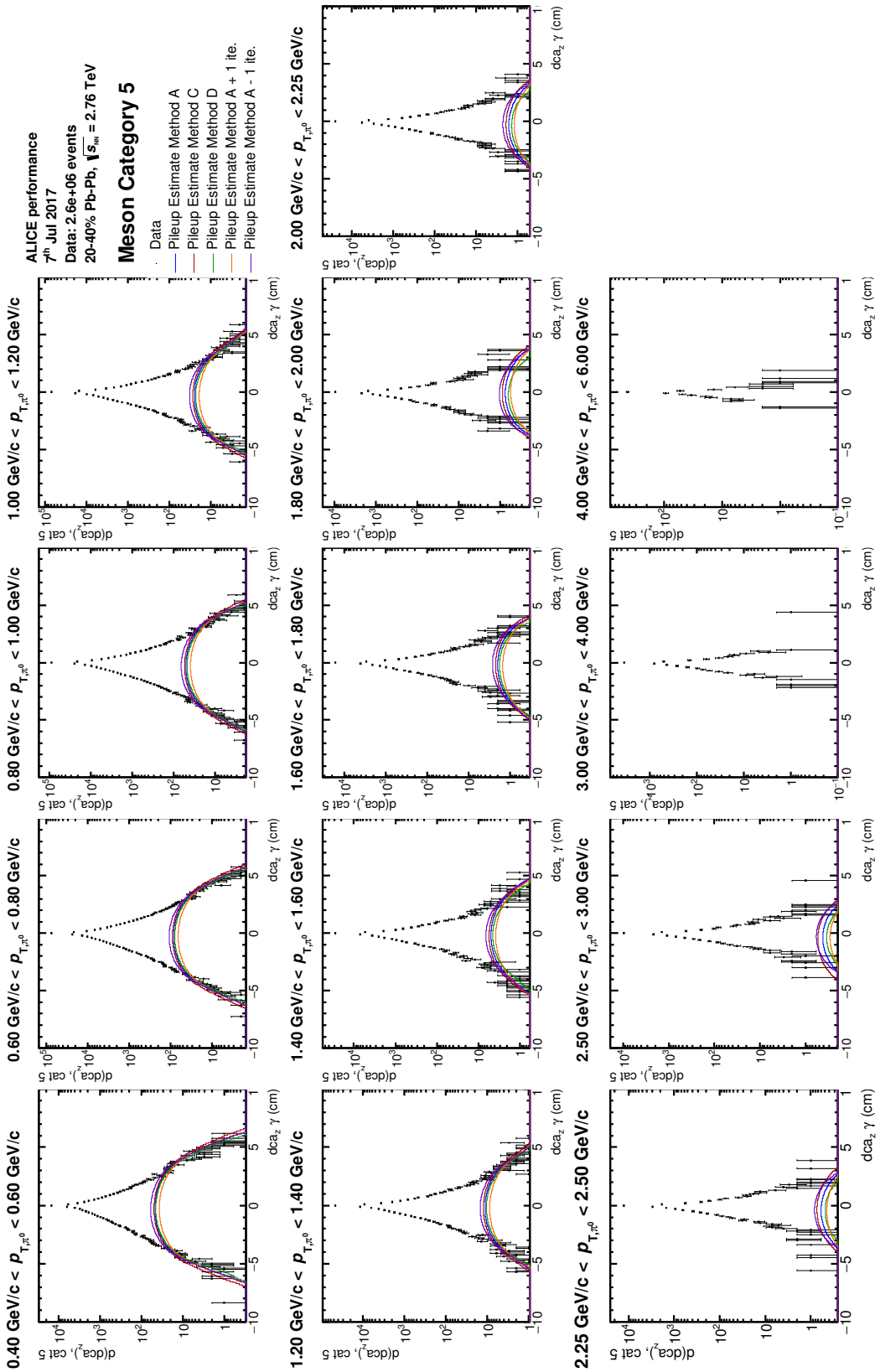

FIGURE B.20: DCA$_z$ distributions for photon from a pair within the π^0 mass region in transverse momentum intervals for meson category five and centrality class 20–40%.

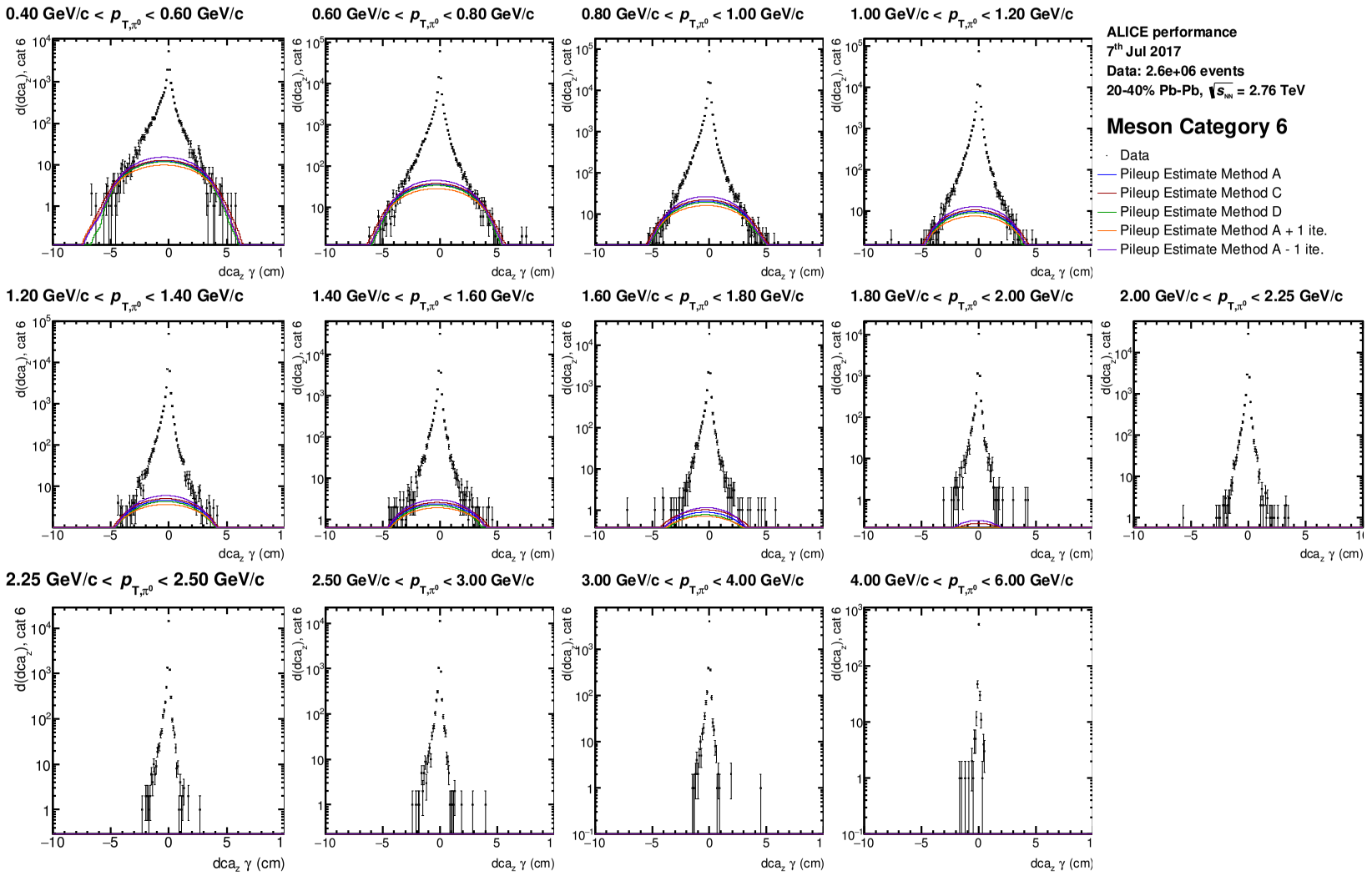

FIGURE B.21: DCA$_z$ distributions for photon from a pair within the π^0 mass region in transverse momentum intervals for meson category six and centrality class 20–40%.

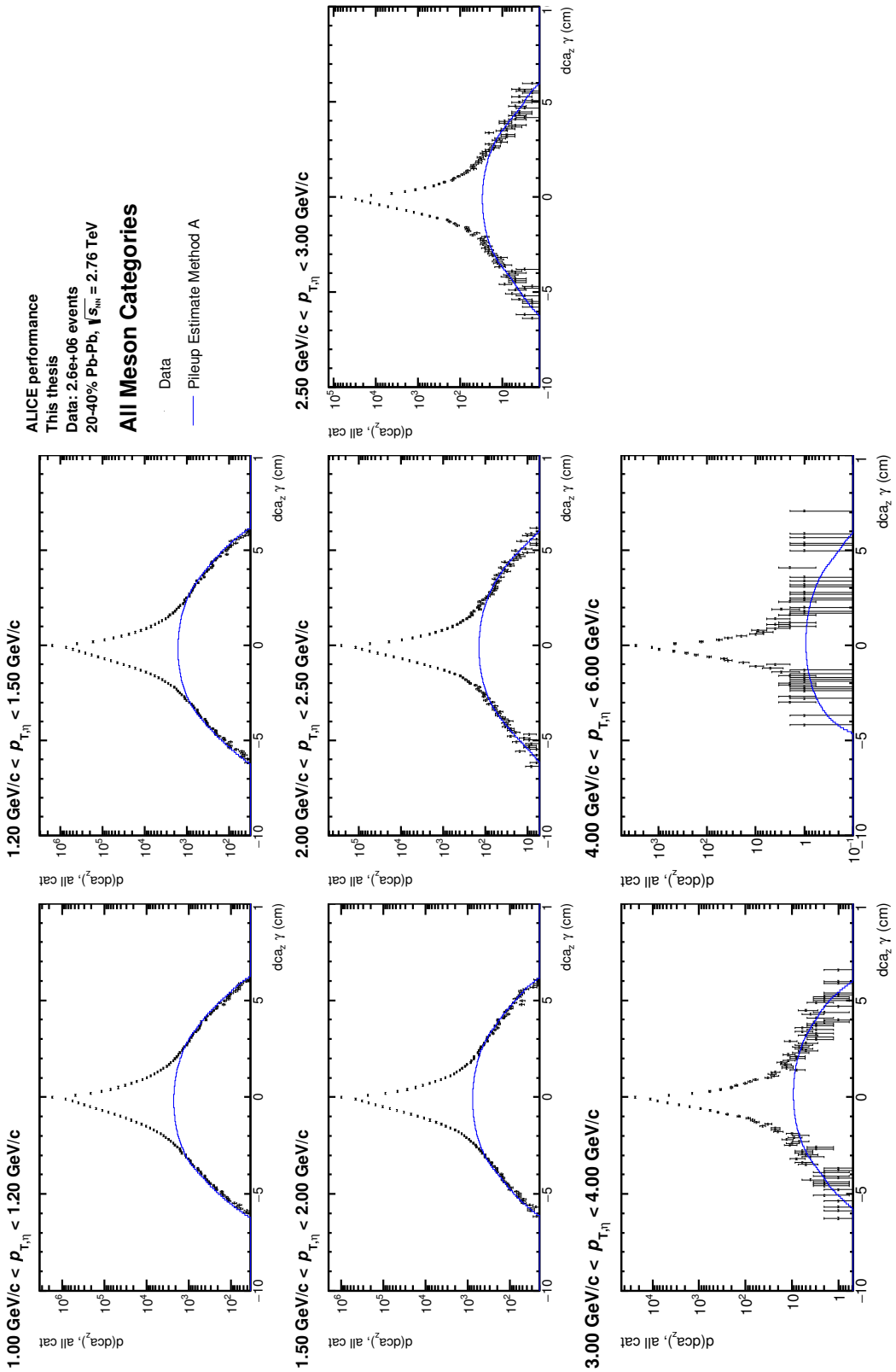

FIGURE B.22: DCA$_z$ distributions for photon from a pair within the η mass region in transverse momentum intervals for the centrality class 20–40%. All the meson categories are shown together.

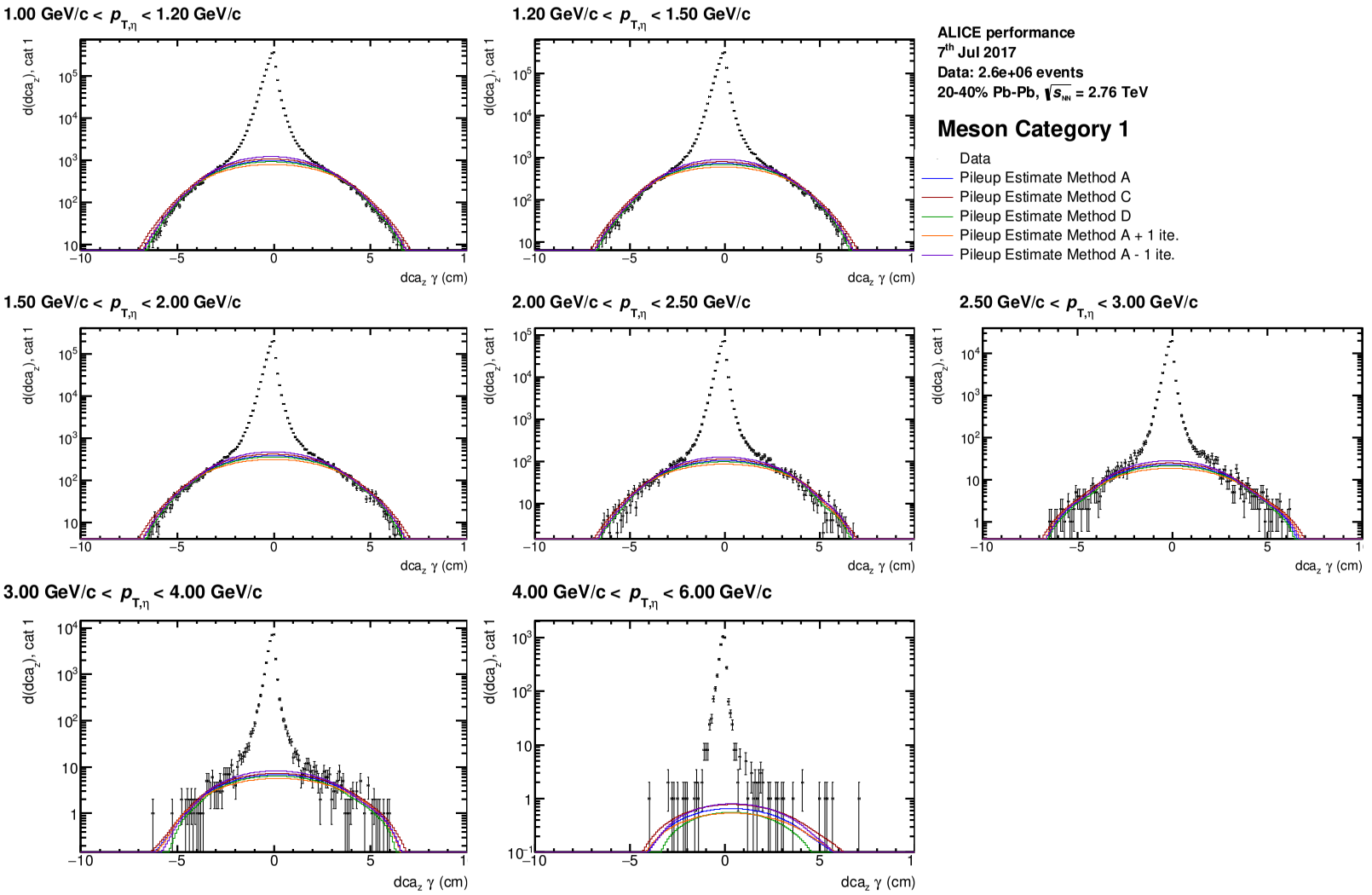

FIGURE B.23: DCA$_z$ distributions for photon from a pair within the η mass region in transverse momentum intervals for meson category one and centrality class 20–40%.

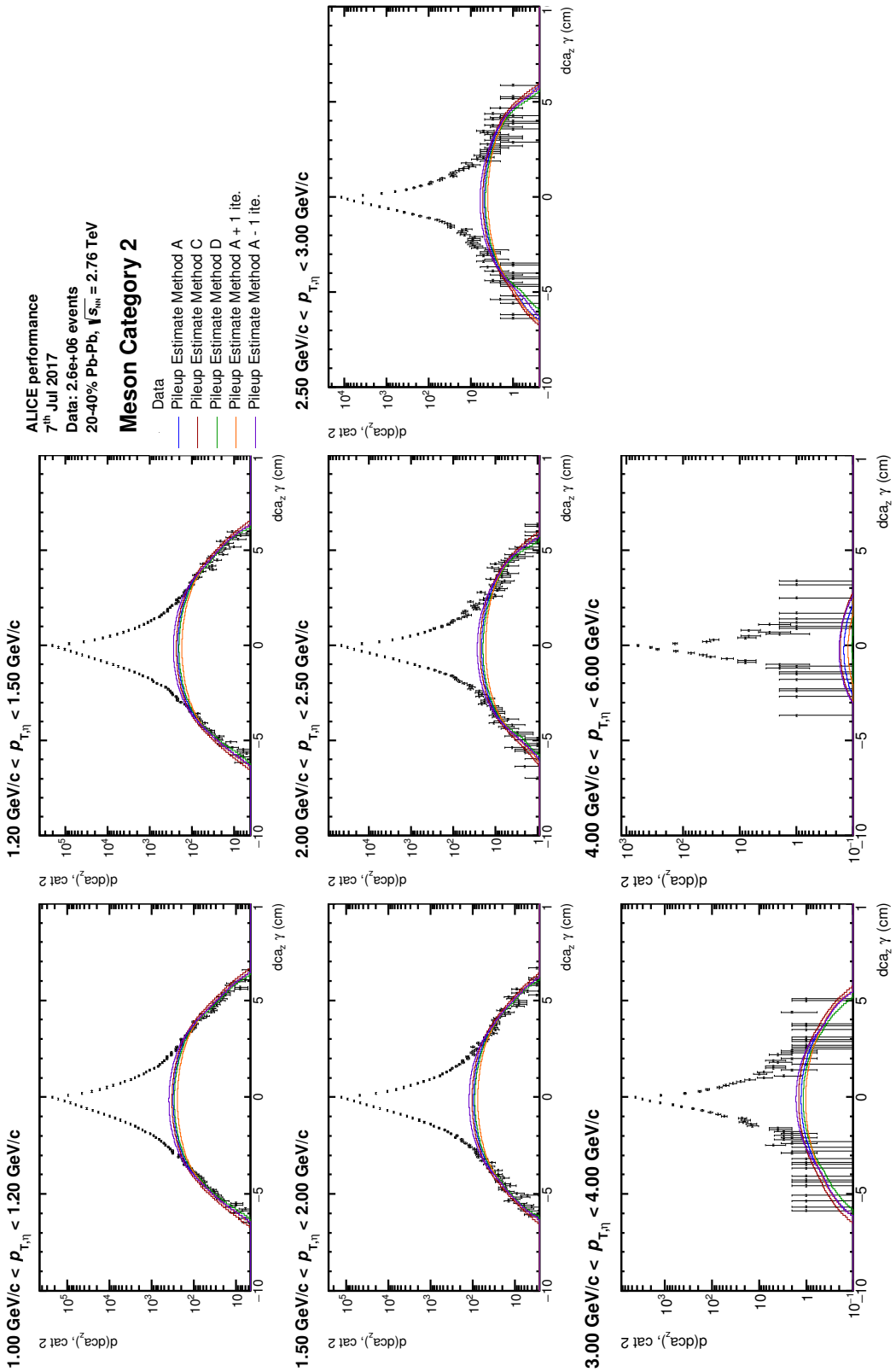

FIGURE B.24: DCA$_z$ distributions for photon from a pair within the η mass region in transverse momentum intervals for meson category two and centrality class 20–40%.

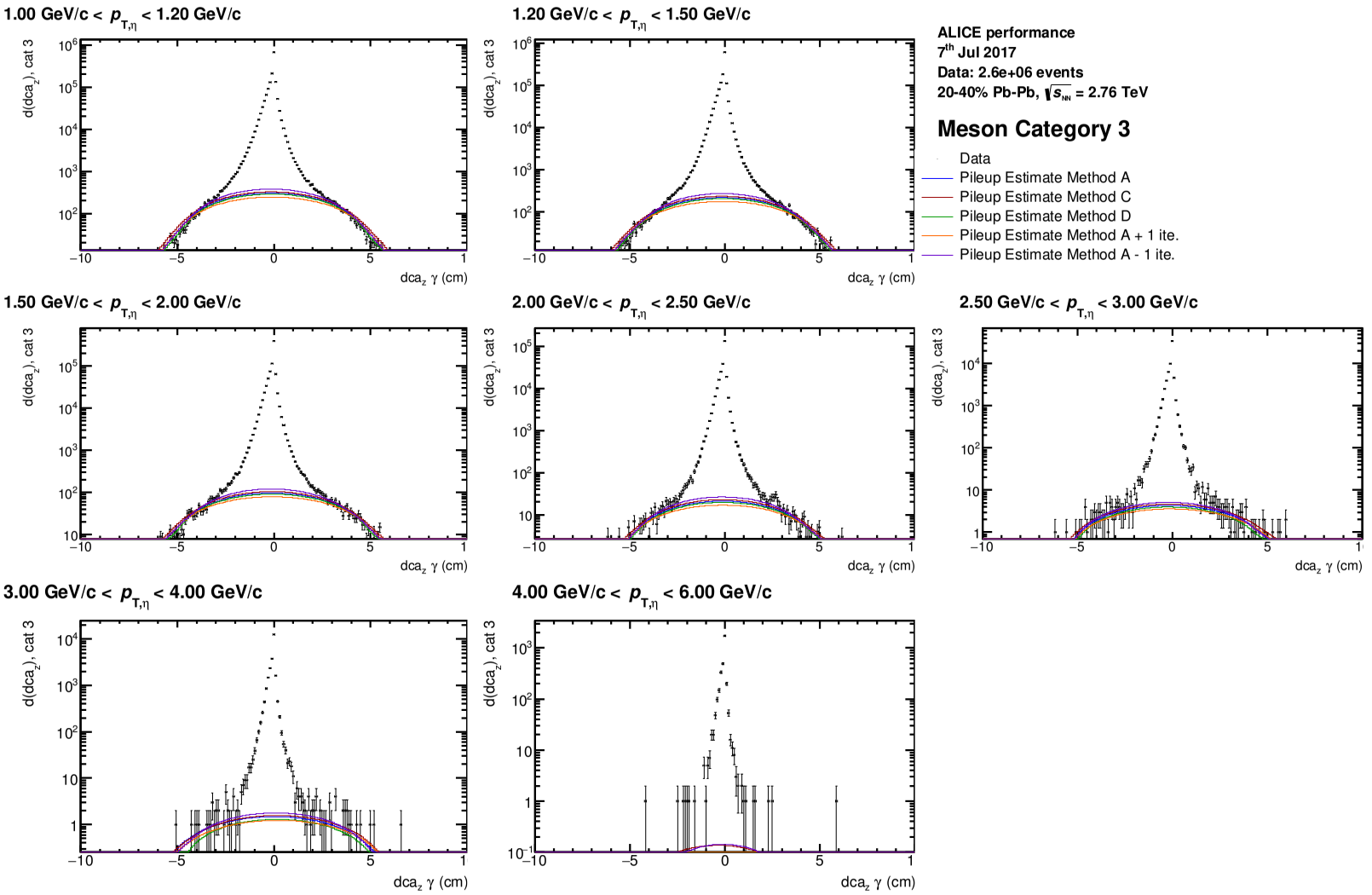

FIGURE B.25: DCA$_z$ distributions for photon from a pair within the η mass region in transverse momentum intervals for meson category three and centrality class 20–40%.

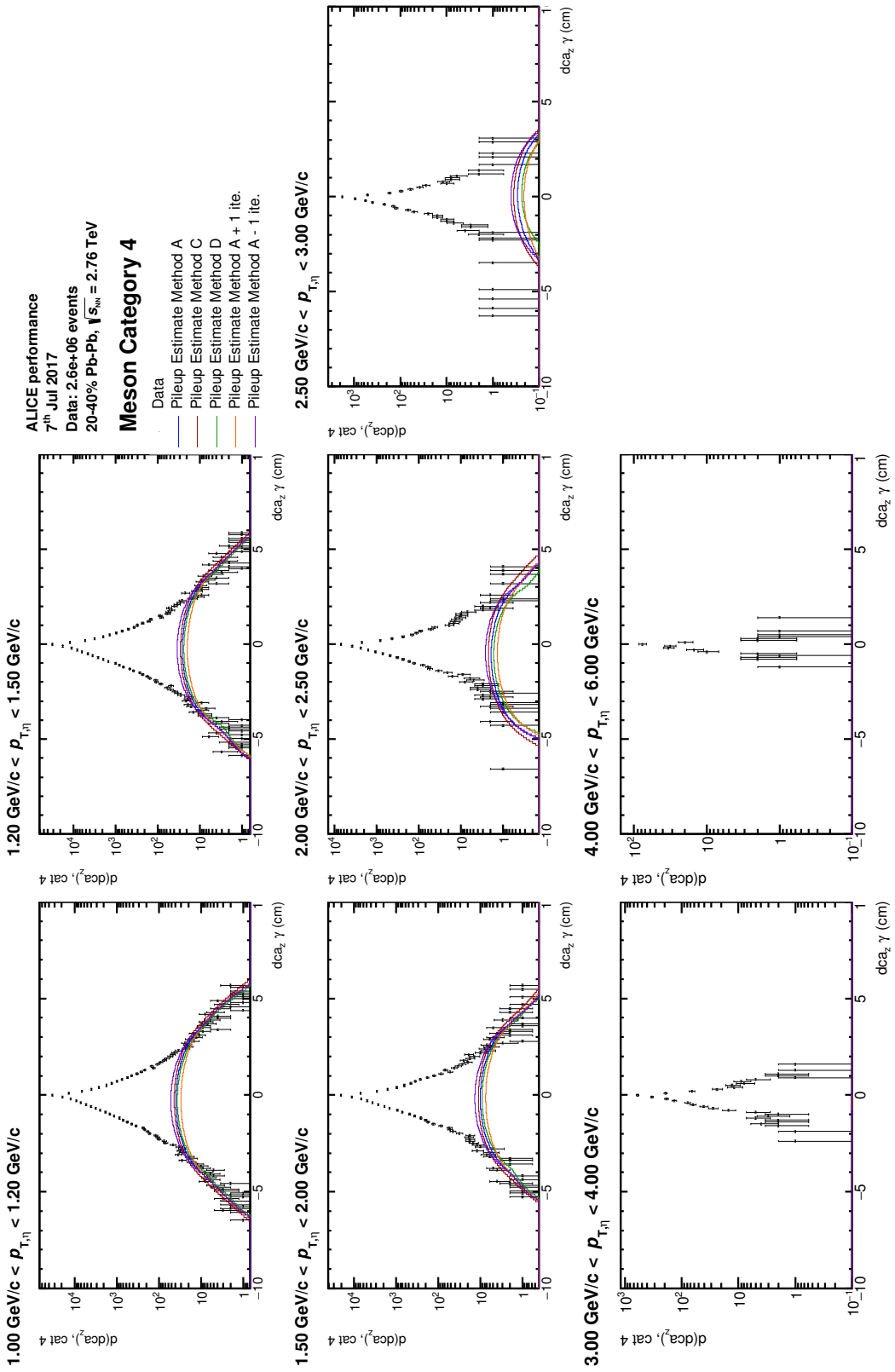

FIGURE B.26: DCA$_z$ distributions for photon from a pair within the η mass region in transverse momentum intervals for meson category four and centrality class 20–40%.

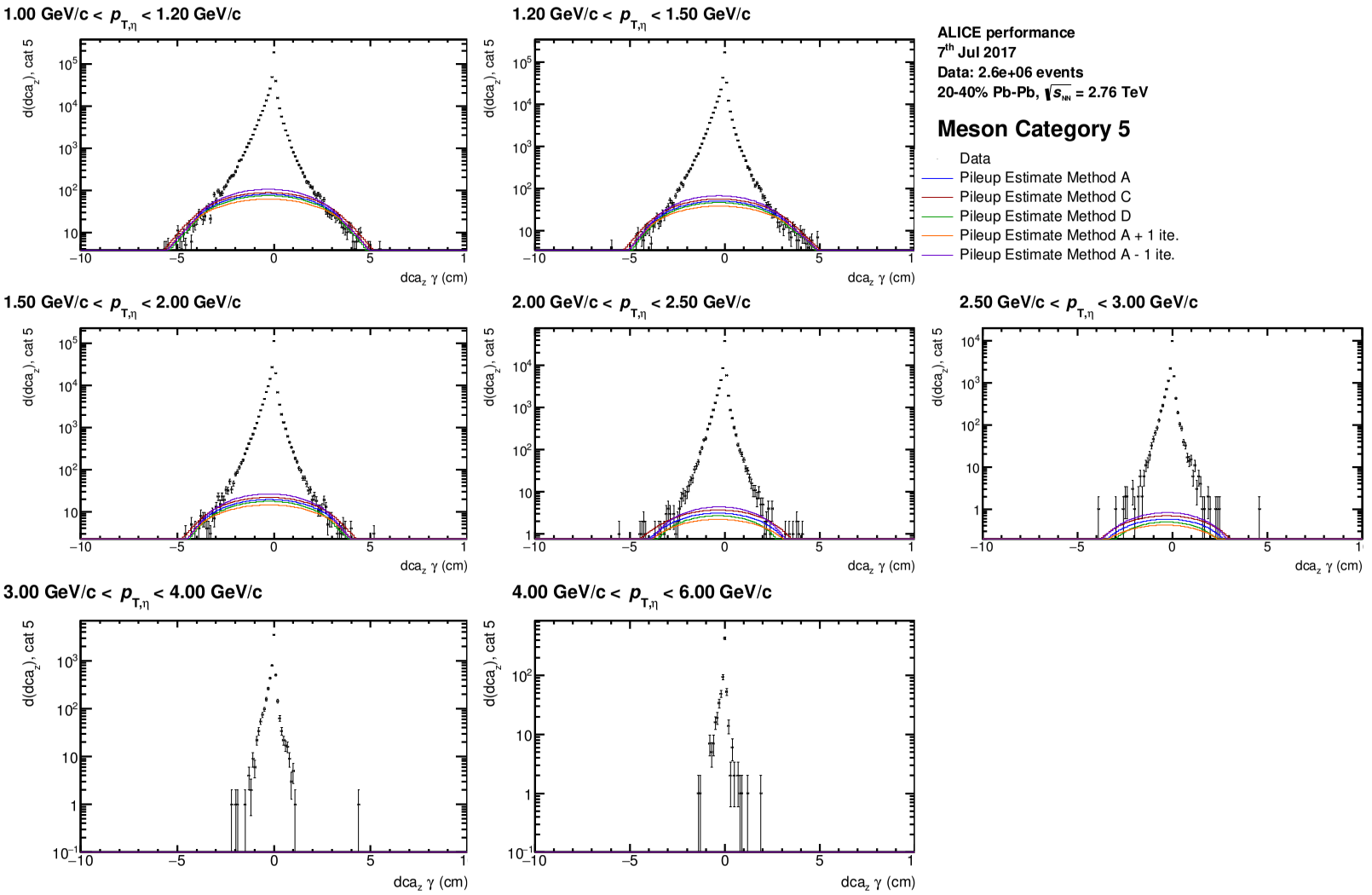

FIGURE B.27: DCA$_z$ distributions for photon from a pair within the η mass region in transverse momentum intervals for meson category five and centrality class 20–40%.

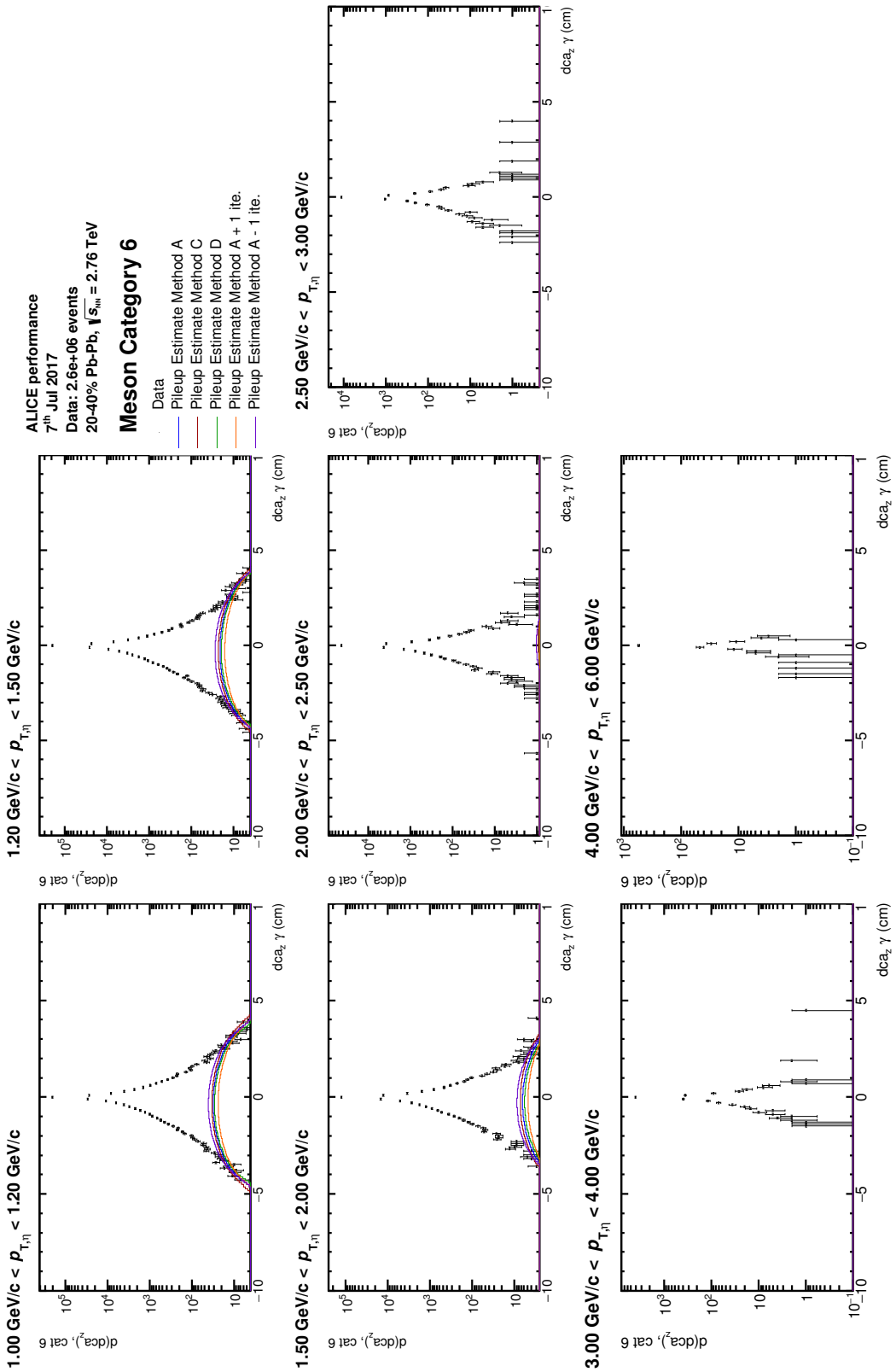

FIGURE B.28: DCA$_z$ distributions for photon from a pair within the η mass region in transverse momentum intervals for meson category six and centrality class 20–40%.

Appendix C

Additional neutral meson results obtained with PCM

The neutral meson performance figures and the final results obtained from the analysis of the centralities 0–5%, 5–10% and 20–40% are reported here for completeness.

C.1 Neutral mesons acceptance and efficiency

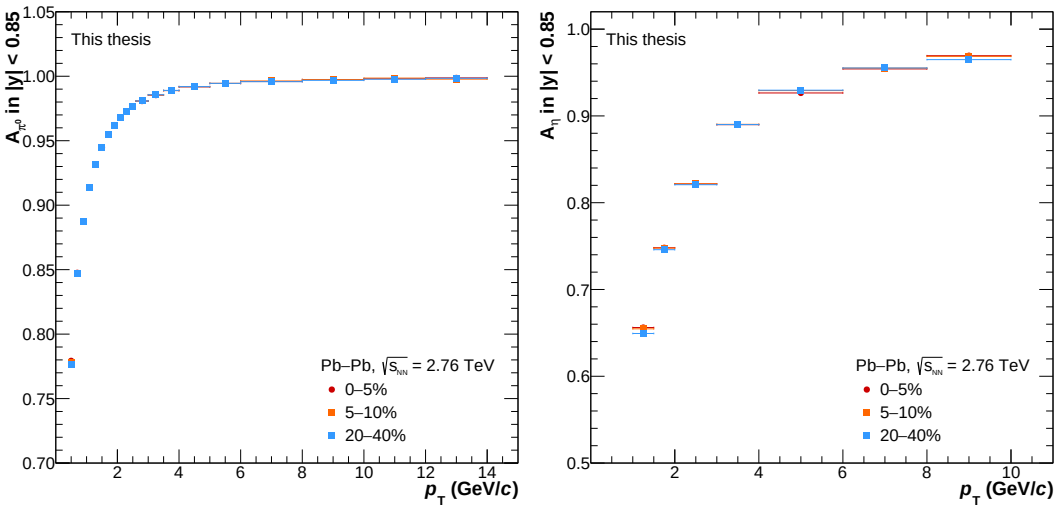

FIGURE C.1: Geometrical acceptance of the π^0 (left) and η (right) meson in the centrality classes 0–5%, 5–10% and 20–40%.

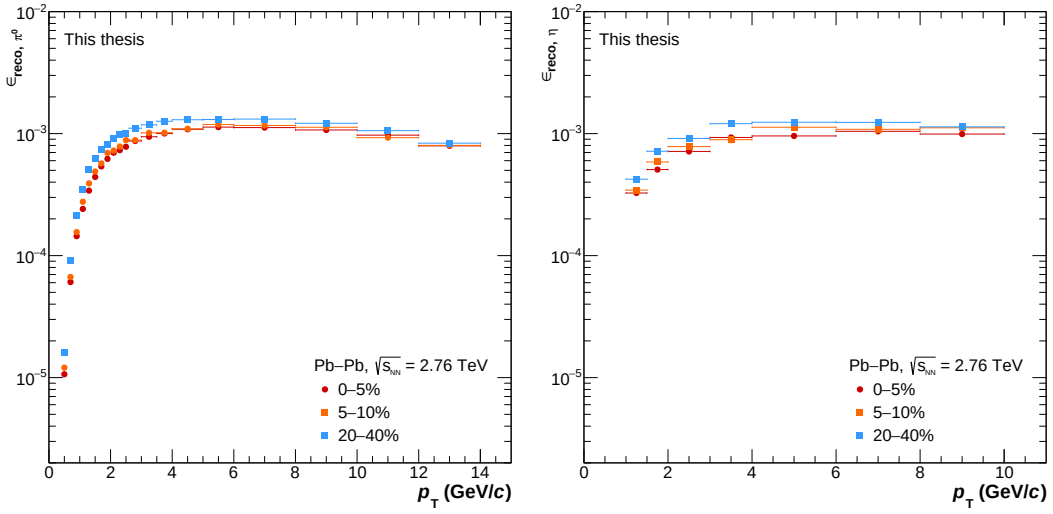

FIGURE C.2: Reconstruction efficiency of the π^0 (left) and η (right) mesons in the centrality classes 0–5%, 5–10% and 20–40%.

C.2 Secondary neutral pions contamination

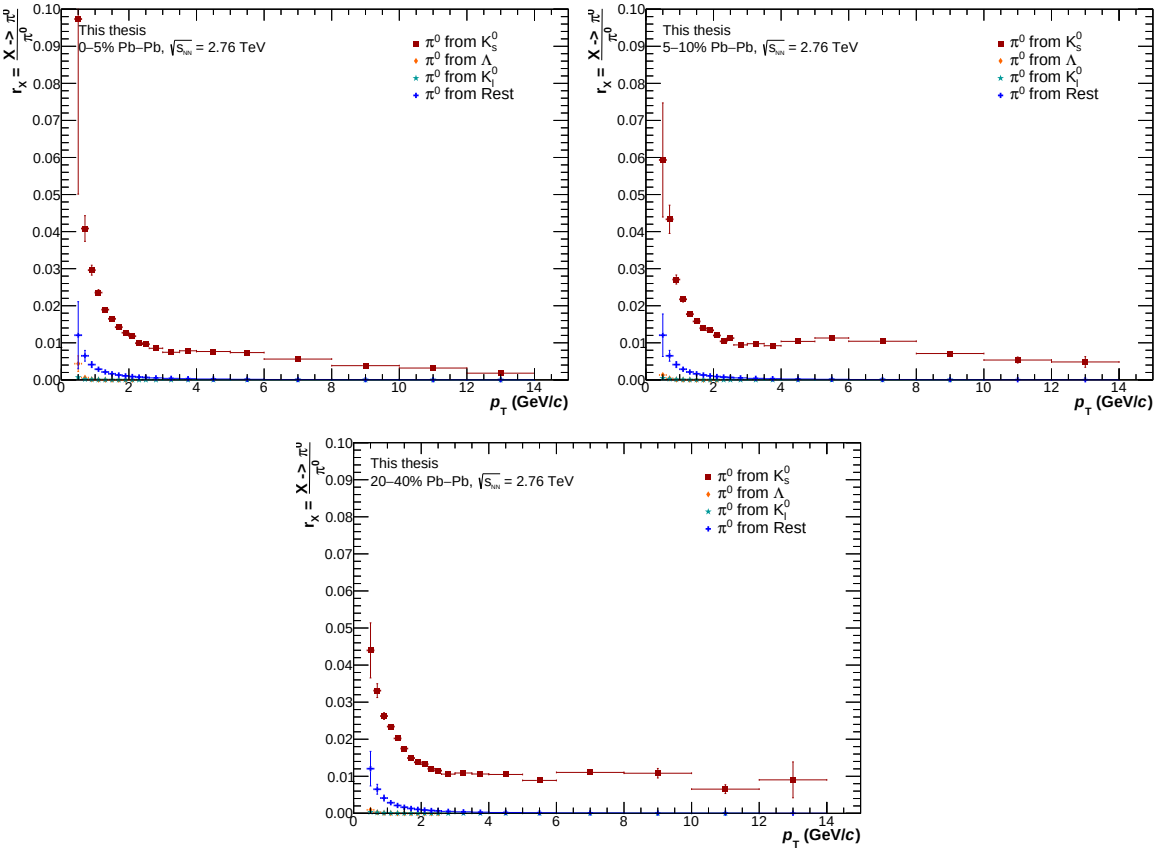

FIGURE C.3: Correction factor for the secondary neutral pions shown separately for each contribution in the centrality classes 0–5% (top left), 5–10% (top right) and 20–40% (bottom).

C.3 Neutral mesons systematic uncertainties

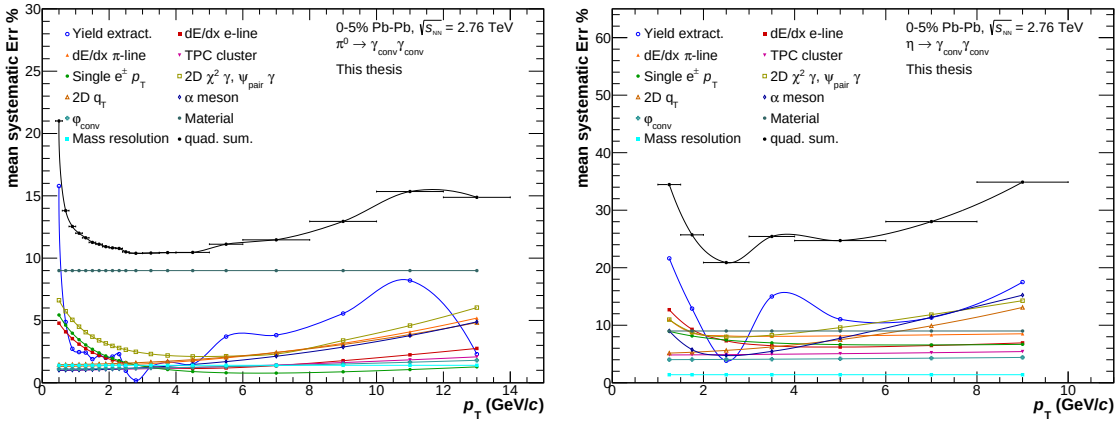

FIGURE C.4: Systematic uncertainties of the π^0 (left) and η (right) mesons in Pb–Pb collisions at $\sqrt{s_{\mathrm{NN}}} = 2.76$ TeV in centrality 0–5%.

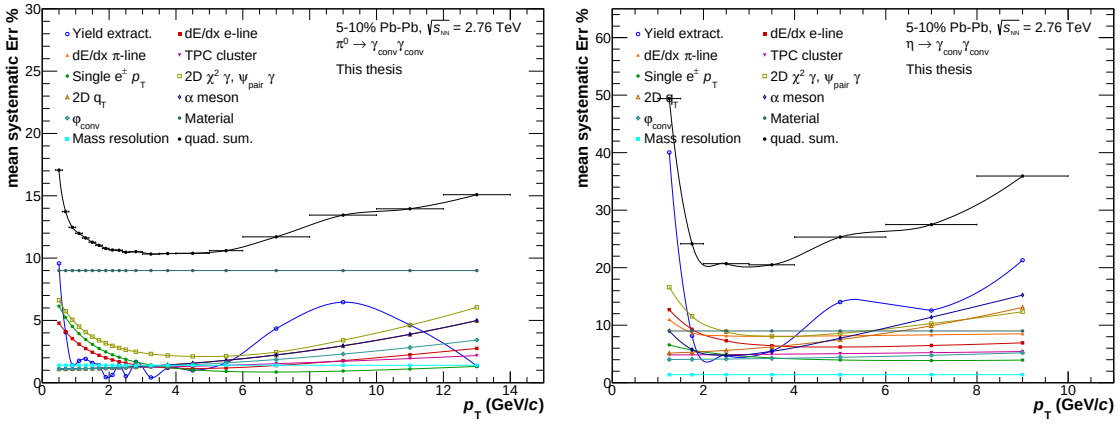

FIGURE C.5: Systematic uncertainties of the π^0 (left) and η (right) mesons in Pb–Pb collisions at $\sqrt{s_{\mathrm{NN}}} = 2.76$ TeV in centrality 5–10%.

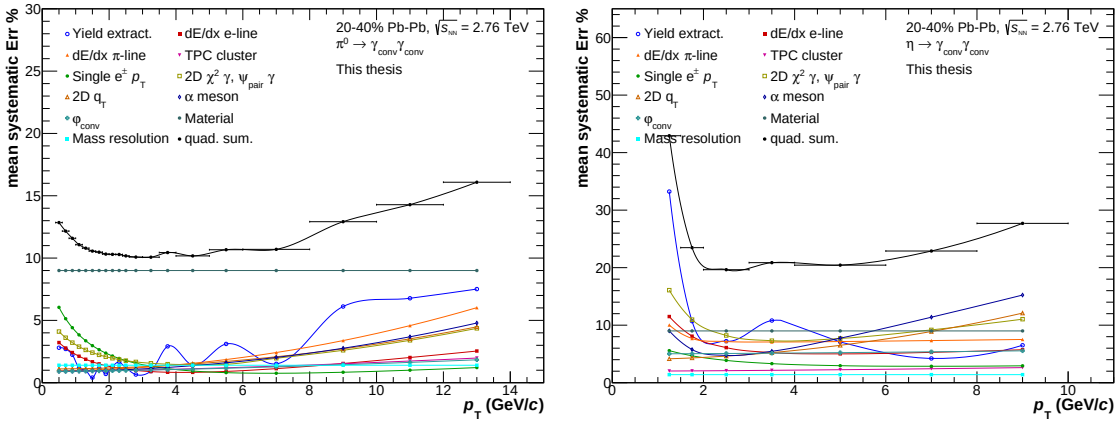

FIGURE C.6: Systematic uncertainties of the π^0 (left) and η (right) mesons in Pb–Pb collisions at $\sqrt{s_{\mathrm{NN}}} = 2.76$ TeV in centrality 20–40%.

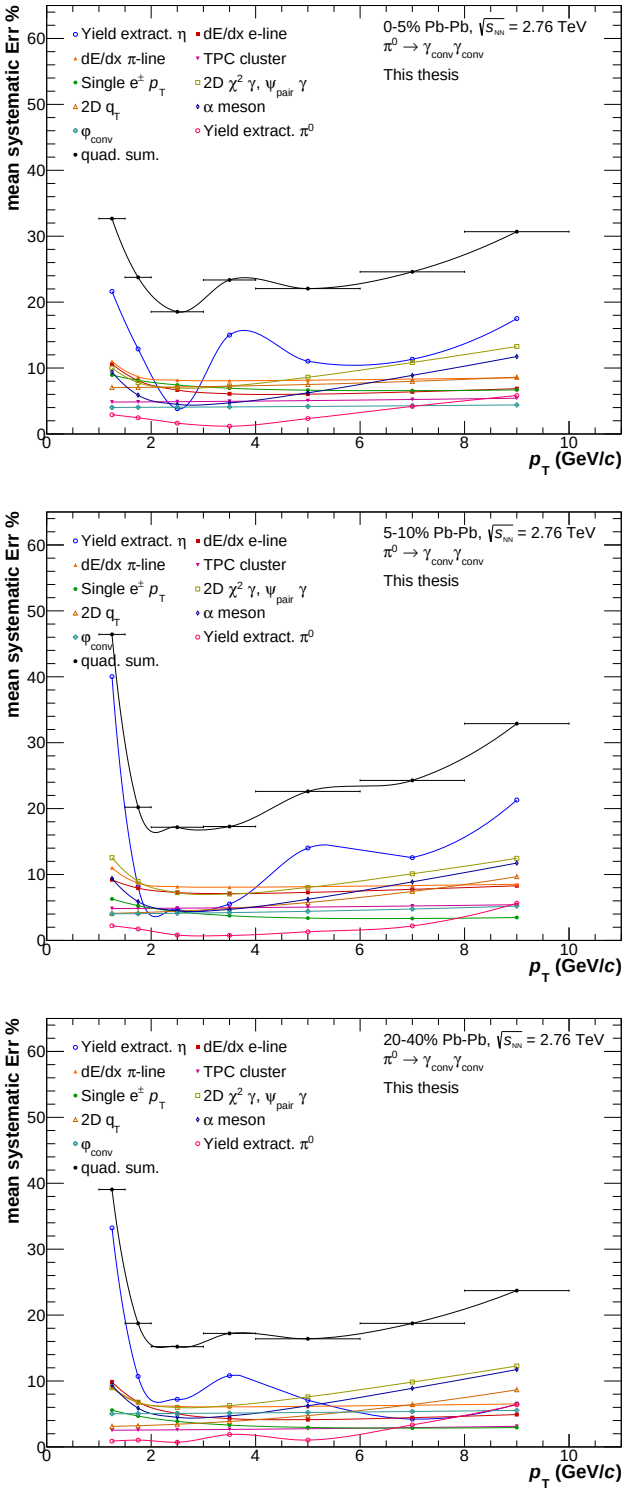

FIGURE C.7: Systematic uncertainties of the η/π^0 ratio for the centrality classes 0–5% (top), 5–10% (middle) and 20–40% (bottom).

C.4 Neutral mesons mass and width

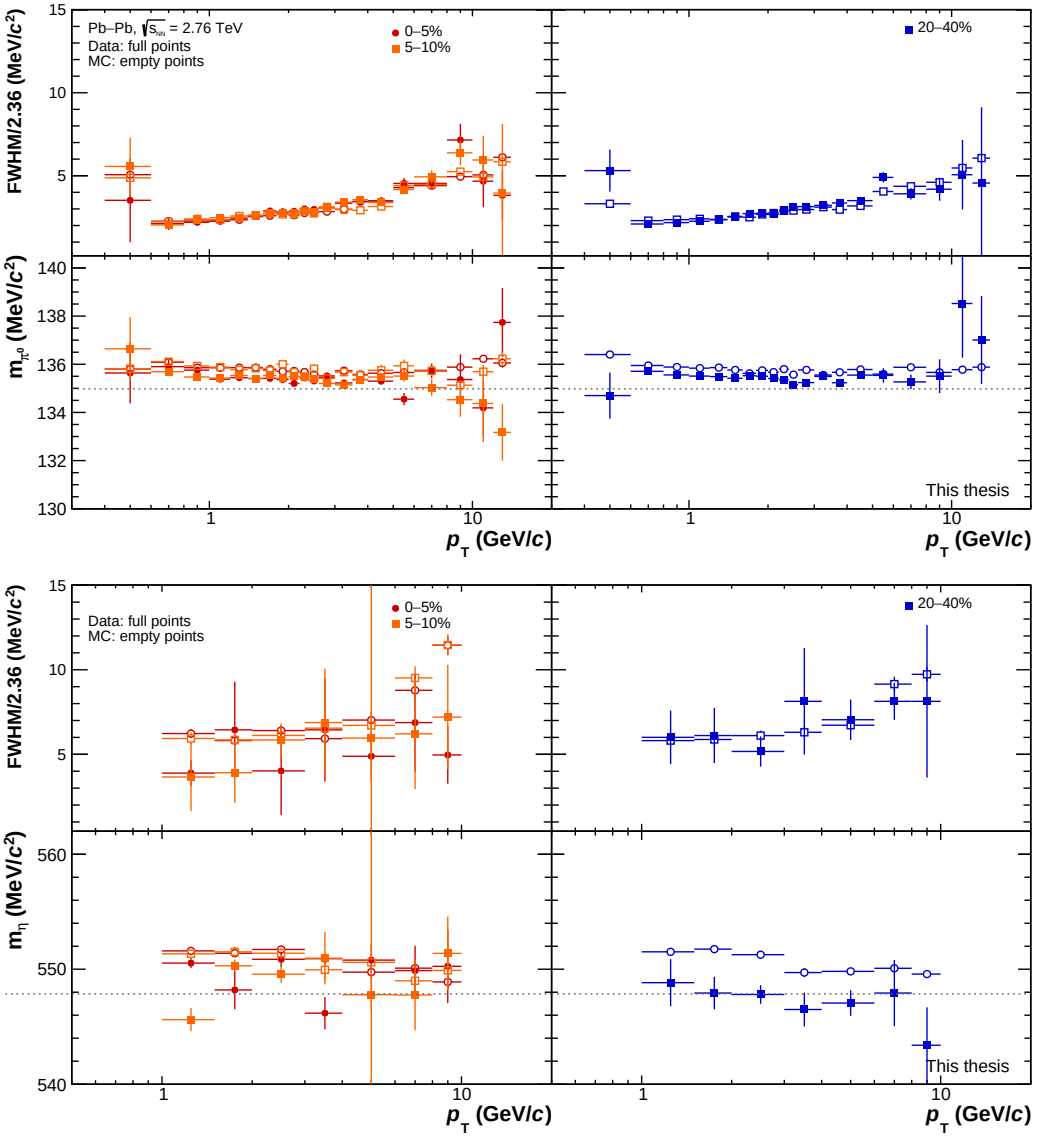

FIGURE C.8: Reconstructed mass resolution (σ = FWHM/2.36, top panels) and mass (bottom panels) for the π^0 (top figure) and η (bottom figure) mesons as a function of the transverse momentum for centrality classes 0–5%, 5–10% and 20–40%. The points for both data (full markers) and simulation (empty markers) are extracted using Equation 5.7.

C.5 Comparison to the published PCM measurements

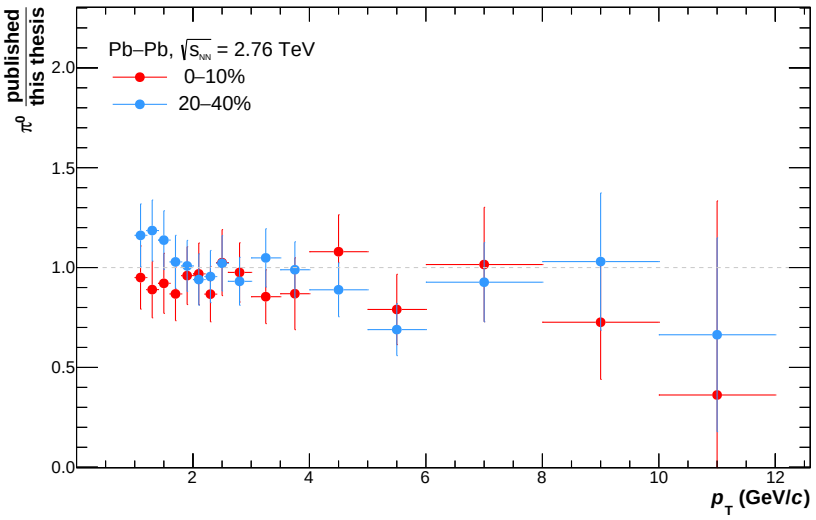

FIGURE C.9: Comparison of the π^0 spectrum from this thesis work to the published PCM measurement [90] for the centrality classes 0–10% and 20–40%. The error bars represent the statistical and systematic uncertainties summed in quadrature.

C.6 Neutral mesons transverse momentum spectra

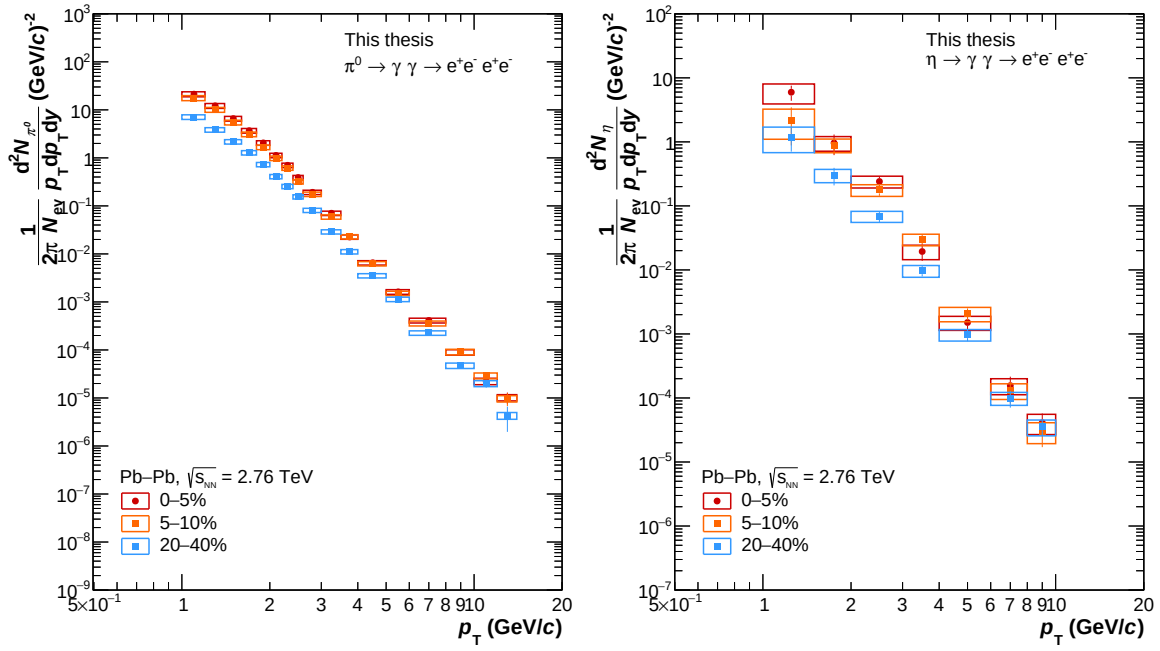

FIGURE C.10: Differential invariant yields for the π^0 (left) and η (right) meson for the centrality classes 0–5%, 5–10% and 20–40% in Pb–Pb collisions at $\sqrt{s_{\mathrm{NN}}} = 2.76$ TeV measured with the PCM. The statistical errors are represented by the vertical bars, the systematic errors by the boxes.

C.7 η/π^0 ratio

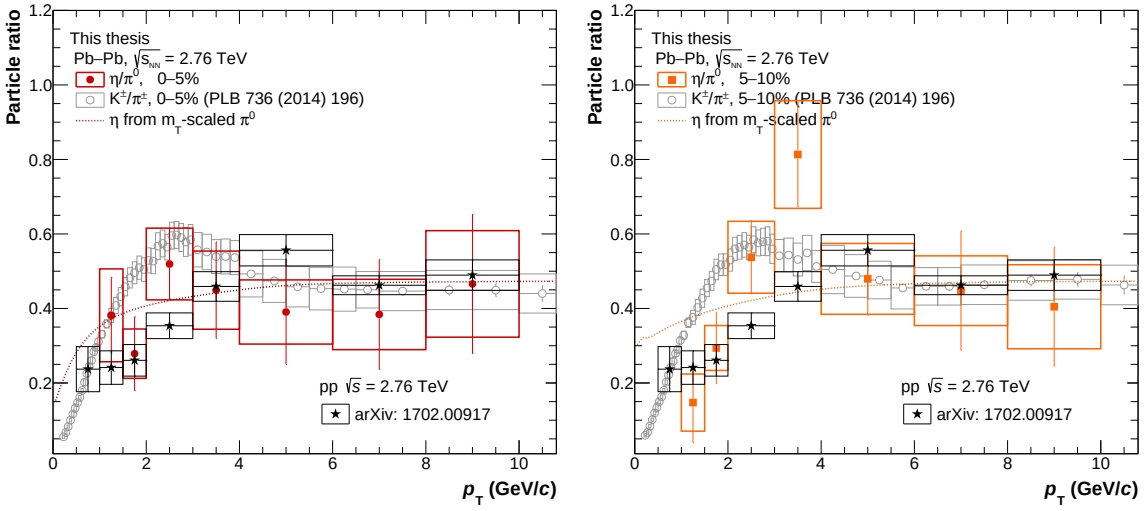

FIGURE C.11: Ratio of the η to π^0 meson for the centrality classes 0–5% and 5–10% in Pb–Pb collisions at $\sqrt{s_{\mathrm{NN}}} = 2.76$ TeV. The ratio is compared to the same measurement in pp collisions at $\sqrt{s} = 2.76$ TeV [206] and to the $\mathrm{K}^{\pm}/\pi^{\pm}$ ratio, at the same centrality and centre-of-mass energy. The dashed lines represent the ratio obtained using the η obtained via m_{T}-scaling from the π^0 meson.

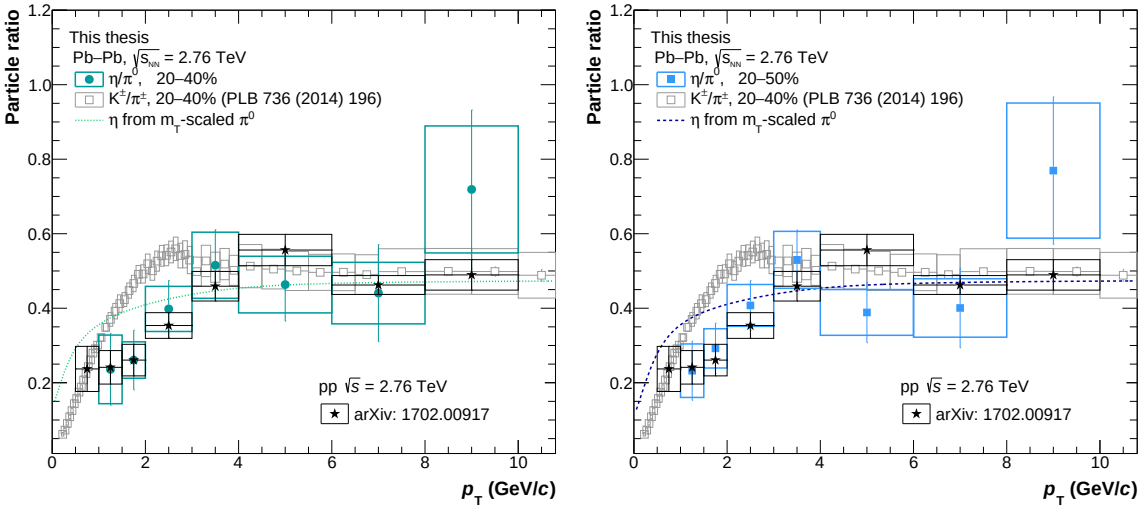

FIGURE C.12: Ratio of the η to π^0 meson for the centrality classes 20–40% and 20–50% in Pb–Pb collisions at $\sqrt{s_{\mathrm{NN}}} = 2.76$ TeV. The ratio is compared to the same measurement in pp collisions at $\sqrt{s} = 2.76$ TeV [206] and to the $\mathrm{K}^{\pm}/\pi^{\pm}$ ratio, at the same centrality (centrality 20–40% is used for the η/π^0 ratio in 20–50%) and centre-of-mass energy. The dashed lines represent the ratio obtained using the η obtained via m_{T}-scaling from the π^0 meson.

C.8 Neutral mesons R_{AA}

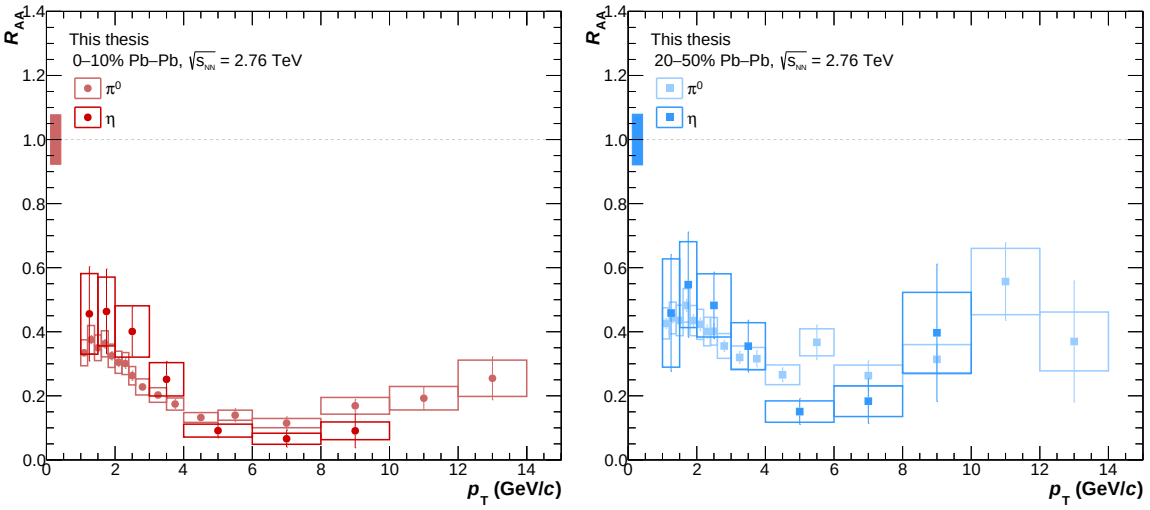

FIGURE C.13: Comparison of the π^0 and η meson nuclear modification factor in the centrality classes 0–10% (left) and 20–50% (right). The coloured boxes around unity reflect the uncertainty of the average nuclear overlap function (T_{AA}) and the normalisation uncertainty of the pp spectrum added in quadrature.

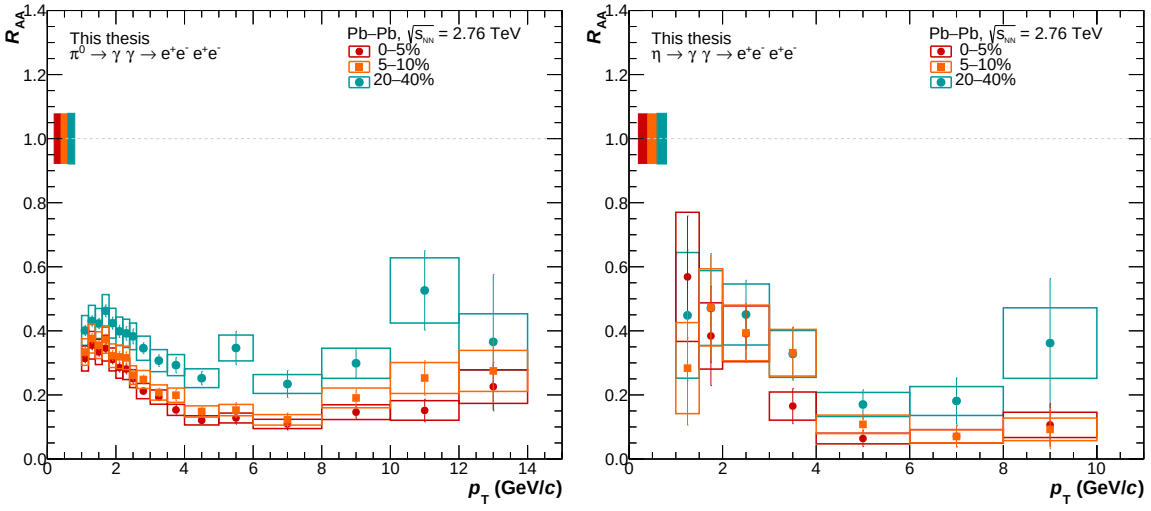

FIGURE C.14: Nuclear modification factor for the π^0 (left) and η (right) meson in the centrality classes 0–5%, 5–10% and 20–40%. The coloured boxes around unity reflect the uncertainty of the average nuclear overlap function (T_{AA}) and the normalisation uncertainty of the pp spectrum added in quadrature.

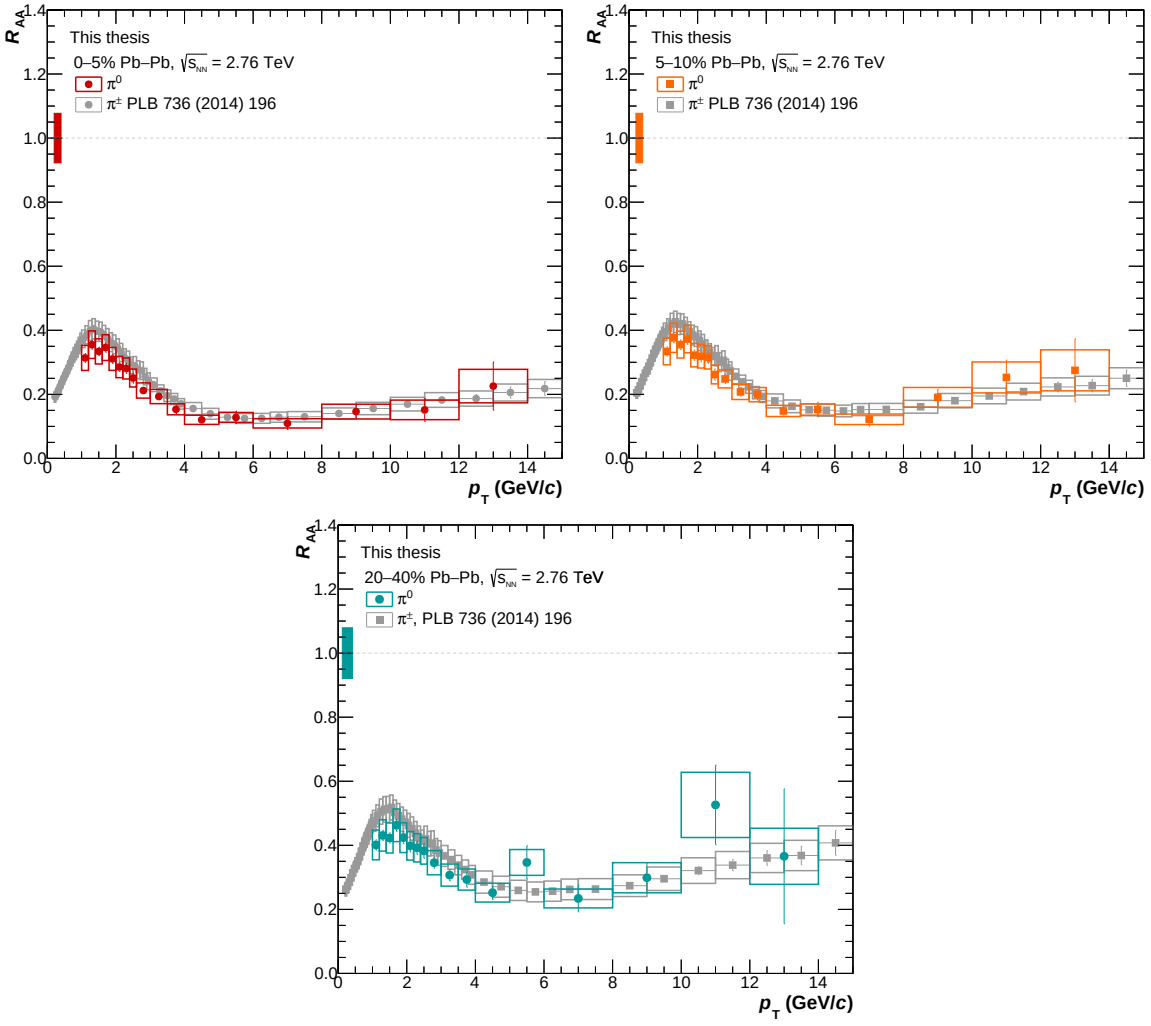

FIGURE C.15: Nuclear modification factor for the π^0 meson in the centrality classes 0–5% (top left), 5–10% (top right) and 20–40% (bottom), compared to the charged pion R_{AA}, in the same centrality classes, measured in Pb–Pb collisions at $\sqrt{s_{\mathrm{NN}}} = 2.76$ TeV [204].

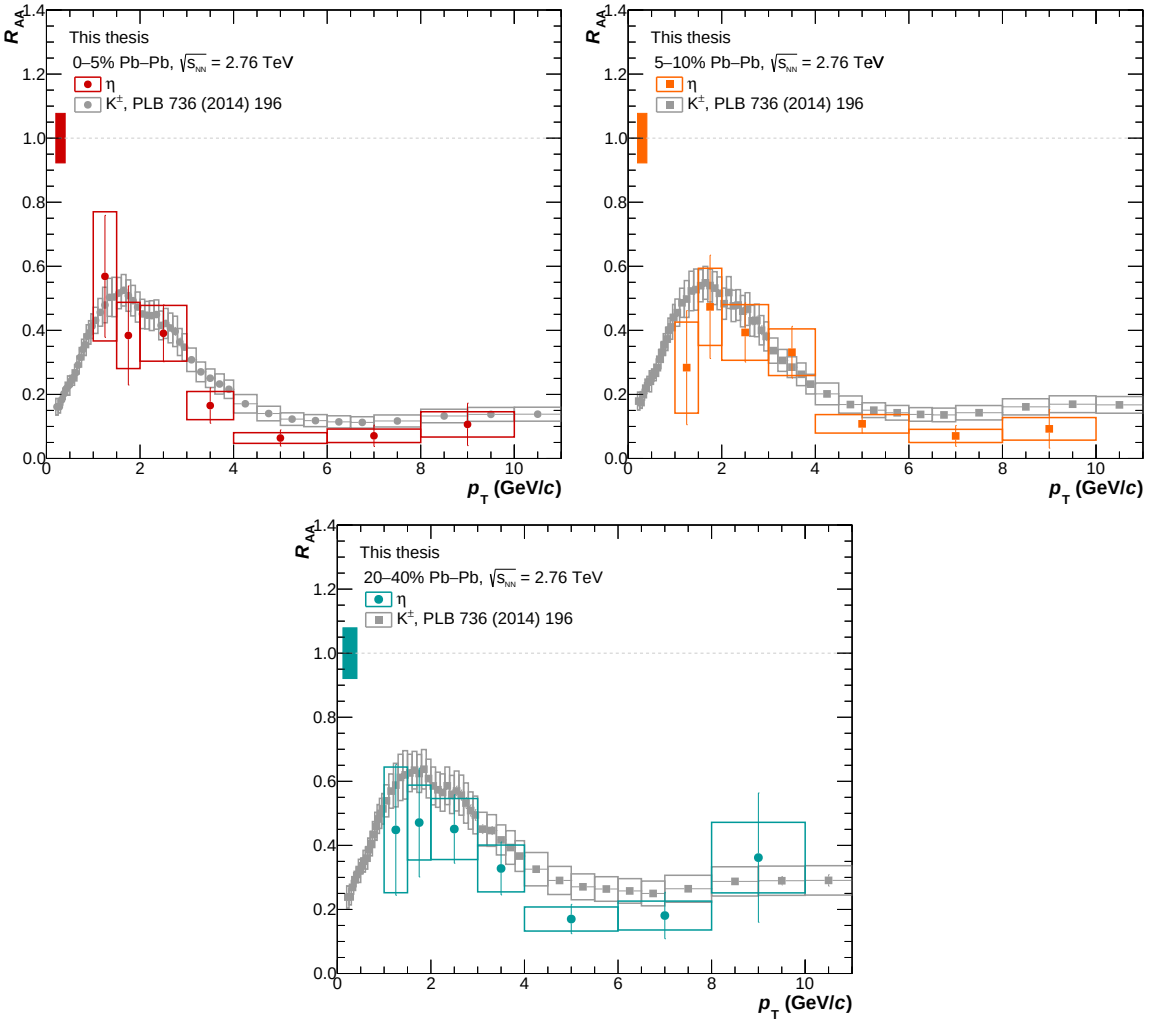

FIGURE C.16: Nuclear modification factor for the η meson in the centrality classes 0–5% (top left), 5–10% (top right) and 20–40% (bottom), compared to the charged kaon R_{AA}, in the same centrality classes, measured in Pb–Pb collisions at $\sqrt{s_{\mathrm{NN}}} = 2.76$ TeV [204].

Appendix D

Additional neutral meson results obtained with the combined PCM, PHOS and EMCal measurement

In this appendix, additional figures from the combination of the PCM, PHOS and EMCal measurements and of the final combined results are reported.

D.1 Uncertainties of the neutral mesons measurements

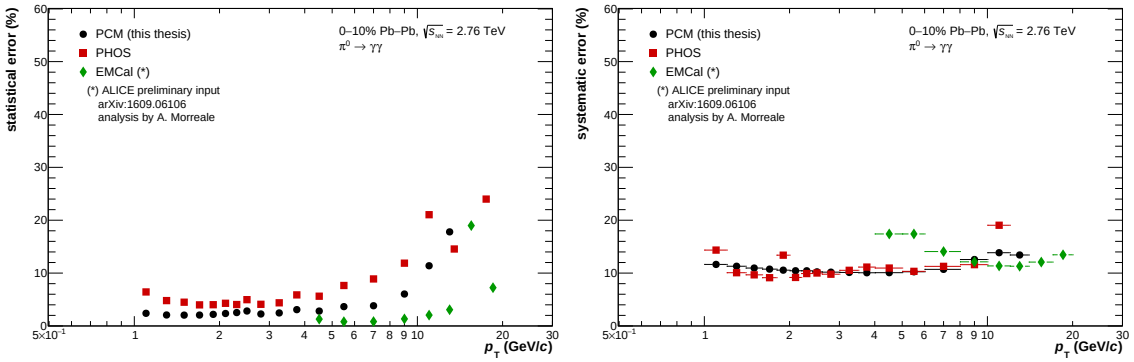

FIGURE D.1: Statistical (left) and systematic (right) uncertainties of the π^0 meson spectrum shown for the individual method measurements in 0–10% Pb–Pb collisions.

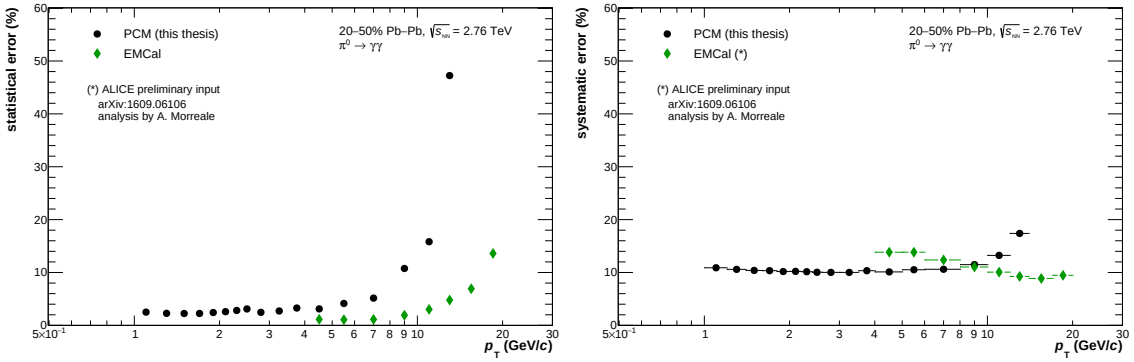

FIGURE D.2: Statistical (left) and systematic (right) uncertainties of the π^0 meson spectrum shown for the individual method measurements in 20–50% Pb–Pb collisions.

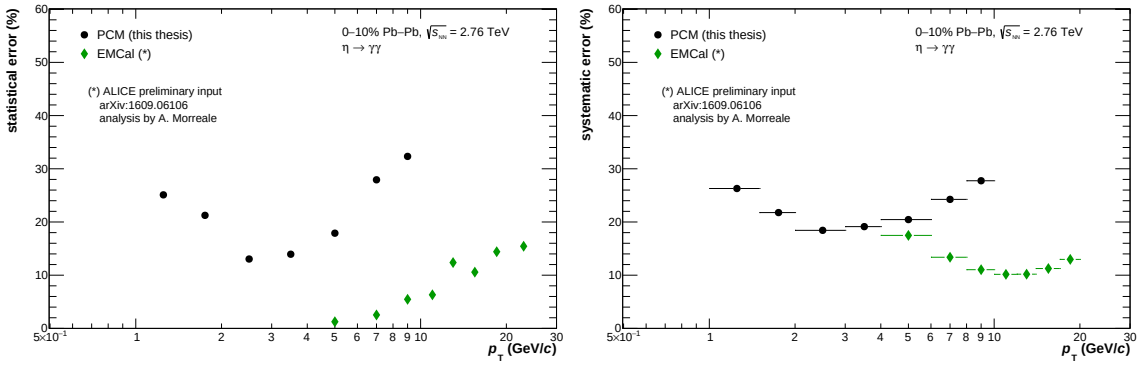

FIGURE D.3: Statistical (left) and systematic (right) uncertainties of the η meson spectrum shown for the individual method measurements in 0–10% Pb–Pb collisions.

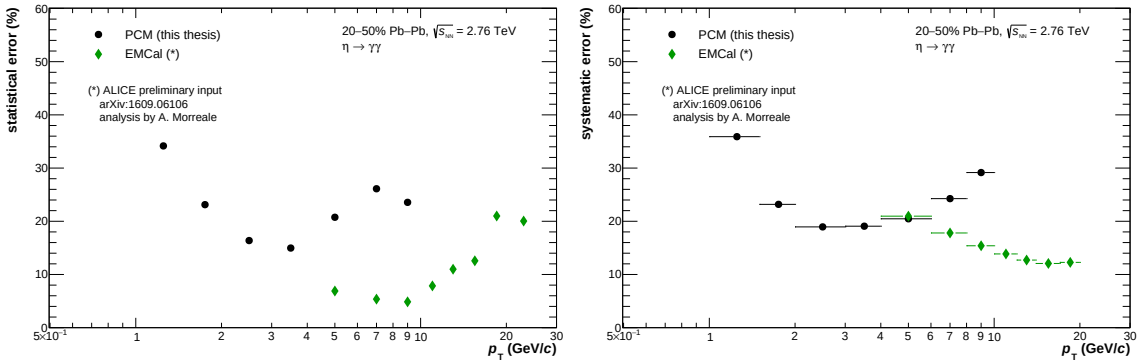

FIGURE D.4: Statistical (left) and systematic (right) uncertainties of the η meson spectrum shown for the individual method measurements in 20–50% Pb–Pb collisions.

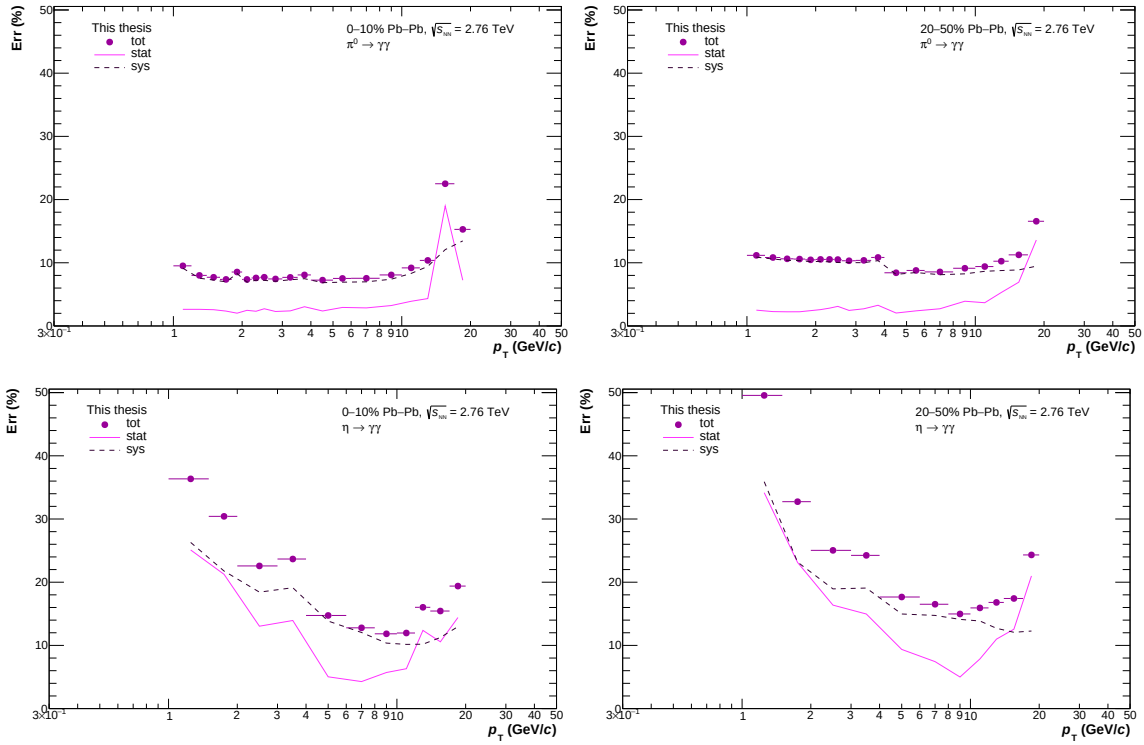

FIGURE D.5: Total, statistical and systematic uncertainties of the combined π^0 (top row) and η (bottom row) meson spectrum in 0–10% (left) and 20–50% (right) Pb–Pb collisions.

D.2 Individual neutral meson measurements

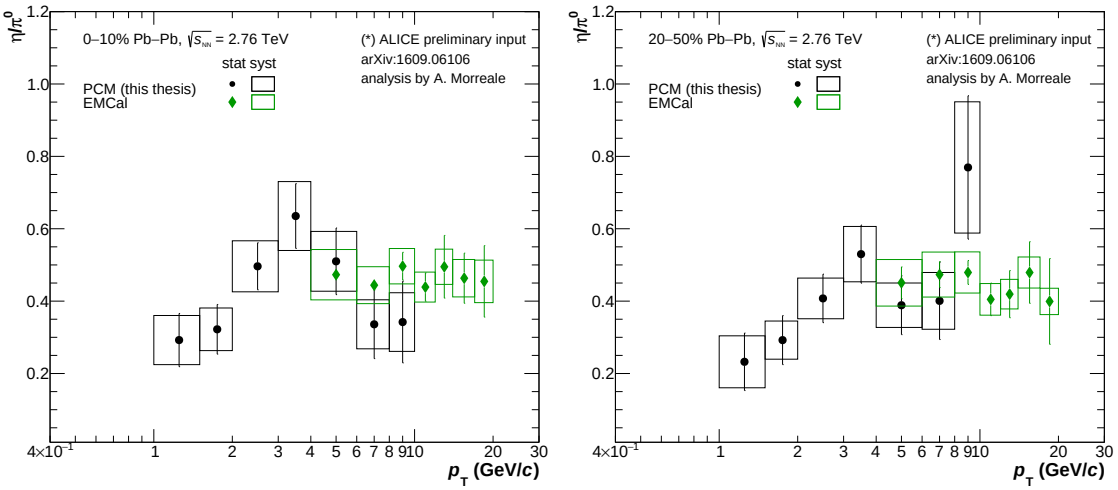

FIGURE D.6: Comparison of the η/π^0 ratio the individual measurements in 0–10% (left) and 20–50% (right) Pb–Pb collisions. The uncertainties are illustrated in the legend.

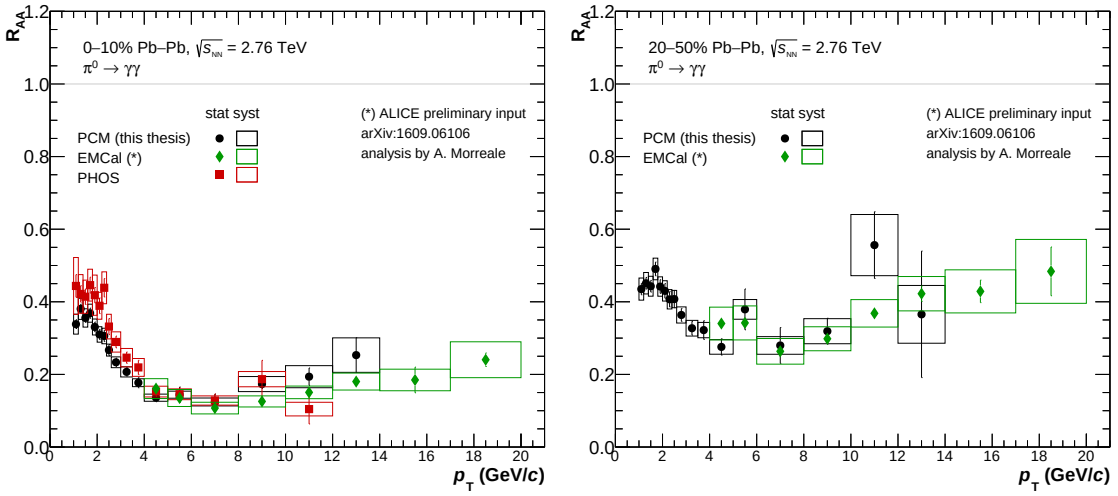

FIGURE D.7: Comparison of the π^0 R_{AA} ratio the individual measurements in 0–10% (left) and 20–50% (right) Pb–Pb collisions. The uncertainties are illustrated in the legend.

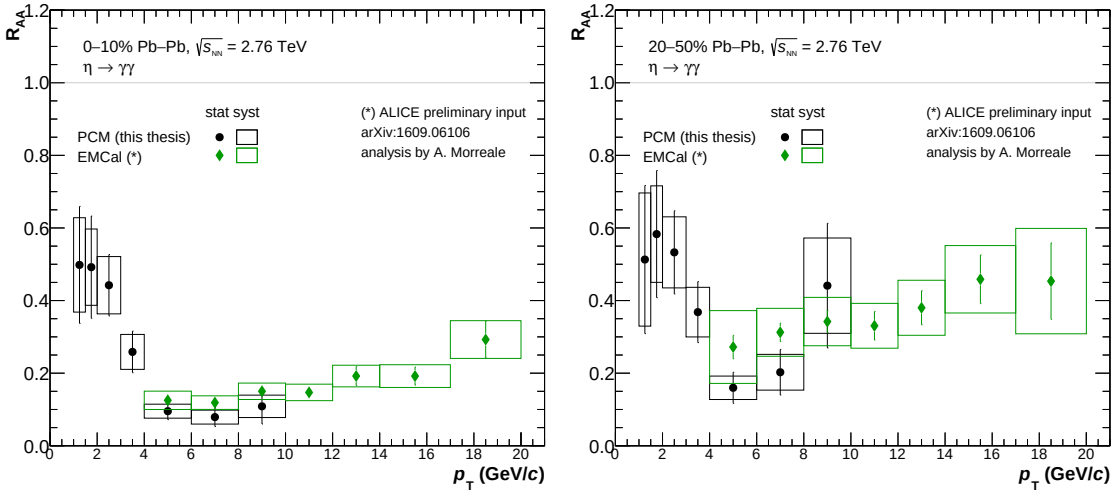

FIGURE D.8: Comparison of the η R_{AA} ratio the individual measurements in 0–10% (left) and 20–50% (right) Pb–Pb collisions. The uncertainties are illustrated in the legend.

D.3 Final results for the neutral meson measurements

D.3.1 Combined η/π^0 ratio

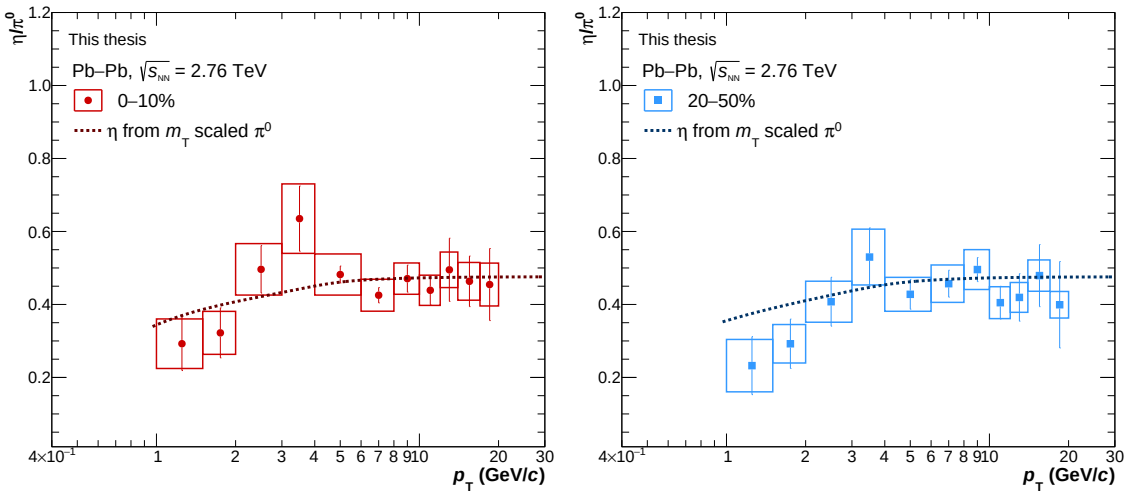

FIGURE D.9: The combined η/π^0 ratio in 0–10% (left) and 20–50% (right) Pb–Pb collisions is plotted together with the respective m_T-scaling curves.

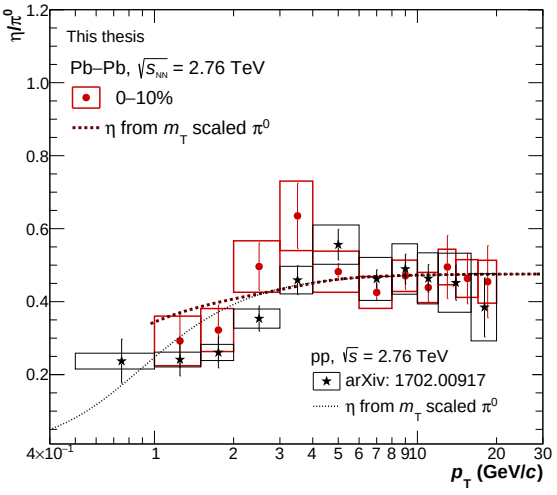

FIGURE D.10: The combined η/π^0 ratio in 0–10% Pb–Pb collisions is plotted together with the ratio measured in pp collisions at the same centre-of-mass energy [206]. The dashed lines represent the ratio obtained using the m_T-scaled η from the π^0 meson measurement in the same collision system.

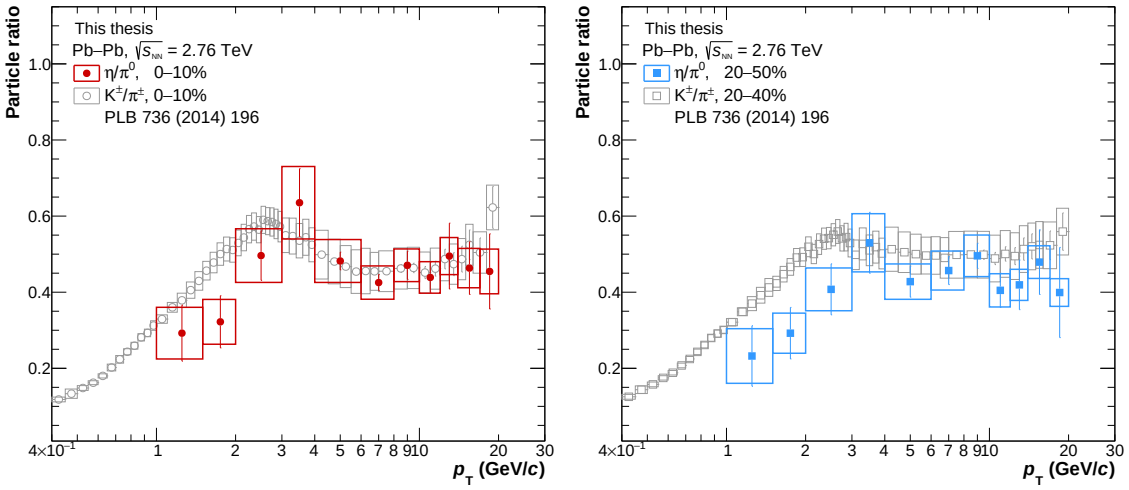

FIGURE D.11: Comparison of the combined η/π^0 ratio in 0–10% (left) and 20–50% (right) Pb–Pb collisions to the charged kaon to pion ratio, at the same centre-of-mass energy, in the centrality classes 0–10% and 20–40%, respectevely.

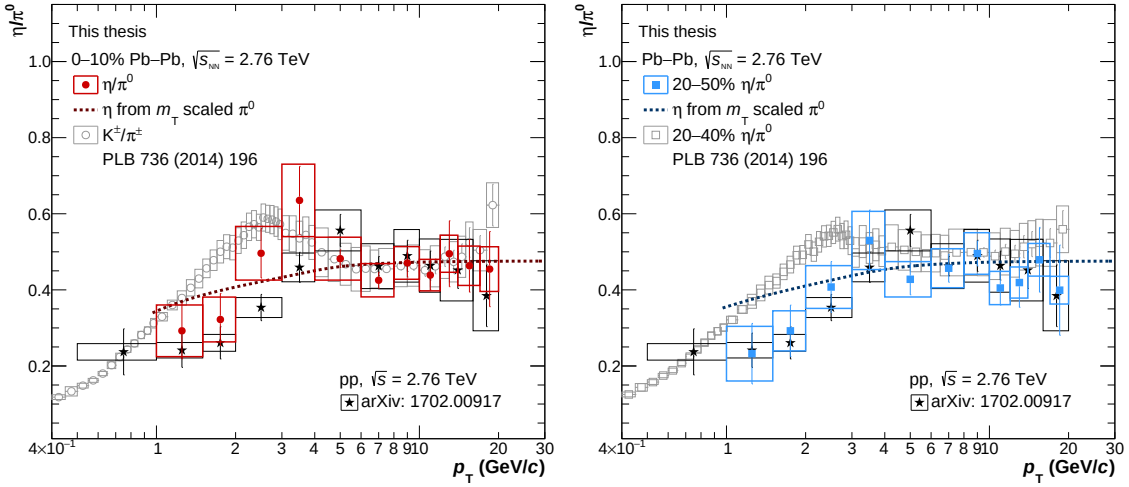

FIGURE D.12: The combined η/π^0 ratio in 0–10% (left) and 20–50% (right) Pb–Pb collisions is plotted together with the respective m_T-scaling curves. Also shown here, the η/π^0 ratio in pp collisions [206] and the charged kaon to pion ratio [204]

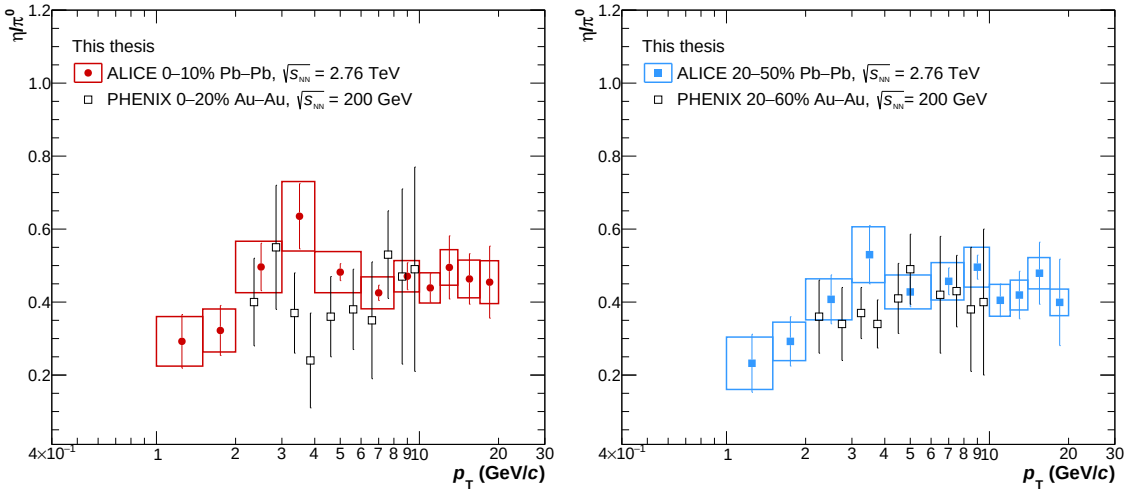

FIGURE D.13: Comparison of the combined η/π^0 ratio in 0–10% (left) and 20–50% (right) Pb–Pb collisions to the RHIC results in 0–20% and 20–60% Au–Au collisions, respectively, at $\sqrt{s_{\mathrm{NN}}} = 200$ GeV [211].

D.3.2 Combined nuclear modification factor R_{AA}

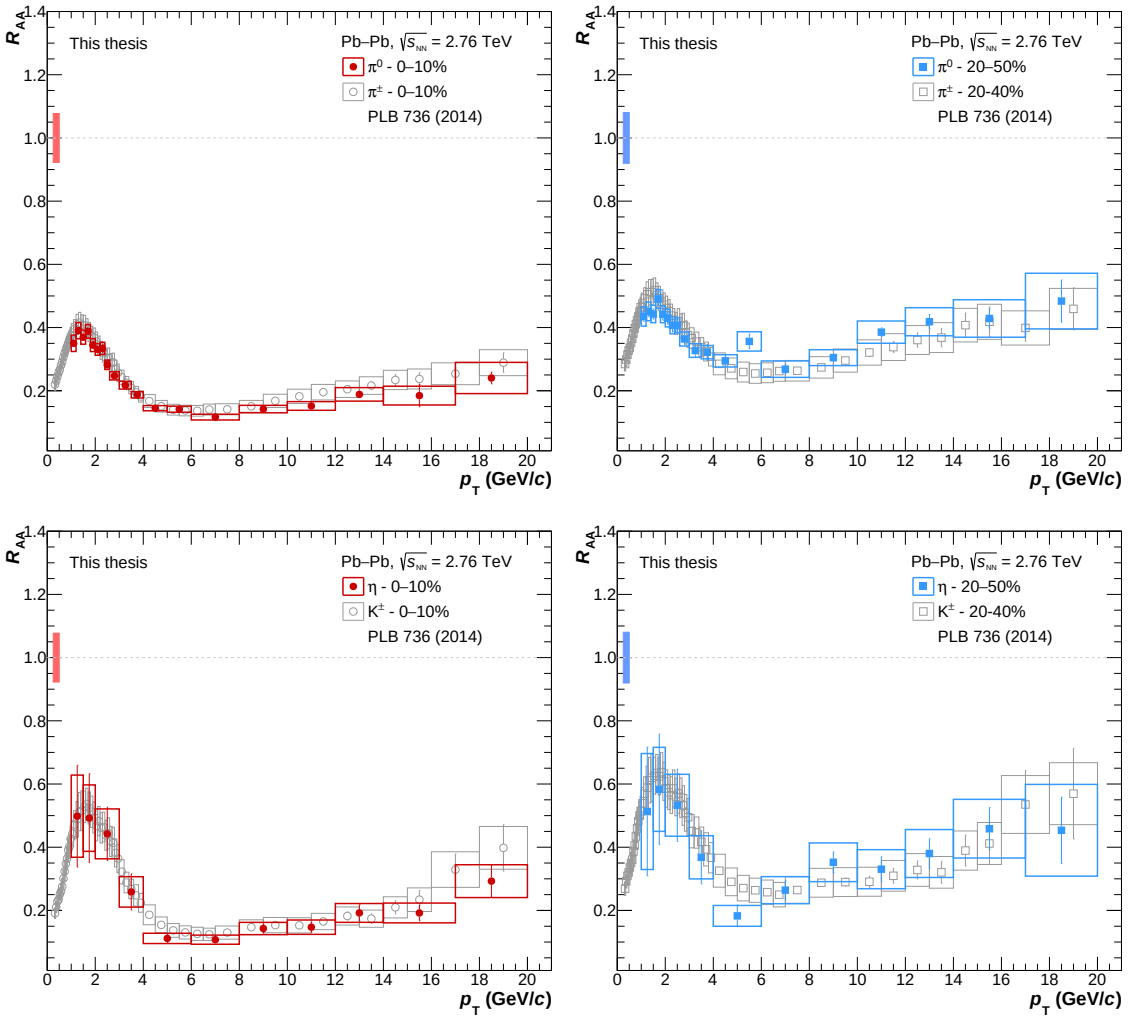

FIGURE D.14: Nuclear modification factor for the combined π^0 (top row) and η (bottom row) meson measurements in the centrality classes 0–10% (left) and 20–50% (right), compared to the charged pion and kaon R_{AA}, respectively, in the same centrality classes, measured in Pb–Pb collisions at $\sqrt{s_{\mathrm{NN}}} = 2.76$ TeV [204].

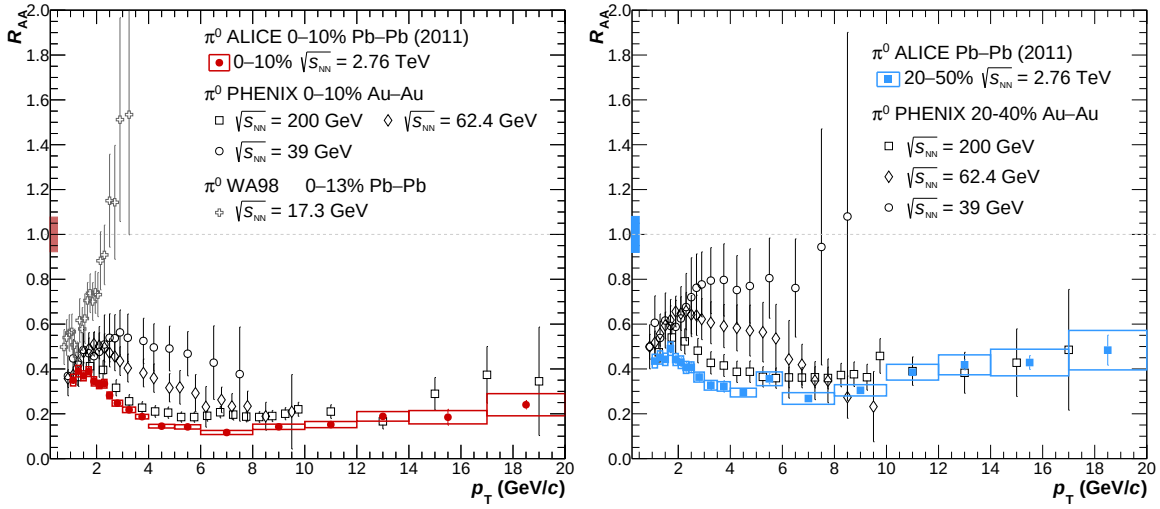

FIGURE D.15: R_{AA} of the combined π^0 meson measurement in Pb–Pb collisions at $\sqrt{s_{\mathrm{NN}}}$ for the 010% (left) and 20–50% (right) centrality classes is compared to the results from experiments at lower energies: from Au–Au collisions at $\sqrt{s_{\mathrm{NN}}} = 39$, 62.4 [91], and 200 GeV [92] at RHIC and, for 0–10% only, the result from the CERN SPS [93] are shown.

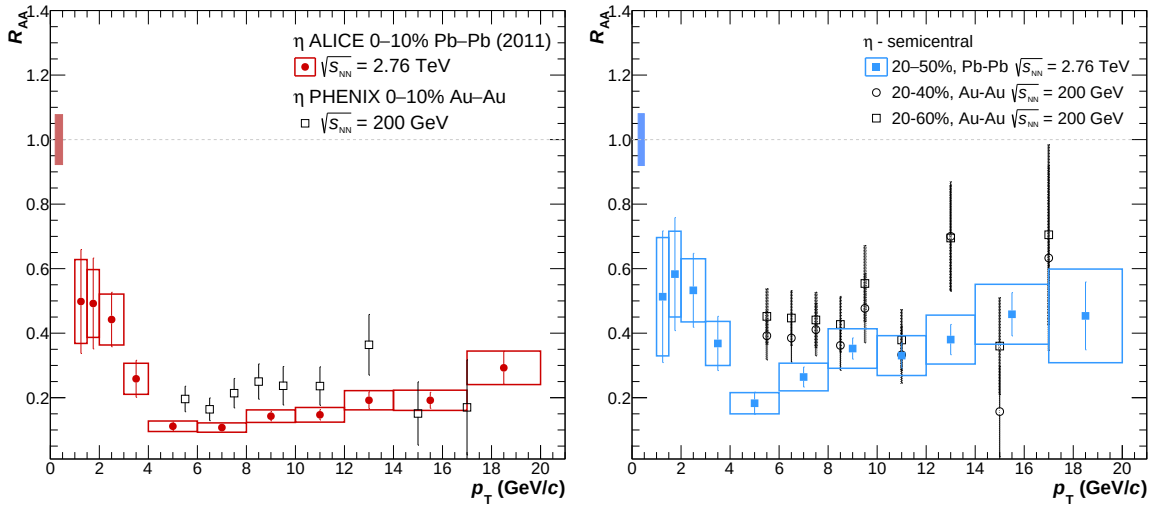

FIGURE D.16: R_{AA} of the combined η meson measurement in Pb–Pb collisions at $\sqrt{s_{\mathrm{NN}}} = 2.76$ TeV for the centrality classes 0–10% (left) and 20–50% (right), compared to results from Au–Au collisions at $\sqrt{s_{\mathrm{NN}}} = 200$ GeV measured at RHIC [211].

Appendix E

List of particles for the cocktail simulation

List of particles used in the cocktail simulation with the respective decays as they are implemented in the Pythia decayer. The last column reports the m_{T}-scaling factor used in the absence of the input spectrum of that specific particle.

Particle	Mass (MeV)	Decay channel	Branching ratio	m_{T}-scaling factor
π^0	134.98	$\gamma\gamma$	98.82%	
		$e^+e^-\gamma$	1.17%	
η	547.85	$\gamma\gamma$	39.41%	0.46
		$\pi^0\gamma\gamma$	2.56×10^{-4}	
		$\pi^+\pi^-\gamma$	4.22×10^{-2}	
		$e^+e^-\gamma$	6.89×10^{-3}	
		$\mu^+\mu^-\gamma$	3.09×10^{-4}	
η'	957.66	$\rho^0\gamma$	2.91%	0.40
		$\omega\gamma$	2.75%	
		$\gamma\gamma$	2.19%	
		$\mu^+\mu^-\gamma$	1.08×10^{-4}	
ω	782.65	$\pi^0\gamma$	8.35%	0.85
		$\eta\gamma$	4.6×10^{-4}	
		$\pi^0\pi^0\gamma$	7.0×10^{-5}	
ρ^0	775.49	$\pi^+\pi^-\gamma$	9.9×10^{-3}	
		$\pi^0\gamma$	6.0×10^{-4}	
		$\eta\gamma$	3.0×10^{-4}	
		$\pi^0\pi^0\gamma$	4.5×10^{-5}	
ρ^+	775.49	$\pi^+\gamma$	4.5×10^{-4}	1.00
ρ^-	775.49	$\pi^-\gamma$	4.5×10^{-4}	1.00

ϕ	1019.46	$\eta\gamma$	1.31%	
		$\pi^0\gamma$	1.27×10^{-3}	
		$\pi^+\pi^-\gamma$	4.10×10^{-5}	
		$\pi^0\pi^0\gamma$	1.13×10^{-4}	
		$\pi^0\eta\gamma$	7.30×10^{-5}	
		$\eta'\gamma$	6.30×10^{-5}	
		$\mu^+\mu^-\gamma$	1.40×10^{-5}	
Δ^0	1232.00	$n\gamma$	6.0×10^{-3}	1.00
Δ^+	1232.00	$p\gamma$	6.0×10^{-3}	1.00
Σ^0	1192.64	$\Lambda\gamma$	100%	0.49
K_S^0	497.61	$\pi^+\pi^-\gamma$	1.79×10^{-3}	
		$\gamma\gamma$	3.00×10^{-6}	
K_L^0	497.61	$\pi^\pm e^\mp\nu\gamma$	3.99×10^{-3}	0.57
		$\pi^\pm\mu^\mp\nu\gamma$	4.92×10^{-4}	
		$\pi^+\pi^-\gamma$	4.2×10^{-5}	
		$\pi^0\gamma\gamma$	1.0×10^{-6}	
		$\gamma\gamma$	5.5×10^{-4}	
		$e^+e^-\gamma$	9.0×10^{-6}	
Λ	1115.68	$n\gamma$	1.75×10^{-3}	
		$p\pi^-\gamma$	8.40×10^{-4}	

TABLE E.1: List of all the particles with photon decays used as sources for the cocktail simulation production, with the relevant photon decays and branching ratios [9].

Appendix F

Additional direct photon results obtained with PCM

In this appendix, additional figures for the direct photon measurement obtained with the photon conversion method are reported. In all the figures, the statistical uncertainties are indicated by the vertical bars, the systematic uncertainties by the boxes.

F.1 Inclusive photon to π^0 ratio

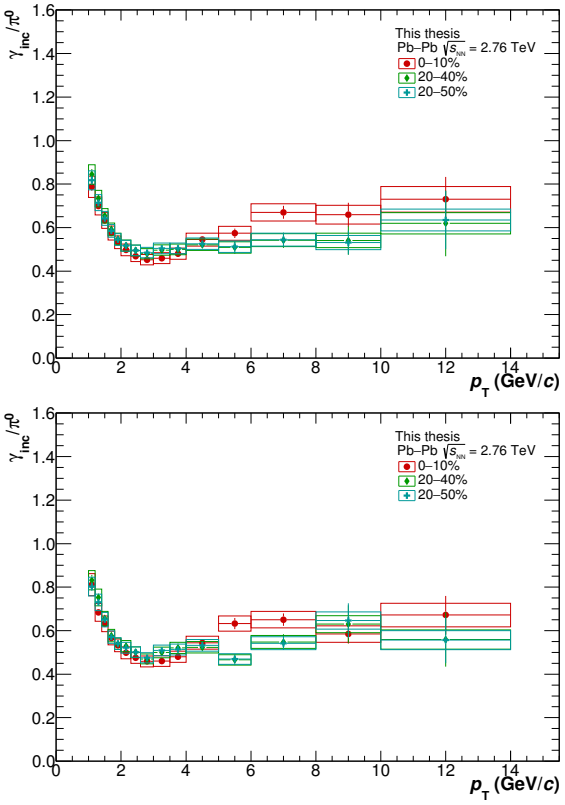

FIGURE F.1: Inclusive photon over the π^0 spectrum ratio for all the centrality classes plotted together. In the top plot, the fit to the π^0 spectrum is used at denominator, while in the bottom plot, the measured data points are used.

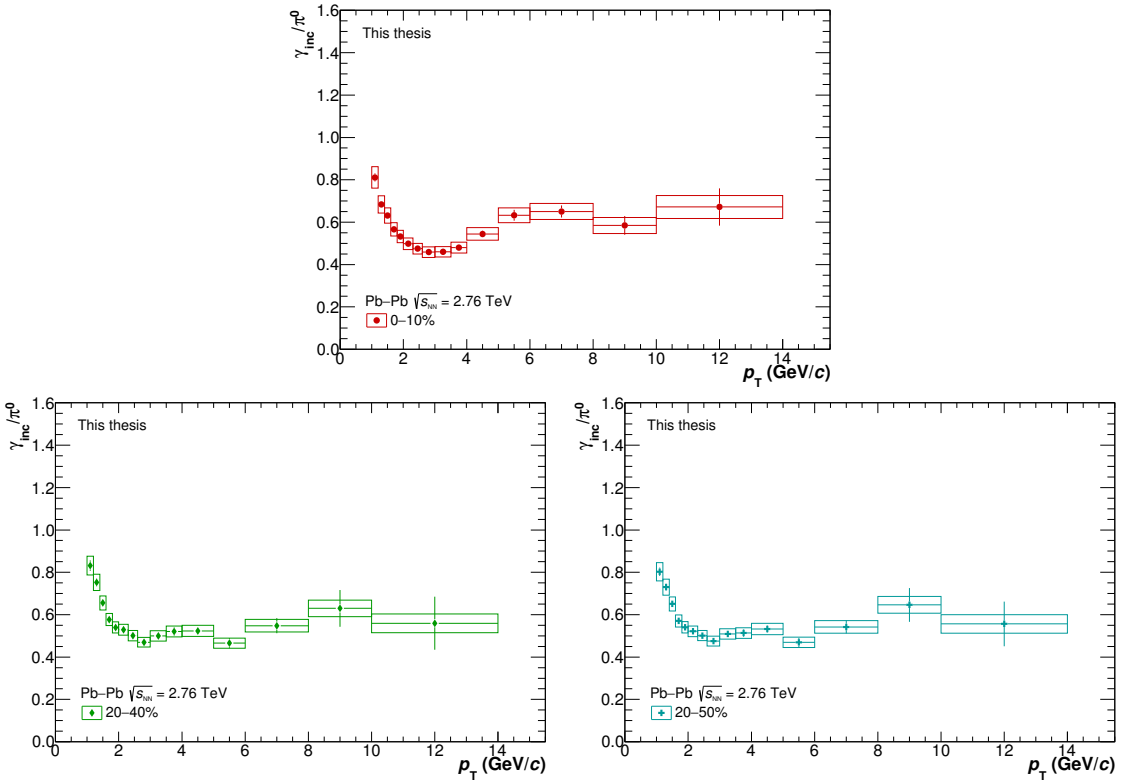

FIGURE F.2: Ratio of the inclusive photon over the measured π^0 spectrum for the centrality classes 0–10% (top), 20–40% (left) and 20–50% (right).

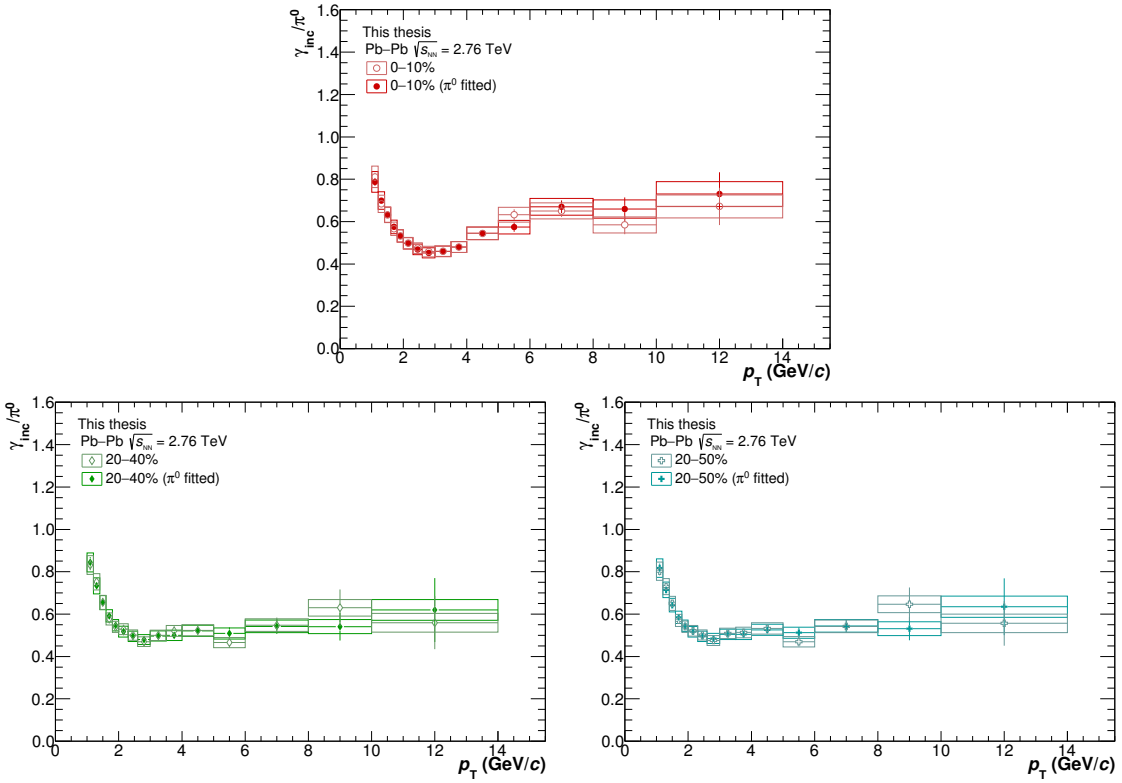

FIGURE F.3: Comparison of the $\gamma_{\mathrm{incl}}/\pi^0$ ratio calculated using the fit to the π^0 spectrum or its data points for the centrality classes 0–10% (top), 20–40% (left) and 20–50% (right).

F.2 Photon double ratio R_γ

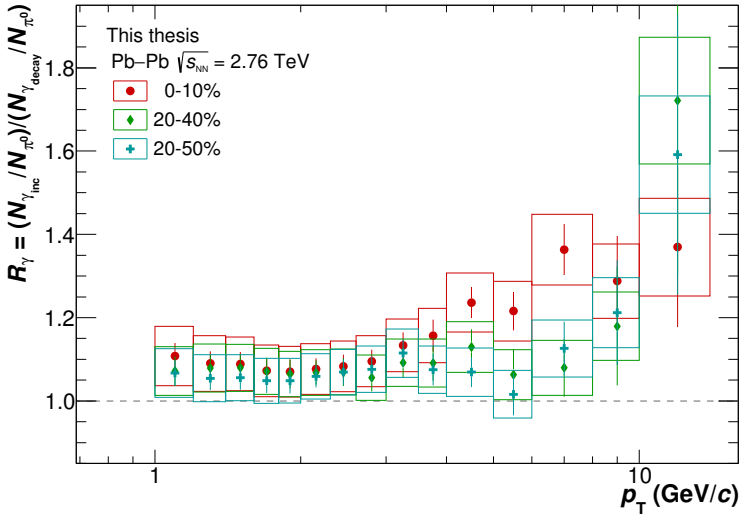

FIGURE F.4: Photon double ratio, R_γ, for all the centrality classes plotted together. The fit to the π^0 spectrum is used here.

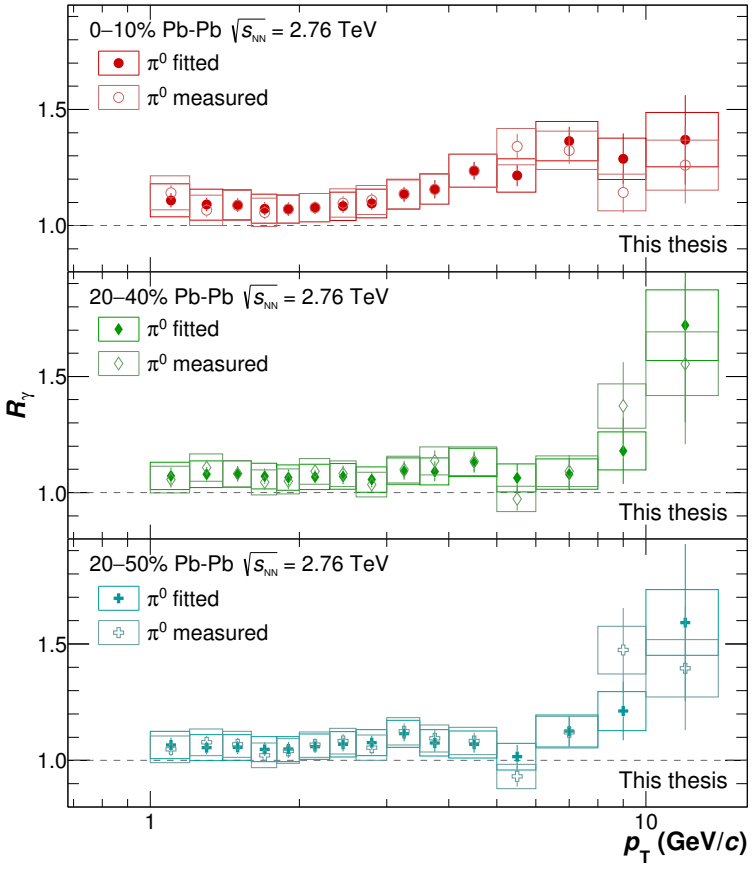

FIGURE F.5: Comparison of the R_γ calculated using the fit to the π^0 spectrum or the π^0 spectrum data points for the centrality classes 0–10%, 20–40% and 20–50%.

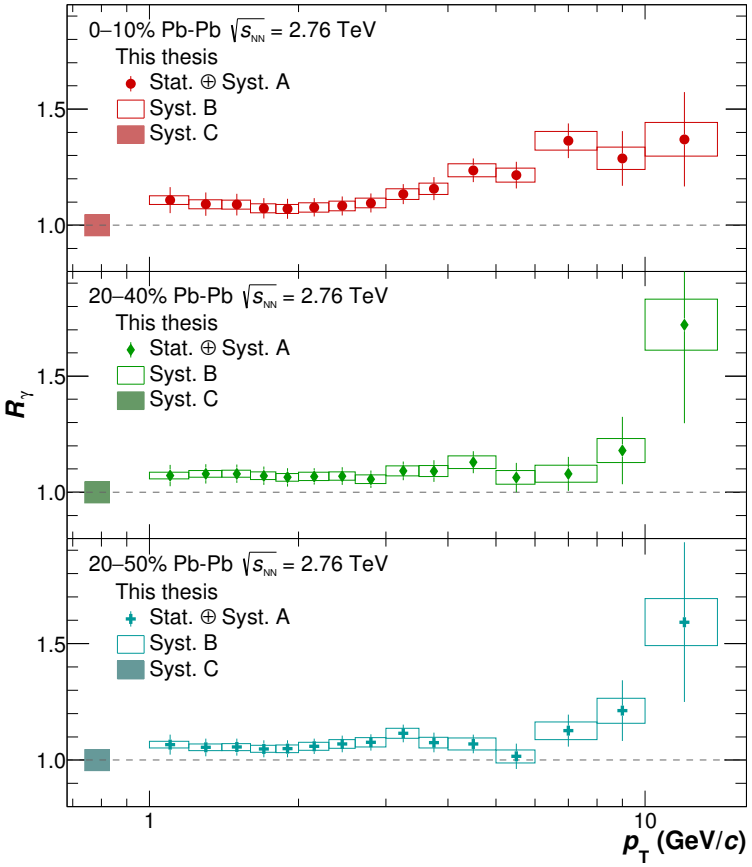

FIGURE F.6: Photon double ratio for the centrality classes 0–10%, 20–40% and 20–50%. The systematic uncertainties are represented separately according to their category: correlated point-by-point (type A), correlated in p_T and of p_T-dependent magnitude (type B) and constant uncertainties (type C).

Transverse momentum range	Signal significance		
	0–10%	20–40%	20–50%
1–1.6 GeV/c *	1.53 σ	1.30 σ	0.92 σ
1–1.8 GeV/c	1.45 σ	1.28 σ	0.87 σ
1–2.0 GeV/c	1.4 σ	1.25 σ	0.84 σ
1–2.3 GeV/c	1.4 σ	1.25 σ	0.88 σ

TABLE F.1: Significance of the direct photon signal estimated in different transverse momentum ranges. The range indicated with an asterisk is the one used for the values quoted in the main text.

F.3 Direct photon spectrum

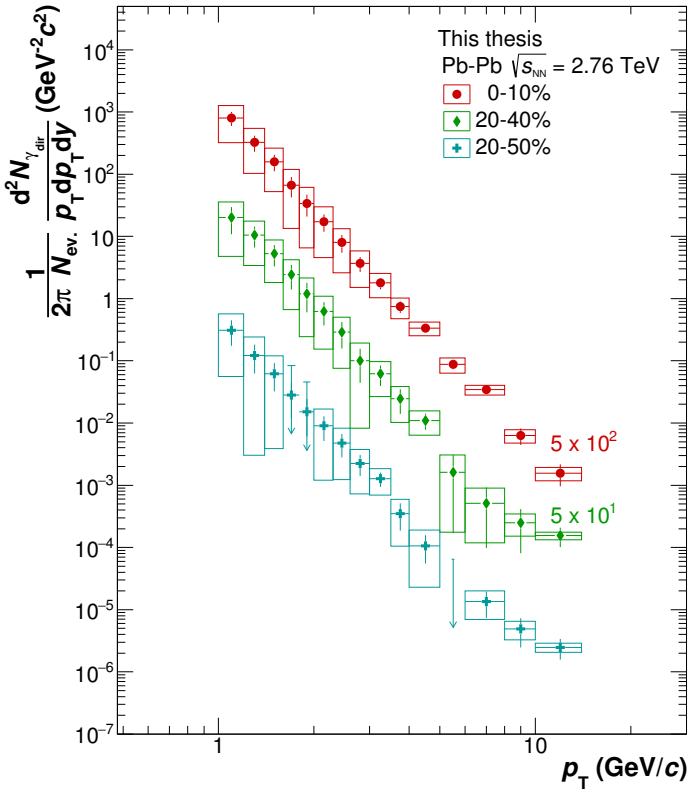

FIGURE F.7: Differential direct photon spectrum measured in the centrality classes 0–10%, 20–40% and 20–50%. The arrows represent upper limits with 95% confidence level.

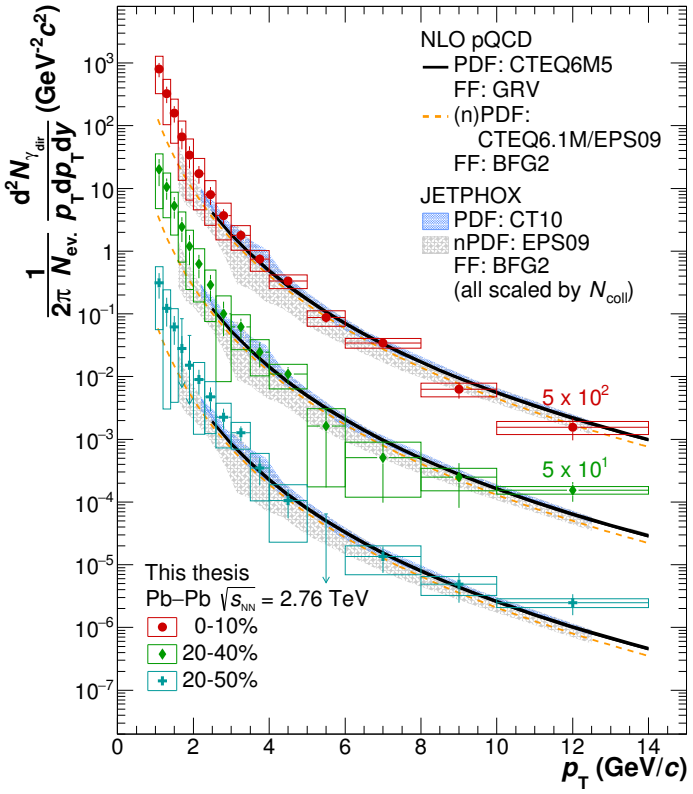

FIGURE F.8: Differential direct photon spectrum measured in the centrality classes 0–10%, 20–40% and 20–50%, compared to NLO pQCD calculations. See main text for references.

Transverse momentum range	$T_{\mathrm{eff}}^{\mathrm{direct}\gamma}$ (MeV)	
	0–10%	20–40%
1–1.6 GeV/c	$246 \pm 61^{\mathrm{stat}} \pm 141^{\mathrm{syst}}$	$300 \pm 130^{\mathrm{stat}} \pm 220^{\mathrm{syst}}$
1–1.8 GeV/c	$244 \pm 41^{\mathrm{stat}} \pm 93^{\mathrm{syst}}$	$284 \pm 76^{\mathrm{stat}} \pm 128^{\mathrm{syst}}$
1–2.0 GeV/c	$250 \pm 33^{\mathrm{stat}} \pm 74^{\mathrm{syst}}$	$281 \pm 56^{\mathrm{stat}} \pm 92^{\mathrm{syst}}$
1–2.3 GeV/c *	$270 \pm 30^{\mathrm{stat}} \pm 65^{\mathrm{syst}}$	$294 \pm 45^{\mathrm{stat}} \pm 78^{\mathrm{syst}}$
	$T_{\mathrm{eff}}^{\mathrm{thermal}\gamma}$ (MeV)	
	0–10%	20–40%
1–1.6 GeV/c	$235 \pm 57^{\mathrm{stat}} \pm 130^{\mathrm{syst}}$	$294 \pm 125^{\mathrm{stat}} \pm 214^{\mathrm{syst}}$
1–1.8 GeV/c	$230 \pm 35^{\mathrm{stat}} \pm 80^{\mathrm{syst}}$	$274 \pm 70^{\mathrm{stat}} \pm 117^{\mathrm{syst}}$
1–2.0 GeV/c	$232 \pm 28^{\mathrm{stat}} \pm 61^{\mathrm{syst}}$	$267 \pm 50^{\mathrm{stat}} \pm 80^{\mathrm{syst}}$
1–2.3 GeV/c *	$245 \pm 23^{\mathrm{stat}} \pm 53^{\mathrm{syst}}$	$276 \pm 38^{\mathrm{stat}} \pm 66^{\mathrm{syst}}$

TABLE F.2: Effective temperature extracted from the fit to the direct photon spectrum before, $T_{\mathrm{eff}}^{\mathrm{direct}\gamma}$, and after, $T_{\mathrm{eff}}^{\mathrm{thermal}\gamma}$, the subtraction of the prompt photon component, in different transverse momentum ranges. The range indicated with an asterisk is the one used for the values quoted in the main text.

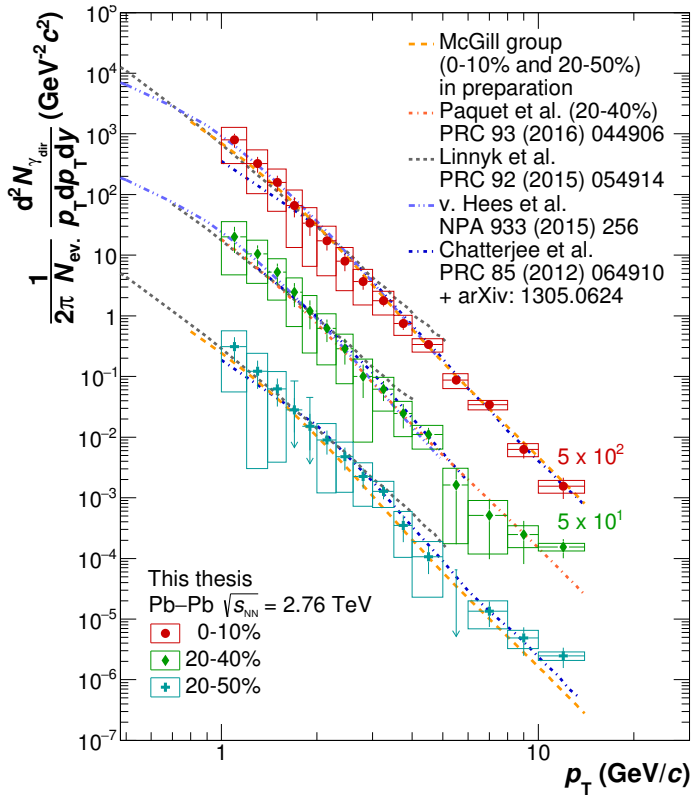

FIGURE F.9: Comparison of the differential direct photon spectrum measured in the centrality classes 0–10%, 20–40% and 20–50% to several direct photon calculations. See main text for references. The full x-axis range is shown here.

F.4 Direct photon nuclear modification factor R_{AA}

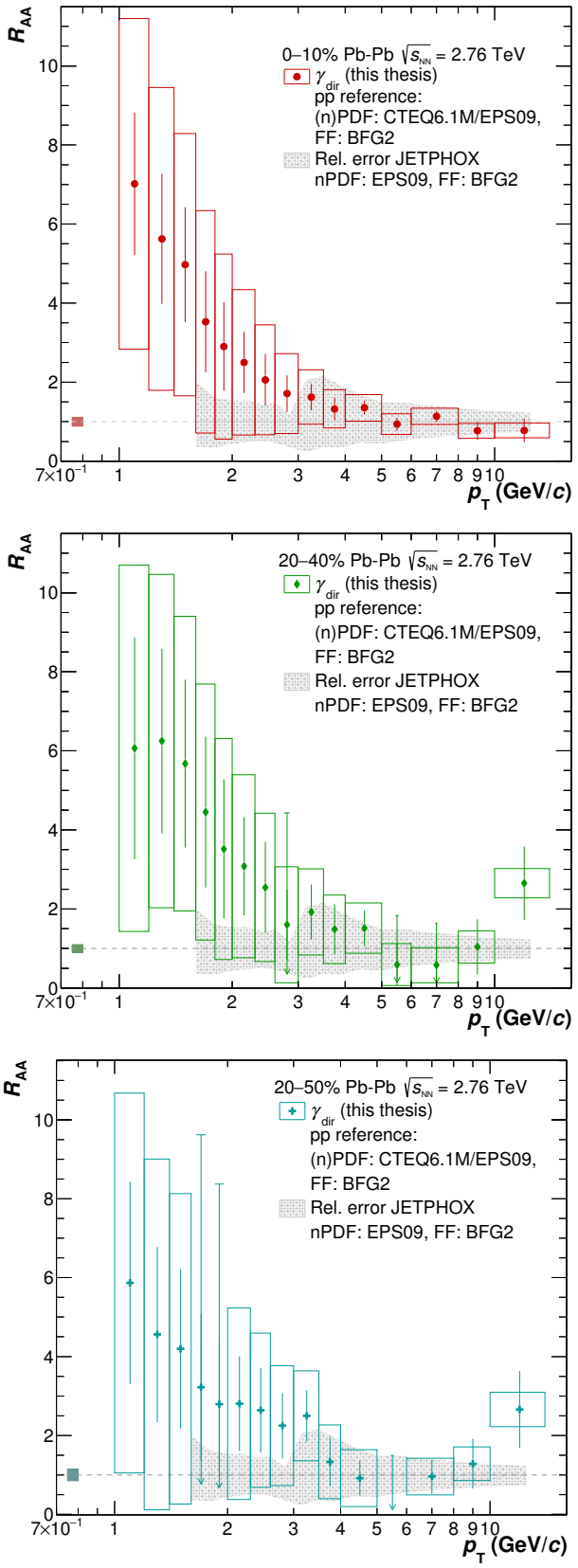

FIGURE F.10: Direct photon R_{AA} for the centrality classes 0–10% (top), 20–40% (middle) and 20–50% (bottom). The pp reference is provided by a pQCD calculation [156]. The box around unity represents the normalisation error while the grey band is the JETPHOX calculation uncertainty.

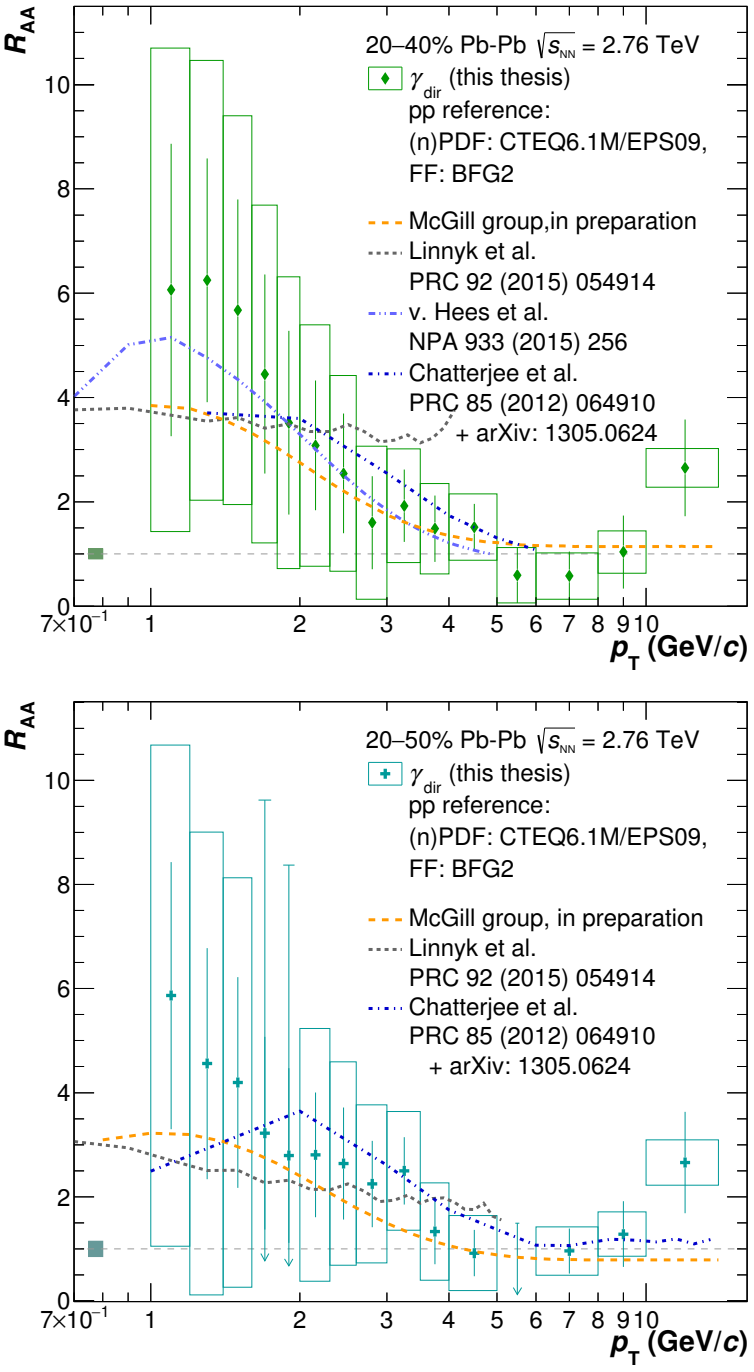

FIGURE F.11: Comparison of the direct photon R_{AA} in the centrality classes 20–40% (top) and 20–50% (bottom) to several direct photon calculations. See main text for references.

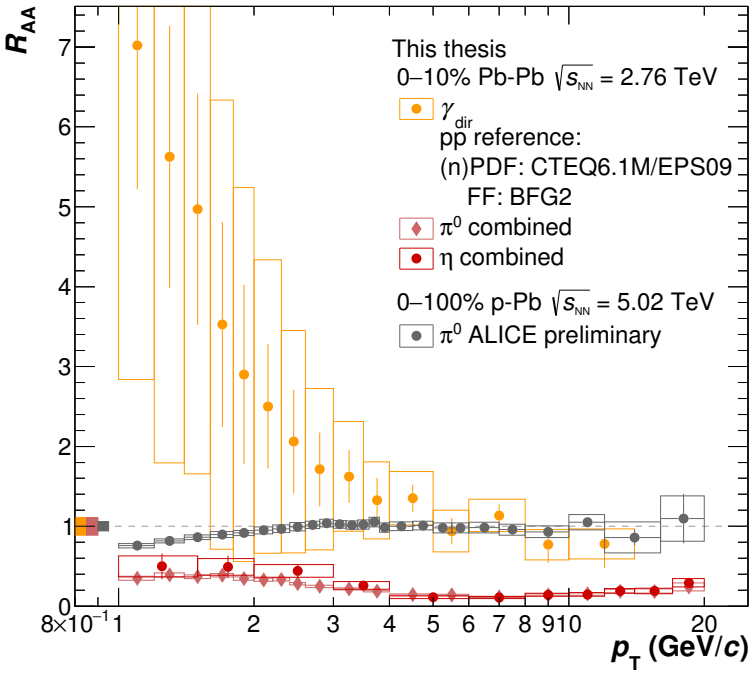

FIGURE F.12: Direct photon R_{AA} in 0–10% Pb–Pb collisions at $\sqrt{s_{NN}} = 2.76$ TeV compared to the neutral pion and η meson R_{AA}, in the same centrality class and collision energy, and to the neutral pion R_{AA} measured in 0–100% p–Pb collisions at $\sqrt{s_{NN}} = 5.02$ TeV centre-of-mass energy. The coloured boxes around unity represent the normalisation uncertainty. See main text for references.

Bibliography

[1] M. Gell-Mann, "The Eightfold Way: A Theory of strong interaction symmetry," 1961.

[2] Y. Ne'eman, "Derivation of strong interactions from a gauge invariance," *Nucl. Phys.* **26** (1961) 222–229.

[3] M. Gell-Mann, "A schematic model of baryons and mesons," *Phys. Lett.* **8** (1964) 214–215.

[4] G. Zweig, "An SU(3) model for strong interaction symmetry and its breaking. Version 1," 1964.

[5] H. Fritzsch and M. Gell-Mann, "Current algebra: Quarks and what else?," *eConf* **C720906V2** (1972) 135–165.

[6] H. Fritzsch, M. Gell-Mann, and H. Leutwyler, "Advantages of the Color Octet Gluon Picture," *Phys. Lett.* **B47** (1973) 365–368.

[7] R. P. Feynman, *The Behavior of Hadron Collisions at Extreme Energies*, pp. 289–304. Springer Netherlands, Dordrecht, 1988.

[8] G. Miller *et al.*, "Inelastic electron-Proton Scattering at Large Momentum Transfers," *Phys. Rev.* **D5** (1972) 528.

[9] **Particle Data Group** Collaboration, C. Patrignani *et al.*, "Review of Particle Physics," *Chin. Phys.* **C40** no. 10, (2016) 100001.

[10] A. Bettini, *Introduction to Elementary Particle Physics*. Cambridge University Press, 2014.

[11] J. D. Bjorken, "Asymptotic Sum Rules at Infinite Momentum," *Phys. Rev.* **179** (1969) 1547–1553.

[12] D. Griffiths, *Introduction to elementary particles*. Wiley, 1987.

[13] K. G. Wilson, "Confinement of Quarks," *Phys. Rev.* **D10** (1974) 2445–2459.

[14] D. J. Gross and F. Wilczek, "Ultraviolet Behavior of Nonabelian Gauge Theories," *Phys. Rev. Lett.* **30** (1973) 1343–1346.

[15] H. D. Politzer, "Reliable Perturbative Results for Strong Interactions?," *Phys. Rev. Lett.* **30** (1973) 1346–1349.

[16] J. C. Collins and M. J. Perry, "Superdense Matter: Neutrons Or Asymptotically Free Quarks?," *Phys. Rev. Lett.* **34** (1975) 1353.

[17] N. Cabibbo and G. Parisi, "Exponential Hadronic Spectrum and Quark Liberation," *Phys. Lett.* **B59** (1975) 67–69.

[18] R. Hagedorn, "Statistical thermodynamics of strong interactions at high-energies," *Nuovo Cim. Suppl.* **3** (1965) 147–186.

[19] H. Sazdjian, "Introduction to chiral symmetry in QCD," *EPJ Web Conf.* **137** (2017) 02001, arXiv:1612.04078 [hep-ph].

[20] H.-T. Ding, F. Karsch, and S. Mukherjee, "Thermodynamics of strong-interaction matter from Lattice QCD," *Int. J. Mod. Phys.* **E24** no. 10, (2015) 1530007, arXiv:1504.05274 [hep-lat].

[21] A. Bazavov *et al.*, "The chiral and deconfinement aspects of the QCD transition," *Phys. Rev.* **D85** (2012) 054503, arXiv:1111.1710 [hep-lat].

[22] Y. Aoki, Z. Fodor, S. D. Katz, and K. K. Szabo, "The QCD transition temperature: Results with physical masses in the continuum limit," *Phys. Lett.* **B643** (2006) 46–54, arXiv:hep-lat/0609068 [hep-lat].

[23] **Wuppertal-Budapest** Collaboration, S. Borsanyi, Z. Fodor, C. Hoelbling, S. D. Katz, S. Krieg, C. Ratti, and K. K. Szabo, "Is there still any T_c mystery in lattice QCD? Results with physical masses in the continuum limit III," *JHEP* **09** (2010) 073, arXiv:1005.3508 [hep-lat].

[24] F. Karsch, E. Laermann, and A. Peikert, "Quark mass and flavor dependence of the QCD phase transition," *Nucl. Phys.* **B605** (2001) 579–599, arXiv:hep-lat/0012023 [hep-lat].

[25] F. Karsch, "Lattice results on QCD thermodynamics," *Nucl. Phys.* **A698** (2002) 199–208, arXiv:hep-ph/0103314 [hep-ph].

[26] G. Baym, "Confinement of quarks in nuclear matter," *Physica A: Statistical Mechanics and its Applications* **96** (1979) 131 – 135.

[27] T. Celik, F. Karsch, and H. Satz, "A percolation approach to strongly interacting matter," *Phys. Lett.* **B97** (1980) 128–130.

[28] K. Redlich and H. Satz, "The Legacy of Rolf Hagedorn: Statistical Bootstrap and Ultimate Temperature," in *Melting Hadrons, Boiling Quarks - From Hagedorn Temperature to Ultra-Relativistic Heavy-Ion Collisions at CERN: With a Tribute to Rolf Hagedorn*, J. Rafelski, ed., pp. 49–68. 2016. arXiv:1501.07523 [hep-ph]. https://inspirehep.net/record/1342017/files/arXiv:1501.07523.pdf.

[29] A. Andronic, P. Braun-Munzinger, K. Redlich, and J. Stachel, "Hadron yields, the chemical freeze-out and the QCD phase diagram," *J. Phys. Conf. Ser.* **779** no. 1, (2017) 012012, arXiv:1611.01347 [nucl-th].

[30] Experiment Proposals on QCD Physics, "FAIR - Baseline Technical Report, Vol. 3a," tech. rep., 2006.

[31] **STAR** Collaboration, L. Adamczyk *et al.*, "Bulk Properties of the Medium Produced in Relativistic Heavy-Ion Collisions from the Beam Energy Scan Program," arXiv:1701.07065 [nucl-ex].

[32] F. Becattini, J. Steinheimer, R. Stock, and M. Bleicher, "Hadronization conditions in relativistic nuclear collisions and the QCD pseudo-critical line," *Phys. Lett.* **B764** (2017) 241–246, arXiv:1605.09694 [nucl-th].

[33] **HotQCD** Collaboration, A. Bazavov *et al.*, "Equation of state in (2+1)-flavor QCD," *Phys. Rev.* **D90** (2014) 094503, arXiv:1407.6387 [hep-lat].

[34] A. Bazavov *et al.*, "The QCD Equation of State to $\mathcal{O}(\mu_B^6)$ from Lattice QCD," *Phys. Rev.* **D95** no. 5, (2017) 054504, arXiv:1701.04325 [hep-lat].

[35] A. Dainese, *Charm production and in-medium QCD energy loss in nucleus nucleus collisions with ALICE: A Performance study.* PhD thesis, Padua U., 2003. arXiv:nucl-ex/0311004 [nucl-ex].

[36] M. L. Miller, K. Reygers, S. J. Sanders, and P. Steinberg, "Glauber modeling in high energy nuclear collisions," *Ann. Rev. Nucl. Part. Sci.* **57** (2007) 205–243, arXiv:nucl-ex/0701025 [nucl-ex].

[37] P. F. Kolb and U. W. Heinz, "Hydrodynamic description of ultrarelativistic heavy ion collisions," arXiv:nucl-th/0305084 [nucl-th].

[38] P. Huovinen, "Hydrodynamical description of collective flow. Chapter 1.," arXiv:nucl-th/0305064 [nucl-th].

[39] T. Hirano and K. Tsuda, "Collective flow and two pion correlations from a relativistic hydrodynamic model with early chemical freezeout," *Phys. Rev.* **C66** (2002) 054905, arXiv:nucl-th/0205043 [nucl-th].

[40] C. Gale, S. Jeon, and B. Schenke, "Hydrodynamic Modeling of Heavy-Ion Collisions," *Int. J. Mod. Phys.* **A28** (2013) 1340011, arXiv:1301.5893 [nucl-th].

[41] H. Song and U. W. Heinz, "Extracting the QGP viscosity from RHIC data - A Status report from viscous hydrodynamics," *J. Phys.* **G36** (2009) 064033, arXiv:0812.4274 [nucl-th].

[42] P. Braun-Munzinger, K. Redlich, and J. Stachel, "Particle production in heavy-ion collisions," arXiv:nucl-th/0304013 [nucl-th].

[43] P. Braun-Munzinger, J. Stachel, and C. Wetterich, "Chemical freezeout and the QCD phase transition temperature," *Phys. Lett.* **B596** (2004) 61–69, arXiv:nucl-th/0311005 [nucl-th].

[44] **ALICE** Collaboration, J. Adam *et al.*, "Centrality dependence of the charged-particle multiplicity density at midrapidity in Pb-Pb collisions at $\sqrt{s_{\rm NN}} = 5.02$ TeV," *Phys. Rev. Lett.* **116** no. 22, (2016) 222302, arXiv:1512.06104 [nucl-ex].

[45] **ALICE** Collaboration, K. Aamodt *et al.*, "Centrality dependence of the charged-particle multiplicity density at mid-rapidity in Pb-Pb collisions at $\sqrt{s_{NN}} = 2.76$ TeV," *Phys. Rev. Lett.* **106** (2011) 032301, arXiv:1012.1657 [nucl-ex].

[46] **ATLAS** Collaboration, G. Aad *et al.*, "Measurement of the centrality dependence of the charged particle pseudorapidity distribution in lead-lead collisions at $\sqrt{s_{NN}} = 2.76$ TeV with the ATLAS detector," *Phys. Lett.* **B710** (2012) 363–382, arXiv:1108.6027 [hep-ex].

[47] **CMS** Collaboration, S. Chatrchyan *et al.*, "Dependence on pseudorapidity and centrality of charged hadron production in PbPb collisions at a nucleon-nucleon centre-of-mass energy of 2.76 TeV," *JHEP* **08** (2011) 141, arXiv:1107.4800 [nucl-ex].

[48] **NA50** Collaboration, M. C. Abreu *et al.*, "Scaling of charged particle multiplicity in Pb Pb collisions at SPS energies," *Phys. Lett.* **B530** (2002) 43–55.

[49] **BRAHMS** Collaboration, I. G. Bearden *et al.*, "Charged particle densities from Au+Au collisions at $\sqrt{s_{NN}} = 130$-GeV," *Phys. Lett.* **B523** (2001) 227–233, arXiv:nucl-ex/0108016 [nucl-ex].

[50] **BRAHMS** Collaboration, I. G. Bearden *et al.*, "Pseudorapidity distributions of charged particles from Au+Au collisions at the maximum RHIC energy," *Phys. Rev. Lett.* **88** (2002) 202301, arXiv:nucl-ex/0112001 [nucl-ex].

[51] **PHENIX** Collaboration, K. Adcox *et al.*, "Centrality dependence of charged particle multiplicity in Au - Au collisions at $\sqrt{s_{NN}} = 130$-GeV," *Phys. Rev. Lett.* **86** (2001) 3500–3505, arXiv:nucl-ex/0012008 [nucl-ex].

[52] **PHOBOS** Collaboration, B. Alver *et al.*, "Phobos results on charged particle multiplicity and pseudorapidity distributions in Au+Au, Cu+Cu, d+Au, and p+p collisions at ultra-relativistic energies," *Phys. Rev.* **C83** (2011) 024913, arXiv:1011.1940 [nucl-ex].

[53] **STAR** Collaboration, B. I. Abelev *et al.*, "Systematic Measurements of Identified Particle Spectra in pp, d+Au and Au+Au Collisions from STAR," *Phys. Rev.* **C79** (2009) 034909, arXiv:0808.2041 [nucl-ex].

[54] **ALICE** Collaboration, J. Adam *et al.*, "Charged-particle multiplicities in protonproton collisions at $\sqrt{s} = 0.9$ to 8 TeV," *Eur. Phys. J.* **C77** no. 1, (2017) 33, arXiv:1509.07541 [nucl-ex].

[55] **CMS** Collaboration, V. Khachatryan *et al.*, "Pseudorapidity distribution of charged hadrons in proton-proton collisions at $\sqrt{s} = 13$ TeV," *Phys. Lett.* **B751** (2015) 143–163, arXiv:1507.05915 [hep-ex].

[56] **ALICE** Collaboration, J. Adam *et al.*, "Pseudorapidity and transverse-momentum distributions of charged particles in protonproton collisions at $\sqrt{s} = 13$ TeV," *Phys. Lett.* **B753** (2016) 319–329, arXiv:1509.08734 [nucl-ex].

[57] **ALICE** Collaboration, B. Abelev *et al.*, "Pseudorapidity density of charged particles in p + Pb collisions at $\sqrt{s_{NN}} = 5.02$ TeV," *Phys. Rev. Lett.* **110** no. 3, (2013) 032301, arXiv:1210.3615 [nucl-ex].

[58] **PHOBOS** Collaboration, B. B. Back *et al.*, "Pseudorapidity distribution of charged particles in d + Au collisions at $\sqrt{s_{NN}} = 200$-GeV," *Phys. Rev. Lett.* **93** (2004) 082301, arXiv:nucl-ex/0311009 [nucl-ex].

[59] H. Niemi, K. J. Eskola, and R. Paatelainen, "Event-by-event fluctuations in a perturbative QCD + saturation + hydrodynamics model: Determining QCD matter shear viscosity in ultrarelativistic heavy-ion collisions," *Phys. Rev.* **C93** no. 2, (2016) 024907, arXiv:1505.02677 [hep-ph].

[60] H. Niemi, K. J. Eskola, R. Paatelainen, and K. Tuominen, "Predictions for 5.023 TeV Pb + Pb collisions at the CERN Large Hadron Collider," *Phys. Rev.* **C93** no. 1, (2016) 014912, arXiv:1511.04296 [hep-ph].

[61] W.-T. Deng, X.-N. Wang, and R. Xu, "Hadron production in p+p, p+Pb, and Pb+Pb collisions with the HIJING 2.0 model at energies available at the CERN Large Hadron Collider," *Phys. Rev.* **C83** (2011) 014915, arXiv:1008.1841 [hep-ph].

[62] A. Dumitru, D. E. Kharzeev, E. M. Levin, and Y. Nara, "Gluon Saturation in pA Collisions at the LHC: KLN Model Predictions For Hadron Multiplicities," *Phys. Rev.* **C85** (2012) 044920, arXiv:1111.3031 [hep-ph].

[63] J. L. Albacete, A. Dumitru, and Y. Nara, "CGC initial conditions at RHIC and LHC," *J. Phys. Conf. Ser.* **316** (2011) 012011, arXiv:1106.0978 [nucl-th].

[64] J. L. Albacete and A. Dumitru, "A model for gluon production in heavy-ion collisions at the LHC with rcBK unintegrated gluon densities," arXiv:1011.5161 [hep-ph].

[65] N. Armesto, C. A. Salgado, and U. A. Wiedemann, "Relating high-energy lepton-hadron, proton-nucleus and nucleus-nucleus collisions through geometric scaling," *Phys. Rev. Lett.* **94** (2005) 022002, arXiv:hep-ph/0407018 [hep-ph].

[66] D. Kharzeev, E. Levin, and M. Nardi, "Color glass condensate at the LHC: Hadron multiplicities in pp, pA and AA collisions," *Nucl. Phys.* **A747** (2005) 609–629, arXiv:hep-ph/0408050 [hep-ph].

[67] T. Pierog, I. Karpenko, J. M. Katzy, E. Yatsenko, and K. Werner, "EPOS LHC: Test of collective hadronization with data measured at the CERN Large Hadron Collider," *Phys. Rev.* **C92** no. 3, (2015) 034906, arXiv:1306.0121 [hep-ph].

[68] J. D. Bjorken, "Highly Relativistic Nucleus-Nucleus Collisions: The Central Rapidity Region," *Phys. Rev.* **D27** (1983) 140–151.

[69] **ALICE** Collaboration, J. Adam *et al.*, "Measurement of transverse energy at midrapidity in Pb-Pb collisions at $\sqrt{s_{\rm NN}} = 2.76$ TeV," *Phys. Rev.* **C94** no. 3, (2016) 034903, arXiv:1603.04775 [nucl-ex].

[70] **E-802** Collaboration, L. Ahle *et al.*, "Global transverse energy distributions in Si + Al, Au at 14.6-A/GeV/c and Au + Au at 11.6-A.GeV/c," *Phys. Lett.* **B332** (1994) 258–264.

[71] **NA49** Collaboration, T. Alber *et al.*, "Transverse energy production in Pb-208 + Pb collisions at 158-GeV per nucleon," *Phys. Rev. Lett.* **75** (1995) 3814–3817.

[72] **WA98** Collaboration, M. M. Aggarwal *et al.*, "Scaling of particle and transverse energy production in Pb-208 + Pb-208 collisions at 158-A-GeV," *Eur. Phys. J.* **C18** (2001) 651–663, arXiv:nucl-ex/0008004 [nucl-ex].

[73] **PHENIX** Collaboration, S. S. Adler *et al.*, "Systematic studies of the centrality and $\sqrt{s_{NN}}$ dependence of the $dE_T/d\eta$ and $dN_{ch}/d\eta$ in heavy ion collisions at mid-rapidity," *Phys. Rev.* **C71** (2005) 034908, arXiv:nucl-ex/0409015 [nucl-ex]. [Erratum: Phys. Rev.C71,049901(2005)].

[74] **STAR** Collaboration, J. Adams *et al.*, "Measurements of transverse energy distributions in Au + Au collisions at $\sqrt{s_{NN}}$ = 200-GeV," *Phys. Rev.* **C70** (2004) 054907, arXiv:nucl-ex/0407003 [nucl-ex].

[75] **PHENIX** Collaboration, A. Adare *et al.*, "Transverse energy production and charged-particle multiplicity at midrapidity in various systems from $\sqrt{s_{NN}}$ = 7.7 to 200 GeV," *Phys. Rev.* **C93** no. 2, (2016) 024901, arXiv:1509.06727 [nucl-ex].

[76] **CMS** Collaboration, S. Chatrchyan *et al.*, "Measurement of the pseudorapidity and centrality dependence of the transverse energy density in PbPb collisions at $\sqrt{s_{NN}}$ = 2.76 TeV," *Phys. Rev. Lett.* **109** (2012) 152303, arXiv:1205.2488 [nucl-ex].

[77] F. Becattini, J. Cleymans, A. Keranen, E. Suhonen, and K. Redlich, "Features of particle multiplicities and strangeness production in central heavy ion collisions between 1.7A-GeV/c and 158A-GeV/c," *Phys. Rev.* **C64** (2001) 024901, arXiv:hep-ph/0002267 [hep-ph].

[78] S. Wheaton and J. Cleymans, "THERMUS: A Thermal model package for ROOT," *Comput. Phys. Commun.* **180** (2009) 84–106, arXiv:hep-ph/0407174 [hep-ph].

[79] E. Schnedermann, J. Sollfrank, and U. W. Heinz, "Thermal phenomenology of hadrons from 200-A/GeV S+S collisions," *Phys. Rev.* **C48** (1993) 2462–2475, arXiv:nucl-th/9307020 [nucl-th].

[80] X. Luo, "Exploring the QCD Phase Structure with Beam Energy Scan in Heavy-ion Collisions," *Nucl. Phys.* **A956** (2016) 75–82, arXiv:1512.09215 [nucl-ex].

[81] C. Blume, "Is there Life after Hadronization? An Experimental Overview," *Acta Phys. Polon.* **B43** (2012) 577–586, arXiv:1111.7140 [nucl-ex].

[82] **ALICE** Collaboration, B. Abelev *et al.*, "Centrality Dependence of Charged Particle Production at Large Transverse Momentum in Pb–Pb Collisions at $\sqrt{s_{\rm NN}}$ = 2.76 TeV," *Phys. Lett.* **B720** (2013) 52–62, arXiv:1208.2711 [hep-ex].

[83] **CMS** Collaboration, S. Chatrchyan *et al.*, "Study of high-pT charged particle suppression in PbPb compared to *pp* collisions at $\sqrt{s_{NN}}$ = 2.76 TeV," *Eur. Phys. J.* **C72** (2012) 1945, arXiv:1202.2554 [nucl-ex].

[84] **CMS** Collaboration, S. Chatrchyan *et al.*, "Measurement of isolated photon production in *pp* and PbPb collisions at $\sqrt{s_{NN}}$ = 2.76 TeV," *Phys. Lett.* **B710** (2012) 256–277, arXiv:1201.3093 [nucl-ex].

[85] **CMS** Collaboration, S. Chatrchyan *et al.*, "Study of Z production in PbPb and pp collisions at $\sqrt{s_{\mathrm{NN}}} = 2.76$ TeV in the dimuon and dielectron decay channels," *JHEP* **03** (2015) 022, arXiv:1410.4825 [nucl-ex].

[86] **CMS** Collaboration, S. Chatrchyan *et al.*, "Study of W boson production in PbPb and pp collisions at $\sqrt{s_{NN}} = 2.76$ TeV," *Phys. Lett.* **B715** (2012) 66–87, arXiv:1205.6334 [nucl-ex].

[87] **ALICE** Collaboration, B. B. Abelev *et al.*, "Transverse momentum dependence of inclusive primary charged-particle production in p-Pb collisions at $\sqrt{s_{\mathrm{NN}}} = 5.02$ TeV," *Eur. Phys. J.* **C74** no. 9, (2014) 3054, arXiv:1405.2737 [nucl-ex].

[88] "Ellipsix Informatics." http://www.ellipsix.net/blog/tagged/heavy%20ion%20physics.html. Accessed: 2017-05-07.

[89] R. Baier, Y. L. Dokshitzer, A. H. Mueller, S. Peigne, and D. Schiff, "Radiative energy loss of high-energy quarks and gluons in a finite volume quark - gluon plasma," *Nucl. Phys.* **B483** (1997) 291–320, arXiv:hep-ph/9607355 [hep-ph].

[90] **ALICE** Collaboration, B. B. Abelev *et al.*, "Neutral pion production at midrapidity in pp and Pb-Pb collisions at $\sqrt{s_{\mathrm{NN}}} = 2.76\,\mathrm{TeV}$," *Eur. Phys. J.* **C74** no. 10, (2014) 3108, arXiv:1405.3794 [nucl-ex].

[91] **PHENIX** Collaboration, A. Adare *et al.*, "Evolution of π^0 suppression in Au+Au collisions from $\sqrt{s_{NN}} = 39$ to 200 GeV," *Phys. Rev. Lett.* **109** (2012) 152301, arXiv:1204.1526 [nucl-ex].

[92] **PHENIX** Collaboration, A. Adare *et al.*, "Suppression pattern of neutral pions at high transverse momentum in Au + Au collisions at $\sqrt{s_{NN}} = 200$-GeV and constraints on medium transport coefficients," *Phys. Rev. Lett.* **101** (2008) 232301, arXiv:0801.4020 [nucl-ex].

[93] **WA98** Collaboration, M. M. Aggarwal *et al.*, "Suppression of High-p(T) Neutral Pions in Central Pb+Pb Collisions at $\sqrt{s_{NN}} = 17.3$-GeV," *Phys. Rev. Lett.* **100** (2008) 242301, arXiv:0708.2630 [nucl-ex].

[94] F. Cooper and G. Frye, "Comment on the Single Particle Distribution in the Hydrodynamic and Statistical Thermodynamic Models of Multiparticle Production," *Phys. Rev.* **D10** (1974) 186.

[95] **Helios** Collaboration, T. Akesson *et al.*, "Inclusive Negative Particle $p(T)$ Spectra in P - Nucleus and Nucleus-nucleus Collisions at 200-GeV Per Nucleon," *Z. Phys.* **C46** (1990) 361–368.

[96] **E-802** Collaboration, T. Abbott *et al.*, "Kaon and pion production in central Si + Au collisions at 14.6-A/GeV/c.," *Phys. Rev. Lett.* **64** (1990) 847–850.

[97] **ALICE** Collaboration, B. Abelev *et al.*, "Centrality dependence of π, K, p production in Pb-Pb collisions at $\sqrt{s_{NN}} = 2.76$ TeV," *Phys. Rev.* **C88** (2013) 044910, arXiv:1303.0737 [hep-ex].

[98] **STAR** Collaboration, J. Adams *et al.*, "Experimental and theoretical challenges in the search for the quark gluon plasma: The STAR Collaboration's critical assessment of the evidence from RHIC collisions," *Nucl. Phys.* **A757** (2005) 102–183, arXiv:nucl-ex/0501009 [nucl-ex].

[99] U. W. Heinz, "Concepts of heavy ion physics," in *2002 European School of high-energy physics, Pylos, Greece, 25 Aug-7 Sep 2002: Proceedings*, pp. 165–238. 2004. arXiv:hep-ph/0407360 [hep-ph]. http://doc.cern.ch/yellowrep/CERN-2004-001.

[100] **PHENIX** Collaboration, S. S. Adler *et al.*, "Identified charged particle spectra and yields in Au+Au collisions at $\sqrt{s}_{NN}$ = 200-GeV," *Phys. Rev.* **C69** (2004) 034909, arXiv:nucl-ex/0307022 [nucl-ex].

[101] J. Stachel and K. Reygers, "Quark-Gluon Plasma Physics: from fixed target to the LHC - Lecture 6." http://www.physi.uni-heidelberg.de/~reygers/lectures/2015/qgp/qgp_lecture_ss2015.html, 2015.

[102] S. Voloshin and Y. Zhang, "Flow study in relativistic nuclear collisions by Fourier expansion of Azimuthal particle distributions," *Z. Phys.* **C70** (1996) 665–672, arXiv:hep-ph/9407282 [hep-ph].

[103] **ALICE** Collaboration, B. Abelev *et al.*, "Directed Flow of Charged Particles at Midrapidity Relative to the Spectator Plane in Pb-Pb Collisions at $\sqrt{s_{NN}}$=2.76 TeV," *Phys. Rev. Lett.* **111** no. 23, (2013) 232302, arXiv:1306.4145 [nucl-ex].

[104] **ALICE** Collaboration, B. B. Abelev *et al.*, "Elliptic flow of identified hadrons in Pb-Pb collisions at $\sqrt{s_{\rm NN}}$ = 2.76 TeV," *JHEP* **06** (2015) 190, arXiv:1405.4632 [nucl-ex].

[105] **ALICE** Collaboration, J. Adam *et al.*, "Anisotropic flow of charged particles in Pb-Pb collisions at $\sqrt{s_{\rm NN}}$ = 5.02 TeV," *Phys. Rev. Lett.* **116** no. 13, (2016) 132302, arXiv:1602.01119 [nucl-ex].

[106] **ALICE** Collaboration, K. Aamodt *et al.*, "Elliptic flow of charged particles in Pb-Pb collisions at 2.76 TeV," *Phys. Rev. Lett.* **105** (2010) 252302, arXiv:1011.3914 [nucl-ex].

[107] **ALICE** Collaboration, K. Aamodt *et al.*, "Higher harmonic anisotropic flow measurements of charged particles in Pb-Pb collisions at $\sqrt{s_{NN}}$=2.76 TeV," *Phys. Rev. Lett.* **107** (2011) 032301, arXiv:1105.3865 [nucl-ex].

[108] **ALICE** Collaboration, J. Adam *et al.*, "Higher harmonic flow coefficients of identified hadrons in Pb-Pb collisions at $\sqrt{s_{\rm NN}}$ = 2.76 TeV," *JHEP* **09** (2016) 164, arXiv:1606.06057 [nucl-ex].

[109] T. Matsui and H. Satz, "J/ψ Suppression by Quark-Gluon Plasma Formation," *Phys. Lett.* **B178** (1986) 416–422.

[110] H. Satz, "Color Screening in SU(N) Gauge Theory at Finite Temperature," *Nucl. Phys.* **A418** (1984) 447C–465C.

[111] S. J. Brodsky and A. H. Mueller, "Using Nuclei to Probe Hadronization in QCD," *Phys. Lett.* **B206** (1988) 685–690.

[112] N. Armesto and A. Capella, "A Quantitative reanalysis of J / psi suppression in nuclear collisions," *Phys. Lett.* **B430** (1998) 23–31, arXiv:hep-ph/9705275 [hep-ph].

[113] F. Becattini, L. Maiani, F. Piccinini, A. D. Polosa, and V. Riquer, "Correlating strangeness enhancement and J/psi suppression in heavy ion collisions at s(NN)**1/2 = 17.2-GeV," *Phys. Lett.* **B632** (2006) 233–237, arXiv:hep-ph/0508188 [hep-ph].

[114] P. Braun-Munzinger and J. Stachel, "The quest for the quark-gluon plasma," *Nature* **448** (2007) 302–309.

[115] P. Braun-Munzinger and J. Stachel, "Charmonium from Statistical Hadronization of Heavy Quarks: A Probe for Deconfinement in the Quark-Gluon Plasma," *Landolt-Bornstein* **23** (2010) 424, arXiv:0901.2500 [nucl-th].

[116] **NA38** Collaboration, M. C. Abreu *et al.*, "J / psi, psi-prime and Drell-Yan production in S U interactions at 200-GeV per nucleon," *Phys. Lett.* **B449** (1999) 128–136.

[117] **NA38** Collaboration, M. C. Abreu *et al.*, "Charmonia production in 450-GeV/c proton induced reactions," *Phys. Lett.* **B444** (1998) 516–522.

[118] M. C. Abreu *et al.*, "J / psi and psi-prime production in p, O and S induced reactions at SPS energies," *Phys. Lett.* **B466** (1999) 408–414.

[119] **NA50** Collaboration, M. C. Abreu *et al.*, "Evidence for deconfinement of quarks and gluons from the J / psi suppression pattern measured in Pb + Pb collisions at the CERN SPS," *Phys. Lett.* **B477** (2000) 28–36.

[120] L. Kluberg and H. Satz, "Color Deconfinement and Charmonium Production in Nuclear Collisions," arXiv:0901.3831 [hep-ph].

[121] A. Andronic *et al.*, "Heavy-flavour and quarkonium production in the LHC era: from protonproton to heavy-ion collisions," *Eur. Phys. J.* **C76** no. 3, (2016) 107, arXiv:1506.03981 [nucl-ex].

[122] J. Rafelski and B. Muller, "Strangeness Production in the Quark - Gluon Plasma," *Phys. Rev. Lett.* **48** (1982) 1066. [Erratum: Phys. Rev. Lett.56,2334(1986)].

[123] P. Koch, B. Muller, and J. Rafelski, "Strangeness in Relativistic Heavy Ion Collisions," *Phys. Rept.* **142** (1986) 167–262.

[124] **ALICE** Collaboration, B. B. Abelev *et al.*, "Multi-strange baryon production at mid-rapidity in Pb-Pb collisions at $\sqrt{s_{NN}} = 2.76$ TeV," *Phys. Lett.* **B728** (2014) 216–227, arXiv:1307.5543 [nucl-ex]. [Erratum: Phys. Lett.B734,409(2014)].

[125] T. Sjostrand, S. Mrenna, and P. Z. Skands, "A Brief Introduction to PYTHIA 8.1," *Comput. Phys. Commun.* **178** (2008) 852–867, arXiv:0710.3820 [hep-ph].

[126] C. Flensburg, G. Gustafson, and L. Lonnblad, "Inclusive and Exclusive Observables from Dipoles in High Energy Collisions," *JHEP* **08** (2011) 103, arXiv:1103.4321 [hep-ph].

[127] C. Bierlich, G. Gustafson, L. Lnnblad, and A. Tarasov, "Effects of Overlapping Strings in pp Collisions," *JHEP* **03** (2015) 148, arXiv:1412.6259 [hep-ph].

[128] C. Bierlich and J. R. Christiansen, "Effects of color reconnection on hadron flavor observables," *Phys. Rev.* **D92** no. 9, (2015) 094010, arXiv:1507.02091 [hep-ph].

[129] **ALICE** Collaboration, B. B. Abelev *et al.*, "Multiplicity Dependence of Pion, Kaon, Proton and Lambda Production in p-Pb Collisions at $\sqrt{s_{NN}} = 5.02$ TeV," *Phys. Lett.* **B728** (2014) 25–38, arXiv:1307.6796 [nucl-ex].

[130] **ALICE** Collaboration, J. Adam *et al.*, "Multi-strange baryon production in p-Pb collisions at $\sqrt{s_{\mathbf{NN}}} = 5.02$ TeV," *Phys. Lett.* **B758** (2016) 389–401, arXiv:1512.07227 [nucl-ex].

[131] C. Blume and C. Markert, "Strange hadron production in heavy ion collisions from SPS to RHIC," *Prog. Part. Nucl. Phys.* **66** (2011) 834–879, arXiv:1105.2798 [nucl-ex].

[132] **NA57** Collaboration, F. Antinori *et al.*, "Enhancement of hyperon production at central rapidity in 158-A-GeV/c Pb-Pb collisions," *J. Phys.* **G32** (2006) 427–442, arXiv:nucl-ex/0601021 [nucl-ex].

[133] **NA57** Collaboration, F. Antinori *et al.*, "Strangeness enhancements at central rapidity in 40 A GeV/c Pb-Pb collisions," *J. Phys.* **G37** (2010) 045105, arXiv:1001.1884 [nucl-ex].

[134] **STAR** Collaboration, B. I. Abelev *et al.*, "Enhanced strange baryon production in Au + Au collisions compared to p + p at $\sqrt{s_{NN}} = 200$ GeV," *Phys. Rev.* **C77** (2008) 044908, arXiv:0705.2511 [nucl-ex].

[135] **ALICE** Collaboration, J. Adam *et al.*, "Enhanced production of multi-strange hadrons in high-multiplicity proton-proton collisions," *Nature Phys.* (2017) , arXiv:1606.07424 [nucl-ex].

[136] S. Campbell, "Photon production from gluon-mediated quark–anti-quark annihilation at confinement," *Phys. Rev.* **C92** no. 1, (2015) 014907, arXiv:1504.01654 [nucl-ex].

[137] P. Aurenche, M. Fontannaz, J.-P. Guillet, E. Pilon, and M. Werlen, "A New critical study of photon production in hadronic collisions," *Phys. Rev.* **D73** (2006) 094007, arXiv:hep-ph/0602133 [hep-ph].

[138] **PHENIX** Collaboration, A. Adare *et al.*, "Enhanced production of direct photons in Au+Au collisions at $\sqrt{s_{NN}} = 200$ GeV and implications for the initial temperature," *Phys. Rev. Lett.* **104** (2010) 132301, arXiv:0804.4168 [nucl-ex].

[139] **PHENIX** Collaboration, S. S. Adler *et al.*, "Measurement of direct photon production in p + p collisions at $\sqrt{s_{NN}} = 200$ GeV," *Phys. Rev. Lett.* **98** (2007) 012002, arXiv:hep-ex/0609031 [hep-ex].

[140] **PHENIX** Collaboration, S. S. Adler *et al.*, "Centrality dependence of direct photon production in $\sqrt{s_{NN}} = 200$ GeV Au + Au collisions," *Phys. Rev. Lett.* **94** (2005) 232301, arXiv:nucl-ex/0503003 [nucl-ex].

[141] S. Turbide, R. Rapp, and C. Gale, "Hadronic production of thermal photons," *Phys. Rev.* **C69** (2004) 014903, arXiv:hep-ph/0308085 [hep-ph].

[142] **PHENIX** Collaboration, S. S. Adler *et al.*, "Suppressed π^0 production at large transverse momentum in central Au+ Au collisions at $\sqrt{s_{NN}} = 200$ GeV," *Phys. Rev. Lett.* **91** (2003) 072301, arXiv:nucl-ex/0304022 [nucl-ex].

[143] **PHENIX** Collaboration, S. S. Adler *et al.*, "High transverse momentum η meson production in p^+p, d^+ Au and Au+Au collisions at $\sqrt{s_{NN}} = 200$ GeV," *Phys. Rev.* **C75** (2007) 024909, arXiv:nucl-ex/0611006 [nucl-ex].

[144] L. E. Gordon and W. Vogelsang, "Polarized and unpolarized prompt photon production beyond the leading order," *Phys. Rev.* **D48** (1993) 3136–3159.

[145] L. E. Gordon and W. Vogelsang, "Polarized and unpolarized isolated prompt photon production beyond the leading order," *Phys. Rev.* **D50** (1994) 1901–1916.

[146] P. Aurenche, A. Douiri, R. Baier, M. Fontannaz, and D. Schiff, "Prompt Photon Production at Large p(T) in QCD Beyond the Leading Order," *Phys. Lett.* **B140** (1984) 87–92.

[147] P. Aurenche, R. Baier, M. Fontannaz, and D. Schiff, "Prompt photon production at large p_T scheme invariant qcd predictions and comparison with experiment," *Nuclear Physics B* **297** no. 4, (1988) 661 – 696. http://www.sciencedirect.com/science/article/pii/0550321388905536.

[148] I. Vitev and M. Gyulassy, "High p_T tomography of d + Au and Au+Au at SPS, RHIC, and LHC," *Phys. Rev. Lett.* **89** (2002) 252301, arXiv:hep-ph/0209161 [hep-ph].

[149] I. Vitev, "Jet tomography," *J. Phys.* **G30** (2004) S791–S800, arXiv:hep-ph/0403089 [hep-ph].

[150] J. Berges, K. Reygers, N. Tanji, and R. Venugopalan, "Parametric estimate of the relative photon yields from the glasma and the quark-gluon plasma in heavy-ion collisions," *Phys. Rev.* **C95** no. 5, (2017) 054904, arXiv:1701.05064 [nucl-th].

[151] R. Baier, A. H. Mueller, D. Schiff, and D. T. Son, "'Bottom up' thermalization in heavy ion collisions," *Phys. Lett.* **B502** (2001) 51–58, arXiv:hep-ph/0009237 [hep-ph].

[152] M. Chiu, T. K. Hemmick, V. Khachatryan, A. Leonidov, J. Liao, and L. McLerran, "Production of Photons and Dileptons in the Glasma," *Nucl. Phys.* **A900** (2013) 16–37, arXiv:1202.3679 [nucl-th].

[153] O. Linnyk, V. Konchakovski, T. Steinert, W. Cassing, and E. L. Bratkovskaya, "Hadronic and partonic sources of direct photons in relativistic heavy-ion collisions," *Phys. Rev.* **C92** no. 5, (2015) 054914, arXiv:1504.05699 [nucl-th].

[154] **ALICE** Collaboration, J. Adam *et al.*, "Direct photon production in Pb-Pb collisions at $\sqrt{s_{NN}} = 2.76$ TeV," *Phys. Lett.* **B754** (2016) 235–248, arXiv:1509.07324 [nucl-ex].

[155] **PHENIX** Collaboration, A. Adare *et al.*, "Centrality dependence of low-momentum direct-photon production in Au+Au collisions at $\sqrt{s_{NN}} = 200$ GeV," *Phys. Rev.* **C91** no. 6, (2015) 064904, arXiv:1405.3940 [nucl-ex].

[156] J.-F. Paquet, C. Shen, G. S. Denicol, M. Luzum, B. Schenke, S. Jeon, and C. Gale, "Production of photons in relativistic heavy-ion collisions," *Phys. Rev.* **C93** no. 4, (2016) 044906, arXiv:1509.06738 [hep-ph].

[157] H. van Hees, M. He, and R. Rapp, "Pseudo-critical enhancement of thermal photons in relativistic heavy-ion collisions?," *Nucl. Phys.* **A933** (2015) 256–271, arXiv:1404.2846 [nucl-th].

[158] R. Chatterjee, H. Holopainen, T. Renk, and K. J. Eskola, "Collision centrality and τ_0 dependence of the emission of thermal photons from fluctuating initial state in ideal hydrodynamic calculation," *Phys. Rev.* **C85** (2012) 064910, arXiv:1204.2249 [nucl-th].

[159] L. Evans and P. Bryant, "LHC Machine," *JINST* **3** (2008) S08001.

[160] "The CERN Document Server." http://cds.cern.ch. Accessed: 2016-05-16.

[161] **ALICE** Collaboration, K. Aamodt *et al.*, "The ALICE experiment at the CERN LHC," *JINST* **3** (2008) S08002.

[162] **ATLAS** Collaboration, G. Aad *et al.*, "The ATLAS Experiment at the CERN Large Hadron Collider," *JINST* **3** (2008) S08003.

[163] **CMS** Collaboration, S. Chatrchyan *et al.*, "The CMS Experiment at the CERN LHC," *JINST* **3** (2008) S08004.

[164] **LHCb** Collaboration, A. A. Alves, Jr. *et al.*, "The LHCb Detector at the LHC," *JINST* **3** (2008) S08005.

[165] **TOTEM** Collaboration, G. Anelli *et al.*, "The TOTEM experiment at the CERN Large Hadron Collider," *JINST* **3** (2008) S08007.

[166] **LHCf** Collaboration, O. Adriani *et al.*, "The LHCf detector at the CERN Large Hadron Collider," *JINST* **3** (2008) S08006.

[167] J. L. Pinfold, "The MoEDAL Experiment at the LHC a New Light on the Terascale Frontier," *J. Phys. Conf. Ser.* **631** no. 1, (2015) 012014.

[168] **MoEDAL** Collaboration, V. A. Mitsou, "The MoEDAL experiment at the LHC: status and results," in *5th Symposium on Prospects in the Physics of Discrete Symmetries (DISCRETE 2016) Warsaw, Poland, November 28-December 3, 2016*. 2017. arXiv:1703.07141 [hep-ex]. https://inspirehep.net/record/1518614/files/arXiv:1703.07141.pdf.

[169] **ALICE** Collaboration, B. B. Abelev *et al.*, "Performance of the ALICE Experiment at the CERN LHC," *Int. J. Mod. Phys.* **A29** (2014) 1430044, arXiv:1402.4476 [nucl-ex].

[170] **ALICE** Collaboration, K. Aamodt *et al.*, "Alignment of the ALICE Inner Tracking System with cosmic-ray tracks," *JINST* **5** (2010) P03003, arXiv:1001.0502 [physics.ins-det].

[171] J. Alme *et al.*, "The ALICE TPC, a large 3-dimensional tracking device with fast readout for ultra-high multiplicity events," *Nucl. Instrum. Meth.* **A622** (2010) 316–367, arXiv:1001.1950 [physics.ins-det].

[172] **ALICE** Collaboration, S. Acharya *et al.*, "The ALICE Transition Radiation Detector: construction, operation, and performance," arXiv:1709.02743 [physics.ins-det].

[173] **ALICE** Collaboration, P. Cortese *et al.*, "ALICE electromagnetic calorimeter technical design report,".

[174] **ALICE EMCal** Collaboration, J. Allen *et al.*, "Performance of prototypes for the ALICE electromagnetic calorimeter," *Nucl. Instrum. Meth.* **A615** (2010) 6–13, arXiv:0912.2005 [physics.ins-det].

[175] **ALICE** Collaboration, E. Abbas *et al.*, "Performance of the ALICE VZERO system," *JINST* **8** (2013) P10016, arXiv:1306.3130 [nucl-ex].

[176] M. Bondila *et al.*, "ALICE T0 detector," *IEEE Trans. Nucl. Sci.* **52** (2005) 1705–1711.

[177] R. Brun and F. Rademakers, "ROOT: An object oriented data analysis framework," *Nucl. Instrum. Meth.* **A389** (1997) 81–86.

[178] I. Antcheva *et al.*, "ROOT: A C++ framework for petabyte data storage, statistical analysis and visualization," *Comput. Phys. Commun.* **180** (2009) 2499–2512, arXiv:1508.07749 [physics.data-an].

[179] "ALICE software repository." https://github.com/alisw/.

[180] **LHCb** Collaboration, L. Massacrier, "First LHCb results from pA and Pb-Pb collisions," *PoS* **LHCP2016** (2016) 124, arXiv:1609.06477 [nucl-ex].

[181] M. Winn, "Heavy flavour production in proton-lead and lead-lead collisions with LHCb," in *26th International Conference on Ultrarelativistic Nucleus-Nucleus Collisions (Quark Matter 2017) Chicago,Illinois, USA, February 6-11, 2017*. 2017. arXiv:1704.04217 [nucl-ex]. https://inspirehep.net/record/1591532/files/arXiv:1704.04217.pdf.

[182] **ALICE** Collaboration, T. Kollegger, "The ALICE high level trigger: The 2011 run experience," in *Proceedings, 18th Real-Time Conference (RT2012): Berkley, USA, June 11-15, 2012*. 2012.

[183] **ALICE** Collaboration, M. Richter, "Data compression in ALICE by on-line track reconstruction and space point analysis," *J. Phys. Conf. Ser.* **396** (2012) 012043.

[184] D. A. Huffman, "A method for the construction of minimum-redundancy codes," *Resonance* **11** no. 2, (2006) 91–99. http://dx.doi.org/10.1007/BF02837279.

[185] **ALICE** Collaboration, B. Abelev *et al.*, "Centrality determination of Pb-Pb collisions at $\sqrt{s_{NN}} = 2.76$ TeV with ALICE," *Phys. Rev.* **C88** no. 4, (2013) 044909, arXiv:1301.4361 [nucl-ex].

[186] M. Rybczynski and W. Broniowski, "Wounded nucleon model with realistic nucleon-nucleon collision profile and observables in relativistic heavy-ion collisions," *Phys. Rev.* **C84** (2011) 064913, arXiv:1110.2609 [nucl-th].

[187] T. Sjostrand, S. Mrenna, and P. Z. Skands, "PYTHIA 6.4 Physics and Manual," *JHEP* **05** (2006) 026, arXiv:hep-ph/0603175 [hep-ph].

[188] S. Roesler, R. Engel, and J. Ranft, "The Monte Carlo event generator DPMJET-III," in *Advanced Monte Carlo for radiation physics, particle transport simulation and applications. Proceedings, Conference, MC2000, Lisbon, Portugal, October 23-26, 2000*, pp. 1033–1038. 2000. arXiv:hep-ph/0012252 [hep-ph]. http://www-public.slac.stanford.edu/sciDoc/docMeta.aspx?slacPubNumber=SLAC-PUB-8740.

[189] R. Engel and J. Ranft, "Hadronic photon-photon interactions at high-energies," *Phys. Rev.* **D54** (1996) 4244–4262, arXiv:hep-ph/9509373 [hep-ph].

[190] R. Brun, F. Bruyant, M. Maire, A. C. McPherson, and P. Zanarini, *GEANT 3: user's guide Geant 3.10, Geant 3.11; rev. version.* CERN, Geneva, 1987. https://cds.cern.ch/record/1119728.

[191] R. Brun, F. Bruyant, M. Maire, A. C. McPherson, and P. Zanarini, "GEANT3,".

[192] B. Andersson, G. Gustafson, and B. Nilsson-Almqvist, "A Model for Low p(t) Hadronic Reactions, with Generalizations to Hadron - Nucleus and Nucleus-Nucleus Collisions," *Nucl. Phys.* **B281** (1987) 289–309.

[193] B. Nilsson-Almqvist and E. Stenlund, "Interactions Between Hadrons and Nuclei: The Lund Monte Carlo, Fritiof Version 1.6," *Comput. Phys. Commun.* **43** (1987) 387.

[194] A. Capella, U. Sukhatme, C.-I. Tan, and J. Tran Thanh Van, "Dual parton model," *Phys. Rept.* **236** (1994) 225–329.

[195] W.-T. Deng, X.-N. Wang, and R. Xu, "Gluon shadowing and hadron production in heavy-ion collisions at LHC," *Phys. Lett.* **B701** (2011) 133–136.

[196] M. Gluck, E. Reya, and A. Vogt, "Dynamical parton distributions of the proton and small x physics," *Z. Phys.* **C67** (1995) 433–448.

[197] "The Kalman Filter." http://www.cs.unc.edu/~welch/kalman/. Accessed: 2016-05-16.

[198] L. Milano, "Vertex and track reconstruction with the ALICE inner tracking system." The 5th International Nordic "LHC and Beyond" Workshop, 2010.

[199] Y. Belikov, M. Ivanov, K. Safarik, and J. Bracinik, "TPC tracking and particle identification in high density environment," *eConf* **C0303241** (2003) TULT011, arXiv:physics/0306108 [physics].

[200] F. Bock, "ALICE Capabilities for Studying Photon Physics with the Conversion Method at LHC Energies," Bachelor thesis, Heidelberg University, 2010.

[201] W. Blum, W. Riegler, L. Rolandi, *Particle Detection with Drift Chambers*. Springer-Verlag, 2008.

[202] T. Dahms, "Measurement of photons via conversion pairs with the PHENIX experiment at RHIC." Doctoral thesis, 2005.

[203] G. D. Lafferty and T. R. Wyatt, "Where to stick your data points: The treatment of measurements within wide bins," *Nucl. Instrum. Meth.* **A355** (1995) 541–547.

[204] **ALICE** Collaboration, B. B. Abelev *et al.*, "Production of charged pions, kaons and protons at large transverse momenta in pp and PbPb collisions at $\sqrt{s_{\rm NN}}$ =2.76 TeV," *Phys. Lett.* **B736** (2014) 196–207, arXiv:1401.1250 [nucl-ex].

[205] **ALICE** Collaboration, B. Abelev *et al.*, "Pion, Kaon, and Proton Production in Central Pb–Pb Collisions at $\sqrt{s_{NN}} = 2.76$ TeV," *Phys. Rev. Lett.* **109** (2012) 252301, arXiv:1208.1974 [hep-ex].

[206] **ALICE** Collaboration, S. Acharya *et al.*, "Production of π^0 and η mesons up to high transverse momentum in pp collisions at 2.76 TeV," *Eur. Phys. J.* **C77** no. 5, (2017) 339, arXiv:1702.00917 [hep-ex].

[207] M. Bourquin and J. M. Gaillard, "A Simple Phenomenological Description of Hadron Production," *Nucl. Phys.* **B114** (1976) 334–364.

[208] K. Jiang, Y. Zhu, W. Liu, H. Chen, C. Li, L. Ruan, Z. Tang, Z. Xu, and Z. Xu, "Onset of radial flow in p+p collisions," *Phys. Rev.* **C91** no. 2, (2015) 024910, arXiv:1312.4230 [nucl-ex].

[209] G. Agakishiev *et al.*, "Neutral meson production in p Be and p Au collisions at 450-GeV beam energy," *Eur. Phys. J.* **C4** (1998) 249–257.

[210] P. K. Khandai, P. Shukla, and V. Singh, "Meson spectra and m_T scaling in $p + p$, d+Au, and Au + Au collisions at $\sqrt{s_{NN}} = 200$ GeV," *Phys. Rev.* **C84** (2011) 054904, arXiv:1110.3929 [hep-ph].

[211] **PHENIX** Collaboration, S. S. Adler *et al.*, "Common suppression pattern of eta and pi0 mesons at high transverse momentum in Au+Au collisions at $\sqrt{s_{NN}} = 200$-GeV," *Phys. Rev. Lett.* **96** (2006) 202301, arXiv:nucl-ex/0601037 [nucl-ex].

[212] Okubo, Tsubasa, "Neutral meson production in p-pb collisions with alice at the lhc," *EPJ Web Conf.* **141** (2017) 08010. https://doi.org/10.1051/epjconf/201714108010.

[213] F. Arleo, "Quenching of Hadron Spectra in Heavy Ion Collisions at the LHC," arXiv:1703.10852 [hep-ph].

[214] **ALICE** Collaboration, A. Morreale, "Production of π^0, $K^{\pm}$ and η mesons in Pb-Pb and pp collisions at $\sqrt{s_{\rm NN}}$ =2.76 TeV measured with the ALICE detector at the LHC," *J. Phys. Conf. Ser.* **779** no. 1, (2017) 012051, arXiv:1609.06106 [hep-ex].

[215] A. A. Bylinkin and A. A. Rostovtsev, "Parametrization of the shape of hadron-production spectra in high-energy particle interactions," *Phys. Atom. Nucl.* **75** (2012) 999–1005. [Yad. Fiz.75,1060(2012)].

[216] A. Bylinkin, N. S. Chernyavskaya, and A. A. Rostovtsev, "Predictions on the transverse momentum spectra for charged particle production at LHC-energies from a two component model," *Eur. Phys. J.* **C75** no. 4, (2015) 166, arXiv:1501.05235 [hep-ph].

[217] V. Begun, W. Florkowski, and M. Rybczynski, "Explanation of hadron transverse-momentum spectra in heavy-ion collisions at $\sqrt{s}_{NN} = 2.76$ TeV within chemical non-equilibrium statistical hadronization model," *Phys. Rev.* **C90** no. 1, (2014) 014906, arXiv:1312.1487 [nucl-th].

[218] Viktor Begun, "Resonances in a sudden chemical freeze-out model." International Conference on Strangeness in Quark Matter (SQM 2017), 2017.

[219] K. Werner, I. Karpenko, M. Bleicher, T. Pierog, and S. Porteboeuf-Houssais, "Jets, Bulk Matter, and their Interaction in Heavy Ion Collisions at Several TeV," *Phys. Rev.* **C85** (2012) 064907, arXiv:1203.5704 [nucl-th].

[220] W. Broniowski and W. Florkowski, "Explanation of the RHIC p(T) spectra in a thermal model with expansion," *Phys. Rev. Lett.* **87** (2001) 272302, arXiv:nucl-th/0106050 [nucl-th].

[221] A. Kisiel, T. Taluc, W. Broniowski, and W. Florkowski, "THERMINATOR: THERMal heavy-IoN generATOR," *Comput. Phys. Commun.* **174** (2006) 669–687, arXiv:nucl-th/0504047 [nucl-th].

[222] M. Petran and J. Rafelski, "Universal hadronization condition in heavy ion collisions at $\sqrt{s_{\rm NN}} = 62$ GeV and at $\sqrt{s_{\rm NN}} = 2.76$ TeV," *Phys. Rev.* **C88** no. 2, (2013) 021901, arXiv:1303.0913 [hep-ph].

[223] M. Petrn, J. Letessier, V. Petrek, and J. Rafelski, "Hadron production and quark-gluon plasma hadronization in Pb-Pb collisions at $\sqrt{s_{NN}} = 2.76$ TeV," *Phys. Rev.* **C88** no. 3, (2013) 034907, arXiv:1303.2098 [hep-ph].

[224] V. Begun, W. Florkowski, and M. Rybczynski, "Transverse-momentum spectra of strange particles produced in Pb+Pb collisions at $\sqrt{s_{\rm NN}} = 2.76$ TeV in the chemical non-equilibrium model," *Phys. Rev.* **C90** no. 5, (2014) 054912, arXiv:1405.7252 [hep-ph].

[225] B. Andersson, *The Lund Model*. Cambridge University Press, 1998.

[226] W. Dai, X.-F. Chen, B.-W. Zhang, and E. Wang, "η meson production of high-energy nuclear collisions at NLO," *Phys. Lett.* **B750** (2015) 390–395, arXiv:1506.00838 [nucl-th].

[227] S. Albino, B. A. Kniehl, and G. Kramer, "Fragmentation functions for light charged hadrons with complete quark flavor separation," *Nucl. Phys.* **B725** (2005) 181–206, arXiv:hep-ph/0502188 [hep-ph].

[228] S. Albino, B. A. Kniehl, and G. Kramer, "AKK Update: Improvements from New Theoretical Input and Experimental Data," *Nucl. Phys.* **B803** (2008) 42–104, arXiv:0803.2768 [hep-ph].

[229] C. A. Aidala, F. Ellinghaus, R. Sassot, J. P. Seele, and M. Stratmann, "Global Analysis of Fragmentation Functions for Eta Mesons," *Phys. Rev.* **D83** (2011) 034002, arXiv:1009.6145 [hep-ph].

[230] K. J. Eskola, H. Paukkunen, and C. A. Salgado, "EPS09: A New Generation of NLO and LO Nuclear Parton Distribution Functions," *JHEP* **04** (2009) 065, arXiv:0902.4154 [hep-ph].

[231] W. A. Horowitz, "LHC Predictions from an extended theory with Elastic, Inelastic, and Path Length Fluctuating Energy Loss," *Int. J. Mod. Phys.* **E16** (2007) 2193–2199, arXiv:nucl-th/0702084 [NUCL-TH].

[232] S. Wicks, W. Horowitz, M. Djordjevic, and M. Gyulassy, "Elastic, inelastic, and path length fluctuations in jet tomography," *Nucl. Phys.* **A784** (2007) 426–442, arXiv:nucl-th/0512076 [nucl-th].

[233] W. A. Horowitz and M. Gyulassy, "The Surprising Transparency of the sQGP at LHC," *Nucl. Phys.* **A872** (2011) 265–285, arXiv:1104.4958 [hep-ph].

[234] M. Djordjevic, "Collisional energy loss in a finite size QCD matter," *Phys. Rev.* **C74** (2006) 064907, arXiv:nucl-th/0603066 [nucl-th].

[235] M. Djordjevic, "Theoretical formalism of radiative jet energy loss in a finite size dynamical QCD medium," *Phys. Rev.* **C80** (2009) 064909, arXiv:0903.4591 [nucl-th].

[236] M. Djordjevic, M. Djordjevic, and B. Blagojevic, "RHIC and LHC jet suppression in non-central collisions," *Phys. Lett.* **B737** (2014) 298–302, arXiv:1405.4250 [nucl-th].

[237] D. de Florian, R. Sassot, and M. Stratmann, "Global analysis of fragmentation functions for pions and kaons and their uncertainties," *Phys. Rev.* **D75** (2007) 114010, arXiv:hep-ph/0703242 [HEP-PH].

[238] **ALICE** Collaboration, J. Adam *et al.*, "$\mathrm{K}^*(892)^0$ and $\phi(1020)$ meson production at high transverse momentum in pp and Pb-Pb collisions at $\sqrt{s_{\mathrm{NN}}} = 2.76$ TeV," *Phys. Rev.* **C95** no. 6, (2017) 064606, arXiv:1702.00555 [nucl-ex].

[239] **ALICE** Collaboration, B. B. Abelev *et al.*, "K^0_S and Λ production in Pb-Pb collisions at $\sqrt{s_{NN}} = 2.76$ TeV," *Phys. Rev. Lett.* **111** (2013) 222301, arXiv:1307.5530 [nucl-ex].

[240] K. Reygers. Private communication.

[241] **PHENIX** Collaboration, A. Adare *et al.*, "Detailed measurement of the e^+e^- pair continuum in $p+p$ and Au+Au collisions at $\sqrt{s_{NN}} = 200$ GeV and implications for direct photon production," *Phys. Rev.* **C81** (2010) 034911, arXiv:0912.0244 [nucl-ex].

[242] G. D'Agostini, "A Multidimensional unfolding method based on Bayes' theorem," *Nucl. Instrum. Meth.* **A362** (1995) 487–498.

[243] "RooUnfold: ROOT Unfolding Framework." `http://hepunx.rl.ac.uk/~adye/software/unfold/RooUnfold.html`.

[244] H. B. Prosper and L. Lyons, eds., *Proceedings, PHYSTAT 2011 Workshop on Statistical Issues Related to Discovery Claims in Search Experiments and Unfolding, CERN,Geneva, Switzerland 17-20 January 2011*, CERN. CERN, Geneva, 2011. `http://inspirehep.net/record/1087459/files/CERN-2011-006.pdf`.

[245] **ALICE collaboration** Collaboration, "Supplemental figures: Direct photon production in Pb-Pb collisions at $\sqrt{s_{\rm NN}} = 2.76$ TeV,". `https://cds.cern.ch/record/2102398`.

[246] W. Vogelsang and M. R. Whalley, "A Compilation of data on single and double prompt photon production in hadron hadron interactions," *J. Phys.* **G23** (1997) A1–A69.

[247] M. Gluck, E. Reya, and A. Vogt, "Parton fragmentation into photons beyond the leading order," *Phys. Rev.* **D48** (1993) 116. [Erratum: Phys. Rev.D51,1427(1995)].

[248] M. Klasen, C. Klein-Bsing, F. Knig, and J. P. Wessels, "How robust is a thermal photon interpretation of the ALICE low-p_T data?," *JHEP* **10** (2013) 119, `arXiv:1307.7034 [hep-ph]`.

[249] H.-L. Lai, M. Guzzi, J. Huston, Z. Li, P. M. Nadolsky, J. Pumplin, and C. P. Yuan, "New parton distributions for collider physics," *Phys. Rev.* **D82** (2010) 074024, `arXiv:1007.2241 [hep-ph]`.

[250] L. Bourhis, M. Fontannaz, and J. P. Guillet, "Quarks and gluon fragmentation functions into photons," *Eur. Phys. J.* **C2** (1998) 529–537, `arXiv:hep-ph/9704447 [hep-ph]`.

[251] C. Shen, U. W. Heinz, J.-F. Paquet, and C. Gale, "Thermal photons as a quark-gluon plasma thermometer reexamined," *Phys. Rev.* **C89** no. 4, (2014) 044910, `arXiv:1308.2440 [nucl-th]`.

[252] S. Ryu, J. F. Paquet, C. Shen, G. S. Denicol, B. Schenke, S. Jeon, and C. Gale, "Importance of the Bulk Viscosity of QCD in Ultrarelativistic Heavy-Ion Collisions," *Phys. Rev. Lett.* **115** no. 13, (2015) 132301, `arXiv:1502.01675 [nucl-th]`.

[253] B. Schenke, P. Tribedy, and R. Venugopalan, "Fluctuating Glasma initial conditions and flow in heavy ion collisions," *Phys. Rev. Lett.* **108** (2012) 252301, `arXiv:1202.6646 [nucl-th]`.

[254] S. A. Bass *et al.*, "Microscopic models for ultrarelativistic heavy ion collisions," *Prog. Part. Nucl. Phys.* **41** (1998) 255–369, `arXiv:nucl-th/9803035 [nucl-th]`. [Prog. Part. Nucl. Phys.41,225(1998)].

[255] M. Heffernan, P. Hohler, and R. Rapp, "Universal Parametrization of Thermal Photon Rates in Hadronic Matter," *Phys. Rev.* **C91** no. 2, (2015) 027902, `arXiv:1411.7012 [hep-ph]`.

[256] N. P. M. Holt, P. M. Hohler, and R. Rapp, "Thermal photon emission from the system," *Nucl. Phys.* **A945** (2016) 1–20, arXiv:1506.09205 [hep-ph].

[257] O. Linnyk, E. L. Bratkovskaya, and W. Cassing, "Effective QCD and transport description of dilepton and photon production in heavy-ion collisions and elementary processes," *Prog. Part. Nucl. Phys.* **87** (2016) 50–115, arXiv:1512.08126 [nucl-th].

[258] W. Cassing and E. L. Bratkovskaya, "Parton-Hadron-String Dynamics: an off-shell transport approach for relativistic energies," *Nucl. Phys.* **A831** (2009) 215–242, arXiv:0907.5331 [nucl-th].

[259] E. L. Bratkovskaya, W. Cassing, V. P. Konchakovski, and O. Linnyk, "Parton-Hadron-String Dynamics at Relativistic Collider Energies," *Nucl. Phys.* **A856** (2011) 162–182, arXiv:1101.5793 [nucl-th].

[260] M. He, R. J. Fries, and R. Rapp, "Ideal Hydrodynamics for Bulk and Multistrange Hadrons in $\sqrt{s_{NN}}$=200 AGeV Au-Au Collisions," *Phys. Rev.* **C85** (2012) 044911, arXiv:1112.5894 [nucl-th].

[261] J. P. Boris and D. L. Book, "Flux-corrected transport. I. SHASTA, a fluid transport algorithm that works," *J. Comput. Phys.* **11** no. 1, (1973) 38–69.

[262] M. Laine and Y. Schroder, "Quark mass thresholds in QCD thermodynamics," *Phys. Rev.* **D73** (2006) 085009, arXiv:hep-ph/0603048 [hep-ph].

[263] P. B. Arnold, G. D. Moore, and L. G. Yaffe, "Photon emission from quark gluon plasma: Complete leading order results," *JHEP* **12** (2001) 009, arXiv:hep-ph/0111107 [hep-ph].

Acknowledgements

I would like to thank my supervisor Prof. Dr. Johanna Stachel for the support given me during my doctoral studies and for the many opportunities to learn and grow as a researcher.
My sincere gratitude also to my supervisor Ana Marín, for teaching me, for her continuous support and encouragement.
Thanks to Friederike, for introducing me to the world of photon conversions and for the constructive discussions. And also for teaching me that everything is better if you have a cup of coffee in your hand.
Mein Dank gilt Michael, der mir seine große Leidenschaft für die Physik und die deutsche Kultur übermittelt hat. Aus diesem Grunde bin ich froh, mein Dankeschön auf Deutsch äußern zu können.
My thanks to all of those who helped me with the proofreading. Your patience is much appreciated.

Thanks to Ludwig. Our dinners together saved my sanity more than once.
Thanks to Michael, for the much needed coffee breaks.
To both, I am happy to have met you, I had fun these past years.

A Elena, Francesco, Gianmatteo. La vostra amicizia è un conforto e un piacere.

A mia madre, mio padre, mio fratello. Voi ringrazio con tutta me stessa. Per l'appoggio, per i sacrifici, per la sopportazione di malumori e lamentele, per aver avuto fiducia in me quando io per prima non ne avevo. La lista è infinita ma una sola cosa è importante.
Siete una famiglia splendida.